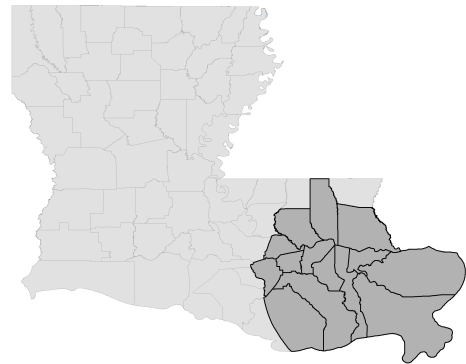


Flood Insurance Study: Southeastern Parishes, Louisiana

Intermediate Submission 2: Offshore Water Levels and Waves

24 July 2008



**Federal Emergency
Management Agency**
Region 6



**US Army Corps
of Engineers** ®
New Orleans District

Contributors

J. Westerink, J. Dietrich, S. Bunya, H. Westerink, S. Tanaka, R. Martyr,
M. Hope, L. Westerink; University of Notre Dame
J. Atkinson, L. Zevenbergen; Ayres Associates
H. Roberts, F. Clark; ARCADIS U.S., Inc.
B. Ebersole, J. Smith, R. Jensen, D. Resio, M. Cialone, T. Wamsley,
A. Sleath; USACE ERDC
J. Ratcliff, H. Pourtaheri, N. Powell, D. Elzey, V. Brisley, H. Winer, J. Hote,
V. Stutts; USACE MVN
C. Dawson, E. Kubatko; University of Texas at Austin
W. deJong; Royal Haskoning
R. Kolar, K. Dresback; University of Oklahoma
R. Luettich, B. Blanton, J. Flemming; University of North Carolina
at Chapel Hill
V. Cardone, A. Cox; Oceanweather, Inc.
M. Powell; HRD/NOAA

TABLE OF CONTENTS

1.0	INTRODUCTION	1
1.1	Purpose of Study	1
1.2	Authority and Acknowledgments	1
2.0	AREA STUDIED	1
2.1	Scope of Study	1
2.2	Community Description	2
2.2.1	Population	2
2.2.2	Study Setting Background	2
2.3	Principal Flood Problems	3
2.4	Flood Protection Measures	3
3.0	ENGINEERING METHODS	4
3.1	Physical and Hydrodynamic Description of the Region	5
3.1.1	Topographic and Bathymetric Data	6
3.1.1.1	Horizontal/Vertical Datum/Survey Control Data	6
3.1.1.2	Topographic Data from Aerial Photography	9
3.1.1.3	Topographic Surveys/Data	9
3.1.1.4	Bathymetric Surveys/Data	12
3.1.1.5	Vertical Features with Small Horizontal Scales	13
3.1.2	Influence of Coastal Vegetation	14
3.1.3	Site Reconnaissance	16
3.1.4	Technical Approach	17
3.1.4.1	Overview	17
3.1.4.2	Storm Selection	17
3.1.4.3	Winds	17
3.1.4.4	Surge Model	18

Table of Contents

3.1.4.5	Wave Models	18
3.1.4.6	Statistical Analysis	18
3.1.4.7	Workflow and Automation	18
3.1.4.8	ADCIRC Grids	19
3.1.4.9	Automation Process	19
3.2	Hydraulic Analysis	25
3.2.1	Modeling Strategy and System	25
3.2.2	Wind Models	27
3.2.2.1	Overview	27
3.2.2.2	Kinematic H*WIND/IOKA Procedure	27
3.2.2.3	Dynamic – PBL Wind Modeling	28
3.2.3	Wave Models	31
3.2.3.1	Offshore Waves – WAM	31
3.2.3.2	Production Summary	46
3.2.3.3	Summary and Conclusions	47
3.2.4	Nearshore Waves	48
3.2.4.1	STWAVE Overview	48
3.2.4.2	Nearshore Wave Model STWAVE	48
3.2.4.3	Wave Model Inputs	50
3.2.4.4	Wave Model Outputs	50
3.2.4.5	Nearshore Wave Modeling Methodology	50
3.2.4.6	Lake Pontchartrain Grid	51
3.2.4.7	Louisiana Southeast and South Grids and Mississippi/Alabama Grid	51
3.2.4.8	Comparison to Available Data	51
3.2.4.9	Sensitivity Analysis	52
3.2.4.10	Wind Input Sensitivity	53
3.2.4.11	Bathymetry Sensitivity	54
3.2.4.12	Time Dependent Simulations	55
3.2.4.13	Summary	55

Table of Contents

3.2.5	Circulation Model	56
3.2.5.1	ADCIRC Overview	56
3.2.5.2	ADCIRC Model Description	56
3.2.5.3	SL15 Domain/Grid Definition	61
3.2.5.4	Bathymetric/Topographic Definition	65
3.2.5.5	Feature Definition	67
3.2.5.6	Bottom and Lateral Friction Process	68
3.2.5.7	Tide and River Forcing Functions	69
3.2.5.8	LMSL and Steric Water Level Adjustments	70
3.2.5.9	Atmospheric Forcing Functions	71
3.2.5.10	Wave Radiation Stress Forcing	75
3.2.5.11	Model Operational Parameter Definitions	75
3.2.5.12	ADCIRC and STWAVE Model Performance	76
3.3	Hydrodynamic Modeling System Validation	76
3.3.1	Overview	76
3.3.2	Tidal Validation	77
3.3.3	Katrina Hindcast/Validation	81
3.3.3.1	Overview	81
3.3.3.2	Katrina WAM Computations/Validation	81
3.3.3.3	ADCIRC Parameter Definitions	81
3.3.3.4	ADCIRC Water Level and Current Computations	82
3.3.3.5	System Validation Using HWMs and Hydrographs	87
3.3.4	Rita Hindcast/Validation	91
3.3.4.1	Overview	91
3.3.4.2	Rita WAM Computations/Validation	92
3.3.4.3	Rita STWAVE Computations and Wave Radiation Stress	92
3.3.4.4	ADCIRC Parameter Definitions	94
3.3.4.5	ADCIRC Surge and Current Computations - Rita	94
3.3.4.6	System Validation using HWMs and Hydrographs	111

Table of Contents

3.4	Wind Forcing Model Sensitivities	118
3.4.1	Overview	118
3.4.2	Hurricane Katrina	118
3.4.3	Hurricane Rita	120
3.5	Quality Assurance/Quality Control Procedures	121
3.5.1	Overview	121
3.5.2	Nearshore Wave Model, STWAVE	121
3.5.2.1	Post-processing	121
3.5.2.2	Limited Review	122
3.5.3	Hydrodynamic Storm Surge Model, ADCIRC	124
3.5.3.1	Post-processing	124
3.5.3.2	Levee Treatment Validations under High Flow Conditions	125
3.5.3.3	Limited Review	126
3.5.3.4	Detailed Review	127
3.5.3.5	Mass Balance	128
4.0	STORM CLIMATOLOGY AND STORM WIND-FIELD METHODOLOGY	129
4.1	Storm Climatology and Joint Probability Method Introduction	129
4.1.1	The Joint Probability Method	129
4.1.2	JPM Measures of Variability in Expected Extremes	131
4.1.3	The Modified JPM (JPM-OS)	131
4.1.3.1	Estimation of Spatially Varying Probabilities	131
4.1.3.2	Estimation of the ϵ Term	135
4.1.3.3	Treatment of Subsidence and Sea Level Rise	137
4.1.3.4	Sampling of Storm Parameters for the JPM-OS	138
4.1.3.5	Specification of Variations in Pre-landfalling Hurricanes	139
4.1.4	Summary	139
4.2	Expedient Estimation of Return Periods for Specific Historical Storms	140

Table of Contents

4.2.1	Application to Hurricane Katrina	141
4.2.2	Application to Hurricane Rita	143
4.3	Selection of Wind Model for Coastal Surge Estimation	143
4.4	Selection of Period of Record for Surge Estimation and Consideration of the Effects of Climatic Variability on Surge Extremes	147
4.5	Selected Storm Sample for Simulations	150
4.5.1	Primary Tracks	155
4.5.2	Secondary Tracks	156
4.6	Characteristics of Holland B Parameter and Rmax	157
4.6.1	Introduction	157
4.6.2	Flight Level Data Analysis Methodology	158
4.6.3	Supplemental H*WIND Data	160
4.6.4	Statistical Model for Rmax	161
4.6.4.1	All Hurricanes	161
4.6.4.2	Gulf of Mexico Hurricanes	162
4.6.5	RMW (Rmax) for Landfalling Storms	163
4.6.6	Statistical Model for Holland's B Parameter	164
4.6.7	Comparisons of Flight Level vs. Landfall Analysis B Values	166
4.6.8	Summary	167
4.7	Integration Method	167
4.7.1	The Case of Simple Models Combined with Many Simulations	168
4.7.2	The Case of Optimized Category Definition	169
4.7.3	The Case of Structured Interpolation on a Response Surface	169
4.8	Estimation of Confidence Bands for Surge Estimates	173
4.9	JPM-OS Implementation Methodology	176

4.9.1	Overview	176
4.9.2	JPM-OS Software Input Requirements	176
4.9.3	Methodology Steps	176
4.9.4	JPM-OS Computation	177
4.9.5	JPM-OS Results	177
4.9.6	Methodology Used for Adding 10-Year Storm Information to the JPM-OS Estimates for Low-Intensity Storms	177
4.9.7	Blending Across Louisiana-Mississippi Border	179
5.0	REFERENCES	180

FIGURES (VOLUMES 3-6)

- Figure 1: Location map of Study Area.
- Figure 2: Inventory of existing levees.
- Figure 3: Topographic data source distribution.
- Figure 4: Topographic data sources for barrier islands on Louisiana and Mississippi coasts.
- Figure 5: Individually meshed water bodies throughout Southern Louisiana.
- Figure 6: Individually meshed water bodies in Southwestern Louisiana.
- Figure 7: Individually meshed water bodies in the southern Atchafalaya Basin.
- Figure 8: Individually meshed water bodies near Barataria Bay.
- Figure 9: Individually meshed water bodies around New Orleans.
- Figure 10: Louisiana Gap Analysis Program (LA-GAP) map
- Figure 11: Mississippi Gap Analysis Program (MS-GAP) map.
- Figure 12: Louisiana National Land Cover Data (NLCD) and enhanced NLCD map.
- Figure 13: Mississippi National Land Cover Data map.
- Figure 14: Texas National Land Cover Data map.
- Figure 15: Alabama National Land Cover Data map.
- Figure 16: National Land Cover Data Classifications used on Figures 12 through 15.

FIGURES (Continued)

- Figure 17: Process flow diagram.
- Figure 18: Footprints of the various model domains for the coupled ADCIRC/STWAVE system.
- Figure 19: ADCIRC bathymetry (in meters) for the SL15 grids along the northern Gulf of Mexico coast.
- Figure 20: ADCIRC grid detail in the New Orleans East area.
- Figure 21: Boundaries of the five STWAVE model domains and the PBL wind model northern extent used in the current implementation of the production simulation system.
- Figure 22: Water elevations along the Mississippi and Atchafalaya rivers showing the spin-up of the initial condition.
- Figure 23: Wind and pressure fields for storm 042 at landfall.
- Figure 24: Timeline for Production System simulations.
- Figure 25: Tracks used to define the 152 Louisiana Coastal Protection and Restoration storms.
- Figure 26: ADCIRC solution sampling points that define the station output in the fort.61 file.
- Figure 27: Data flow controlled by the Production System script prep_prod_sim.pl.
- Figure 28: Central angle tracks (RICK-fan set).
- Figure 29: Target domain for wind, pressure, and offshore wave estimates.
- Figure 30: Water depth contours for offshore wave model simulations.
- Figure 31: Refined version of the water depth grid used in offshore wave model simulations.
- Figure 32: The BRICKA (Betsy, Rita, Ivan, Camille, Katrina, and Andrew) storm tracks and wave measurement sites, where ST 1 through 6 are Ocean Data Gathering Project locations.
- Figure 33: Time plot at NDBC Buoy 42001 for Hurricane Rita, BRICKA storm verification simulations.
- Figure 34: Time plot at NDBC Buoy 42040 for Hurricane Ivan, BRICKA storm verification simulations.
- Figure 35: Time plot at ODGP Station 1 for Hurricane Camille, BRICKA storm verification simulations.
- Figure 36: Time plot at NDBC Buoy 42007 for Hurricane Katrina, BRICKA storm verification simulations.
- Figure 37: Time plot at NDBC Buoy 42003 for Hurricane Andrew, BRICKA storm verification simulations.
- Figure 38: The BRICKA (Betsy, Rita, Ivan, Camille, Katrina, and Andrew) storm WAM verification runs for significant wave height.

FIGURES (Continued)

- Figure 39: The BRICKA (Betsy, Rita, Ivan, Camille, Katrina, and Andrew) storm WAM verification runs for peak wave period.
- Figure 40: Time plot at NDBC Buoy 42001 for Hurricane Rita, BRICKA storm verification.
- Figure 41: Time plot at NDBC Buoy 42002 for Hurricane Rita, BRICKA storm verification.
- Figure 42: Time plot at NDBC Buoy 42007 for Hurricane Rita, BRICKA storm verification.
- Figure 43: Time plot at NDBC Buoy 42019 for Hurricane Rita, BRICKA storm verification.
- Figure 44: Time plot at NDBC Buoy 42020 for Hurricane Rita, BRICKA storm verification.
- Figure 45: Time plot at NDBC Buoy 42035 for Hurricane Rita, BRICKA storm verification.
- Figure 46: Time plot at NDBC Buoy 42036 for Hurricane Rita, BRICKA storm verification.
- Figure 47: Time plot at NDBC Buoy 42038 for Hurricane Rita, BRICKA storm verification.
- Figure 48: Time plot at NDBC Buoy 42039 for Hurricane Rita, BRICKA storm verification.
- Figure 49: Time plot at NDBC Buoy 42040 for Hurricane Rita, BRICKA storm verification.
- Figure 50: Time plot at NDBC Buoy 42055 for Hurricane Rita, BRICKA storm verification.
- Figure 51: Time plot at NDBC Buoy 42001 for Hurricane Ivan, BRICKA storm verification.
- Figure 52: Time plot at NDBC Buoy 42002 for Hurricane Ivan, BRICKA storm verification.
- Figure 53: Time plot at NDBC Buoy 42003 for Hurricane Ivan, BRICKA storm verification.
- Figure 54: Time plot at NDBC Buoy 42007 for Hurricane Ivan, BRICKA storm verification.
- Figure 55: Time plot at NDBC Buoy 42019 for Hurricane Ivan, BRICKA storm verification.
- Figure 56: Time plot at NDBC Buoy 42020 for Hurricane Ivan, BRICKA storm verification.
- Figure 57: Time plot at NDBC Buoy 42035 for Hurricane Ivan, BRICKA storm verification.
- Figure 58: Time plot at NDBC Buoy 42036 for Hurricane Ivan, BRICKA storm verification.
- Figure 59: Time plot at NDBC Buoy 42038 for Hurricane Ivan, BRICKA storm verification.
- Figure 60: Time plot at NDBC Buoy 42039 for Hurricane Ivan, BRICKA storm verification.
- Figure 61: Time plot at NDBC Buoy 42040 for Hurricane Ivan, BRICKA storm verification.
- Figure 62: Time plot at NDBC Buoy 42041 for Hurricane Ivan, BRICKA storm verification.

FIGURES (Continued)

- Figure 63: Time plot at ODGP Station 1 for Hurricane Camille, BRICKA storm verification.
- Figure 64: Time plot at ODGP Station 2 for Hurricane Camille, BRICKA storm verification.
- Figure 65: Time plot at ODGP Station 3 for Hurricane Camille, BRICKA storm verification.
- Figure 66: Time plot at NDBC Buoy 42001 for Hurricane Katrina, BRICKA storm verification
- Figure 67: Time plot at NDBC Buoy 42002 for Hurricane Katrina, BRICKA storm verification.
- Figure 68: Time plot at NDBC Buoy 42003 for Hurricane Katrina, BRICKA storm verification.
- Figure 69: Time plot at NDBC Buoy 42007 for Hurricane Katrina, BRICKA storm verification.
- Figure 70: Time plot at NDBC Buoy 42019 for Hurricane Katrina, BRICKA storm verification.
- Figure 71: Time plot at NDBC Buoy 42020 for Hurricane Katrina, BRICKA storm verification.
- Figure 72: Time plot at NDBC Buoy 42035 for Hurricane Katrina, BRICKA storm verification.
- Figure 73: Time plot at NDBC Buoy 42036 for Hurricane Katrina, BRICKA storm verification.
- Figure 74: Time plot at NDBC Buoy 42038 for Hurricane Katrina, BRICKA storm verification.
- Figure 75: Time plot at NDBC Buoy 42039 for Hurricane Katrina, BRICKA storm verification.
- Figure 76: Time plot at NDBC Buoy 42040 for Hurricane Katrina, BRICKA storm verification.
- Figure 77: Time plot at NDBC Buoy 42055 for Hurricane Katrina, BRICKA storm verification.
- Figure 78: Time plot at NDBC Buoy 42025 for Hurricane Andrew, BRICKA storm verification.
- Figure 79: Time plot at NDBC Buoy 42001 for Hurricane Andrew, BRICKA storm verification.
- Figure 80: Time plot at NDBC Buoy 42002 for Hurricane Andrew, BRICKA storm verification.
- Figure 81: Time plot at NDBC Buoy 42003 for Hurricane Andrew, BRICKA storm verification.
- Figure 82: Time plot at NDBC Buoy 42019 for Hurricane Andrew, BRICKA storm verification.
- Figure 83: Time plot at NDBC Buoy 42020 for Hurricane Andrew, BRICKA storm verification.
- Figure 84: Maximum H_{m0} for Hurricane Betsy OWI-wind forcing.
- Figure 85: Maximum H_{m0} for Hurricane Rita OWI-wind forcing.
- Figure 86: Maximum H_{m0} for Hurricane Ivan OWI-wind forcing.
- Figure 87: Maximum H_{m0} for Hurricane Camille OWI-wind forcing.

FIGURES (Continued)

- Figure 88: Maximum H_{m0} for Hurricane Katrina OWI-wind forcing.
- Figure 89: Maximum H_{m0} for Hurricane Andrew OWI-wind forcing.
- Figure 90: Maximum H_{m0} difference between PBL-forced and OWI-forced conditions for Hurricane Betsy.
- Figure 91: Maximum H_{m0} difference between PBL-forced and OWI-forced conditions for Hurricane Rita.
- Figure 92: Maximum H_{m0} difference between PBL-forced and OWI-forced conditions for Hurricane Ivan.
- Figure 93: Maximum H_{m0} difference between PBL-forced and OWI-forced conditions for Hurricane Camille.
- Figure 94: Maximum H_{m0} difference between PBL-forced and OWI-forced conditions for Hurricane Katrina.
- Figure 95: Maximum H_{m0} difference between PBL-forced and OWI-forced conditions for Hurricane Andrew.
- Figure 96: Spatial and temporal variation in the H_{m0} for the 119 boundary output locations for the PBL-wind forcing of Hurricane Katrina.
- Figure 97: Summary of all 152 JPM storm simulations, track's maximum wind speed, and significant wave height results.
- Figure 98: STWAVE modeling domains.
- Figure 99: Lake Pontchartrain Bathymetry Grid (depths in feet, NAVD88 2004.65).
- Figure 100: Louisiana Southeast Bathymetry Grid (depths in feet, NAVD88 2004.65).
- Figure 101: Louisiana South Bathymetry Grid (depths in feet, NAVD88 2004.65).
- Figure 102: Mississippi/Alabama Bathymetry Grid (depths in feet, NAVD88 2004.65).
- Figure 103: Lake Pontchartrain measured and modeled significant wave height.
- Figure 104: Lake Pontchartrain measured and modeled peak wave period.
- Figure 105: Differences in maximum wave height for sensitivity run with 5 percent increase in wind speed for Lake Pontchartrain (plus 5 percent – base).
- Figure 106: Differences in maximum wave height for sensitivity run with 5 percent decrease in wind speed for Lake Pontchartrain (minus 5 percent – base).
- Figure 107: Differences in maximum wave height for sensitivity run with 5 percent increase in wind speed for Southeast Louisiana (plus 5 percent – base).

FIGURES (Continued)

- Figure 108: Chandeleur Islands depth differences used in bathymetry sensitivity runs (degraded bathymetry – base).
- Figure 109: Differences in maximum wave height for sensitivity run with Chandeleur Islands degraded for Southeast Louisiana (degraded bathymetry – base).
- Figure 110: Time-dependent and steady-state SWAN and STWAVE modeled significant wave heights for Lake Pontchartrain measured and measured wave height.
- Figure 111: Time-dependent and steady-state SWAN and STWAVE modeled peak wave periods for Lake Pontchartrain measured and measured periods.
- Figure 112: The unstructured ADCIRC SL15 grid of the total domain.
- Figure 113: ADCIRC SL15 with bathymetry (in meters) for the total domain.
- Figure 114: Detail of the SL15 domain with bathymetry and topography (in meters) across Southern Louisiana with raised features, such as levees, railroads, and highways, shown in brown.
- Figure 115: Detail of the SL15 domain with bathymetry and topography (in meters) across Southwestern Louisiana with raised features, such as levees, railroads, and highways, shown in brown.
- Figure 116: Detail of the SL15 domain with bathymetry and topography (in meters) across Southeastern Louisiana with raised features, such as levees, railroads, and highways, shown in brown.
- Figure 117: Detail of the SL15 domain with bathymetry and topography (in meters) across the area around New Orleans and Lake Pontchartrain with raised features shown in brown.
- Figure 118: Detail of the SL15 domain with bathymetry and topography (in meters) across the area between Lake Pontchartrain and Lake Borgne with raised features shown in brown.
- Figure 119: Detail of the SL15 domain with bathymetry and topography (in meters) across New Orleans with raised features shown in brown.
- Figure 120: Detail of the unstructured ADCIRC SL15 grid in Southern Louisiana with raised features, such as levees, railroads, and highways, shown in brown.
- Figure 121: Detail of the unstructured ADCIRC SL15 grid in Southwestern Louisiana with raised features, such as levees, railroads, and highways, shown in brown.
- Figure 122: Detail of the unstructured ADCIRC SL15 grid in Southeastern Louisiana with raised features, such as levees, railroads, and highways, shown in brown.
- Figure 123: Detail of the unstructured ADCIRC SL15 grid in the area around New Orleans and Lake Pontchartrain with raised features, such as levees, railroads, and highways, shown in brown.
- Figure 124: Detail of the unstructured ADCIRC SL15 grid in the area between Lake Pontchartrain and Lake Borgne with raised features, such as levees, railroads, and highways, shown in brown.

FIGURES (Continued)

- Figure 125: Detail of the unstructured ADCIRC SL15 grid in New Orleans with raised features shown in brown.
- Figure 126: Contour map of the size of the elements (feet) in the ADCIRC SL15 grid for the total domain.
- Figure 127: Contour map of the size of the elements (feet) in the ADCIRC SL15 grid for Southwestern Louisiana.
- Figure 128: Contour map of the size of the elements (feet) in the ADCIRC SL15 grid for Southeastern Louisiana.
- Figure 129: Contour map of the size of the elements (feet) in the ADCIRC SL15 grid for the area around New Orleans and Lake Pontchartrain.
- Figure 130: Contour map of the size of the elements (feet) in the ADCIRC SL15 grid for the area between Lake Pontchartrain and Lake Borgne.
- Figure 131: Detail of the applied roughness (Manning friction coefficients) for Southwestern Louisiana.
- Figure 132: Detail of the applied roughness (Manning friction coefficients) for Southeastern Louisiana.
- Figure 133: Detail of the applied roughness (Manning friction coefficients) for the area around New Orleans and Lake Pontchartrain.
- Figure 134: Detail of the applied roughness (Manning friction coefficients) for the area between Lake Pontchartrain and Lake Borgne.
- Figure 135: Open water surface elevations (meters) along the Louisiana and Mississippi coastline.
- Figure 136: Detail of the applied directional wind reduction factor for northerly winds for Southwestern Louisiana.
- Figure 137: Detail of the applied directional wind reduction factor for southerly winds for Southwestern Louisiana.
- Figure 138: Detail of the applied directional wind reduction factor for westerly winds for Southwestern Louisiana.
- Figure 139: Detail of the applied directional wind reduction factor for easterly winds for Southwestern Louisiana.
- Figure 140: Detail of the applied directional wind reduction factor for northerly winds for Southeastern Louisiana.
- Figure 141: Detail of the applied directional wind reduction factor for southerly winds for Southeastern Louisiana.
- Figure 142: Detail of the applied directional wind reduction factor for westerly winds for Southeastern Louisiana.

FIGURES (Continued)

- Figure 143: Detail of the applied directional wind reduction factor for easterly winds for Southeastern Louisiana.
- Figure 144: Detail of the applied directional wind reduction factor for northerly winds for the area around New Orleans and Lake Pontchartrain.
- Figure 145: Detail of the applied directional wind reduction factor for southerly winds for the area around New Orleans and Lake Pontchartrain.
- Figure 146: Detail of the applied directional wind reduction factor for westerly winds for the area around New Orleans and Lake Pontchartrain.
- Figure 147: Detail of the applied directional wind reduction factor for easterly winds for the area around New Orleans and Lake Pontchartrain.
- Figure 148: Detail of the applied directional wind reduction factor for northerly winds for the area between Lake Pontchartrain and Lake Borgne.
- Figure 149: Detail of the applied directional wind reduction factor for southerly winds for the area between Lake Pontchartrain and Lake Borgne.
- Figure 150: Detail of the applied directional wind reduction factor for westerly winds for the area between Lake Pontchartrain and Lake Borgne.
- Figure 151: Detail of the applied directional wind reduction factor for easterly winds for the area between Lake Pontchartrain and Lake Borgne.
- Figure 152: Detail of the heavily forested areas in Southwestern Louisiana where a canopy factor has been applied.
- Figure 153: Detail of the heavily forested areas in Southeastern Louisiana where a canopy factor has been applied.
- Figure 154: Detail of the areas in Southeastern Louisiana that are categorized as initially dry, even if the areas are below sea level.
- Figure 155: Tidal gauge station map, showing locations of stations used in model validation.
- Figure 156: Scatter plot of the measured and observed amplitudes of the seven harmonic constituents at ten stations in Florida.
- Figure 157: Scatter plot of the measured and computed phases for the seven harmonic constituents at ten stations in Florida.
- Figure 158: Scatter plot of the measured and observed amplitudes of the seven harmonic constituents at 11 stations in Mississippi and Alabama.
- Figure 159: Scatter plot of the measured and computed phases for the seven harmonic constituents at 11 stations in Mississippi and Alabama.

FIGURES (Continued)

- Figure 160: Scatter plot of the measured and observed amplitudes of the seven harmonic constituents at 15 stations in Louisiana.
- Figure 161: Scatter plot of the measured and computed phases for the seven harmonic constituents at 15 stations in Louisiana.
- Figure 162: Scatter plot of the measured and observed amplitudes of the seven harmonic constituents at four stations in Texas.
- Figure 163: Scatter plot of the measured and computed phases for the seven harmonic constituents at four stations in Texas.
- Figure 164: ADCIRC contour maps of the wind speed (in knots) and wind vectors (in knots) for Hurricane Katrina at 7:00 UTC on August 29, 2005, for Southeastern Louisiana.
- Figure 165: ADCIRC contour maps of the wind speed (in knots) and wind vectors (in knots) for Hurricane Katrina at 10:00 UTC on August 29, 2005, for Southeastern Louisiana.
- Figure 166: ADCIRC contour maps of the wind speed (in knots) and wind vectors (in knots) for Hurricane Katrina at 11:00 UTC on August 29, 2005, for Southeastern Louisiana.
- Figure 167: ADCIRC contour maps of the wind speed (in knots) and wind vectors (in knots) for Hurricane Katrina at 12:00 UTC on August 29, 2005, for Southeastern Louisiana.
- Figure 168: ADCIRC contour maps of the wind speed (in knots) and wind vectors (in knots) for Hurricane Katrina at 13:00 UTC on August 29, 2005, for Southeastern Louisiana.
- Figure 169: ADCIRC contour maps of the wind speed (in knots) and wind vectors (in knots) for Hurricane Katrina at 14:00 UTC on August 29, 2005, for Southeastern Louisiana.
- Figure 170: ADCIRC contour maps of the wind speed (in knots) and wind vectors (in knots) for Hurricane Katrina at 15:00 UTC on August 29, 2005, for Southeastern Louisiana.
- Figure 171: ADCIRC contour maps of the wind speed (in knots) and wind vectors (in knots) for Hurricane Katrina at 16:00 UTC on August 29, 2005, for Southeastern Louisiana.
- Figure 172: ADCIRC contour maps of the wind speed (in knots) and wind vectors (in knots) for Hurricane Katrina at 17:00 UTC on August 29, 2005, for Southeastern Louisiana.
- Figure 173: ADCIRC contour maps of the wind speed (in knots) and wind vectors (in knots) for Hurricane Katrina at 20:00 UTC on August 29, 2005, for Southeastern Louisiana.
- Figure 174: ADCIRC contour maps of the wind speed (in knots) and wind vectors (in knots) for Hurricane Katrina at 23:00 UTC on August 29, 2005, for Southeastern Louisiana.
- Figure 175: ADCIRC elevation contours (in feet) and wind vectors (in knots) for Hurricane Katrina at 7:00 UTC on August 29, 2005, for Southeastern Louisiana.
- Figure 176: ADCIRC elevation contours (in feet) and wind vectors (in knots) for Hurricane Katrina at 10:00 UTC on August 29, 2005, for Southeastern Louisiana.

FIGURES (Continued)

- Figure 177: ADCIRC elevation contours (in feet) and wind vectors (in knots) for Hurricane Katrina at 11:00 UTC on August 29, 2005, for Southeastern Louisiana.
- Figure 178: ADCIRC elevation contours (in feet) and wind vectors (in knots) for Hurricane Katrina at 12:00 UTC on August 29, 2005, for Southeastern Louisiana.
- Figure 179: ADCIRC elevation contours (in feet) and wind vectors (in knots) for Hurricane Katrina at 13:00 UTC on August 29, 2005, for Southeastern Louisiana.
- Figure 180: ADCIRC elevation contours (in feet) and wind vectors (in knots) for Hurricane Katrina at 14:00 UTC on August 29, 2005, for Southeastern Louisiana.
- Figure 181: ADCIRC elevation contours (in feet) and wind vectors (in knots) for Hurricane Katrina at 15:00 UTC on August 29, 2005, for Southeastern Louisiana.
- Figure 182: ADCIRC elevation contours (in feet) and wind vectors (in knots) for Hurricane Katrina at 16:00 UTC on August 29, 2005, for Southeastern Louisiana.
- Figure 183: ADCIRC elevation contours (in feet) and wind vectors (in knots) for Hurricane Katrina at 17:00 UTC on August 29, 2005, for Southeastern Louisiana.
- Figure 184: ADCIRC elevation contours (in feet) and wind vectors (in knots) for Hurricane Katrina at 20:00 UTC on August 29, 2005, for Southeastern Louisiana.
- Figure 185: ADCIRC elevation contours (in feet) and wind vectors (in knots) for Hurricane Katrina at 23:00 UTC on August 29, 2005, for Southeastern Louisiana.
- Figure 186: ADCIRC current contours (in feet/second) and current vectors (in feet/second) for Hurricane Katrina at 7:00 UTC on August 29, 2005, for Southeastern Louisiana.
- Figure 187: ADCIRC current contours (in feet/second) and current vectors (in feet/second) for Hurricane Katrina at 10:00 UTC on August 29, 2005, for Southeastern Louisiana.
- Figure 188: ADCIRC current contours (in feet/second) and current vectors (in feet/second) for Hurricane Katrina at 11:00 UTC on August 29, 2005, for Southeastern Louisiana.
- Figure 189: ADCIRC current contours (in feet/second) and current vectors (in feet/second) for Hurricane Katrina at 12:00 UTC on August 29, 2005, for Southeastern Louisiana.
- Figure 190: ADCIRC current contours (in feet/second) and current vectors (in feet/second) for Hurricane Katrina at 13:00 UTC on August 29, 2005, for Southeastern Louisiana.
- Figure 191: ADCIRC current contours (in feet/second) and current vectors (in feet/second) for Hurricane Katrina at 14:00 UTC on August 29, 2005, for Southeastern Louisiana.
- Figure 192: ADCIRC current contours (in feet/second) and current vectors (in feet/second) for Hurricane Katrina at 15:00 UTC on August 29, 2005, for Southeastern Louisiana.
- Figure 193: ADCIRC current contours (in feet/second) and current vectors (in feet/second) for Hurricane Katrina at 16:00 UTC on August 29, 2005, for Southeastern Louisiana.

FIGURES (Continued)

- Figure 194: ADCIRC current contours (in feet/second) and current vectors (in feet/second) for Hurricane Katrina at 17:00 UTC on August 29, 2005, for Southeastern Louisiana.
- Figure 195: ADCIRC current contours (in feet/second) and current vectors (in feet/second) for Hurricane Katrina at 20:00 UTC on August 29, 2005, for Southeastern Louisiana.
- Figure 196: ADCIRC current contours (in feet/second) and current vectors (in feet/second) for Hurricane Katrina at 23:00 UTC on August 29, 2005, for Southeastern Louisiana.
- Figure 197: ADCIRC maximum wind velocities (in knots) during Hurricane Katrina on August 29, 2005, for Southeastern Louisiana.
- Figure 198: ADCIRC maximum elevation contours (in feet) during Hurricane Katrina on August 29, 2005, for Southeastern Louisiana.
- Figure 199: ADCIRC maximum current contours (in feet/second) during Hurricane Katrina on August 29, 2005, for Southeastern Louisiana.
- Figure 200: ADCIRC contour maps of the wind speed (in knots) and wind vectors (in knots) for Hurricane Katrina at 7:00 UTC on August 29, 2005, for the area around New Orleans and Lake Pontchartrain.
- Figure 201: ADCIRC contour maps of the wind speed (in knots) and wind vectors (in knots) for Hurricane Katrina at 10:00 UTC on August 29, 2005, for the area around New Orleans and Lake Pontchartrain.
- Figure 202: ADCIRC contour maps of the wind speed (in knots) and wind vectors (in knots) for Hurricane Katrina at 11:00 UTC on August 29, 2005, for the area around New Orleans and Lake Pontchartrain.
- Figure 203: ADCIRC contour maps of the wind speed (in knots) and wind vectors (in knots) for Hurricane Katrina at 12:00 UTC on August 29, 2005, for the area around New Orleans and Lake Pontchartrain.
- Figure 204: ADCIRC contour maps of the wind speed (in knots) and wind vectors (in knots) for Hurricane Katrina at 13:00 UTC on August 29, 2005, for the area around New Orleans and Lake Pontchartrain.
- Figure 205: ADCIRC contour maps of the wind speed (in knots) and wind vectors (in knots) for Hurricane Katrina at 14:00 UTC on August 29, 2005, for the area around New Orleans and Lake Pontchartrain.
- Figure 206: ADCIRC contour maps of the wind speed (in knots) and wind vectors (in knots) for Hurricane Katrina at 15:00 UTC on August 29, 2005, for the area around New Orleans and Lake Pontchartrain.
- Figure 207: ADCIRC contour maps of the wind speed (in knots) and wind vectors (in knots) for Hurricane Katrina at 16:00 UTC on August 29, 2005, for the area around New Orleans and Lake Pontchartrain.

FIGURES (Continued)

- Figure 208: ADCIRC contour maps of the wind speed (in knots) and wind vectors (in knots) for Hurricane Katrina at 17:00 UTC on August 29, 2005, for the area around New Orleans and Lake Pontchartrain
- Figure 209: ADCIRC contour maps of the wind speed (in knots) and wind vectors (in knots) for Hurricane Katrina at 20:00 UTC on August 29, 2005, for the area around New Orleans and Lake Pontchartrain.
- Figure 210: ADCIRC contour maps of the wind speed (in knots) and wind vectors (in knots) for Hurricane Katrina at 23:00 UTC on August 29, 2005, for the area around New Orleans and Lake Pontchartrain.
- Figure 211: ADCIRC elevation contours (in feet) and wind vectors (in knots) for Hurricane Katrina at 7:00 UTC on August 29, 2005, for the area around New Orleans and Lake Pontchartrain.
- Figure 212: ADCIRC elevation contours (in feet) and wind vectors (in knots) for Hurricane Katrina at 10:00 UTC on August 29, 2005, for the area around New Orleans and Lake Pontchartrain.
- Figure 213: ADCIRC elevation contours (in feet) and wind vectors (in knots) for Hurricane Katrina at 11:00 UTC on August 29, 2005, for the area around New Orleans and Lake Pontchartrain.
- Figure 214: ADCIRC elevation contours (in feet) and wind vectors (in knots) for Hurricane Katrina at 12:00 UTC on August 29, 2005, for the area around New Orleans and Lake Pontchartrain.
- Figure 215: ADCIRC elevation contours (in feet) and wind vectors (in knots) for Hurricane Katrina at 13:00 UTC on August 29, 2005, for the area around New Orleans and Lake Pontchartrain.
- Figure 216: ADCIRC elevation contours (in feet) and wind vectors (in knots) for Hurricane Katrina at 14:00 UTC on August 29, 2005, for the area around New Orleans and Lake Pontchartrain.
- Figure 217: ADCIRC elevation contours (in feet) and wind vectors (in knots) for Hurricane Katrina at 15:00 UTC on August 29, 2005, for the area around New Orleans and Lake Pontchartrain.
- Figure 218: ADCIRC elevation contours (in feet) and wind vectors (in knots) for Hurricane Katrina at 16:00 UTC on August 29, 2005, for the area around New Orleans and Lake Pontchartrain.
- Figure 219: ADCIRC elevation contours (in feet) and wind vectors (in knots) for Hurricane Katrina at 17:00 UTC on August 29, 2005, for the area around New Orleans and Lake Pontchartrain.
- Figure 220: ADCIRC elevation contours (in feet) and wind vectors (in knots) for Hurricane Katrina at 20:00 UTC on August 29, 2005, for the area around New Orleans and Lake Pontchartrain.
- Figure 221: ADCIRC elevation contours (in feet) and wind vectors (in knots) for Hurricane Katrina at 23:00 UTC on August 29, 2005, for the area around New Orleans and Lake Pontchartrain.
- Figure 222: ADCIRC current contours (in feet/second) and current vectors (in feet/second) for Hurricane Katrina at 7:00 UTC on August 29, 2005, for the area around New Orleans and Lake Pontchartrain.

FIGURES (Continued)

- Figure 223: ADCIRC current contours (in feet/second) and current vectors (in feet/second) for Hurricane Katrina at 10:00 UTC on August 29, 2005, for the area around New Orleans and Lake Pontchartrain.
- Figure 224: ADCIRC current contours (in feet/second) and current vectors (in feet/second) for Hurricane Katrina at 11:00 UTC on August 29, 2005, for the area around New Orleans and Lake Pontchartrain.
- Figure 225: ADCIRC current contours (in feet/second) and current vectors (in feet/second) for Hurricane Katrina at 12:00 UTC on August 29, 2005, for the area around New Orleans and Lake Pontchartrain.
- Figure 226: ADCIRC current contours (in feet/second) and current vectors (in feet/second) for Hurricane Katrina at 13:00 UTC on August 29, 2005, for the area around New Orleans and Lake Pontchartrain.
- Figure 227: ADCIRC current contours (in feet/second) and current vectors (in feet/second) for Hurricane Katrina at 14:00 UTC on August 29, 2005, for the area around New Orleans and Lake Pontchartrain.
- Figure 228: ADCIRC current contours (in feet/second) and current vectors (in feet/second) for Hurricane Katrina at 15:00 UTC on August 29, 2005, for the area around New Orleans and Lake Pontchartrain.
- Figure 229: ADCIRC current contours (in feet/second) and current vectors (in feet/second) for Hurricane Katrina at 16:00 UTC on August 29, 2005, for the area around New Orleans and Lake Pontchartrain.
- Figure 230: ADCIRC current contours (in feet/second) and current vectors (in feet/second) for Hurricane Katrina at 17:00 UTC on August 29, 2005, for the area around New Orleans and Lake Pontchartrain.
- Figure 231: ADCIRC current contours (in feet/second) and current vectors (in feet/second) for Hurricane Katrina at 20:00 UTC on August 29, 2005, for the area around New Orleans and Lake Pontchartrain.
- Figure 232: ADCIRC current contours (in feet/second) and current vectors (in feet/second) for Hurricane Katrina at 23:00 UTC on August 29, 2005, for the area around New Orleans and Lake Pontchartrain.
- Figure 233: ADCIRC maximum wind velocities (in knots) during Hurricane Katrina on August 29, 2005, for the area around New Orleans and Lake Pontchartrain.
- Figure 234: ADCIRC maximum elevation contours (in feet) during Hurricane Katrina on August 29, 2005, for the area around New Orleans and Lake Pontchartrain.
- Figure 235: ADCIRC maximum current contours (in feet/second) during Hurricane Katrina on August 29, 2005, for the area around New Orleans and Lake Pontchartrain.

FIGURES (Continued)

- Figure 236: ADCIRC elevation contours (in feet) and wind vectors (in knots) for Hurricane Katrina at 7:00 UTC on August 29, 2005, for the area between Lake Pontchartrain and Lake Borgne.
- Figure 237: ADCIRC elevation contours (in feet) and wind vectors (in knots) for Hurricane Katrina at 10:00 UTC on August 29, 2005, for the area between Lake Pontchartrain and Lake Borgne.
- Figure 238: ADCIRC elevation contours (in feet) and wind vectors (in knots) for Hurricane Katrina at 11:00 UTC on August 29, 2005, for the area between Lake Pontchartrain and Lake Borgne.
- Figure 239: ADCIRC elevation contours (in feet) and wind vectors (in knots) for Hurricane Katrina at 12:00 UTC on August 29, 2005, for the area between Lake Pontchartrain and Lake Borgne.
- Figure 240: ADCIRC elevation contours (in feet) and wind vectors (in knots) for Hurricane Katrina at 13:00 UTC on August 29, 2005, for the area between Lake Pontchartrain and Lake Borgne.
- Figure 241: ADCIRC elevation contours (in feet) and wind vectors (in knots) for Hurricane Katrina at 14:00 UTC on August 29, 2005, for the area between Lake Pontchartrain and Lake Borgne.
- Figure 242: ADCIRC elevation contours (in feet) and wind vectors (in knots) for Hurricane Katrina at 15:00 UTC on August 29, 2005, for the area between Lake Pontchartrain and Lake Borgne.
- Figure 243: ADCIRC elevation contours (in feet) and wind vectors (in knots) for Hurricane Katrina at 16:00 UTC on August 29, 2005, for the area between Lake Pontchartrain and Lake Borgne.
- Figure 244: ADCIRC elevation contours (in feet) and wind vectors (in knots) for Hurricane Katrina at 17:00 UTC on August 29, 2005, for the area between Lake Pontchartrain and Lake Borgne.
- Figure 245: ADCIRC elevation contours (in feet) and wind vectors (in knots) for Hurricane Katrina at 20:00 UTC on August 29, 2005, for the area between Lake Pontchartrain and Lake Borgne.
- Figure 246: ADCIRC elevation contours (in feet) and wind vectors (in knots) for Hurricane Katrina at 23:00 UTC on August 29, 2005, for the area between Lake Pontchartrain and Lake Borgne.
- Figure 247: ADCIRC current contours (in feet/second) and current vectors (in feet/second) for Hurricane Katrina at 7:00 UTC on August 29, 2005, for the area between Lake Pontchartrain and Lake Borgne.
- Figure 248: ADCIRC current contours (in feet/second) and current vectors (in feet/second) for Hurricane Katrina at 10:00 UTC on August 29, 2005, for the area between Lake Pontchartrain and Lake Borgne.
- Figure 249: ADCIRC current contours (in feet/second) and current vectors (in feet/second) for Hurricane Katrina at 11:00 UTC on August 29, 2005, for the area between Lake Pontchartrain and Lake Borgne.
- Figure 250: ADCIRC current contours (in feet/second) and current vectors (in feet/second) for Hurricane Katrina at 12:00 UTC on August 29, 2005, for the area between Lake Pontchartrain and Lake Borgne.

FIGURES (Continued)

- Figure 251: ADCIRC current contours (in feet/second) and current vectors (in feet/second) for Hurricane Katrina at 13:00 UTC on August 29, 2005, for the area between Lake Pontchartrain and Lake Borgne.
- Figure 252: ADCIRC current contours (in feet/second) and current vectors (in feet/second) for Hurricane Katrina at 14:00 UTC on August 29, 2005, for the area between Lake Pontchartrain and Lake Borgne.
- Figure 253: ADCIRC current contours (in feet/second) and current vectors (in feet/second) for Hurricane Katrina at 15:00 UTC on August 29, 2005, for the area between Lake Pontchartrain and Lake Borgne.
- Figure 254: ADCIRC current contours (in feet/second) and current vectors (in feet/second) for Hurricane Katrina at 16:00 UTC on August 29, 2005, for the area between Lake Pontchartrain and Lake Borgne.
- Figure 255: ADCIRC current contours (in feet/second) and current vectors (in feet/second) for Hurricane Katrina at 17:00 UTC on August 29, 2005, for the area between Lake Pontchartrain and Lake Borgne.
- Figure 256: ADCIRC current contours (in feet/second) and current vectors (in feet/second) for Hurricane Katrina at 20:00 UTC on August 29, 2005, for the area between Lake Pontchartrain and Lake Borgne.
- Figure 257: ADCIRC current contours (in feet/second) and current vectors (in feet/second) for Hurricane Katrina at 23:00 UTC on August 29, 2005, for the area between Lake Pontchartrain and Lake Borgne.
- Figure 258: ADCIRC maximum wind velocities (in knots) during Hurricane Katrina on August 29, 2005, for the area between Lake Pontchartrain and Lake Borgne.
- Figure 259: ADCIRC maximum elevation contours (in feet) during Hurricane Katrina on August 29, 2005, for the area between Lake Pontchartrain and Lake Borgne.
- Figure 260: ADCIRC maximum current contours (in feet/second) during Hurricane Katrina on August 29, 2005, for the area between Lake Pontchartrain and Lake Borgne.
- Figure 261: Comparisons between observed high-water marks and ADCIRC maximum surges at 206 locations shown on Figure 263 (USACE marks).
- Figure 262: Comparisons between observed high-water marks and ADCIRC maximum surges at 193 locations shown on Figure 265 (URS marks).
- Figure 263: Locations of 206 high-water marks provided by the U.S. Army Corps of Engineers.
- Figure 264: The points indicated by red circles are 18 high-water marks found on the south shore of Lake Pontchartrain out of 206 high-water marks provided by the U.S. Army Corps of Engineers.
- Figure 265: Locations of 193 high-water marks provided by URS Corporation.

FIGURES (Continued)

- Figure 266: The points indicated by a red circle are 5 high-water marks found on the south shore of Lake Pontchartrain out of 193 high-water marks provided by URS Corporation.
- Figure 267: Distribution of errors between observed high-water marks and temporal maximums of ADCIRC Katrina hindcast solution.
- Figure 268: Distribution of errors between observed high-water marks and temporal maximums of ADCIRC Katrina hindcast solution.
- Figure 269: Distribution of errors between observed high-water marks and temporal maximums of ADCIRC Katrina hindcast solution.
- Figure 270: Distribution of errors between observed high-water marks and temporal maximums of ADCIRC Katrina hindcast solution.
- Figure 271: Distribution of errors between observed high-water marks and temporal maximums of ADCIRC Katrina hindcast solution.
- Figure 272: Distribution of errors between observed high-water marks and temporal maximums of ADCIRC Katrina hindcast solution.
- Figure 273: Distribution of errors between observed high-water marks and temporal maximums of ADCIRC Katrina hindcast solution.
- Figure 274: Distribution of errors between observed high-water marks and temporal maximums of ADCIRC Katrina hindcast solution.
- Figure 275: Distribution of errors between observed high-water marks and temporal maximums of ADCIRC Katrina hindcast solution.
- Figure 276: Distribution of errors between observed high-water marks and temporal maximums of ADCIRC Katrina hindcast solution.
- Figure 277: Locations of hydrograph stations.
- Figure 278: Observed and computed hydrographs at the stations shown on Figure 277.
- Figure 279: Maximum significant wave height during Hurricane Rita validation (West grid).
- Figure 280: Mean wave period during Hurricane Rita validation (West grid).
- Figure 281: Maximum significant wave height during Hurricane Rita validation (nearshore scale for West grid).
- Figure 282: Maximum significant wave height during Hurricane Rita validation (South grid).
- Figure 283: Mean wave period during Hurricane Rita validation (South grid).
- Figure 284: Magnitude of the maximum value of radiation stress gradient during Hurricane Rita validation (offshore area including all grids).

FIGURES (Continued)

- Figure 285: Magnitude of the maximum value of radiation stress gradient during Hurricane Rita validation (western Louisiana area).
- Figure 286: Wind contours and vectors (in knots) for Hurricane Rita at 12:00 UTC on September 23, 2005, for Southwestern Louisiana.
- Figure 287: Wind contours and vectors (in knots) for Hurricane Rita at 12:00 UTC on September 23, 2005, for Southeastern Louisiana.
- Figure 288: Wind contours and vectors (in knots) for Hurricane Rita at 18:00 UTC on September 23, 2005, for Southwestern Louisiana.
- Figure 289: Wind contours and vectors (in knots) for Hurricane Rita at 18:00 UTC on September 23, 2005, for Southeastern Louisiana.
- Figure 290: Wind contours and vectors (in knots) for Hurricane Rita at 24:00 UTC on September 23, 2005, for Southwestern Louisiana.
- Figure 291: Wind contours and vectors (in knots) for Hurricane Rita at 24:00 UTC on September 23, 2005, for Southeastern Louisiana.
- Figure 292: Wind contours and vectors (in knots) for Hurricane Rita at 03:00 UTC on September 24, 2005, for Southwestern Louisiana.
- Figure 293: Wind contours and vectors (in knots) for Hurricane Rita at 03:00 UTC on September 24, 2005, for Southeastern Louisiana.
- Figure 294: Wind contours and vectors (in knots) for Hurricane Rita at 06:00 UTC on September 24, 2005, for Southwestern Louisiana.
- Figure 295: Wind contours and vectors (in knots) for Hurricane Rita at 06:00 UTC on September 24, 2005, for Southeastern Louisiana.
- Figure 296: Wind contours and vectors (in knots) for Hurricane Rita at 07:00 UTC on September 24, 2005, for Southwestern Louisiana.
- Figure 297: Wind contours and vectors (in knots) for Hurricane Rita at 07:00 UTC on September 24, 2005, for Southeastern Louisiana.
- Figure 298: Wind contours and vectors (in knots) for Hurricane Rita at 08:00 UTC on September 24, 2005, for Southwestern Louisiana.
- Figure 299: Wind contours and vectors (in knots) for Hurricane Rita at 08:00 UTC on September 24, 2005, for Southeastern Louisiana.
- Figure 300: Wind contours and vectors (in knots) for Hurricane Rita at 09:00 UTC on September 24, 2005, for Southwestern Louisiana.
- Figure 301: Wind contours and vectors (in knots) for Hurricane Rita at 09:00 UTC on September 24, 2005, for Southeastern Louisiana.

FIGURES (Continued)

- Figure 302: Wind contours and vectors (in knots) for Hurricane Rita at 10:00 UTC on September 24, 2005, for Southwestern Louisiana.
- Figure 303: Wind contours and vectors (in knots) for Hurricane Rita at 10:00 UTC on September 24, 2005, for Southeastern Louisiana.
- Figure 304: Wind contours and vectors (in knots) for Hurricane Rita at 11:00 UTC on September 24, 2005, for Southwestern Louisiana.
- Figure 305: Wind contours and vectors (in knots) for Hurricane Rita at 11:00 UTC on September 24, 2005, for Southeastern Louisiana.
- Figure 306: Wind contours and vectors (in knots) for Hurricane Rita at 12:00 UTC on September 24, 2005, for Southwestern Louisiana.
- Figure 307: Wind contours and vectors (in knots) for Hurricane Rita at 12:00 UTC on September 24, 2005, for Southeastern Louisiana.
- Figure 308: Wind contours and vectors (in knots) for Hurricane Rita at 15:00 UTC on September 24, 2005, for Southwestern Louisiana.
- Figure 309: Wind contours and vectors (in knots) for Hurricane Rita at 15:00 UTC on September 24, 2005, for Southeastern Louisiana.
- Figure 310: Wind contours and vectors (in knots) for Hurricane Rita at 18:00 UTC on September 24, 2005, for Southwestern Louisiana.
- Figure 311: Wind contours and vectors (in knots) for Hurricane Rita at 18:00 UTC on September 24, 2005, for Southeastern Louisiana.
- Figure 312: Wind contours and vectors (in knots) for Hurricane Rita at 21:00 UTC on September 24, 2005, for Southwestern Louisiana.
- Figure 313: Wind contours and vectors (in knots) for Hurricane Rita at 21:00 UTC on September 24, 2005, for Southeastern Louisiana.
- Figure 314: ADCIRC elevation contours (in feet above NAVD88) and wind vectors (in knots) for Hurricane Rita at 12:00 UTC on September 23, 2005, for Southwestern Louisiana.
- Figure 315: ADCIRC elevation contours (in feet above NAVD88) and wind vectors (in knots) for Hurricane Rita at 12:00 UTC on September 23, 2005, for Southeastern Louisiana.
- Figure 316: ADCIRC elevation contours (in feet above NAVD88) and wind vectors (in knots) for Hurricane Rita at 18:00 UTC on September 23, 2005, for Southwestern Louisiana.
- Figure 317: ADCIRC elevation contours (in feet above NAVD88) and wind vectors (in knots) for Hurricane Rita at 18:00 UTC on September 23, 2005, for Southeastern Louisiana.
- Figure 318: ADCIRC elevation contours (in feet above NAVD88) and wind vectors (in knots) for Hurricane Rita at 24:00 UTC on September 23, 2005, for Southwestern Louisiana.

FIGURES (Continued)

- Figure 319: ADCIRC elevation contours (in feet above NAVD88) and wind vectors (in knots) for Hurricane Rita at 24:00 UTC on September 23, 2005, for Southeastern Louisiana.
- Figure 320: ADCIRC elevation contours (in feet above NAVD88) and wind vectors (in knots) for Hurricane Rita at 03:00 UTC on September 24, 2005, for Southwestern Louisiana.
- Figure 321: ADCIRC elevation contours (in feet above NAVD88) and wind vectors (in knots) for Hurricane Rita at 03:00 UTC on September 24, 2005, for Southeastern Louisiana.
- Figure 322: ADCIRC elevation contours (in feet above NAVD88) and wind vectors (in knots) for Hurricane Rita at 06:00 UTC on September 24, 2005, for Southwestern Louisiana.
- Figure 323: ADCIRC elevation contours (in feet above NAVD88) and wind vectors (in knots) for Hurricane Rita at 06:00 UTC on September 24, 2005, for Southeastern Louisiana.
- Figure 324: ADCIRC elevation contours (in feet above NAVD88) and wind vectors (in knots) for Hurricane Rita at 07:00 UTC on September 24, 2005, for Southwestern Louisiana.
- Figure 325: ADCIRC elevation contours (in feet above NAVD88) and wind vectors (in knots) for Hurricane Rita at 07:00 UTC on September 24, 2005, for Southeastern Louisiana.
- Figure 326: ADCIRC elevation contours (in feet above NAVD88) and wind vectors (in knots) for Hurricane Rita at 08:00 UTC on September 24, 2005, for Southwestern Louisiana.
- Figure 327: ADCIRC elevation contours (in feet above NAVD88) and wind vectors (in knots) for Hurricane Rita at 08:00 UTC on September 24, 2005, for Southeastern Louisiana.
- Figure 328: ADCIRC elevation contours (in feet above NAVD88) and wind vectors (in knots) for Hurricane Rita at 09:00 UTC on September 24, 2005, for Southwestern Louisiana.
- Figure 329: ADCIRC elevation contours (in feet above NAVD88) and wind vectors (in knots) for Hurricane Rita at 09:00 UTC on September 24, 2005, for Southeastern Louisiana.
- Figure 330: ADCIRC elevation contours (in feet above NAVD88) and wind vectors (in knots) for Hurricane Rita at 10:00 UTC on September 24, 2005, for Southwestern Louisiana.
- Figure 331: ADCIRC elevation contours (in feet above NAVD88) and wind vectors (in knots) for Hurricane Rita at 10:00 UTC on September 24, 2005, for Southeastern Louisiana.
- Figure 332: ADCIRC elevation contours (in feet above NAVD88) and wind vectors (in knots) for Hurricane Rita at 11:00 UTC on September 24, 2005, for Southwestern Louisiana.
- Figure 333: ADCIRC elevation contours (in feet above NAVD88) and wind vectors (in knots) for Hurricane Rita at 11:00 UTC on September 24, 2005, for Southeastern Louisiana.
- Figure 334: ADCIRC elevation contours (in feet above NAVD88) and wind vectors (in knots) for Hurricane Rita at 12:00 UTC on September 24, 2005, for Southwestern Louisiana.
- Figure 335: ADCIRC elevation contours (in feet above NAVD88) and wind vectors (in knots) for Hurricane Rita at 12:00 UTC on September 24, 2005, for Southeastern Louisiana.

FIGURES (Continued)

- Figure 336: ADCIRC elevation contours (in feet above NAVD88) and wind vectors (in knots) for Hurricane Rita at 15:00 UTC on September 24, 2005, for Southwestern Louisiana.
- Figure 337: ADCIRC elevation contours (in feet above NAVD88) and wind vectors (in knots) for Hurricane Rita at 15:00 UTC on September 24, 2005, for Southeastern Louisiana.
- Figure 338: ADCIRC elevation contours (in feet above NAVD88) and wind vectors (in knots) for Hurricane Rita at 18:00 UTC on September 24, 2005, for Southwestern Louisiana.
- Figure 339: ADCIRC elevation contours (in feet above NAVD88) and wind vectors (in knots) for Hurricane Rita at 18:00 UTC on September 24, 2005, for Southeastern Louisiana.
- Figure 340: ADCIRC elevation contours (in feet above NAVD88) and wind vectors (in knots) for Hurricane Rita at 21:00 UTC on September 24, 2005, for Southwestern Louisiana.
- Figure 341: ADCIRC elevation contours (in feet above NAVD88) and wind vectors (in knots) for Hurricane Rita at 21:00 UTC on September 24, 2005, for Southeastern Louisiana.
- Figure 342: ADCIRC velocity contours and vectors (in feet/second) for Hurricane Rita at 12:00 UTC on September 23, 2005, for Southwestern Louisiana.
- Figure 343: ADCIRC velocity contours and vectors (in feet/second) for Hurricane Rita at 12:00 UTC on September 23, 2005, for Southeastern Louisiana.
- Figure 344: ADCIRC velocity contours and vectors (in feet/second) for Hurricane Rita at 18:00 UTC on September 23, 2005, for Southwestern Louisiana.
- Figure 345: ADCIRC velocity contours and vectors (in feet/second) for Hurricane Rita at 18:00 UTC on September 23, 2005, for Southeastern Louisiana.
- Figure 346: ADCIRC velocity contours and vectors (in feet/second) for Hurricane Rita at 00:00 UTC on September 24, 2005, for Southwestern Louisiana.
- Figure 347: ADCIRC velocity contours and vectors (in feet/second) for Hurricane Rita at 00:00 UTC on September 24, 2005, for Southeastern Louisiana.
- Figure 348: ADCIRC velocity contours and vectors (in feet/second) for Hurricane Rita at 03:00 UTC on September 24, 2005, for Southwestern Louisiana.
- Figure 349: ADCIRC velocity contours and vectors (in feet/second) for Hurricane Rita at 03:00 UTC on September 24, 2005, for Southeastern Louisiana.
- Figure 350: ADCIRC velocity contours and vectors (in feet/second) for Hurricane Rita at 06:00 UTC on September 24, 2005, for Southwestern Louisiana.
- Figure 351: ADCIRC velocity contours and vectors (in feet/second) for Hurricane Rita at 06:00 UTC on September 24, 2005, for Southeastern Louisiana.
- Figure 352: ADCIRC velocity contours and vectors (in feet/second) for Hurricane Rita at 07:00 UTC on September 24, 2005, for Southwestern Louisiana.

FIGURES (Continued)

- Figure 353: ADCIRC velocity contours and vectors (in feet/second) for Hurricane Rita at 07:00 UTC on September 24, 2005, for Southeastern Louisiana.
- Figure 354: ADCIRC velocity contours and vectors (in feet/second) for Hurricane Rita at 08:00 UTC on September 24, 2005, for Southwestern Louisiana.
- Figure 355: ADCIRC velocity contours and vectors (in feet/second) for Hurricane Rita at 08:00 UTC on September 24, 2005, for Southeastern Louisiana.
- Figure 356: ADCIRC velocity contours and vectors (in feet/second) for Hurricane Rita at 09:00 UTC on September 24, 2005, for Southwestern Louisiana.
- Figure 357: ADCIRC velocity contours and vectors (in feet/second) for Hurricane Rita at 09:00 UTC on September 24, 2005, for Southeastern Louisiana.
- Figure 358: ADCIRC velocity contours and vectors (in feet/second) for Hurricane Rita at 10:00 UTC on September 24, 2005, for Southwestern Louisiana.
- Figure 359: ADCIRC velocity contours and vectors (in feet/second) for Hurricane Rita at 10:00 UTC on September 24, 2005, for Southeastern Louisiana.
- Figure 360: ADCIRC velocity contours and vectors (in feet/second) for Hurricane Rita at 11:00 UTC on September 24, 2005, for Southwestern Louisiana.
- Figure 361: ADCIRC velocity contours and vectors (in feet/second) for Hurricane Rita at 11:00 UTC on September 24, 2005, for Southeastern Louisiana.
- Figure 362: ADCIRC velocity contours and vectors (in feet/second) for Hurricane Rita at 12:00 UTC on September 24, 2005, for Southwestern Louisiana.
- Figure 363: ADCIRC velocity contours and vectors (in feet/second) for Hurricane Rita at 12:00 UTC on September 24, 2005, for Southeastern Louisiana.
- Figure 364: ADCIRC velocity contours and vectors (in feet/second) for Hurricane Rita at 15:00 UTC on September 24, 2005, for Southwestern Louisiana.
- Figure 365: ADCIRC velocity contours and vectors (in feet/second) for Hurricane Rita at 15:00 UTC on September 24, 2005, for Southeastern Louisiana.
- Figure 366: ADCIRC velocity contours and vectors (in feet/second) for Hurricane Rita at 18:00 UTC on September 24, 2005, for Southwestern Louisiana.
- Figure 367: ADCIRC velocity contours and vectors (in feet/second) for Hurricane Rita at 18:00 UTC on September 24, 2005, for Southeastern Louisiana.
- Figure 368: ADCIRC velocity contours and vectors (in feet/second) for Hurricane Rita at 21:00 UTC on September 24, 2005, for Southwestern Louisiana.
- Figure 369: ADCIRC velocity contours and vectors (in feet/second) for Hurricane Rita at 21:00 UTC on September 24, 2005, for Southeastern Louisiana.

FIGURES (Continued)

- Figure 370: ADCIRC maximum elevation contours (in feet above NAVD88) for Hurricane Rita for Southwestern Louisiana.
- Figure 371: ADCIRC maximum elevation contours (in feet above NAVD88) for Hurricane Rita for Southeastern Louisiana.
- Figure 372: ADCIRC maximum velocity contours (in feet/second) for Hurricane Rita for Southwestern Louisiana.
- Figure 373: ADCIRC maximum velocity contours (in feet/second) for Hurricane Rita for Southeastern Louisiana.
- Figure 374: Distribution of errors between measured high-water marks and temporal maximums of the ADCIRC Rita hindcast solution, for Southwestern Louisiana.
- Figure 375: Distribution of errors between measured high-water marks and temporal maximums of the ADCIRC Rita hindcast solution, for Southeastern Louisiana.
- Figure 376: Scatter plot of high-water marks for Hurricane Rita.
- Figure 377: Bar graph of errors between measured and predicted peak values.
- Figure 378: Locations of the 23 USGS stations in Southwestern Louisiana.
- Figure 379: Hydrographs for Hurricane Rita at the first 12 USGS stations.
- Figure 380: Hydrographs for Hurricane Rita at the last 11 USGS stations.
- Figure 381: Maximum wind speed differences from H*WIND/IOKA wind generated results less PBL wind generated results for Hurricane Katrina in Southeastern Louisiana.
- Figure 382: Maximum wind speed differences from H*WIND/IOKA wind generated results less PBL wind generated results for Hurricane Katrina in Southwestern Louisiana.
- Figure 383: Maximum water level differences from H*WIND/IOKA wind generated results less PBL wind generated results for Hurricane Katrina in Southeastern Louisiana.
- Figure 384: Maximum water level differences from H*WIND/IOKA wind generated results less PBL wind generated results for Hurricane Katrina in Southwestern Louisiana.
- Figure 385: Histogram of water level surfaces differences for H*WIND/IOKA wind generated results less PBL wind generated results for Hurricane Katrina.
- Figure 386: Comparison of observed USACE High-Water Marks (HWMs) for Hurricane Katrina and the simulation using the H*WIND/IOKA wind fields.
- Figure 387: Comparison of observed USACE HWMs for Hurricane Katrina and the simulation using the PBL wind fields.

FIGURES (Continued)

- Figure 388: Comparison of observed URS HWMs for Hurricane Katrina and the simulation using the H*WIND/IOKA wind fields.
- Figure 389: Comparison of observed URS HWMs for Hurricane Katrina and the simulation using the PBL wind fields.
- Figure 390: Maximum wind speed differences from H*WIND/IOKA wind generated results less PBL wind generated results for Hurricane Rita in Southwestern Louisiana.
- Figure 391: Maximum wind speed differences from H*WIND/IOKA wind generated results less PBL wind generated results for Hurricane Rita in Southeastern Louisiana.
- Figure 392: Maximum water level differences from H*WIND/IOKA wind generated results less PBL wind generated results for Hurricane Rita in Southwestern Louisiana.
- Figure 393: Maximum water level differences from H*WIND/IOKA wind generated results less PBL wind generated results for Hurricane Rita in Southeastern Louisiana.
- Figure 394: Histogram of water level surfaces differences for H*WIND/IOKA wind generated results less PBL wind generated results for Hurricane Rita.
- Figure 395: Comparison of observed High-Water Marks (HWMs) for Hurricane Rita and the simulation using the H*WIND/IOKA wind fields.
- Figure 396: Comparison of observed High-Water Marks (HWMs) for Hurricane Rita and the simulation using the PBL wind fields.
- Figure 397: Plot of maximum wave heights on the SE STWAVE grid for storm 051.
- Figure 398: Plot of mean wave period on the SE STWAVE grid for storm 051.
- Figure 399: Results for storm 126 on the SE STWAVE grid; note the physically unrealistic striping that resulted from using a bad interpolation file; the correct behavior should be similar to Figure 397.
- Figure 400: Snapshot from a quality assurance/quality control movie product that animates wave height (color contours) and wind field (black vectors) for storm 056.
- Figure 401: Skeleton view of Southern Louisiana showing the box outlines for the ADCIRC zooms used in the post-production process; only east ("E") results reported herein.
- Figure 402: Plot of differences between the maximum elevations for the case of the railroad treated as a submerged levee versus the railroad gridded over and treated as a bathymetric rise; storm 087 is a high-intensity storm.
- Figure 403: Plot of differences between the maximum elevations for the case of the railroad treated as a submerged levee versus the railroad gridded over and treated as a bathymetric rise; storm 029 is a low-intensity storm.
- Figure 404: Zoom of the Golden Meadow region that illustrates the artificial flooding that can occur if the natural levees along canals are not properly resolved by the grid (note flooding in lower right).

Table of Contents

- Figure 405: Zoom of the Golden Meadow region with the natural levees properly resolved, resulting in no artificial flooding.
- Figure 406: Snapshot from a quality assurance/quality control movie product that animates surface water elevation (color contours) and wind field (black vectors) for storm 087.
- Figure 407: Histogram of relative mass balance error that is relative to still water volume, for storm 002; vertical axis is % of total domain area. Errors represent the average per time step error over the course of the simulation.
- Figure 408: Zoomed region near a levee (Figure 408A) and wetting front (Figure 408B) illustrating the spatial distribution of local mass balance error in these zones where the highest errors were clustered.
- Figure 409: Central pressure in landfalling storms plotted against distance from the coast.
- Figure 410: Tracks of all hurricanes (1941-2005) making landfall in the western Gulf of Mexico for storms that attained a central pressure of 955 millibars or lower during its transit through the Gulf of Mexico.
- Figure 411: Tracks of all hurricanes (1941-2005) making landfall in the central Gulf of Mexico for storms that attained a central pressure of 955 millibars or lower during its transit through the Gulf of Mexico.
- Figure 412: Tracks of all hurricanes (1941-2005) making landfall in the eastern Gulf of Mexico for storms that attained a central pressure of 955 millibars or lower during its transit through the Gulf of Mexico.
- Figure 413: Location of line for analysis of hurricane landfalling characteristics.
- Figure 414: Analysis of hurricane frequency from Toro (Risk Engineering) from an analysis using an optimized spatial kernel.
- Figure 415: Frequency of hurricanes along reference line with annotated geographic locators, based on 22-storm sample.
- Figure 416: Gumbel coefficients for locations along reference line, based on 22-storm sample.
- Figure 417: Distribution of 50-year, 100-year, and 500-year central pressures along the reference line shown on Figure 415, using both Oceanweather, Inc., data and official NOAA values.
- Figure 418: Comparison of Vickery's analysis of the combination of distributions for landfalling central pressures from all coastal segments compared to the distribution of all landfalling central pressures within the Gulf of Mexico.
- Figure 419: Same as Figure 418 except specific to the 1-degree increment centered on 7.
- Figure 420: Independent estimate of storm probabilities in the Mississippi coastal area by Gabriel Toro (for FEMA Region 4) compared to estimate based on Gumbel segments developed in this white paper.

FIGURES (Continued)

Figure 421: Relationship between size scaling parameter (R_p) versus Central Pressure for the 52-storm set in Gulf of Mexico (off coast; all storms > Cat 2).

Figure 422: Relationship between size scaling parameter (R_p) at landfall versus Central Pressure for the 22-storm set in Gulf of Mexico (off coast; all storms with central pressure < 955 at time of minimum pressure in the Gulf of Mexico).

Figure 423: Plot of mean storm heading angle and standard deviation around this angle as a function of location along reference line.

Figure 424: Plot of forward speed of storm at landfall versus central pressure at landfall.

Figure 425: Plot of storm heading and forward speed at time of landfall for only central Gulf landfalling storms.

Figure 426: Plot of storm heading and forward speed at time of landfall for the entire 22-storm sample.

Figure 427: Tracks from southeast at 45-degree angle to RICK-fan set.

Figure 428: Tracks from southwest at 45-degree angle to RICK-fan set.

Figure 429: Percentage of deviations per 0.1-foot class as a function of deviation in feet.

Figure 430: Increase in hurricane size during approach to coast, as seen in recent, well-documented storms.

Figure 431: Contour plot of peak surge levels along a straight coast with a constant offshore slope as a function of storm size and storm intensity.

Figure 432: Regions of size-intensity domain expected to contribute to surges greater than or equal to that of Hurricane Katrina.

Figure 433: Plot of wind speeds (in meters per second) along east-west transects through Hurricane Katrina.

Figure 434: Plot of wind speeds (in meters per second) along north-south transects through Hurricane Katrina.

Figure 435: Plot of wind speeds (in meters per second) along north-south (N-S) and east-west (E-W) transects through Hurricane Betsy.

Figure 436: Plot of estimated cumulative kinetic energy for all storms at time of maximum surface winds within each year: 1941-2005.

Figure 437: Estimated return periods for 4 separate analyses: Low-Activity years only; High Activity Years only; All years into a single analysis; and estimate based on combined analysis of two populations

Figure 438: Distribution of normalized maximum surges along the coast.

Figure 439: Distribution of normalized maximum surges along the coast.

FIGURES (Continued)

- Figure 440: Distribution of normalized maximum surges along the coast.
- Figure 441: Distribution of normalized storm surge as a function of normalized distance along the coast.
- Figure 442: Figure 442-A shows an idealized representation of the New Orleans coastal area, with a section of land protruding from a generalized straight-line coast. Figure 442-B shows that the resulting surge distributions along the coast. Figure 442-C shows that surge values for this coastal configuration tend to be about 10 to 20 percent higher than the corresponding surges on a straight-line coast.
- Figure 443: Figures 443-A through 443-C re-plotted with lines approximately 31 nautical miles drawn for the case in which the peak falls midway between the two tracks.
- Figure 444: Sample time plot of the variation in central pressure, maximum wind speed, R_p , and forward storm speed used in quality control check of storm parameter behavior for first storm in JPM sequence.
- Figure 445: Variation in maximum storm surge produced by hurricanes approaching a straight, shallow-sloping (1:10,000) coast relative to the maximum surge produced by a storm moving perpendicularly to the coast.
- Figure 446: Examples of the eliminated profiles.
- Figure 447: Examples of surface pressure profiles for a traverse across a given hurricane.
- Figure 448: (continued) Examples of surface pressure profiles for a traverse across a given hurricane.
- Figure 449: Geographical distribution of all the filtered profiles.
- Figure 450: Examples of Smoothed (line) and Point Estimates (symbols) of RMW and B derived from 700-millibar level pressure data.
- Figure 451: (continued) Examples of Smoothed (line) and Point Estimates (symbols) of RMW and B derived from 700-millibar level pressure data.
- Figure 452: (concluded) Examples of Smoothed (line) and Point Estimates (symbols) of RMW and B derived from 700-millibar level pressure data.
- Figure 453: Smoothed (line) and Point Estimates (symbols) of RMW and B derived from H*Wind data.
- Figure 454: (continued) Smoothed (line) and Point Estimates (symbols) of RMW and B derived from H*Wind data. Vertical line(s) represent time of landfall.
- Figure 455: (concluded) Smoothed (line) and Point Estimates (symbols) of RMW and B derived from H*Wind data.
- Figure 456: Absolute value of RMW model error vs. $\bullet p$.
- Figure 457: Modeled and observed RMW vs. $\bullet p$ for all hurricanes.

FIGURES (Continued)

- Figure 458: Absolute value of RMW model error vs. $\bullet p$ for Gulf of Mexico hurricanes.
- Figure 459: Modeled and observed RMW vs. $\bullet p$ for Gulf of Mexico hurricanes.
- Figure 460: Comparison of all hurricanes model predicted median RMW to Gulf of Mexico model median RMW.
- Figure 461: RMW for landfalling storms along the Gulf and Atlantic Coasts of the U.S.
- Figure 462: Relationships between the Holland B parameter, latitude, RMW, $\bullet p$, and T_s .
- Figure 463: Relationship between the Holland B parameter dimensionless parameter, A .
- Figure 464: Holland B parameter vs. RMW for storms with central pressure < 930 millibars.
- Figure 465: Relationship between the Holland B parameter and the dimensionless parameter, A , comparing the all hurricane data with the Gulf of Mexico hurricane data.
- Figure 466: Comparison of Holland B parameters derived from flight level data to those derived using a post landfall windfield analysis.
- Figure 467: Comparison of Holland B parameters derived from flight level data to those derived using a post landfall windfield analysis for hurricanes with central pressures ≤ 964 millibars.
- Figure 468: Surge levels (feet) at coastal stations (Station Numbers denoted on right hand side of chart) along Mississippi coast as a function of pressure differential (millibars).
- Figure 469: Response surface showing integerized surge values in feet as a function of row from top to bottom and column from left to right.
- Figure 470: Surge levels (feet) at coastal stations (Station numbers denoted on right hand side of chart) along Mississippi coast as a function of angle of storm approach to land.
- Figure 471: Surge levels (feet) at coastal stations along Mississippi coast as a function of forward speed of storm (mph).
- Figure 472: Comparison of Return Periods for surges estimated from 3-millibar and 30-millibar categories compared to a continuous function.
- Figure 473: Comparison of results from Track 1a (midway between Tracks 1 and 2) to interpolated values using information from Tracks 1 and 2 for a set of points spread throughout the entire New Orleans region.
- Figure 474: Comparison of results from Track 2a (midway between Tracks 2 and 3) to interpolated values using information from Tracks 2 and 3 for a set of points spread throughout the entire New Orleans region.
- Figure 475: Comparison of results from Track 3a (midway between Tracks 3 and 4) to interpolated values using information from Tracks 3 and 4 for a set of points spread throughout the entire New Orleans region.

FIGURES (Continued)

Figure 476: Comparison of results from Track 4a (midway between Tracks 4 and 5) to interpolated values using information from Tracks 4 and 5 for a set of points spread throughout the entire New Orleans region.

TABLES (VOLUME 6)

Table 1.	Communities Covered Under Scope of Work.
Table 2.	Parish Population Statistics and Communities.
Table 3.	Historical Flooding Events, 1978 to Present.
Table 4.	New Local Mean Sea Level (2001-2005 NTDE) – NAVD88 (2004.65).
Table 5.	Bathymetric Data Source for Inland Water Bodies.
Table 6.	Manning-n Values for Louisiana Gap (LA-GAP) Classification.
Table 7.	Manning-n Values for Mississippi Gap (MS-GAP) Classification.
Table 8.	Manning-n Values for 1992 NLCD Classification.
Table 9.	1992 NLCD Nominal Land Roughness Values.
Table 10.	Basic Configurations of the High-Performance Computer Systems Used for Storm-Surge Simulations.
Table 11.	Storm Parameters for 152 Probable Storms.
Table 12.	Storm Parameters for PBL Model Validation Storms.
Table 13.	Wave Field Domain Characterization.
Table 14.	BRICKA Hurricane Simulation Information.
Table 15.	BRICKA Wave Gauge Information.
Table 16.	BRICKA Peak Wave Comparisons.
Table 17.	Maximum Wave Heights for BRICKA Storms OWI-Forcing.
Table 18.	Maximum Wind Speed and Heights for JPM-FEMA Storms.
Table 19.	STWAVE Grid Specifications.
Table 20.	SSA and SA Tidal Components Recorded at NOAA Stations along the Gulf Coast.
Table 21.	NOAA Stations Used in the Tide Error Analysis.

TABLES (Continued)

Table 22.	Current NOAA Tidal Harmonic Constituent Data at 40 Selected Stations in the Gulf of Mexico.
Table 23.	Tidal Potential Constants for Principal Tidal Constituents and Associated Periods, Amplitudes and Effective Earth Elasticity Factors.
Table 24.	SL15 Model Harmonic Constituents Used to Decompose Model Time Histories Into Harmonic Constituents.
Table 25.	Correlation Coefficients R2 for the Four Groups of NOAA Stations.
Table 26.	SL15 Model to NOAA Measured/Analyzed Error Statistics for the Four Groups of NOAA Stations.
Table 27.	Summary of SL15 Computed and NOAA Measurement-Analysis Errors for Each Harmonic Constituent and NOAA Measured/Analyzed Data Error Estimates.
Table 28.	Previously Published NOAA Tidal Harmonic Constituent Data in the Gulf of Mexico used in Estimating Errors in the NOAA Harmonic Constituents.
Table 29.	Summary of USGS Water-Level Sensor Locations and Their Approximations in ADCIRC.
Table 30.	Statistical Data for Comparisons between Observed High-Water Marks (HWMs) and Simulated Values for Hurricane Katrina for Both H*WIND/IOKA and PBL Wind Fields.
Table 31.	Statistical Data for Comparisons between Observed High-Water Marks (HWMs) and Simulated Values for Hurricane Rita for Both H*WIND/IOKA and PBL Wind Fields.
Table 32.	Longitude and Latitude limits for zooms shown on Figure 401.
Table 33.	Example of Expected Surge Values as a Function of Return Period With and Without •-Term Included.
Table 34.	Estimated Changes in Extreme Waves Heights and Surges for Selected Return Periods, Given a Doubling of Years with High Hurricane Activity.
Table 35.	Distribution of Filtered Pressure Profiles Based on Filtering Criteria.
Table 36.	Percentage of Flight Level Pressure Profiles Retained.
Table 37.	Tendency of Holland B Parameter for Landfalling Storms.
Table 38.	Low-Intensity Storm Parameters.
Table 39.	East Low-Intensity Storms.
Table 40.	West Low-Intensity Storms.

APPENDICES (VOLUME 7)

Appendix A OWI Storm Data

Appendix B OWI Model Sample Files – Storm Track

Appendix C OWI Model Sample Files – TROP Format

Appendix D OWI Model Sample Files – PRE/WIN Format

Intermediate Submission No. 2 – Offshore Water Levels and Waves

1.0 INTRODUCTION

1.1 Purpose of Study

This Flood Insurance Study (FIS) investigates the existence and severity of flood hazards in the areas listed in Table 1 and aids in the administration of the National Flood Insurance Act of 1968 and the Flood Disaster Protection Act of 1973. This study will develop flood risk data for various areas of the community that will be used to establish actuarial flood insurance rates and to assist the community in its efforts to promote sound floodplain management. Minimum floodplain management requirements for participation in the National Flood Insurance Program are set forth at 44 Code of Federal Regulations 60.3.

In some states or communities, floodplain management criteria or regulations may exist that are more restrictive or comprehensive than the minimum federal requirements. In such cases, the more restrictive criteria take precedence and the state (or other jurisdictional agency) will be able to explain them.

1.2 Authority and Acknowledgments

The sources of authority for this FIS are the National Flood Insurance Act of 1968 and the Flood Disaster Protection Act of 1973.

The hydrologic and hydraulic analyses for this study will be performed by the U.S. Army Corps of Engineers (USACE) for the Federal Emergency Management Agency (FEMA).

2.0 AREA STUDIED

2.1 Scope of Study

The Study Area for this coastal FIS is comprised of 13 parishes: Ascension, Assumption, Jefferson, Lafourche, Livingston, Orleans, Plaquemines, St. Bernard, St. Charles, St. James, St. John the Baptist, St. Tammany, Tangipahoa, and the Eastern half of Terrebonne. The Study Area is bounded on the east by the state of Mississippi and the Gulf of Mexico; on the south by the Gulf of Mexico; on the west by Bayou Lafourche; and on the north by the state of Mississippi and/or the 10-meter elevation contour, which will be used in this study as the effective limit of inundation. This FIS covers the areas of Southeastern Louisiana listed in Table 1 and shown on Figure 1.

2.2 Community Description

2.2.1 Population

The total population of the Study Area is approximately 1,847,000, based on 2005 U.S. Census Bureau estimates. Population estimates of individual parishes are listed in Table 2. Due in large part to the effects of Hurricanes Katrina and Rita, populations of all of the parishes in the Study Area have changed significantly in the period of time leading up to this study and continue to change. The trends of population change for most of the parishes follow those presented in Table 2. The populations of Orleans, Plaquemines, and St. Bernard parishes significantly declined after Hurricane Katrina. According to a recent report by the Brookings Institution dated December 12, 2006, the population of Orleans Parish has decreased by 58 percent, to 191,139. Other parishes, including Ascension, Livingston, and Tangipahoa, grew due to the migration of residents of the parishes more heavily damaged by the 2005 storms. There have been population changes within parishes, such as in St. Tammany, where residents of coastal areas moved inland within the parish, and displaced residents of St. Bernard and Orleans parishes migrated into St. Tammany Parish.

2.2.2 Study Setting Background

Southern Louisiana is defined by a low-lying coastal floodplain situated adjacent to a broad continental shelf. A large delta has been formed by the Mississippi River which extends nearly to the continental shelf break. The region is covered by interconnected estuaries, bays, marshes, lakes, rivers, channels, while the major relief is defined by features such as river banks and an extensive system of levees and raised roads. Louisiana has a generalized coastline 397 miles long (639 kilometers [km]) along the Gulf of Mexico. Due to its complex geometry, Louisiana's tidal shoreline, including bays, offshore islands, and deltaic features, is 7,721 miles (12,426 km) long. The region is changing significantly in time due to natural morphological evolution and more dramatically due to manmade levees and dredged channels which have led to a sediment-starved delta that is slowly subsiding. The low-lying topography, the ubiquitous water bodies, and the intricate system of raised features make the region very susceptible to flooding from hurricane storm surge. Hurricane surges can propagate rapidly across the floodplain, can come from many directions, and can experience dramatic localized amplification due to the topography and raised features. This region is geometrically and hydrodynamically complex.

Soil type in the Study Area varies, but its formation is dominated by alluvial processes. Much of the area is covered by alluvium deposited during various delta-building cycles of the Mississippi River, as well as by various smaller rivers and bayous. Muck and peat soils are found within the coastal marshes, while the bottom soils of the Mississippi River valley are composed of alluvial clastic material, from gravel to clay.

The climate of Southeastern Louisiana is hot, humid, and subtropical. Louisiana receives a yearly average of 57 inches of precipitation. The average January temperature is 55 degrees Fahrenheit, and the July average temperature is 82 degrees Fahrenheit.

2.3 Principal Flood Problems

FEMA maintains a listing of recent significant floods, which are defined as floods with 1,500 or more paid losses. Many of these have occurred in South Louisiana. FEMA lists 89 significant floods nationwide from 1978 to present. Twenty-one of these affected Louisiana. Table 3 includes a listing of these significant flooding events. Of the 21 significant floods, 11 were caused by tropical storms and hurricanes. Causes of the remaining 10 significant floods were not listed, but are assumed to be related to rainfall and local riverine flooding events. Based on these data, it can be concluded that the number of significant floods caused by tropical storms and hurricanes is equal to the sum of all other causes of significant floods. According to data in Table 3, 95 percent of the total amount paid for damages in this time period was accounted for by tropical storms and hurricanes, as compared to 5 percent for all other causes of flooding.

2.4 Flood Protection Measures

Southeastern Louisiana is subject to heavy property damage and high risk to human life from hurricane-induced flooding. The first attempt to address this problem occurred when Congress authorized Lake Pontchartrain, Louisiana, in the Flood Control Act of 1946. This project was completed in 1965 and its purpose was to protect Jefferson Parish from storm-induced flooding from Lake Pontchartrain for 30-year frequency storms. Since that time, Congress has authorized additional projects at various locations in Southeast Louisiana.

Since its founding in 1718, the city of New Orleans has struggled against the annual flooding of the Mississippi River and the occasional storm surge flooding brought by tropical cyclones. Private river levees were constructed almost from the beginning. Federal participation in these efforts included establishment of the Mississippi River Commission in 1879 and the Mississippi River and Tributaries project in 1928.

Originally situated on the relatively high ground near the river, the city continued to grow and expand through the 20th century. Marsh land north of the city was drained for development up to the shore of Lake Pontchartrain. Protected from the seasonal floods of the river, attention shifted to building levees along Lake Pontchartrain to the north and Lake Borgne to the east of the city.

Surrounding parishes experienced collateral growth, particularly with the development of the fossil fuel extraction and processing industry and the growing prominence of Louisiana's seafood industry. During the past 40 years, as infrastructure and population expanded, the Hurricane Protection System (HPS) was expanded to include protection for national economic assets. An overview of the HPS is included as Figure 2.

While levees provided protection from rising tides and storm surges, they also hydraulically isolate urban and industrialized areas. Rainfall runoff can be significant in Southeast Louisiana even without the fuel of a tropical cyclone. The average annual rainfall for the New Orleans area is 60 inches. Nearly all runoff must be pumped out of the protected area, or basin, to prevent flooding. The interior drainage system is designed for removing storm water from rainfall events, not removing water that enters the area from levee or floodwall overtopping or breaches (Link et al., 2006; Ebersole et al., 2007).

3.0 ENGINEERING METHODS

State-of-the-art atmospheric and coastal ocean hydrodynamic analysis methods will be used to determine the flood hazard data required for this study. The Joint Coastal Surge (JCS) Analysis procedures were developed by USACE and FEMA in order to provide a unified technical approach to determine 100-year storm water surface elevations across the Gulf Coast. These methodologies were largely developed as a result of various coastal surge analyses conducted following Hurricanes Katrina and Rita (Link et al., 2006; Ebersole et al., 2007). In order to avoid confusion and inconsistencies among the federal agencies, the USACE and FEMA held a series of meetings in August 2006 to discuss the proposed methodology described herein. The general analysis strategy consists of applying a sequence of deterministic coastal ocean hydrodynamic models used to ascertain maximum water levels subject to a specific set of meteorological and other forcing functions. The deterministic hydrodynamic modeling component is then combined with a stochastic component to define the atmospheric conditions to which Southern Louisiana is exposed.

The coastal hydrodynamic modeling methods used to determine water levels were selected and implemented based on the following criteria:

- An extensive understanding of the physical system as a whole and its individual consequential components;
- Inclusion of all significant physical processes affecting water levels;
- Full consideration of the interaction between physical processes;
- Characterization of forcing functions that correspond with real world observations;
- Accurate definition of boundary conditions; and
- Generation of discrete numerical grids to resolve the physical and energetic processes consistently and accurately within the models.

Thus, the goal is to implement a modeling capability that represents the basic physics of the system as it is observed in nature and does not require ad hoc model tuning. Therefore, the models should define the physical system as it exists, which includes the consideration of wind, atmospheric pressure, short-period wind waves, tides, and riverine flows in a comprehensive way. In order to achieve the required accuracy, a sequence of state-of-the-art, well-verified, and validated wind, short-period wind-wave, and coastal circulation models were

IDS 2

coupled together as an atmospheric-hydrodynamic modeling system and applied to Southern Louisiana and Mississippi.

The stochastic procedures were then applied to identify a suite of storms that together characterize the inherent and current storm surge inundation risk in Southern Louisiana. Because historical records are sparse and storm data are unreliable dating back more than 30 years, the stochastic procedures must be utilized to generate storms that correctly characterize the storm surge danger in the region. The atmospheric-hydrodynamic computational system was applied to establish peak surface water elevation-frequency relationships for hurricane winds and pressures, major riverine flows (the Mississippi and Atchafalaya rivers), wave forcing, and tides affecting the region. Wind, atmospheric pressure, and riverine forcing functions are applied and quantified using statistical methods. Tides are forced deterministically. The atmospheric forcing functions are typically generated using a dynamically based synthetic hurricane generator and applied as input into coastal wind-wave and circulation models to compute the associated water levels. The resulting water levels are then analyzed in a stochastic framework resulting in the desired flooding probabilities.

Subsequent sections describe:

- The physical data collected to define and validate the computational models;
- The atmospheric-hydrodynamic modeling system and its various components;
- The validation of the deterministic hydrodynamic computational system by applying the system to Hurricanes Katrina and Rita and comparing results to high-water marks (HWMs) and water gauge data;
- The definition of the storm set used to define the risk to which Southern Louisiana is exposed;
- The computation of these storms within the atmospheric-hydrodynamic system; and
- The subsequent analysis of risk.

3.1 Physical and Hydrodynamic Description of the Region

The computational modeling process requires that the physical system is accurately described and characterized. This means that the bathymetry, topography, and surface roughness characteristics of the region are accurately represented. In addition, all vertical geometric features such as levees, river banks, and roads must be incorporated into the model. These small-scale features require careful consideration because they can impede the flow and focus the storm surge. Topographical mappings and surveys, including high-resolution light detection and ranging (lidar)-based surveys, can easily neglect these features due to their relatively small horizontal scale. Such small horizontal scales require special handling in order to concisely represent each feature in the models. In addition, the wind, wave, and circulation models all require a description of the terrain roughness over which the wind blows and waves and surge propagate.

IDS 2

In addition to the description of the geographic and vegetative characteristics, the models also require wind, atmospheric pressure, wave, water level, and flow information at various scales and sampling times. This information is used both to validate the models that comprise the atmospheric-hydrodynamic modeling system as well as to help force the system. Examples of this are the riverine flows in the Mississippi and Atchafalaya rivers used as boundary forcings, as well as historical wind fields employed for validating historical storms.

The models applied in the flood level evaluation process must be validated over a range of conditions to ensure that the flow physics of the system are being accurately characterized. Whenever possible, it is desirable to separately validate the various processes. Wind information can be used to both force surge models and validate how accurately the synthetic hurricane wind and pressure fields are represented during a hurricane event. Tides are a fairly low-energy process in coastal Southern Louisiana and thus can be used to separately validate the integrity of the water level model for modest flow conditions and water levels. In addition, wave characteristics can be compared at locations where these data have been collected for low-energy and high-energy wind events. The fully integrated system model validation has been implemented by comparing results to measurements from recent powerful storms, in particular Hurricanes Katrina and Rita. This set of validation storms was chosen due to the fact that more accurate measurements of wind, atmospheric pressure, waves, and surge levels exist for these very powerful and recent storms; measurement techniques for older large storms were not as comprehensive. In addition, the physical characterization of the system for these storms is more accurate than that for earlier major storms, largely due to the availability of high definition lidar topographic data and comprehensive satellite-based land use/type classification data.

In the following sections, there are detailed descriptions of the map-based information including the datum, the bathymetry, topography, and land use. This information is used to describe the physical system to the atmospheric-hydrodynamic models used to assess flooding risk. In addition, a description is given of the available historical fluid flow data that quantify the movement and state of the air and water for both low- and high-energy flow processes. These data include information about tides, riverine flows, wind, waves, and hurricane-driven storm surge and are used primarily to validate the hydrodynamic modeling system in Southern Louisiana.

3.1.1 Topographic and Bathymetric Data

3.1.1.1 Horizontal/Vertical Datum/Survey Control Data

The vertical datum provides a starting point against which ground, structure, feature, and water level elevations can be referenced and compared. Until recently, the standard vertical datum in use was the National Geodetic Vertical Datum of 1929 (NGVD29). With the finalization of the North American Vertical Datum of 1988 (NAVD88), a significant amount of vertical topographic and bathymetric data are now referenced to the NAVD88. NAVD88 was released for Louisiana in 1992. Nonetheless, much of the data, including topographic and feature data and especially water level data, for both

hydrographs and HWMs are referenced to the older NGVD29. There are a number of different epochs or corrections to NGVD29. In addition, an updated epoch to NAVD88, referred to as NAVD88 (2004.65), was recently released (Garster et al., 2007). The NAVD88 (2004.65) datum was established in order to correct for initial errors in the NAVD88 datum, as well as adjust for subsidence in Southern Louisiana, especially for the subsidence of the benchmarks in the region. Much of the post-Katrina feature data as well as the HWMs in the region were referenced to NAVD88 (2004.65).

Bathymetric data are typically referenced to Mean Lower Low Water (MLLW), the average of the lower low water height of each tidal day observed over the National Tidal Datum Epoch. Because tide range changes considerably in U.S. Coastal waters, this reference is useful for navigational purposes but is not nearly as useful in terms of referencing to a vertical datum such as NAVD88. The National Oceanic and Atmospheric Administration (NOAA) is currently computing vertical adjustments to MLLW-based bathymetric values in their VDatum studies which compute the tides in the region, estimate the local tide range and offset between MLLW and Mean Sea Level (MSL), and make the appropriate vertical adjustment.

This study will reference water level data to NAVD88 (2004.65) and incorporate vertical data referenced to NAVD88 (2004.65) when feasible. Note that the topographic lidar data in Louisiana (Louisiana State University [LSU], 2004) and Mississippi (URS Corporation [URS], 2006c) are available relative to NAVD88. Although some of these data have been mapped to NAVD88 (2004.65) in portions of Louisiana, the warping surface used to perform the transformation appears to be of insufficient quality to apply throughout Southern Louisiana. This is related to the fact that the density of control points defined in the Interagency Performance Evaluation Taskforce (IPET) Geodetic study (Garster et al., 2007) is not sufficient to reliably apply throughout the entire southern portion of the state. Therefore, topographic values are applied using NAVD88 as the vertical reference throughout Louisiana and Mississippi. However differences between the NAVD88 and NAVD88 (2004.65) should be no more than 1.06 feet throughout Southern Louisiana (Garster et al., 2007). Applying current warping surfaces available for Southern Louisiana will lead to errors larger than this. Federal levees were incorporated using NAVD88 (2004.65) as the vertical datum because these were resurveyed and/or were adjusted to the new NAVD88 (2004.65) as part of the IPET study using reliable and sufficiently dense control points (Garster et al., 2007).

Bathymetric depths were adjusted to NAVD88 (2004.65) in order to be consistent with topographic data. Examination of NOAA benchmarks by the IPET geodetic survey task in Southeastern Louisiana shows that on average Local MSL (LMSL) is approximately 0.5 foot above MLLW. The regionally averaged offset between LMSL and NAVD88 (2004.65) based on 11 out of 12 stations reported by Garster et al. (2007) within

Southern Louisiana is 0.44 foot with a standard deviation equal to 0.15 foot. All 12 reported stations are listed in Table 4. For this study, we did not use Shell Beach in our adjustment estimate because this station was an outlier and we apply one global adjustment to the entire Louisiana and Mississippi coasts. Thus, LMSL regionally lies above NAVD88 (2004.65) by 0.44 foot. LMSL regionally lies above MLLW by 0.50 foot. This means that regionally NAVD88 (2004.65) lies above MLLW by 0.06 foot in areas not largely affected by riverine flows. This will allow for a regional adjustment of bathymetric depth to NAVD88 (2004.65) by adding on average 0.06 foot to the MLLW reference. Localization of this procedure would improve the accuracy of the adjustment once more comprehensive information becomes available. Also, it is noted that subsidence and eustatic sea level rise rates will quickly override the adjustment values used. However, the current maps are for the situation as it exists today. In the long term, the computations will have to be updated to include the subsidence and sea level rise that has occurred. As part of the Louisiana Coastal Protection and Restoration (LACPR) project, sensitivity studies are being performed to investigate the effect of sea level rise.

The NAVD88 (2004.65) datum, unlike the NGVD29 datum, is a geodetic equipotential surface and therefore provides a sound reference for our computations when adjusted for the offset to LMSL. This then also requires that initial water levels be raised in the model to account for the fact that during the year, on average, LMSL lies 0.44 foot above NAVD88 (2004.65). Because the computations are barotropic, it is also necessary to account for the annual fluctuation in sea level due to thermal expansion of the upper layers of the Gulf of Mexico and by other effects including coastal currents, riverine runoff, salinity, seasonal prevailing winds, and atmospheric pressure. This annual sea surface fluctuation, largely due to the steric effect, clearly presents itself in water level time history records (i.e., hydrographs) as well as long-term harmonic tidal analyses. For harmonic analyses, this effect is especially apparent for the solar annual and semiannual (Sa and Ssa) tidal constituents. The sea surface differential can be estimated based on NOAA long-term sea level stations in the region (NOAA, 2007). We can accurately adjust the initial water levels in the model to correctly define unforced water levels prior to the storm (i.e., no tidal or riverine forcing nor wind and/or atmospheric pressure forcing). More details concerning this annual sea surface fluctuation adjustment are presented in Section 3.2.4.8.

Finally, it was noted that some regional variability exists in LMSL due to local thermal regimes and other factors that vary spatially causing small perturbations in LMSL. This is partly reflected in the standard deviations in the offset between LMSL and NAVD88 (2004.65). Flows from major rivers, the Mississippi and Atchafalaya, are explicitly incorporated into the model and their effect on LMSL is accounted for explicitly. Not all river flows are included in the model, which can result in small, localized increases in open water LMSL. However, river flows were only absent in the

model when their effects are assumed to have an insignificant effect on the resulting water levels.

3.1.1.2 Topographic Data from Aerial Photography

Aerial photography was not utilized as a source of bathymetric or topographic definition in this study. However, once topography and bathymetry were defined using the most accurate data available, major vertical features such as salt domes and river banks were checked against aerial photographs using both satellite images as well as Google Earth images (Google, 2007). There were numerous mounds that showed up in the topography as raised features in otherwise flat adjacent regions that proved to be landfills. The location of the shoreline was checked by accounting for the position of MSL relative to NAVD88 or NAVD88 (2004.65) defined bathymetric and topographic values as well as assuming a summertime steric expansion and checking the position of this shoreline against both visual satellite images by comparing within ARC Geographic Information System (GIS). In addition, comparisons were made to shoreline positions as defined in the Gap Analysis Program (GAP) land use maps as well as Louisiana and Mississippi lidar sets. Similar checks could be done in the future for interior marshes and channel geometries as well. Presently, some areas, such as the Inner Harbor Navigation Canal (IHNC) locks, have geometric simplifications that can be improved upon in future revisions of the mesh.

3.1.1.3 Topographic Surveys/Data

Accurate mapping of the region's topography is essential to correctly simulate inland flood propagation. Topography influences wind-wave and surge propagation speed and direction, as well as frictional dissipation. In addition, topography can both regionally amplify and attenuate storm surge. For these reasons, the topography in Southern Louisiana and Mississippi was mapped in our hydrodynamic model using the most accurate and current topographic survey data. The various topographic data sources for coastal Louisiana and Mississippi are summarized on Figures 3 and 4.

Topographic values were applied from a variety of data sources. The most recent and most trusted topographic values came from the LSU-Atlas Lidar data set. The lidar data were not available for the entire region; thus, many gaps did exist where topographic values had to come from the 30-meter National Elevation Dataset (NED). For regions where neither Atlas Lidar nor NED had coverage, estimates of topography and bathymetry were made from the National Land Cover Data (NLCD) set. These approximations were based upon reviewing how elevation and land-cover type were correlated in nearby regions where coverage did exist. The nodal elevations in the ADvanced CIRCulation (ADCIRC) mesh were carefully reviewed at the interface between data sources and adjusted to smooth out any discontinuities. All data sets were

converted to Geographic North American Datum of 1983 (NAD83) and elevations adjusted to the NAVD88-2004.65 datum.

Topographic data for the majority of the terrain in Louisiana were obtained from the U.S. Geologic Survey (USGS)/State of Louisiana Atlas lidar database (LSU, 2004). These data are available in Digital Elevation Model (DEM) form on a 5-meter by 5-meter basis. These data were obtained beginning in March 2004, although they were released as early as 2003 and surveys were performed as early as 2002. Prior to release, the data have been checked for quality assurance (QA) and cleaned of signals created by buildings, trees, and shrubbery, resulting in a "so-called" bare earth model. Nonetheless, small-scale hydrodynamically relevant features, such as levees, river banks, and road beds, do appear in the data.

Lidar data are significantly more accurate than previously available non-lidar based USGS NED data (USGS, 2004). The Atlas lidar data are stated to be accurate to +/- 0.50 foot in the vertical with accuracy being best for flat hard surfaces. There are, however, some regions of Southern Louisiana that have been identified as possibly having larger errors. Dokka (2006a and 2006b) found that less than 90 percent of the sampled points were accurate within +/- 0.8 foot. These areas, which are located throughout the state, especially in the Atchafalaya flood basin, were discovered using preliminary analyses which compare the lidar data to high precision Global Positioning System measurements including portions of the Atchafalaya flood basin (Dokka, 2006a and 2006b). In addition, questions remain as to whether additional errors are occurring due to the lack of consistency of the vertical datum used as well as because of the ever-changing datum itself over time. The Atlas lidar data were referenced to NAVD88, which has changed in time. The IPET study established NAVD88 (2004.65) and made localized adjustments to the Atlas data in the New Orleans metropolitan region and for Plaquemines Parish. Control points that were established have been applied for this and a mapping or so-called warping surface for Southern Louisiana as a whole has been developed. It was found that the density of the control points was such that the warping surface was based extensively on either poorly interpolated regions or regions that were extrapolated. The resulting adjusted topography showed unrealistic features with extensive regions having errors that were larger than the differences between NAVD88 and NAVD88 (2004.65) at the control points themselves. Therefore, the original NAVD88 datum for the Atlas lidar data was retained.

Note that at the time of this study, Atlas lidar coverage was not available for all of Southern Louisiana. These regions are shown on Figure 3. In small portions of western Southern Louisiana, east Texas, and to the west of Simmesport, Louisiana, 30-meter by 30-meter USGS NED data were used to fill the voids left by the Atlas lidar (USGS, 2004). Though not as high resolution as the lidar data and with unknown accuracy, the NED data were the most comprehensive data available in these areas.

Furthermore, Atlas lidar does not generally extend into many of the marshes and wetlands within Southern Louisiana as is detailed on Figure 3. In these regions, estimates of topographic and bathymetric depths have been applied based on USGS GAP land use maps which clearly define the coastal marshes (USGS, 2000). The land use maps were coupled with controlled marsh elevation approximations and adjacent water depth estimates relative to NAVD88 (2004.65). Marsh topography and water bathymetry were approximated based on nearby marshes where lidar data were available. The base of the marshland was assumed to be 0.80 meter above the NAVD88 (2004.65) geoid and the depth in water areas within the marsh was assumed to be 0.40 meter below the NAVD88 (2004.65) geoid. Nodal elevations were then set by tallying the number of marsh pixels and water pixels within the elements surrounding each node and finding an average value based on the elevation assumptions. Any errors created by assuming marsh elevations should not greatly affect the results due to the fact that the marshes have small elevation gradients; thus, small inaccuracies in elevation data should not affect surge results considerably when the surge is large. Grid scale averaging was also applied as follows:

$$z = \frac{h_{water} \times n_{water}}{n_{total}} + \frac{h_{land} \times n_{land}}{n_{total}} \quad (1)$$

where:

z is the grid scale averaged elevation referenced to the NAVD88 (2004.65) datum;

h_{water} is an approximated water elevation of 0.40 foot below the NAVD88 (2005.65) geoid.

n_{water} is the total number of land use pixels defined as water within a nodal control volume;

h_{land} is an approximated marsh elevation of 0.80 foot above the NAVD88 (2004.65) geoid;

n_{land} is the total number of land use pixels defined as marsh within a nodal control volume; and

n_{total} is the total number of land use pixels within a nodal control volume.

As shown on Figure 3, topographic data in Mississippi were obtained from lidar surveys from the Mississippi Coastal Analysis Project, Geospatial Technology Task supplied to our team by URS. These data were available relative to NAVD88. Lidar survey and

quality control (QC) specifics can be found in two separate reports. The first is a FEMA report titled "HMTAP Task Order 18 Mississippi Coastal Analysis Project Geospatial Technical Task Report (Task 3)", dated December 5, 2006 (URS, 2006c). The second report is a USACE, Mobile District report titled "Lidar Report: Mississippi and Alabama Coastal Mapping", dated November 2005 (USACE, 2005).

Finally, barrier island topographic elevations were incorporated from a variety of sources as summarized on Figure 4. The Chandeleur Islands topographic elevations were obtained from post-Katrina lidar surveys performed by the USGS (Salinger, personal communication, 2006). The Mississippi Sound islands were obtained from post-Katrina lidar surveys performed by the USACE (Lillicrop, personal communication, 2006). Half Moon Island, which is at the entrance of Lake Borgne, Deer Island, which protects Biloxi Bay, and Singing River Island, which lies southwest of Pascagoula, all had topography extracted from the Mississippi Automated Resource Information System (MARIS) 10-meter by 10-meter DEM database (MARIS, 2006).

It is noted that bathymetry and topography were predominantly defined for the condition that existed prior to August 2005 and Hurricane Katrina as defined with the available data. Many of the bathymetric surveys were collected over decades prior to 2005 while the topographic lidar data for Louisiana were collected beginning in 2002. Lidar data for the Mississippi coastline were collected post-Katrina in September and October 2005. The other notable exception to incorporating pre-Katrina topographic data was for the lidar-based surveys of the Chandeleur and Mississippi Sound islands. Because these barrier islands represent critical controls to flow and induce significant wave radiation stress setup during the peak of the storm and our modeling does not include active degradation of these offshore sediment features, these are included in their post-Katrina configuration. The significant wave action would have degraded these barrier islands early in the Katrina event and their configuration during Hurricane Katrina, Hurricane Rita, and for future storm events will be closer to the post-Katrina configuration than to the pre-Katrina configuration.

3.1.1.4 Bathymetric Surveys/Data

Accurate model bathymetry is crucial to accurately represent the flow physics of a region. In fact, bathymetry controls physical processes including long wave and short wind-wave propagation speed and direction, structure, and dissipation. Bathymetry in the regions in the Western North Atlantic, Gulf of Mexico, and Caribbean Sea that are included in the models was drawn from a number of sources including the raw bathymetric sounding database from the National Ocean Service (NOS), the Digital Nautical Charts (DNC) bathymetric database, and ETOPO5 (Mukai et al., 2001a; Mukai et al., 2001b). Bathymetry for shelf and ocean waters is comprehensively

described in Mukai et al. (2001a and b). The NOS raw sounding database provides the most comprehensive coverage over U.S. continental shelf waters, which include more than 13 million sounding values and is the basis of NOS/NOAA bathymetric charts. Although the surveys are not as comprehensive as the NOS raw soundings, DNC values are available within the Gulf of Mexico and much of the western North Atlantic and Caribbean Sea, while ETOPO5 coverage is worldwide. Data accuracy and preferences are in the order NOS, DNC, and finally ETOPO5 (Mukai et al., 2001a; Mukai et al., 2001b). Bathymetry for inland waterways in Southern Louisiana is provided by regional bathymetric surveys and dredging surveys typically from the USACE New Orleans District (MVN). Figures 5 through 9 and Table 5 define the inland and protected coastal water locations and list the data source.

It was noted that NAVD88 (2004.65) lies above MLLW by, on average, 0.06 foot. This will allow for a regional adjustment of bathymetric depth to NAVD88 (2004.65). All bathymetric data were adjusted based on the closest lying NOAA long-term tidal station. This offset was added to the bathymetric data resulting in depth being defined relative to NAVD88 (2004.65).

3.1.1.5 Vertical Features with Small Horizontal Scales

In addition to describing bathymetry and topography, the model must account for pronounced vertical features with small horizontal scales relative to the grid scale. While features such as barrier islands, river banks, and salt domes as well as the associated flows are generally well resolved in grids with resolutions down to about 100 feet, features such as levees, floodwalls, railroads, and raised highways will not be sufficiently well resolved with 100-foot grid resolution. These small-scale features can, of course, be significant horizontal obstructions to flow causing water to rise or be diverted elsewhere. These obstructions must therefore be incorporated into the model as sub-grid scale features. These features were included as sub- and super-critical weirs. Their horizontal and vertical position must be well defined.

Figure 2 shows all the federal levees. Federal levee centerline alignments were defined using the USACE GIS database. Levee elevations were incorporated using two configurations. The first configuration is an assembly of survey data of pre-Hurricane Katrina conditions in 2005 and is used for hindcasting recent historical storms including Katrina and Rita. The configuration and position of these levees were checked against 1-foot by 1-foot lidar data available prior to Hurricane Katrina (USACE, 2000; Garster et al., 2007). The second source corresponds to authorized levee design elevations to be implemented into the protection system by June 2007. This set of levee definitions is used to simulate the existing conditions in the summer of 2007 and is the basis of the FEMA flood insurance rate maps.

Federal, state, and local roads as well as railroads were positioned in the horizontal using the USACE GIS database and had vertical positions defined from the Louisiana and Mississippi lidar datasets (LSU, 2004; URS, 2006c). The crown height was obtained automatically by searching a defined region around the raised feature's point of interest. Limited detailed comparisons between lidar data and ground surveys were done by URS and show elevation differences of approximately 1 foot for raised features in this region (Suhayda, personal communication, 2007). Lidar information was still utilized due to the fact that the data set was the most comprehensive set available, outside of the survey sources used for the federal levees. Features were only included if the crown height was more than 3 feet above the adjacent topography.

In select areas, railroad crown heights were modified from the lidar defined height data. The CSX railroad between Chef Menteur Pass and the Pearl River Basin between Lake Pontchartrain and Lake Borgne where the railroad is exposed to open water or low-lying non-forested marsh was lowered by about 5 feet from the lidar-defined heights. Much of this railroad was degraded during Hurricane Katrina due to severe wave action and the high overtopping rates in this region. CSX engineers on site involved in the post-Katrina railroad reconstruction indicated to our team (Ebersole et al., 2007) the level of degradation that occurred during the storm. Essentially, the top layer of gravel ballast was washed off together with the railroad tracks while the more solid clay core of the railroad bed remained intact. Farther into Mississippi, where the railroad is well protected by forests, the railroad appears to have suffered much less and the lidar-based crown heights in these regions are not degraded. Raised road beds were typically defined using the lidar-based crown height and assumed not to be degraded during a storm event. The exception to this was U.S. Highway 90 (US 90) between the Chef Menteur Pass and the Rigolets, which were degraded, because it was washed out in sections and is likely to be washed out during severe storm events (based on a site visit by Ebersole and Westerink, 2006). Note that US 90 in Mississippi was not included as a sub-grid scale feature because this road is very limited in its vertical definition and can be well represented using standard grid meshing.

3.1.2 Influence of Coastal Vegetation

Surface roughness significantly influences the flow of the overlying fluid, whether it is water or air. In the case of water flowing or waves propagating over a surface, the bottom friction force that is developed is an important resistance mechanism that must be accurately quantified. The Manning n bottom friction resistance formulation is applied in this study. This formulation is a widely used standard applied in hydraulic computations. In the case of air flowing over a rough surface, the wind boundary layer is modified and the resulting 10 meters above ground level wind speed that is used to compute the surface drag is modified. The wind boundary layer does not adjust instantaneously to the local roughness but adjusts slowly based on the upwind roughness. Finally, it can be shown that very little wind momentum transfers through heavily

forested canopies (Reid and Whitaker, 1976). In order to evaluate the hydraulic bottom drag force, the surface roughness adjusted or so called land masked air-sea drag force, and to account for the canopied areas where little or no momentum is transferred to the water column, the roughness of the land surface needs to be described.

Land roughness in overland regions is characterized by land use conditions such as urban, forested, agricultural, or marsh as described by the USGS NLCD Classification raster map based upon Landsat imagery (Vogelmann et al., 2001) and the USGS GAP data (Hartley et al., 2000). Note that the aerial coverage of GAP data is not as widespread as NLCD. There are further differences between the NLCD and GAP with the NLCD being a "national" data set and being most reliable at large regional averages and not as good for capturing local details. On the other hand, the GAP data sets better characterize the small-scale variation of vegetation types near the coastal margin. GAP has been field checked by biologists and botanists and is considered to be more reliable. For example, NLCD only includes two classifications for wetlands: woody wetland and emergent herbaceous wetland. Most of Louisiana wetlands are classified as emergent herbaceous wetland. However, ground verification of these data through on-site visits, as well as by examining both satellite imagery and raw lidar images (i.e., no bare earth), indicates that this land classification is applied to grassy marshland as well as to thickly covered cypress forest covered marshes. On the other hand, the GAP database for Louisiana defines 11 classifications of wetland including Fresh Marsh, Intermediate Marsh, Brackish Marsh, Saline Marsh, Wetland Forest – Deciduous, Wetland Forest – Evergreen, Wetland Forest – Mixed, Wetland Scrub/Shrub – Deciduous, Wetland Scrub/Shrub – Evergreen, Wetland Scrub/Shrub – Mixed, and Wetland Barren. The Wetland Forest – Evergreen, for example, concisely defined the ubiquitous cypress forests in Louisiana.

The combined Louisiana and Mississippi GAP data and classifications, supplemented with NLCD over areas where GAP data were not available (Texas and Alabama), have been used to define the hydraulic bottom roughness. The Louisiana GAP (LA-GAP) map is shown on Figure 10 and the Mississippi GAP (MS-GAP) map is shown on Figure 11. Note that each state has somewhat different GAP land classifications to tailor the classification to the particular region. The NLCD in Louisiana, Mississippi, Texas, and Alabama are shown on Figures 12 through 15 with the classifications defined on Figure 16. The Manning n associated with these land classifications was selected or interpolated/extrapolated from standard hydraulic literature (Chow, 1959; Henderson, 1966; Arcement and Schneider, 1989; Barnes, 1967). The LA-GAP, MS-GAP, and NLCD classifications associated with Manning n that were selected are given in Tables 6 through 8. It is noted that the Residential GAP classification in Mississippi has a Manning n defined more like a forested region because aerial photographs indicated that these regions more closely resembled densely forested regions.

The roughness lengths or more specifically "nominal" roughness lengths $z_{o,land}$ used to adjust the wind boundary layer are defined by the FEMA HAZUS program (FEMA, 2005). Because the FEMA HAZUS definitions were specifically defined for the NLCD, a modified form of the

NLCD were used in order to define the roughness lengths. As was noted earlier, the NLCD were missing the cypress forests. Therefore, any areas in the NLCD where GAP coverage indicated Wetland Forest – Evergreen have been overwritten in Louisiana. In effect, an additional cypress forest classification was created for the NLCD in Louisiana. This combined classification was used to define the roughness lengths shown on Figures 12 through 15 and defined in Table 9 as per the FEMA HAZUS values. Note that a Woody Wetland roughness length was used to define the cypress forest.

Canopied areas can be identified with regions where the modified NLCD defines Deciduous Forest, Evergreen Forest, Mixed Forest, Woody Wetland, or Cypress Forest. Canopies are assumed to be so high that no water overtops them and that they are thick enough for wind not to penetrate them. Away from canopies, inundation of the physical roughness scales is not allowed because the areas are flooded and reduce the wind roughness as is described later in this report.

3.1.3 Site Reconnaissance

After Hurricanes Katrina and Rita, extensive site reconnaissance was undertaken in the Study Area. Two types of data were collected: HWMs and hydrographs. HWMs were identified and surveyed throughout the region. Hydrographs were collected from instrumentation and were also reconstructed using partial instrument records and photographic evidence.

HWMs are collected using a two-step process. The first step is identification and documentation of the mark including photographs or electronic images, location (local landmarks and latitude, longitude coordinates), type of mark (e.g., mud line on interior or exterior of a building), the vertical distance above some fixed permanent object or structure such as a concrete foundation slab, and any other noteworthy characteristics, such as length. This step is performed as rapidly as possible because the marks are perishable and subject to eradication by natural causes or human activity.

The second step is termed “recovery” of the mark and refers to the vertical leveling of the mark relative to an established and accepted vertical datum such as NAVD88 or NAVD88 (2004.65). This second step typically is more time consuming and expensive than the first, but the HWMs would be of little value if not surveyed to a common datum. Acquisition of HWMs following Hurricane Katrina was performed by three federal agencies, USGS, USACE, and FEMA (or a FEMA contractor), and the State of Louisiana through LSU. All four entities shared the data. Marks identified by USACE, FEMA, and LSU were also recovered by each respective agency. Most of the marks identified by USGS were recovered by FEMA (or a FEMA contractor). A selected subset of approximately 50 marks identified by USGS was also recovered by USGS field crews to confirm elevations provided by FEMA contractors.

Acquisition of HWMs following Hurricane Rita was performed by FEMA as well. The field crews identified a subset of 80 HWMs as being of good or excellent quality. Hydrograph data

IDS 2

were collected by USGS at 23 locations throughout Southwestern Louisiana (McGee et al., 2005). These hydrographs were located along roads, bridges, streams, etc., that were expected to be inundated. These data were collected using instruments with a typical accuracy of 0.1 to 0.2 foot if all the National Geodetic Survey standards are followed. The surveys were done to the NAVD88 (2004.65) vertical datum. Note that HWM analyses done for the various storm data sets showed higher actual errors with a standard deviation of 0.6 foot. This will be detailed in the validation section of the FEMA IDS 2 Report.

A complete description of HWM and hydrograph collection for Hurricane Katrina, as well as an inventory of the HWMs and hydrographs, can be found in Ebersole et al. (2007). Collected Hurricane Rita HWM data are described by URS (2006a; 2006b), and the quality of the data was later identified and refined (Niedoroda, personal communication, 2007).

3.1.4 Technical Approach

3.1.4.1 Overview

The JCS Analysis procedures were developed by the USACE and FEMA in order to provide a unified technical approach to determine 100-year storm water surface elevations across the Gulf Coast. This methodology was developed as a result of various coastal surge analyses being conducted following Hurricanes Katrina and Rita. In order to avoid confusion and inconsistencies among the federal agencies, USACE and FEMA held a series of meetings in August 2006 to discuss the proposed JCS methodology, generally described below:

3.1.4.2 Storm Selection

A set of 152 storms were developed by combining the “probable” combinations of central pressure, radius to maximum winds, forward speed, angle of track relative to coastline, and track. Tracks were defined by five primary tracks and four secondary tracks (track b). A storm matrix was developed based on these parameters and proposed to FEMA and USACE for concurrence. The estimated range of storm frequencies using the selected parameters was between the 50-year and 500-year events.

3.1.4.3 Winds

Based on the storm set, wind fields were generated for each storm utilizing the Oceanweather, Inc. (OWI), Planetary Boundary Layer (PBL) Model. These wind fields are the required input into the storm surge and wave models. A comparative analysis was done between the PBL and Hurricane Boundary Layer (HBL) models to determine the best fit for this analysis and the PBL was selected (Vickery, personal communication, 2006).

3.1.4.4 Surge Model

The ADCIRC model was selected as the basis for the surge modeling effort. This model has been and continues to be the standard coastal model utilized by USACE. The grid developed for the JCS effort was termed the SL15 Grid. This provides for a common grid from the Sabine River to Mobile Bay. The grid will be used for all coastal analysis for Louisiana and Mississippi to ensure consistency and matching solutions at state line/regional boundaries.

3.1.4.5 Wave Models

Offshore waves are being generated using the WAVE Prediction Model (WAM). This model is the standard employed by the USACE for offshore wave modeling and was utilized by the IPET.

Nearshore waves are being computed using the STEADY STATE spectral WAVE (STWAVE) model. It is also a standard model utilized by the USACE and IPET.

3.1.4.6 Statistical Analysis

A statistical analysis based on the Joint Probability Method (JPM) is being utilized to develop stage frequency relationships for the storm events. This has been termed the Joint Probability Method-Optimal Sampling (JPM-OS) technique. These stage frequency relationships allow the USACE and FEMA to determine an agreed upon 100-year elevation for storm surge.

3.1.4.7 Workflow and Automation

The workflow initiates with the availability of wind fields for the various storms. These are produced and loaded into a predetermined directory on the Engineer Research and Development Center (ERDC) High Performance Computer (HPC) known as Sapphire. This wind field input is executed by ADCIRC, STWAVE, and WAM. The output from WAM is input into STWAVE in order to determine the wave radiation stresses and effects of bottom friction. The outputs from STWAVE are re-run through ADCIRC to develop the hydrographs for each storm at all selected nodes in the ADCIRC grid. A general workflow is shown for one production storm on Figure 17.

The winds and WAM are run as preprocessed steps while the ADCIRC-STWAVE-ADCIRC interaction is completely automated. Four production QA/QC teams review the output from WAM, ADCIRC, and STWAVE to ensure consistent and error free results.

The results of these processes will be utilized to conduct the statistical analysis (JPM-OS) to determine the 100-year water surface elevation to be used in further structural and overtopping calculations.

3.1.4.8 *ADCIRC Grids*

The current SL15v3_2007_r09 is the most comprehensive grid developed to date. There are more than 2 million computational nodes. The 2007 grid (projected levee conditions, authorized grade) is the grid that is being utilized for the 152 production runs. The almost identical SL15v3_2005_r09 grid differs only in the definition of the levee heights that represent the system prior to August 2005. This SL15v3_2005_r09 grid is used for the hindcast validation simulations of Hurricanes Katrina and Rita. The large size of the grid and detail are necessary for use in a FEMA FIS. Several iterations which led to these grids were developed and reviewed by IPET and Independent Technical Review (ITR) staff.

3.1.4.9 *Automation Process*

Ongoing projects for storm-surge and inundation mapping along the U.S. Gulf of Mexico coast require the computation of many simulations using state-of-the-art numerical models and high-performance computational facilities. In this context, the storm-surge model ADCIRC and spectral wave model STWAVE are used in a “coupled” scenario to improve upon the storm surge solutions provided by ADCIRC. Coupling of the models is done through input/output file exchange between the numerical models. The water level and wind field from ADCIRC are provided in the appropriate form for the spectral wave model STWAVE. STWAVE computes the high-frequency wave field, including the wave radiation stress associated with the storm (wind) and simulated water level. This wave radiation stress is then passed to the next ADCIRC simulation as an additional forcing term, in conjunction with the storm wind and pressure field. This model communication through file input/output (I/O) achieves a first-order coupling of the non-linear interaction between the wind-induced storm-surge and the wind-driven higher frequency wave fields.

The primary difficulty with the large number of compute-resource-intensive simulations required by these projects is ensuring that each simulation uses the correct files and that the compute-jobs run to completion with as little intervention as possible. Avoiding human interaction is critical to prevent errors in file input, compute-job staging, and post-processing. To address this problem, a software system has been developed to prepare each required simulation and submit each simulation to the compute-resource job manager. Basic graphics and visualizations are included to aid in QA/QC procedures of the computed results.

IDS 2

This section describes the software production system developed for the coupled ADCIRC/STWAVE simulations. The software, written in the scripting languages perl and bash, manages the gathering and preparation of input files for the ADCIRC/STWAVE models and writes the job control script that submits the compute job to the host machine job manager (e.g., LSF, PBS, LoadLeveler). Technical details of the script procedures and operations are reported in a separate technical report.

The primary requirements for the production system are independently verified and validated numerical models; tested and verified model grids; and runtime inputs to the models (forcing functions). Input files that provide initial conditions and forcing functions to the ADCIRC/STWAVE system are required to be pre-computed. This includes the storm realization (wind and pressure fields computed by the OWI PBL model) and the wave energy spectra for each storm (computed by WAM and interpolated onto the STWAVE model boundaries).

3.1.4.9.1 Computer System

The components of the production system are independent of the UNIX HPC computer system used and can be set up on any system with accessible processing elements, large disk and storage capacity, and a job controller (Load Sharing Facility, Portable Batch System, LoadLeveler, etc.). The scripting language *perl* and shell language *bash* must exist on the computer system (which is generally the case on Linux-based systems). Additional software packages (*GNUplot*, *GMT*) are used to facilitate post-simulation graphical analysis of the solutions.

The production system has been developed on the ERDC Cray XT3 (*Sapphire*) and the University of Texas Dell cluster *LoneStar*. However, the system is easily portable to other high-performance computing facilities with minor changes to the scripts and job controller/manager configurations. This has been tested several times on the following system/job scheduler combinations: NAVO IBM P5 (*Babbage*)/LSF, LONI IBM P5 (*Neptune*)/LoadLeveler, Cray Research Cray XT3 (*Salmon*)/PBS.

For the 2005 and 2007 LACPR simulations, the ERDC Cray XT3 *Sapphire* and University of Texas Dell cluster *LoneStar* are used for the computations. The only required changes to the scripts and setup are the specification of different job control parameters and a different home directory for the system. The basic computer system characteristics for *Sapphire* and *LoneStar* are shown in Table 10.

3.1.4.9.2 Numerical Models in the Production System

The “coupled” approach to the required storm-surge solutions uses the shallow-water finite element surge model ADCIRC (Luettich and Westerink, 2004) in

conjunction with the steady-state spectral wave model STWAVE (Smith et al., 2001). Software versions are 46_48 and greater and ep_110306 and greater for ADCIRC and STWAVE, respectively. Figure 18 shows the extents of the three models' grids. The ADCIRC grids (boundary drawn in black) cover the western North Atlantic Ocean, with the only open boundary at 60 degrees West. All ADCIRC grids in this project use the same footprint and general coverage. However, there are different levee/boundary configurations in Louisiana and the surrounding regions. The OWI PBL model boundary is shown in red, covering the Gulf of Mexico and 0.05-degree resolution. ADCIRC interpolates the PBL grid to the ADCIRC grid and pads the far-field extent with background values. The STWAVE grid boundaries (blue) are shown along the Louisiana, Alabama, and Mississippi coasts. The Lake Pontchartrain domain is barely visible at this scale.

3.1.4.9.2.1 Surge Model – ADCIRC

The storm surge model ADCIRC is a state-of-the-art model that solves the generalized wave-continuity equation on linear triangular elements. The depth-integrated (2D) implementation is used, where the water level and depth-averaged velocity are solved for at each triangle vertex (node), after complete specification of the initial conditions and time history of the boundary conditions (forcing). The finite element grids used in this project are the SL15 grid sequence for the 2005, 2007, and 2010 levee configurations. There are approximately 2.1 million horizontal nodes and 4.2 million elements in this sequence of grids. Ninety percent of the computational grid nodes are within the region shown on Figure 19. The computational domain is decomposed into 256 sub-domains, and each sub-domain problem is allocated to a separate computing processor. Boundary data are communicated between processors through the Message Passing Interface (MPI). Each solution is computed with a time step of 1 second. A detail of the finite element grid is shown on Figure 20 for the New Orleans East area.

For all of the validation hindcasts and all of the production runs, the river flow rates were not allowed to fluctuate during the simulated hurricane event. A steady state representation of the river was used in order for the radiation boundary conditions to work properly and allow tides and surge to pass through and propagate up north and out of the domain instead of reflecting back into the domain. Half-day spinups were used to avoid exciting nonphysical transients, followed by an additional 2 days of constant flux forcing to allow the river to adjust to a steady state over a period of 2 simulated days prior to initiating the tides and/or hurricane forcing. After the 2-day startup, the flow rates remained constant and the river radiation boundary condition was set. This allows the surges to propagate up and out of the river, as they do in nature, while maintaining the flow into the river. The hindcast runs used flow rates appropriate to each historical event being simulated. In contrast, a single set of flow rates was used for all of the

production. A sensitivity of surge on river flow rates is being conducted as part of a separate study for the USACE but is not finished yet.

3.1.4.9.2.2 Wave Model – STWAVE

Five STWAVE grids are used in the current production system implementation covering the Louisiana, Mississippi, and Alabama coastal region. (The “west” W grid is not used for the LA EAST simulations.) The boundaries of the domains are shown on Figure 21. The spatial resolution of each STWAVE grid is 200 meters, and the temporal resolution is set to 30 minutes. The parallel STWAVE implementation is used in this system. In this version, each wave field snapshot is solved for on a separate processing element (cup). The half-plane STWAVE is used for the south (S), Mississippi-Alabama (MS-AL), southeast (SE), and west (W) grids. The full-plane STWAVE model is used for the Lake Pontchartrain domain.

3.1.4.9.2.3 Initial River Conditions for Storm Simulations

The initial condition for the storm-surge simulations is an ADCIRC solution that provides a background river discharge on the Mississippi and Atchafalaya rivers. River inflow to the Mississippi River at Baton Rouge and to the Atchafalaya River at Simmesport is specified as a flux per unit width as defined by a wave radiation boundary. The radiation condition is based on the relationship between the normal flow and elevation at the boundary. The river condition is spun up for 2.0 simulation days, with forcing of normal flow specified at the head of the rivers. A 2-day spin-up period with a half-day hyperbolic ramping function is applied to the river boundary forcing prior to any additional model forcing. While the solution has not quite reached a steady state after this period, the subsequent wind-driven solutions continue this river spinup, and the river stages reach steady state over the next simulation day. The water elevations at the default sampling locations within the two rivers are shown on Figure 22. This initial condition is a pre-computed requirement to each storm-driven simulation. Additional information can be found in the ITR document “ADCIRC and Grid Methodology”.

3.1.4.9.3 Wind Fields for Storms

The primary inputs to the production system are the wind and pressure fields generated by application of the OWI PBL model. The boundary of this domain is shown on Figure 18. Each storm/simulation must be represented by wind and pressure field files (WND/pre) in PBL format, ready to read by ADCIRC and as specified by the parameter NWS=+/-12,212 in the fort.15 file. For the simulated storms, the WND/pre fields were pre-computed, external to the production system, and assumed to exist as input

IDS 2

to the system. An example of the WND/pre fields is shown on Figure 23 for storm number 042.

The WND/pre files must be placed in the \$PSHOME/winds directory to be detected by the production system. In the USACE/FEMA specification of the production system, the landfall date is YYYYMMDDHHMN, where the year is arbitrary and MMDDHHMN is 08010200 (2AM on 01 August). This landfall date is conveyed to the production system scripts by specifying it in system control file (ProdSysDef.pm). It is also assumed that the storm center continues past landfall time for 24 hours. The pre-landfall time length is arbitrary. A graphic timeline is shown at the top of Figure 24.

There are 152 storms defined, each of which has a corresponding PBL WND/pre field. The storms are specified by variations of the hurricane parameters (Tables 11 and 12) along the tracks shown on Figure 25, and detailed in Appendix A.

In addition to the PBL winds, sets of "Best" winds were developed for the two historical hindcast storms (Katrina and Rita). Hurricanes Rita and Katrina were developed by using data assimilation procedures (Interactive Objective Kinematic Analysis [IOKA] and H*WIND) (Cox et al., 1995; Cox and Cardone, 2000; Powell and Houston, 1996; Powell et al., 1996; Powell et al., 1998).

3.1.4.9.4 Wave Boundary Conditions for STWAVE

The half-plane STWAVE model (the full-plane STWAVE version is used for Lake Pontchartrain) requires specification of the wave spectral characteristics on the open boundary. These boundary condition sets are pre-computed by running the WAM for each storm and extracting the wave energy spectra from the WAM solutions at the STWAVE open boundary node locations. The WAM-to-STWAVE procedure is applied for each of the storm wind/pressure fields, and the results are made available to the production system.

3.1.4.9.5 Solution Sampling Locations

Each ADCIRC storm-surge simulation produces water level time series, both for the global model domain and for pre-defined station locations. In the current system implementation, the pre-defined sampling locations are shown on Figure 26. There are three sets of points: for LACPR (blue), Mississippi Coastal Improvement Program (magenta), and IPET (red). The IPET locations correspond to reach locations as defined in the IPET risk model system definition files. The station output from each solution can be visualized using the post-processing code `plotofort61.pl`. This *perl* script generates a time series plot using *GNUplot* to be used for quick inspection of the

fort.61 results. The time series plot for the ADCIRC3 (step 4) part of the process is shown on Figure 26 for storm 042.

3.1.4.9.6 Solution Procedure (Process Management)

Each simulation is performed in four computational parts, as shown in the “Production Steps” part of Figure 24. The initial conditions (River Spinup), PBL wind and pressure fields, and the wave energy spectra boundary conditions (as computed by WAM) are all required inputs to the system.

ADCIRC1: Each simulation is started from the River Spinup (ADCIRC0). ADCIRC is run from the start of the PBL wind field to 24 hours prior to landfall of the storm (ADCIRC1, River+Winds). The model state is output to disk to provide initial conditions for continuation of the simulation (step 2), and for the subsequent rerun of step 2 that includes wave radiation stresses from STWAVE (step 3).

ADCIRC2: The ADCIRC1 solution (River+Winds) is then continued to the termination of the PBL wind/pressure fields. The ADCIRC2 global water level (fort.63) and wind field (fort.74) are output for QA/QC as well as to provide to STWAVE as input.

STWAVE: The ADCIRC2 solution in step 2 is interpolated to the STWAVE domains, and each STWAVE domain is executed to generate wave radiation stress gradients for input back to ADCIRC in step 4.

ADCIRC3: ADCIRC2 is re-run over the same time period as in step 2, but including the wave radiation stress gradient computed by STWAVE and interpolated onto the ADCIRC grid. This is the River+Winds+RadStress solution and is also referred to as the ADCIRC+STWAVE step.

These four steps are coordinated by a *perl* script (prep_prod_sim.pl) that organizes the directory structure for each run, gathers the needed input files (grids, initial conditions), edits the files for the specifics of the current simulation, and writes a job control file for the high-performance computer system job controller (PBS on the ERDC Cray Sapphire and LSF on the University of Texas Lonestar Dell cluster). The data file flow controlled by this script is shown on Figure 27. To stage a specific simulation, this script is executed with the storm number specified on the command line.

3.2 Hydraulic Analysis

3.2.1 Modeling Strategy and System

This study utilizes a systems-based, integrated atmospheric-hydrodynamic modeling technical approach.

The first component in the modeling sequence is the wind and atmospheric pressure field model. For hindcasting historical storms, we have applied kinematic models that use data assimilation methods in order to define wind fields and apply pressure decay relationships in conjunction with observational data (Cox et al., 1995; Cox and Cardone, 2000; Powell and Houston, 1996; Powell et al., 1996; Powell et al., 1998). Data used for assimilation consist of a wide range of sources, including observational data from buoys, ships, aircraft, coastal stations, and satellite measurements before being processed by a spectral model (Cox et al., 1995). Due to the amount of wind data available for Hurricanes Katrina and Rita, we have been able to generate very accurate winds for these storms.

For synthetic hurricanes used in the JPM storm set, we apply a dynamic wind model, the PBL model (Cardone et al., 1992; Cardone et al., 1994; Thompson and Cardone, 1996). This model provides reliable winds for a wide range of storms; however, it may not perfectly re-create a single storm event. Once the winds are generated, the global ocean WAM is run in order to generate deep water waves in a Gulf of Mexico wide domain (Komen et al., 1994). These results are then applied as boundary conditions in a finer scale regional WAM that covers the continental shelf in Southern Louisiana and Mississippi. These later results were then applied as boundary conditions in five regional finer scale STWAVE models that provide comprehensive coverage in Southeastern Louisiana. These boundary conditions are applied using morphic interpolation to prevent peaks from being split due to refraction at adjoining points (Smith, 2002). The STWAVE computations also included preliminary water levels obtained via linear interpolation of ADCIRC wind and atmospheric pressure, riverine flows, and tides for hindcast cases. The last component to be run was the ADCIRC hydrodynamic model, which is run with wind and atmospheric pressure, wind-wave radiation stresses from STWAVE, riverine flows, and tides for hindcast cases.

There is significant interaction between the various component models. The wind models produce marine winds that are reduced for overland areas depending on the upwind roughness length scales and the existence of canopies. However, once an area is inundated, the physical roughness elements are subject to immersion, and the nominal roughness length scales are subsequently reduced. Upon full immersion of the physical roughness elements, marine winds are again applied.

In addition to quantifying the wind waves themselves, wind waves influence surge height with wind-wave radiation stress forcing, modifying bottom friction as well as determining the sea

surface roughness. Modeling studies have shown that the surge increase due to wind wave setup can be proportionally significant for weaker winds and steep bathymetric profiles (Komen et al., 1994; Weaver and Slinn, 2005, manuscript submitted to *Coastal Eng.*). Although wind waves tend to be proportionately less important for strong storms on wide, shallow shelves, they do influence the total surge, affect the time of arrival of the peak surge, and tend to reduce draw-down (Weaver and Slinn 2005, manuscript submitted to *Coastal Eng.*). Wind waves reach shore prior to the peak surge driven by the strongest hurricane winds; therefore, combined wind and wind-wave surge builds up earlier than solely wind-driven surge. Furthermore, draw-down caused by winds coming from shore tends to be reduced by waves that are still coming into shore. In this modeling system, the interaction between wind wave and surge by applying wave radiation stress forcing has been considered. The effect on bottom friction or the influence of waves on surface roughness has not been included because it affects air-sea interaction. We force the ADCIRC computations with wave radiation stresses linearly interpolated from the five localized STWAVE computations for meshes located in Western Louisiana, west of the Mississippi River, east of the Mississippi River, south of the Mississippi-Alabama coasts, and within Lake Pontchartrain. The STWAVE computations themselves were run with boundary forcing information from the regional WAM grid (which is forced with the Gulf-wide WAM solution) as well as preliminary water level and current information linearly interpolated from ADCIRC. The preliminary ADCIRC simulations included all forcing functions with the exception of the wave radiation stresses.

In addition to the effects of waves, there can be significant effects on surge due to coastal tides and riverine currents. Because the tide range in Southeastern Louisiana is very limited (about a 1.5-foot range), the nonlinear impact on the high water is limited (Ebersole et al., 2007). Therefore, when looking at the JPM high-water studies, we can linearly add tides in most areas without incurring significant error. However, previous studies indicate that the shape of the tides is significantly affected by the surge and therefore for purposes of model validation it is of significant interest to include them. Finally, we note that significant currents flow through the Mississippi and Atchafalaya rivers and that these currents strongly interact with tides in these rivers. For example, tides are substantially more attenuated as they propagate up the Mississippi River for high flow/stages compared to low flow/stages. The level of interaction for storm surge wave propagating up the river is unknown but it may be important given the depth of the river and the magnitude of the currents. We therefore made the ADCIRC computations simultaneously including wind, atmospheric pressure, riverine flows, and wave radiation stresses, as well as tides for hindcast studies, so that all significant coastal and riverine current could interact fully nonlinearly in the computation.

3.2.2 Wind Models

3.2.2.1 Overview

The most significant forcing term in the storm surge computations is the wind stress and pressure field. Therefore, the quality of both the air-sea drag law and the wind field (strength and distribution) are critical factors controlling storm surge response within the model. Two methods are used to provide meteorological forcing: a kinematic data-assimilated hurricane wind model and a dynamic wind model that solves the governing equations within the planetary boundary layer.

*3.2.2.2 Kinematic H*WIND/IOKA Procedure*

A data-assimilated hurricane wind field provides the capability to accurately represent the state of the hurricane at each moment the analysis is performed. This may allow for a more accurate characterization of the storm's features than models solving the governing equations due to the fact that significant observational data exist for recent storms and that knowledge of dynamics within tropical cyclones is not complete. Katrina winds were assimilated using NOAA's Hurricane Research Division (HRD) H*WIND system (Powell and Houston, 1996; Powell et al., 1996; Powell et al., 1998) and were then blended with Gulf-scale winds using an IOKA System (Cox et al., 1995; Cox and Cardone, 2000) developed by OWI.

The H*WIND assimilation procedure assimilates all available observations (from aircraft, ships, buoys, and stations) of wind speed and direction during the storm. H*WIND composites all of the observations relative to the storm's center and transforms them to a common reference condition of a 10-meter height, 1-minute averaged wind speed, and marine exposure. These adjustments to the data are based upon Monin-Obukov similarity theory and PBL adjustment relationships and the assumption of a Gaussian distribution of wind speeds, which typically is valid for these storms (Hsu, 1988). This data assimilation procedure provides a series of snapshots of the storm that occur every 1 to 2 hours. Each analysis is done over a set of three or more nested meshes from observations across at least several hours; the result is the mean state of the storm, demonstrating the location and strength of the winds. These analyses are used to produce a meshed wind field by applying a spectral element method that uses a cubic B spline approach to minimize in a least squares sense the deviations between the input observations and the analysis. The H*WIND technique defined the wind conditions to within about 4 degrees of latitude around the storm but peripheral winds are also needed. Accomplishing this task requires background estimates which are derived from the NOAA National Centers for Environmental Prediction/National Center for Atmospheric Research (NCEP/NCAR) Reanalysis Project (Kalnay et al., 1996). The NCEP/NCAR winds are rigorously analyzed and rely on data assimilation methods using data not originally used in the NCEP operational forecast. A final step is to inject local marine data, adjusted to a consistent 10-meter elevation

and adjusted for neutral stability. This procedure uses an IOKA System (Cox et al., 1995; Cox and Cardone, 2000) developed by OWI.

The data assimilation procedure is not applied to the hurricane's pressure field and therefore a regular pressure distribution is assumed and calculated for the storm. This distribution is defined by a parametric relationship defining a hyperbolic pressure field (Holland, 1980). The shape of the pressure field is defined as:

$$p = p_{min} + \Delta p e^{-\left(\frac{R_{max}}{R}\right)^B} \quad (2)$$

where the pressure deficit in the eye is defined as $\Delta p = p_{atm} - p_{min}$, where p_{atm} is the far field atmospheric pressure and p_{min} is the minimum pressure at the eye of the storm, R defines the distance from the eye, R_{max} equals the input radius to maximum wind, and the parameter B defines the shape of the profile and is computed as:

$$B = 1.38 + 0.00184 \Delta p - 0.00309 R_{max} \quad (3)$$

OWI applied Lagrangian-based interpolation to produce the final wind and pressure fields on a regular 0.05-degree x 0.05-degree grid with snapshots every 15 minutes using a 30-minute averaging period. These data are then interpolated onto the ADCIRC unstructured mesh internally to ADCIRC.

Hurricane Rita winds only applied OWI's IOKA procedure (Cox et al., 1995; Cox and Cardone, 2000).

3.2.2.3 Dynamic – PBL Wind Modeling

3.2.2.3.1 Overview

For the JPM simulations, we apply the PBL model to develop input wind and pressure fields (Cardone et al., 1992; Cardone et al., 1994; Thompson and Cardone, 1996). The model is based on the equations of horizontal motion, vertically averaged through the PBL, and is driven by specification of the storm location, minimum central pressure (p_{min}), and maximum wind speed. We apply track data for four hourly values. The PBL model is able to account for an unsymmetrical wind flow about the eye with use of a steering parameter. The Holland B parameter, which controls the shape of the wind field, was set to values ranging from 1.0 to 1.3. The PBL model simulates the tropical cyclone in steady state as a snapshot centered at the storm's eye. This is a valid approach because hurricane structure changes relatively slowly in time; however, its location does not and a series of snapshots are computed sequentially to describe the evolution of the storm. OWI applied Lagrangian-based interpolation to produce the final wind and

IDS 2

pressure fields on a regular 0.05-degree x 0.05-degree grid with snaps every 15 minutes. Reynold's averaging of the governing equations causes wind output to be described on a 30-minute time scale, at the 10-meter level, within the planetary boundary layer for the entire time history of a storm.

All wind fields used in this study were created by an updated version of Tropical Cyclone Model of 1996 (TC96) developed by OWI. The complete physics of this PBL model is documented in the USACE CERC-94-14 and 92-1 Reports, included as Appendices B and C. The model has been in use for more than a decade and has been validated and published in numerous peer-reviewed journals.

This report describes the method of implementation of this model within these coastal storm surge study analyses. Essentially, TC96 was used to create a wind field for each of the storms required by this study. The storm fields are represented by two files, one containing pressures and the other containing wind speed and direction, across the entire domain, for the time length of the storm.

3.2.2.3.2 Storm Tracks and Parameters

The set of tracks, nicknamed "RICK-fan", was created by the interpolation of storm tracks of Hurricanes Rita, Ivan, Camille, and Katrina. Track 1 is westernmost and Track 5 is easternmost in this set (Figure 28).

Along each of the tracks modeled, the central pressure is allowed to vary during a simulated intensification interval until its intensity reaches a plateau. This plateau is maintained until the storm comes within 90 nautical miles of the coast and then the pressures decay as described in Section 4.1.3. The Radius to Maximum Winds (Rmax) and Holland B parameter are allowed to vary linearly over the same distance as Cp for all storms except the smallest storm class also as described in Section 4.1. Four different Cp and Rp (Pressure Scaling Radius) combinations were defined for created groups of storms. Using these Cp and Rp groups, along with forward speed variations and angled tracks, a total of 152 synthetic storms were created for simulation.

3.2.2.3.3 Track and TROP File Generation

The OWI TC96 model requires storm parameters to be defined in what is called a TROP file. A TROP file is specific to each storm. TROP files were created in two separate steps. First, computer code was created to generate the primary storm track and its parameters for each of the 152 storms. The result of this program was a simple file for each storm which contained the storm position (latitude, longitude), central pressure, radius to max winds, forward velocity, and Holland B factor at 1-hour time steps for the entire storm. All tracks were normalized to make landfall at August 01,

IDS 2

0100, although each storm was set at a unique year where possible. A sample file is shown in Appendix B. The second step was the creation of the TROP file using another utility program. The simple formatted track files were input to this program which then created a file in the OWI TROP format. The TROP format is described in Appendix C together with a sample TROP file. This utility code computed the storm direction, steering flow, and far-field pressure. The far-field pressure, which determines the total pressure deficit, was set to 1,013 millibars (mb). Although this is a somewhat arbitrary value, the statistics are actually computed on the total pressure drop (Pfar-Po). Also, in the TC96 model the radius of maximum winds is not an input parameter but rather the result of the input parameters described above in conjunction with the scale radius of the pressure profile (Rp).

3.2.2.3.4 Wind Field Creation

Each storm TROP file was used as input to OWI's TC96 PBL model, which created a wide pressure file and wind speed and direction file with domain to include the entire Gulf of Mexico and into the state of Louisiana north to 30.5 degrees latitude. Appendix D contains a description of the OWI PRE/WIN file formats. A 15-minute time step was used for all wind fields with a 0.05-degree delta in both the North-South and East-West directions. Detailed graphics for each storm are tabulated in Appendix A. These show the variation in all primary characteristics to include central pressure, Rmax, forward velocity, and Holland B parameter.

3.2.2.3.5 ADCIRC/STWAVE Wind Field Processing

All wind files were created prior to simulation initiations. These files were organized in a separate folder and the automation scripts performed a system check for all wind files as well as other input data requirements before simulation execution. Additionally, the time stamps in the wind files were checked to ensure the consistent landfall time stamp was encoded for synchronization of ADCIRC and STWAVE timesteps. ADCIRC reads the wind files directly to obtain the wind forcing and performs wind reduction calculations as described in the ADCIRC model documentation. The global ocean WAM is ran for each storm prior to ADCIRC/STWAVE simulation executions. WAM is a third-generation wave model that predicts directional spectra as well as wave properties such as significant wave height, mean wave direction and frequency, swell wave height and mean direction, and wind stress fields corrected by including the wave-induced stress and the drag coefficient at each grid point at chosen output times. WAM reads the wind files and produces the wave spectra boundary conditions for the STWAVE model for each storm. The automation scripts check for all wind files, as well as the WAM spectra files, and if in place, the storm simulation is initiated.

3.2.3 Wave Models

Offshore waves are being generated using WAM. This model is one of the standard models employed by USACE for offshore wave modeling and was utilized by IPET. Nearshore waves are being computed using the STWAVE model. It is also one of the standard models utilized by USACE and IPET.

3.2.3.1 Offshore Waves – WAM

The objective of this section is to develop a description of the time and space evolution of the offshore surface gravity spectral wave field used as boundary condition information to the nearshore hydraulics section of the project.

All hydrodynamic and storm producing surface gravity wave estimations are based on the accuracy in the forcing functions. The development of a suite of simulated design level hurricanes and proper estimates of the winds are the most critical factors in the success of the project. The surge and wave estimates are scaled to the wind speed squared, so that any misrepresentation in the meteorological conditions will be amplified in the subsequent hydrodynamic results. Emphasis is placed on the verification of six tropical systems inter-comparing high-quality wind-field forcing versus a PBL methodology used in the synthesis of hypothetical hurricanes impacting the Louisiana coastline.

This section is divided into four parts. The first section, Section 3.2.3.1.1, is devoted to a brief overview of the Study Area. Section 3.2.3.1.2 is a summary of the wave model technology and formulation of the I/O specification. Section 3.2.3.1.3 is devoted to verification/validation of the wave modeling performance for the following Hurricanes: Betsy (1962), Rita (2005), Ivan (2004), Camille (1969), Katrina (2005), and Andrew (1992), termed the BRICKA storms. Section 3.2.3.1.4 summarizes the production procedures, QA /QC of the output products, and a synopsis of resulting offshore wave estimates for the hurricane storm data set as part of the JCS Modeling Study.

3.2.3.1.1 Offshore Wave Domain

The focus of this project is defined as a domain surrounding New Orleans, Louisiana, and the net effects of various hurricane scenarios on structures surrounding this area. To accurately estimate the net effect of surface gravity waves, a target domain needs to be set such that all energy developed in this region is properly defined. The Gulf of Mexico (Figure 29) is a reasonable domain. It is confined by land masses along the north and west and nearly isolated from the Atlantic Ocean along the east and south. There are two open boundaries, defined by the reach from the Florida Keys to the north shore of Cuba and from the Yucatan Peninsula. It is assumed the amount of wave energy transmitted from Atlantic Ocean-based hurricane systems would be minimal. This would include

any forward-moving systems traveling through either of the two reaches. Wind-generated wave energy would ultimately be attenuated by local bathymetry surrounding these land masses.

The generation of wind and pressure fields for all the various hurricane simulations will be made relative to this domain, defined from 98.0 degrees to 80.0 degrees West longitude, and from 18.0 degrees to 31.0 degrees North latitude (Table 13).

The second constraint on the target domain is to define the bathymetry over which the wave energy is developed and propagated, and impacts on the coastal reaches. For all offshore wave modeling applications during this task, one grid system is used. The water depth is assumed to be temporal invariant and defined by a constant water depth grid derived from the General Bathymetric Chart of the Oceans (GEBCO, British Oceanographic Data Centre Centenary Edition-2003, <http://www.bodc.ac.uk>). A 3-arc minute resolution grid was extracted from the GEBCO database. One must realize this digital bathymetric database is a construct of over 100 years of surveys conducted. Differential changes in the water depths will not be reflected and will, at most, only affect the littoral zone. For the generation of offshore wave spectral estimates, these changes should not present a significant problem.

Setting the land/sea boundary is accomplished by using the NOAA National Geophysical Data Center's Global Self-consistent, Hierarchical, High-resolution Shoreline Database (GSHHS; Wessel and Smith, 1996). Combining both the land/sea boundary depicting the shoreline location and the water depth grids necessitated a certain amount of hand editing. In addition, some of the islands not contained in the digital database were manually added for consistency. The final grid composite is presented on Figure 30.

There are identifiable features in this bathymetry requiring closer inspection and shown on Figure 31. In addition, the boundary conditions for the nearshore transformation modeling STWAVE (Smith et al., 2001) are identified by the closed black symbols. There are many distinct features that can affect the incoming wave energy; however, most all, with exception to the Mississippi Canyon, are landward of the defined output boundary for STWAVE. Because of its deep water, the Mississippi Canyon attenuates wave energy. However, in subsequent sections wave estimates derived from the offshore simulations are defined landward of the offshore boundary. These wave estimates were only used for illustrative purposes, supplemented by the STWAVE results discussed in the next chapter.

In summary, a single grid system defined from 98 degrees to 80 degrees West longitude and 18 degrees to 31 degrees North latitude at 0.05 degree is used throughout the simulations. Despite the historical nature of the digital bathymetry database, the offshore wave estimates will not be significantly affected by any long-term changes (decades) or

short-term effects resulting from wind-generated surge. The net product of the offshore wave estimates is to provide directional spectral estimates used for further exploration of nearshore domain.

3.2.3.1.2 Wave Modeling Methodology

The methods for generation of the offshore wave fields resulting from the JCS modeling are presented. This section includes the model selection process, a summary of the modeling approach, input conditions, and the resulting wave computations.

One must understand the quality of any wave estimate is strongly dependent on the quality of the wind fields. Growth characteristics of the significant wave height (defined as the zeroth moment of the energy density spectrum) are proportional to the wind speed squared. Hence, quality is primarily dictated by the accuracy of the forcing function (i.e., the wind). Secondary influences on accuracy would be geographical effects (grid resolution) and resolution of the shoreline and offshore islands. Accurate water depth information is important because many wave parameters are related to water depth through the linear dispersion relation ($\omega^2 = g\kappa \tanh(\kappa h)$) where ω is the radial frequency, κ the wave number, g the gravitational acceleration, and h the water depth). Theoretical scaling of the wave number spectrum is $\kappa^{5/2}$; hence, any substantial inaccuracy in the water depth will have an impact on the wave results. More importantly, close to the coast water depth becomes very important in the spectral collapse associated with wave breaking.

Selection of an appropriate wave modeling technology is critical to provide quality estimates. The spatial and temporal scales associated with tropical systems are very short compared to synoptic-scale events (e.g., Northeasters along the Atlantic coast). The physical processes inherent to these tropical systems, extremely high wind speeds, rapidly turning winds, coupled with active wind-sea and swell interactions, must be accurately modeled. Ultimately, the selection is based on historical performance in the estimation of hurricane-generated waves. There are many wave models that can satisfy these requirements, whether they are second-generation or more recently developed third-generation models. For example, the Wave Information Study (WIS) (http://frf.usace.army.mil/cgi-bin/wis/atl/atl_main.html) has used a second-generation wave model WISWAVE for the generation of a long-term wave climate along the U.S. coastlines (Hubertz, 1992). As a result of the Sea WAVE Modeling Project (SWAMP Group, 1985) third-generation wave models were developed. The main difference in this class of models compared to their predecessors was no "a priori" assumption governing the wave spectrum and inclusion of discrete source terms posed with the same number of degrees of freedom found in the resulting directional wave spectrum. Models of this class include WAM (Komen et al., 1994), WAVEWATCH III (Tolman, 1997; 1999), and most recently SWAN (Ris, 1997; Holthuijsen et al., 1993).

For the most part, WAM, WAVEWATCH III, and SWAN are very similar. There are slight variations in the numerical schemes used and specification of the source-sink terms that, at times, produce different results using the same input conditions. In addition, computational speeds can vary as much as an order of magnitude from model to model. Of the three, only WAM is presently used and supported by the USACE, although the Wave Information Study has been comparing the accuracy of WISWAVE, WAM, and WAVEWATCH III in tests involving long-term wave hindcasting. Over the past 3 years, WAM has undergone major improvements, not only cosmetic (formulation in pure FORTRAN90 schema) but also revisions to source term specification, multi-grid nesting, ice coverage implementation, and, more importantly, depth-limited breaking. These improvements, and 3 years of critical evaluation for the 2003 through the 2006 hurricane seasons (Real-Time Forecasting System of Winds, Waves and Surge in Tropical Cyclones <http://www.hurricanewaves.org>) including a battery of historical tropical storm simulations, have made the choice of WAM Cycle 4.5 (Gunther, 2005) as the technology to be relied upon in this project. It is not suggested that WAVEWATCH III, SWAN, or WISWAVE would provide inferior results, but WAM has recently been through a rigorous testing cycle for hurricanes and is of greatest familiarity to USACE staff that are doing the work (Jensen et al., 2006).

The generation of the wave field and directional wave spectra for the various hurricane storm tracks is based on the implementation of a third-generation discrete spectral wave model called WAM (Komen et al., 1994). This model solves the action balance equation:

$$\frac{\partial N}{\partial t} + c_G \frac{\partial N}{\partial x} = \omega^{-1} \cdot \sum_i S_i \quad (4)$$

where N is the action density defined by $F(f, \theta, x_i, t)/\omega$, where F is the energy density spectrum defined in frequency (f), direction (θ), over space (x_i), and time (t), and the radial frequency ω is equal to $2\pi f$. S_i represents the source-sink terms:

$$\sum_i S_i = S_{in} + S_{nl} + S_{ds} + S_{w-b} + S_{bk} \quad (5)$$

and S_{in} is the atmospheric input, S_{nl} represents the nonlinear wave-wave interactions, S_{ds} is the high frequency breaking (white-capping), S_{w-b} is wave bottom effects (bottom friction), and S_{bk} is depth-limited wave breaking. The solution is solved for the spatial and temporal variation of action in frequency f, direction θ , over a fixed grid defined in x_i (generally a fixed longitude latitude geospatial grid).

Computationally, Equation 4 is solved in two steps. The advection term (second term in Equation 4) is solved first accounting for the propagation of wave energy. Each packet of energy in frequency and direction is moved based on the group speed of that particular

frequency band and water depth. This assumes linear theory and superposition of wave packets. In a fixed longitude latitude grid system, curvature effects are resolved where the energy is propagated in a spherical coordinate system (or along great circle paths). As the water depth decreases, the full dispersion relationship is applied. Wave shoaling and refraction will affect the propagation of the energy packets.

After every propagation step, the solution to the time rate of change in the action density is solved including the source term integration. The wind field is read, and the atmospheric input source (S_{in}) is applied. The nonlinear wave-wave interaction source term is the mechanism that self-stabilizes the spectral energy, transferring portions of the energy to the forward face and high-frequency tail. Dissipation (S_{ds}) removes portions of energy that become too energetic for the given frequency band. For application in arbitrary depths, energy is removed via the wave-bottom sink (S_{w-b}) and ultimately in very shallow water the spectrum releases much of its available energy due to breaking (S_{bk}). A more complete theoretical derivation with formulation of the source terms can be found in Komen et al. (1994).

Two time steps are applied in the wave model simulations. The propagation time step is set so that numerical stability is attained. In the second time step, the source term integration is set to the physical processes and relaxation times of S_{in} , S_{nl} , S_{ds} , S_{w-b} . In addition, the time steps are required to be integer multiples of the wind input.

All simulations are initiated from simple fetch laws using the first wind field. In addition, wave field information files are built to illustrate the time and spatial variation of various wave-related parameters for each of the 152 hurricane track cases.

Ultimately, the basis of the offshore wave simulations is to supply the nearshore wave modeling effort supported by STWAVE (Smith et al., 2001). There are 119 special output locations defined in the region-scale WAM grid. The model's directional wave spectra are output every 15 minutes at 28 discrete frequency bands (exponential distribution where $f_{n+1} = 1.1 \cdot f_n$ and $f_0 = 0.031384$), and 24 direction bands centered every 15 degrees starting at $\theta_0 = 7.5$). The location of these special output locations are displayed on Figures 29 and 31.

3.2.3.1.3 Verification/Validation to the BRICKA Storms

The JPM is based on closely controlled parameters used in a PBL (Cardone and Cox, 1992) wind model. The storm track, central pressure, pressure radius, forward speed, and the Holland B (Holland, 1980) were varied over a controlled parameter space to generate a population of wind and pressure fields for 152 unique tropical cyclones. One must realize these simulations are driven by synthetic winds and, thus, surge or wave estimates are relative to the forcing functions.

Verification and validation of the model can only be accomplished by simulating a series of historical storms on the same grid, with the identical modeling technology used in the subsequent generation of the JPM wave and surge estimates. This is accomplished using wind and pressure fields constructed by an IOKA system (Cox et al., 1995; Cox and Cardone, 2000) using all available measurements (point source) and satellite-derived wind estimates blending these into background wind fields. A tropical meteorologist's expertise accompanies this procedure to best estimate the hurricane conditions. For recent storms (dating from the present to about the mid-1980s), there are aircraft reconnaissance dropsonde flights providing timely wind estimates down to the free surface. Prior to that time, no point source land-based or buoy measurements or satellite dropsonde data sets were available. Hence, the generation of the winds is constructed exclusively from a computer algorithm. This will become apparent in the discussion of individual BRICKA simulations below.

The BRICKA storm simulations become an integral part in the evaluation of the wave modeling technique, and an indirect evaluation of the quality of wave estimates that will be generated for the JPM storm population. BRICKA consists of a population directly impacting on the Louisiana coastline (Figure 32). Placing the BRICKA storms in the context of the Study Area, each storm track is plotted along with various point-source measurement sites available during the simulation period.

Table 14 identifies the start and end dates for each of the simulations and the number of measurement sites for the verification study.

Only Betsy does not have wave measurements, while data used in the verification for Camille are derived from hand-digitized wave records. All of NOAA's National Data Buoy Center's (NDBC's) wave and wind data were obtained from archived digital records (Teng and Bouchard, 2005). In addition, the buoy locations, water depth, hull configuration, and designation if directional wave estimates were available are presented in Table 15.

Despite a multitude of point-source buoys available in the Gulf of Mexico (Figure 32), this validation study selects the ones in close proximity to each hurricane storm track. In general for these storms, west of a hurricane track, the wave climate is swell-dominant. To the east, the wave energy is weighted toward wind-seas. In the forward quadrant resides a very complex wave environment containing a mixture of wind seas and swells.

The verification of WAM's performance is based on time comparisons of evolution, statistical testing, and peak-to-peak evaluations. These tests use the integral wave properties, in height, period, and, when available, wave direction. The time plots (Figures 33 through 37) are selected on the location of the measurement device compared to that of the storm track and are identified with the red highlight in Table 16. Because of

the breath of the validation runs and their products, the majority of the presented materials will be based on peak-to-peak comparisons of modeled and measured data sets. As indicated in Table 16, the general trend found is WAM compares within ± 2 meters in the peak H_{m0} of the buoy data when forced by the OWI winds. These differences increase for the PBL-wind forced simulations. There are slight negative biases in the modeled peak significant wave height of -0.43 meter for the OWI-forced simulations and -0.63 meter for the PBL-forced simulation. This is a result of a larger number of paired observations at the lower end of the distribution off-setting the overestimations at the upper end. There are three exceptions to this rule where the model results are biased low (Table 16 green shading) and more than the 2-meter threshold identified above. The first outlier comes from Ivan at NDBC-42007. The buoy measured a 9-meter significant wave height at the peak, whereas in both WAM simulations the maxima were 4.9 and 4.7 meters, respectively. One must note that NDBC-42007 is positioned in a water depth of 14 meters. From physical principles of nearshore wave mechanics, a 9-meter wave height would be virtually impossible to achieve because of depth-induced wave breaking. It was later determined NDBC-42007 broke its mooring during Hurricane Ivan and went adrift, still recording wind and wave conditions. The data were later removed from the NDBC archive because of the suspected errors.

The second outlier comes from the Katrina simulation evaluated at NDBC-42040, where the buoy peak conditions were recorded to be 16.9 meters, whereas in both WAM simulations the peak H_{m0} was estimated to be 14 and 12.2 meters. From alternate related tropical wave simulation work, re-specifying Katrina's wind and pressure fields, the only way to decrease the error at NDBC-42040 would be to significantly increase the overall wave field in the core of Hurricane Katrina with no physical quantification. One could question the accuracy of the buoy data; attempt to match that data set at the expense of all other data represented in this simulation. There is no physical justification to pursue either of these two options. Graphical representations of the results found in Table 16 are shown on Figure 38 for the peak significant wave height, and the accompanying peak wave period is shown on Figure 39.

The peak wave period results follow the general trends established in the H_{m0} values. However, they are accentuated by the wave model's tendency to under-estimate peak wave periods. In nearly all cases, both simulations produce nearly identical results and fall within an error range of ± 2 seconds. There is a persistent negative bias in the model results, accompanied with more outliers (four, identified by the yellow shading in Table 16, compared to two) than in the height results. Most of the large differences are derived from the Rita simulations, where the storm's track position the duration of the storm contained in the Gulf of Mexico would provide the means to generate more swell energy. For these cases, WAM tends to weigh the swell energy over the less dominant local wind-seas, compared to the opposite occurring in the measurements. In all cases, the wave climate is dominated by swells and slightly overestimated from WAM. Two

potential sources of uncertainty could explain these differences. One potential reason is the transition from local wind-seas to swells in the hurricane core. The second could be a potential error in the propagation of the exiting swell energy from the system. Both sources have to remain in doubt without additional data to support these reasons.

Substantiating the added error resulting from the use of PBL-wind-field specifications compared to that of the OWI-wind forcing is on the order of -1 m in height and less than 1 s in peak wave period for all storms. One must realize the majority of the extreme differences result from more recent hurricanes (Rita, Katrina, Ivan) where data are more prominent and accurate and contained in the core of the hurricane. For the earlier storms Andrew, Camille, and Betsy, the differences between the two simulations are reduced. This result is derived by nearly exclusive use of a PBL model in the wind-field specification because the availability of any aircraft-reconnaissance flights or satellite-based remote sensing devices did not exist.

Further evaluation of the similarities and differences between OWI and PBL wind-field specifications for the BRICKA verification runs are presented in the form of time plots. Figures 33 through 37 contain time plots of the significant wave height, peak and mean wave period, vector mean wave direction (when available), and wind speed and direction. Additional time plots can be found on Figures 40 through 83. Note the wave and wind direction are plotted in a meteorological fashion, where 0 degree is winds/waves coming from the north, and 90 degrees is winds/waves coming from the east. The measured wind speed has been modified to reflect a neutral-stable 10-meter wind identical to that provided in OWI and the PBL fields. All measured data are not smoothed and reflect hourly measurements directly accessed from NOAA's NDBC archive. It is also clear from Figures 33 through 37 that wind and wave measurements in tropical storms are extremely difficult to undertake; three of the five sites failed during the peak of the storm.

Time plots show the subtle similarities and differences between model and measurements for wind and wave parameters. Validation beyond recovering the peak wave conditions is a necessary step in this procedure where growth of the wave climate and decay is also critical. One further evaluation of the PBL-forced wave estimates will yield critical information to the remainder of the 152 storm simulations.

This discussion begins with the Rita simulation and the evaluation at NDBC-42001. Time series plots for buoy NDBC-42001 can be seen on Figure 40. Other buoy time series for Hurricane Rita can be found on Figures 41 through 83. Indicated on Figure 32, the track of Rita passed very close to this site. A sharp change in the wind direction and drop in the magnitude are evident and shown on Figure 33. Although the buoy's wind speed did not change as dramatically as in both the OWI and PBL winds, it did reflect a large temporal gradient in the direction changing by about 180 degrees in less than 4 hours. There are differences between OWI and PBL wind speeds, where PBL tends to under-

estimate prior to Rita's peak yet overestimate at the peak and also during the decay of the storm. There is a slight phase difference in the wind directions, where OWI results follow the data more closely (used in their wind-field specification) compared to that of the PBL. For the subtle point-source measurement differences, the resulting wave estimates are similar. The PBL-forced wave heights tend to under-estimate the growth sequence (wave height is proportional to the wind speed squared) and then overestimate the peak condition by 2 meters, whereas the OWI-forced wave estimates compare well to the measurements during growth, yet like PBL overestimate at the peak. However, the decay stages for both simulations are in good agreement to the data. The peak and mean period results derived from both WAM simulations emulate the trends of the buoy data including the sharp transition from local wind-seas to the pre-cursor swells, and then in the decay cycle from a mixed wind-sea/swell regime to local wind-sea domination. The vector mean wave direction WAM results are smooth and nearly constant conditions unlike in the buoy data. However, as Rita passes to the northwest the change in the wave directions are well replicated.

The second example is from the Ivan simulation at NDBC-42040 located just to the west of the storm track. Figure 34 shows this site failed around the peak wind/wave conditions of Ivan. Despite this, the WAM evaluation is instructive. First, the modeled wind speed in both the OWI and PBL emulate the measurements until just before the buoy failure where they tend to be on the order of 5 meters/second higher than what was observed. The modeled wind directions are well replicated. The wave estimates for significant wave height follow the measurements, where the PBL forced conditions are in general higher at the initial stages of growth, then are lower at the storm peak. The peak period comparisons show a stronger trend for the initial swells to arrive earlier compared to the buoy data and also the PBL simulations, but match near the peak. For the mean period, this is also the case. This would suggest the energy derived from the initially forming Ivan to the south of Cuba, and then arriving in the Gulf of Mexico proper, would be more intense in the OWI fields than in the PBL wind estimates. This, in turn, would produce the noticeable phase differences in peak wave period results. The wave direction comparisons show little variation over time for the data and WAM, with the exception of the strong change in direction (OWI-forced) versus a gentler version found in the PBL results. Waves change from landward propagating swells to locally generated wind-seas moving in a seaward direction.

Camille (Figure 35) has been used for more than 2 decades as the baseline tropical system in wave modeling (Komen et al., 1994). It is unfortunate no digital records exist for the data obtained during this hurricane. However, hand-digitized wave data were obtained from graphical products. No wind data were available from this site as indicated on Figure 35, and the gauge failed around the peak of the storm. It is instructive to use this as a validation test despite all its uncertainties. In addition, the lack of aircraft reconnaissance, satellite remote sensing scatterometers, and point-source measurements

will result in little or no value-added to the OWI-wind specification. In general, the winds derived from the PBL and OWI should be, in the domain, very similar. At ODGP Station 1, the wind magnitude and direction show similar trends; however, the PBL results are about 5 meters/second lower at the peak and phase lagged from the OWI wind fields. The wind direction also shows this tendency, but overall the two estimates are very similar. The H_{m0} for both WAM runs closely approximate the gauge data. The PBL does show a similar phase lag to OWI, as well as being lower at the storm peak. However, as previously indicated, knowledge of the true peak wave height condition at Station 1 remains unknown. Whether the PBL or OWI is more consistent will remain in doubt. The pre-swells of the PBL simulation arrive more according to the measurements; however, both models do represent the peak conditions satisfactory.

The Katrina simulation and example are presented on Figure 36, located at NDBC-42007. Despite the failure of this site, it was selected because of the location and the need to evaluate the WAM results in close proximity to the offshore boundary conditions used in the JPM work. Also, this was the most shoreward site and in close proximity to Katrina's landfalling position. The winds derived from the OWI validation fields and the PBL simulations differ slightly. There is far more variability in the OWI wind speed and magnitude that closely resembles the measurements. This is in direct contrast to the PBL-generated winds, where the wind traces (in magnitude and direction) are relatively constant. At the storm peak, both match while at the decay side of the storm the OWI falls faster compared to that of PBL. Differences are nominally around ± 2 meters/second in speed and about 10 to 15 degrees in direction. The net result of using either forcing field is shown in the wave results. The height is well matched until the peak condition (the buoy did break its mooring and was adrift soon after 29 August 0000 UTC), and then emulates the differences found in the winds, indicating a dominance in local wind-wave regime. The peak and mean wave period results between the two simulations also show strong similarities. There are modest phase differences from the pre-swell arrival times, where as in all other cases the PBL-generated swells arrive early, but peak at similar values at the maximum wave height. The vector mean wave directions display little or no variation in the extent of the data set, only modestly rotating toward a northerly propagation direction.

The remaining validation study for Andrew is found on Figure 37. The selected site NDBC-42003 shows the rapid forward speed of this hurricane once it entered into the Gulf of Mexico. Of all the point source measurement comparisons in this set, the Andrew simulation displayed little or no difference in the wind speed or direction between OWI and the PBL cases. In 1992, the relative amount of data was not as prevalent as in the cases of Rita, Ivan, and Katrina; however, it was more substantial than in Betsy and Camille. Despite this, the PBL modeling technology performed well for this case. Given nearly identical winds (at this one location), the anticipated wave parameter comparisons found on Figure 37 should also be similar. That is the case for the H_{m0} , T_p , T_m , and the vector mean wave direction. The rapid growth in height (4 meters in 2 hours) is matched

with WAM using either wind forcing. However, the modeled peak and mean wave periods do not attain the levels found in the measurements. They are about 4 seconds low. It is swell energy that dominates the wave data, whereas the local wind-seas dominate the model results. These differences do not seem to be attributed to the winds at least in the local area because they compare favorably. These differences do not correlate to initial growth stages of Andrew, because the wave heights would show significant differences. The vector mean wave direction results also indicate good correlation to the measurements during the growth and peak conditions. During the decay, there are substantial differences, mostly resulting from very low wave energy, analogous to wind conditions being light and variable.

In the preceding discussion, the maximum wave heights derived from the two different wind forcing conditions have been evaluated at point-source measurement sites. The time variations of wind and wave conditions at a sub-set have also been evaluated. One last analysis is based on the spatial variation in wave height over the entire simulation period. However, to place this analysis in the proper context the maximum wave field for each of the six BRICKA storms is shown. The OWI-wind forcing is used as the baseline for comparison purposes. These graphic products will illustrate the differences/similarities of the six storms.

The generation of the maximum wave height product (Figures 84 through 89) are constructed from 1-hour snapshots of the wave height field interrogating each (I,J) location in the grid containing a finite wave height. As the simulation proceeds, if at any time that particular $H_{mo}(I,J)$ is exceeded by a larger value, it is replaced. At the end of the simulation the file generated contains the maximum significant wave height occurring at a particular (I,J) location for the simulation. Ultimately, this field is color contoured for the range of heights in the domain. One must note for each graphic product defining the hurricane, the contour range (and colors) differ. Each of the six validation hurricanes is unique, from the track position to the intensity, radius to maximum winds, and forward speed as discussed in the previous section. The maximum significant wave height for the six storms and location of the maxima are presented in Table 17. They all fall in a range between 14 to 18 meters where Ivan produced the maximum overall significant wave height. The locations of the maxima are far offshore because of shallow water mechanisms, wave-bottom effects, and ultimate depth-induced wave breaking. This combines with the attenuation of the winds when the hurricanes are making landfall.

The analysis of the individual simulations begins with Betsy (September 1965). The wave height distribution (Figure 84) shows a large extent of H_{mo} values in the range of 12 to 15 meters as indicated by the orange-red contours. In addition, the overall maximum significant wave height is just south of the Mississippi delta. However, the waves undergo dramatic energy attenuation as the water depths decrease, limiting the nearshore waves to

a nominal height of about 8 to 10 meters surrounding the Louisiana coastline. This trend will be found to exist in most all of the BRICKA simulations.

The Rita (September 2005) storm track and landfall is the most westerly of all storms in the validation set (Figure 85). There are noticeable patterns in the wave height contours indicating evolutionary processes, most likely the eyewall replacement. OWI winds were able to better estimate the winds in the core of Hurricane Rita by not only utilizing the available point-source measurements (NDBC buoys), but also using aircraft dropsonde and satellite scatterometer data sets. The other interesting note for this simulation is the widening of the 14 meters plus (orange contours) as Rita approaches the coastline. However, the attenuation of wave energy occurs along the coastline, where a nominal wave height of 6 meters is present.

Ivan (September 2004) generates the largest maximum H_{m0} of all BRICKA storm simulations. Figure 86 suggests a broadening of the 15-meter wave pattern as Ivan approaches the coastline. This pattern emulates the general structure of the bathymetry (Figure 30) where the larger waves will be guided by deeper water. For the shallower water counterparts (about the 20-meter isobath), the wave energy will be attenuated. There is a distinct lobe of energy along the Florida Panhandle just east of Mobile Bay that is particularly high contrasted to the remainder of the coastline. This area is dominated by wind-seas and lower wave periods and less prone to undergo dramatic energy losses.

Camille (August 1969) had been the baseline test for all wave models. Because of its approximate wind speed and sustained intensity as it made landfall, the wave modeling community set all other tropical storm simulations relating to the maxima of Camille. Figure 87 shows a very uniform pattern in the maximum wave height distribution. This result is attributed to using a near exclusive PBL model for the wind generation. In 1969, there were little point-source measurements in the Gulf of Mexico. What did exist generally failed and, therefore, the relative amount of value added information was limited. Along the Mississippi delta there are large-scale wave height gradients in an offshore direction. Attenuation of the wave energy is limited to the extreme-near coastal domain, allowing for a high-energy wave regime to persist much closer to the shore. These results are very similar to that of Betsy (Figure 84); however, the alongshore gradient in the wave heights are much larger than in the previous case.

The results of the Katrina (August 2005) simulation using the OWI-wind forcing are displayed on Figure 88. The breadth of elevated wave heights (12-meter yellow contour level) covers the offshore domain from east of Mobile Bay to just east of Atchafalaya Bay. The major lobe of 15-meter plus conditions centers on the mouth of the Mississippi River. These patterns again emulate the signature of the bottom topography combined with the wind-field patterns. The absolute maximum H_{m0} value is nearly 2 degrees (about 200 km) south of the Louisiana coastline. The available wave energy contained in this storm

sustained itself right into the coastal area. There are subtle patterns contained in this graphic resulting from the OWI-wind forcing such as the filling (yellow contour pattern extending west at about 28 degrees) of Katrina just before it made landfall and the slight stair-step feature near 88 degrees West.

The final BRICKA storm verification (Figure 89) is Hurricane Andrew (August 1992). Based on the absolute maxima, Andrew was the lowest at 14.2 meters (Table 17). The storm envelope appears to be very uniform over the spatial extent of its track. Despite being in a data rich time period, many of the aircraft reconnaissance missions were limited due to Andrew's eastern Florida landfall, thus limiting the value added component to the wind field. Andrew's wave height pattern shows a dominant lobe just south of the Mississippi delta and a westerly lobe extending outward in a west-northwesterly direction. There is a distinct shallow zone just west of Atchafalaya Bay that is generally found in many of the 152 JPM storm simulations for similar storm tracks.

In summary, the maximum significant wave height color contour products have been presented. These serve mainly as illustrations because verification to these field estimates require satellite altimeter passes at particular time periods when the hurricane is present in the Gulf of Mexico. However, the products will become useful QC products for the WAM results in the 152 JPM storm simulations.

The underlying assumption of the JPM is to use PBL wind/pressure modeling methods in the construction of wind and pressure fields for hurricane wave and surge efforts. The fact remains, all of the JPM simulations are based on a set of free parameters describing a tropical system. No measured data exist for these runs and questions regarding the accuracy in the results would persist. The OWI winds and the PBL-wind forcing have been verified to point-source measurements. One additional test would be to determine the spatial differences in the wave fields. The results would only be qualitative because the lack of spatial data coverage is limited. However, if one assumes the OWI winds to be baseline for quality, one can relate the PBL-wind forced wave fields to that of what would be represented as ground truth.

The BRICKA storms were simulated with OWI-wind and PBL-wind forcing. The latter case emulates the techniques used in all of the 152 JPM simulations. Each simulation was run on the identical wave model grid and output the wave field at the same time interval. A simple difference between the TEST (PBL-forced) and BASE (OWI-forced) wave field estimates is defined. The maximum positive (PBL waves are higher than OWI) and negative (OWI wave results are higher than PBL) difference can be determined over the storm duration. The result of this analysis is color contoured in a qualitative fashion to depict the spatial differences between the two simulations. Figures 90 through 95 are the results from this analysis for Betsy (Figure 90), Rita (Figure 91), Ivan (Figure 92), Camille (Figure 93), Katrina (Figure 94), and Andrew (Figure 95).

This analysis is not attempting to negate the use of PBL-wind-field forcing, isolate the differences, or assess the differences. In general, though, the results should provide some credibility for use of the PBL-wind forcing for the JPM study. The results from the Betsy simulation (Figure 90) show the majority of the Gulf of Mexico is covered by red color contours. This indicates the PBL wind fields tend to elevate the resulting wave estimates throughout the domain. The maximum positive (PBL higher) difference is nearly 3 meters whereas the largest negative difference (OWI higher) is 1.6 meters. For both Rita (Figure 91) and Ivan (Figure 92), wave height differences increase dramatically. Rita and Ivan both fall in the time period where there was an abundance of aircraft reconnaissance missions providing the necessary estimates in the core of these hurricanes and added value to the OWI-wind field generation. However, in both cases the maximum positive differences occur just to the right of each of the hurricane tracks, and are on the order of a 5.5-meter (Rita) to 6.3-meter (Ivan) increase in the significant wave heights. Outside this restricted domain, the negative differences (OWI-wind forcing higher) in H_{mo} fall off dramatically, where the maximum differences are in a range between 3 to 4 meters. Camille results (Figure 93) again follow the patterns of Ivan, where the majority of differing wave height results reside in the hurricane core. The maximum positive (PBL higher) results and maximum negative (OWI higher) results are nearly 3 meters. Katrina (Figure 94) demonstrates the value added factor of the OWI-wind forcing where the maximum negative lobe (blue contours) is on the order of 3 meters and is a result of a slight increase in the wind magnitude just before landfall. The marked positive difference again is in the core region of the hurricane and is of the order of a 5-meter increase when PBL winds are used. Andrew (Figure 95) demonstrates when there are limited data available for assimilation into a wind field. Although the domain and color contouring appear to be very complex, the maximum positive (PBL higher) results and negative (OWI higher) is on the order of 1 meter. This time, the OWI-wind forcing indicates a very modest increase in wave height results in the hurricane core.

In general, the analyses presented PBL wind modeling had demonstrated that it can produce good quality wind fields for wave modeling. For the highly variable hurricane situations of the BRICKA storms, maxima in wave heights and their associated periods are well replicated compared to the OWI-forcing. The trends established in the temporal variation of wind and wave conditions during these six storms at selected sites are well defined by PBL-forcing. In general, though, the wave conditions do not show the geophysical variability as in the case of the OWI winds, primarily due the use of all available measurements adding value to the product.

3.2.3.1.4 WAM Production and Quality Control Products

The goal of the JPM task is to run a series of synthetic hurricanes in the Gulf of Mexico and produce two-dimensional spectral estimates along the Alabama, Mississippi, and Louisiana coastlines. These spectra would then be used as input boundary condition

information to STWAVE (Smith, 2001) nearshore wave transformation portion of the project.

In order to achieve this goal in a timely manner, and with quality products, two important factors are required. The first is to build an automated system capable of operating in an efficient manner, minimizing the necessity to correct for human intervention, minimizing the amount of computational time, and producing graphical products to evaluate the results. In the JPM set, there are 152 individual hurricane wind and pressure fields produced. Each of these storms differs from the other from a set of free parameters described in the preceding section on the wind field development.

An automated system was built where there is no human intervention. It generates all required WAM input files (two unique files for each run, a wind file and a general information file), a shell script to be executed on the ERDC's Major Shared Resource Center's (MSRC's) Cray XT3 (sapphire) system. In addition, three post-processing routines requiring their own unique input files are built and executed from the main shell. The only initial requirement established at the onset of this project was to designate a naming convention for the storm set and to require that each storm had its own unique date. The date naming convention was to use 1-year intervals for each JPM storm. The naming convention used as its prefix JPM_FEMA_RUN____. WAM, unfortunately, was modified about a decade ago to efficiently run on vector and shared memory computational platforms. The Cray XT3 is a distributive memory system, and is not capable of vector processing. Given this impediment, a series of unique WAM simulations could be distributed to N different CPUs at one time. Therefore, the architecture of the automated system was built to run a series of JPM hurricane simulations simultaneously. The operation of the WAM system was controlled by two lists, one consisting of available wind files and the other consisting of completed WAM simulations. This avoided duplication of completed runs and provided the means to control the number of runs to about ten per day depending on the availability of the input winds and computation load on the Cray XT3.

Each simulation was initiated with a COLD START and pre-filled with fetch limited wave height estimates generated from the initial wind field. The simulation period for the JPM storms varied from 47 to a maximum of 144 hours depending on the track positioning. However, all storms (with the exception of the BRICKA storms) were synchronized to make landfall 24 hours before the end of the simulation period (1 August 0100 UTC). Three sets of output files are generated. The field files (containing wave parameters on the target grid covering the Gulf of Mexico) were generated every 1,800 seconds. The spectral and mean wave parameter files were generated every 900 seconds.

Checking of each simulation was performed, accessing the WAM general output file detailing the execution time. All files required for post-processing were transferred to

desktop PC and evaluated using various Matlab™ routines. Only a subset of the output files was archived to the ERDC MSRC's Mass Storage Facility as well as resident desktop hard drive.

The QC and analysis of each run was performed by hand inspection of various output files and using graphical products. Two important products used were the color-contoured maximum wave parameter field plots (e.g., Figure 84 for H_{m0}). Other wave parameters such as the H_{m0} of the wind-sea and swell component, the mean wave period, wave stress, wind speed, and drag coefficient were plotted and checked for consistency. Detailed looks at the temporal and spatial changes in the wave conditions were performed by generating a movie loop of wave height and direction fields file. All graphical files have been archived and are not provided in this document. The final product checks for the boundary condition quality. An example of this product is presented on Figure 96. It is a color contour plot of the spatial (x-axis) and temporal (y-axis) variation of the significant wave heights at each of the 119 output locations designated for STWAVE input boundary information. The results are from the PBL-forced Hurricane Katrina run. There are a few identifiable features on Figure 96 that require some explanation. The first is the well-defined discontinuity around Station 25. The locations of Stations 1 through 25 are defined on Figure 29 as the Mississippi-Alabama boundary and also represented on Figure 31 as the horizontal line seaward Mississippi Sound and extending to the west to the Chandeleur Islands. The water depth decreases to about 5 meters at the western extent. This causes the wave heights to diminish to near zero. Station 26 is the start of the Southeast Louisiana boundary (Figure 29), starts just offshore of Station 12, and is oriented in a northeast-southwest direction extending to the tip of Louisiana. The remaining two boundaries front the Louisiana coastline extending to the west; hence, a continuous wave height distribution. Generally, if there is a problem with the WAM simulation for a particular storm, this product will be used to identify the problem.

3.2.3.2 Production Summary

The simulations of the 152 JPM-FEMA hurricanes were completed and evaluated using about 7,000 computer hours on the ERDC MSRC Cray XT3. A total number of 1,216 graphical products were evaluated and checked for consistency. The number of directional spectral files exceeded 18,000. Hence, to summarize this becomes a daunting task. One final graphic illustrates some of the similarities of these simulations. One can plot all tracks and the maximum wind speed and wave height for each simulation on the Gulf of Mexico to show the geographical distribution of the maxima. The summary plot is displayed on Figure 97. One must note that some track positions are duplicated (as illustrated in the previous section on wind modeling) so the population size appears to be much lower than the expected 152 runs. The tracks are indicated by the gray lines, individual simulation maximum wind speed is identified by the blue symbol, and the individual maximum significant wave height is the red symbol. There may be instances

where the maximum wind speed or significant wave height for different simulations are over-plotted. The legend displays the overall maximum wind speed was derived from JPM_FEMA_RUN068, and the maximum H_{m0} was found in JPM_FEMA_RUN009. It is reassuring to note that the wave maxima lead the wind speed locations. The magnitudes of these estimates are found in Table 18. The range in wind speed maxima are from a low of 40 meters/second to the high of about 59 meters/second, while the H_{m0} results are from 11 to nearly 19 meters. In the latter case, these results fall within the range of the BRICKA storm wave height estimates (Table 17).

3.2.3.3 Summary and Conclusions

The motivation of the JCS Modeling Offshore Wave Field Generation was to build a database consisting of directional spectral estimates for a series of hypothetical hurricanes that would make landfall along the Alabama, Mississippi, and Louisiana coastlines. The wind fields used to drive the offshore wave modeling effort were generated using a PBL technique (Thompson and Cardone, 1996) and summarized in the previous section.

Description of the offshore surface gravity waves was estimated using a third generation discrete spectral wave model called WAM Cycle 4.5.2 (Gunther, 2005). One wave model grid domain was used to minimize computational resources and had proved to be useful in past hurricane studies (Jensen et al., 2006). A series of six verification/validation storms were used to determine the quality of the offshore wave estimates. The BRICKA storm set was evaluated based on available point-source measurement sites. In addition, two variants of forcing conditions were implemented. The first set was based on the incorporation of point-measurements, aircraft dropsonde, and satellite-based scatterometer data (Cox and Cardone, 2000). The second set of validation winds was built using the PBL (Cardone et al., 1992). Comparisons of time series, peak-to-peak, and wave height field differences were performed. The peak-to-peak evaluation of the two different forcing fields resulted in biases of -0.47 meter (OWI) and -0.63 meter (PBL). The maximum H_{m0} differences were 4.2 meters (OWI) and 4.7 meters (PBL). The biases in peak spectral wave period ranged from 0.7 second for the OWI simulations and 0.5 second for the PBL BRICKA storms. The maximum peak spectral wave period differences were 8.7 seconds for both simulations (Hurricane Ivan NDBC-42035). Maximum wave height field differences (PBL-OWI) ranged from ± 1 meter for Andrew, +3 meters/-1.6 meters for Betsy, ± 3.3 meters for Camille, +5.5 meters/3.3 meters for Rita, +5.3 meters/-3.2 meters for Katrina, and +6.3 meters/-4.3 meters for Ivan. In general, all of the maximum positive and negative differences were located far from the Louisiana coastline having only a slight impact on the required boundary conditions for STWAVE.

The goal of these tests would demonstrate not only the quality of the wave estimates, but also a means to assess the quality of the PBL-wind forcing on the wave results. This was a

IDS 2

critical step in the evaluation process because the test cases for the final results were based exclusively on hypothetically generated PBL winds with no means to verify their results.

Directional spectral wave estimates were generated based on the 28 frequency and 24 direction bands at the 119 nearshore locations in the WAM grid domain. This information consisted of time (900 seconds) and spatial (0.05 degree) varying energy density (defined here as m^2-s) for the entire storm simulation period. This information will be used as input criteria for STWAVE (Smith and Vincent, 2002) to estimate the nearshore wave environment portion of the project.

3.2.4 Nearshore Waves

3.2.4.1 STWAVE Overview

This section describes the numerical modeling of nearshore wave transformation and generation. Nearshore waves are required to calculate wave runup and overtopping on structures, and the wave momentum (radiation stress) contribution to elevated water levels (wave setup). First, the nearshore wave model STWAVE is briefly described; the modeling methodology is then outlined; and finally, results and sensitivity analyses are presented.

3.2.4.2 Nearshore Wave Model STWAVE

The numerical model STWAVE (Smith, 2000; Smith et al., 2001; Smith and Smith, 2001; Thompson et al., 2004; Smith and Zundel, 2006; Smith and Sherlock, in publication) was used to generate and transform waves to the shore for Hurricane Katrina. STWAVE numerically solves the steady-state conservation of spectral action balance along backward-traced wave rays:

$$(C_{ga})_x \frac{\partial}{\partial x} \frac{C_a C_{ga} \cos(\mu - \alpha) E(f, \alpha)}{\omega_r} + (C_{ga})_y \frac{\partial}{\partial y} \frac{C_a C_{ga} \cos(\mu - \alpha) E(f, \alpha)}{\omega_r} = \sum \frac{S}{\omega_r} \quad (6)$$

where:

- C_{ga} = absolute wave group celerity
- x, y = spatial coordinates, subscripts indicate x and y components
- C_a = absolute wave celerity
- μ = current direction

IDS 2

- α = propagation direction of spectral component
- E = spectral energy density
- f = frequency of spectral component
- ω_r = relative angular frequency (frequency relative to the current)
- S = energy source/sink terms

The source terms include wind input, nonlinear wave-wave interactions, dissipation within the wave field, and surf-zone breaking. The terms on the left-hand side of Equation 6 represent wave propagation (refraction and shoaling), and the source terms on the right-hand side of the equation represent energy growth and decay in the spectrum.

The assumptions made in STWAVE are as follows:

- Mild bottom slope and negligible wave reflection.
- Steady waves, currents, and winds.
- Linear refraction and shoaling.
- Depth-uniform current.

STWAVE can be implemented as either a half-plane model, meaning that only waves propagating toward the coast are represented, or a full-plane model, allowing generation and propagation in all directions. Wave breaking in the surf zone limits the maximum wave height based on the local water depth and wave steepness:

$$H_{m0_{max}} = 0.1L \tanh kd \tag{7}$$

where:

- H_{m0} = zero-moment wave height
- L = wavelength
- k = wave number
- d = water depth

STWAVE is a finite-difference model and calculates wave spectra on a rectangular grid. The model outputs zero-moment wave height, peak wave period (T_p), and mean wave direction (α_m) at all grid points and two-dimensional spectra at selected grid points. Recent upgrades to STWAVE include an option to input spatially variable wind and surge fields. The surge significantly alters the wave transformation and generation for the hurricane simulations in shallow areas (such as Lake Pontchartrain) and where low-lying areas are flooded.

3.2.4.3 Wave Model Inputs

The inputs required to execute STWAVE include:

- a. Bathymetry grid (including shoreline position and grid size and resolution).
- b. Incident frequency-direction wave spectra on the offshore grid boundary.
- c. Current field (optional).
- d. Surge and/or tide fields, wind speed, and wind direction (optional).
- e. Bottom friction coefficients (optional).

3.2.4.4 Wave Model Outputs

The outputs generated by STWAVE include:

- a. Fields of energy-based, zero-moment wave height, peak spectral wave period, and mean direction.
- b. Wave spectra at selected locations.
- c. Fields of radiation stress gradients to use as input to ADCIRC (to calculate wave setup).

3.2.4.5 Nearshore Wave Modeling Methodology

STWAVE was applied on four grids for the Southern Louisiana area: Lake Pontchartrain, Louisiana Southeast, Louisiana South, and Mississippi/Alabama (Figure 98). Four grids were used to take advantage of the efficient half-plane version of STWAVE for the three outer grids (which must approximately align with the shoreline) and to concentrate grid coverage in the areas of interest. The input for each grid includes the bathymetry (interpolated from the ADCIRC domain), surge fields (interpolated from ADCIRC surge

IDS 2

fields), and wind (interpolated from the ADCIRC wind fields, which apply land effects to the OWI wind fields). The wind applied in STWAVE is spatially and temporally variable for all domains. STWAVE was run at 30-minute intervals for 93 quasi-time steps (46.5 hours).

3.2.4.6 *Lake Pontchartrain Grid*

The first grid covers Lake Pontchartrain at a resolution of 656 feet (200 meters). Earlier runs in the IPET study were made at a finer resolution (164 feet [50 meters] by 328 feet [100 meters]), but the results were essentially the same, so the more efficient coarse grid is used for these simulations. The domain is approximately 35.3 by 43.7 miles (56.8 by 70.4 km). Lake Pontchartrain is run with the full-plane STWAVE to include generation and transformation along the entire lake shoreline. The grid parameters are given in Table 19. Figure 99 shows the bathymetry for the Lake Pontchartrain grid relative to NAVD88 (2004.65). Brown areas in the bathymetry plots indicate land areas at 0-foot or higher elevation (reddish brown in the Pontchartrain grid). The bathymetry grid was interpolated from the ADCIRC grid.

3.2.4.7 *Louisiana Southeast and South Grids and Mississippi/Alabama Grid*

The second, third, and fourth grids cover the coastal areas east, southeast, and south of New Orleans at a resolution of 656 feet (200 meters). The domain for the Louisiana Southeast grid is approximately 84.9 by 92.4 miles (136.6 by 148.8 km) and extends from the Mississippi Sound in the northeast to the Mississippi River in the southwest. The domain for the Louisiana South grid is approximately 102.5 by 104.2 miles (165.0 by 167.8 km) and extends from the Mississippi River in the east to the Atchafalaya River in the west. The domain for the Mississippi and Alabama coasts was added to simulate the wave momentum fluxes that increase the surge in the Mississippi Sound and Lake Pontchartrain. The Mississippi/Alabama domain is approximately 70.0 by 75.2 miles (112.6 by 121.0 km) and extends from east of Mobile Bay to Biloxi, Mississippi. These three grids are run with the half-plane STWAVE for computational efficiency. The grid parameters are given in Table 19. Figures 100 to 102 show the bathymetry for the Louisiana Southeast, Louisiana South, and Mississippi/Alabama grids, respectively. All bathymetry grids were interpolated from the ADCIRC grid. These simulations are forced with both the local winds and wave spectra interpolated on the offshore boundary from the regional WAM model.

3.2.4.8 *Comparison to Available Data*

Few data are available to validate STWAVE for hurricanes in Southeastern Louisiana. Three small wave buoys were deployed in Lake Pontchartrain on 27 August 2005 to capture wave conditions in Hurricane Katrina. Two of those gauges were recovered

and provide valuable comparison data. The deployment locations were 30 degrees 2.053 feet north, 90 degrees 7.358 feet west for Gauge 22 and 30 degrees 1.989 feet north, 90 degrees 7.932 feet west for Gauge 23. Gauge 22 was directly north of the 17th Street Canal entrance and Gauge 23 was west of Gauge 22. Both gauges were in approximately 13 feet (4 meters) water depth. The sampling records were a relatively short 8.5 minutes, so there is a lot scatter in the data. At the peak of the storm (approximately 29 August 2005 1200 to 1530 UTC), the measured wave heights drop from approximately 8 feet to 5 feet. This is the time of maximum wind speed and thus the time when the maximum wave height would be expected. The wave height measurements do not appear to be reliable during the storm peak. The buoys may have experienced excessive tilt due to the extreme winds or been submerged or overturned. Figures 103 and 104 show comparisons of significant wave height and peak period, respectively, for the buoy locations. The blue lines are the measurements with the spectra averaged over three records (25.5 minutes), and the red line is the modeled parameters (30-minute average). The STWAVE results are essentially the same for the two gauge sites; therefore, they are given as a single line on Figure 103. The modeled wave heights are an average of 1 foot (0.3 meter) lower than the measurements in the growth stage of the storm (0000-1200 UTC 29 August 2005) and 0.5 foot (0.15 meter) lower than the measurements in the decaying stage of the storm (1530-2200 UTC 29 August 2005). Comparisons at the storm peak are not meaningful because of the questionable accuracy of the data collected at high wind speeds. The modeled peak periods are consistent with the measurements, but 1.0 second shorter in the decaying stage of the storm. The bias of the modeled wave height is 8 percent and bias of the peak period is 7 percent (under-prediction for each) based on an average of the two wave gauges. The 2.5 hours at the peak of the storm when the measured wave heights decreased were omitted in these statistics. The root-mean-square (RMS) errors were 1.2 feet for wave height and 1.6 seconds for peak period. These result in scatter indices of 0.24 and 0.30 for height and period, respectively, where the scatter index is defined as the RMS error divided by the mean measured value. Additional STWAVE validation is provided in a number of references (e.g., Smith et al., 1998; Smith et al., 2000; Smith, 2000; Smith and Smith, 2001; Ris et al., 2002; Thompson et al., 2004).

3.2.4.9 Sensitivity Analysis

STWAVE was not calibrated or turned in any way for the simulations, but all numerical models are sensitive to the quality of the input data. For STWAVE, these inputs include offshore waves, winds, surge, bathymetry, and bottom roughness. To investigate the sensitivity of the STWAVE results to critical input, two sets of sensitivity runs were made using Hurricane Katrina input: wind input and degradation of the Chandeleur Islands (USACE, 2006). These runs were made in coordination with the offshore wave and surge modeling; therefore, modifications were made consistently in all three models: WAM, ADCIRC, and STWAVE. Increasing the wind forcing by ± 5 percent resulted in ± 1 foot changes in wave heights near the levees and degradation of the Chandeleur Islands had

only local effect on the waves, resulting in no difference at the levees. The importance of time dependence was also investigated with the Pontchartrain grid through comparisons of STWAVE with SWAN run in a time-dependent mode. The results from the two models were consistent.

3.2.4.10 Wind Input Sensitivity

Wind input enters into STWAVE in three ways: through the offshore waves input at the boundary, through the surge, and through the local wave generation within the STWAVE grids. The importance of each component varies with location in the grid (offshore areas are influenced more by the offshore input and nearshore, protected areas by the local winds and surge). Two wind sensitivity runs were made: one increased the wind speed by 5 percent and one decreased the wind speed by 5 percent. Local errors in the winds are likely much larger than 5 percent, but they would be random and partially cancel out through the integration of modeling. A simplistic approach was selected to put realistic bounds on the solution. STWAVE was run for all four grids with the ± 5 percent winds (and the offshore wave and surge generated from the same ± 5 percent wind fields).

In Lake Pontchartrain, the maximum increase in wave height due to the +5 percent winds is approximately 0.8 foot on the southeast shore of the lake (Figure 105) and the maximum decrease due to the -5 percent winds is approximately 0.4 foot (Figure 106). For both cases, there are some larger differences on the periphery of the lake, particularly the northeast shore, where the surge is a large percentage of the water depth. The differences in wave height increase across the lake (northwest to southeast), then decrease where the waves are locally depth limited, and then increase again very near the shore due to the increase in local water depth due to the differences in surge in very shallow water.

For the southeast grid, the maximum increase in wave height due to the +5 percent winds is approximately 0.5 to 1 foot along the levees (Figure 107), and the maximum decrease due to the -5 percent winds is approximately 0.5 to 1 foot. There are larger differences outside the Chandeleur Islands (increase of 2 to 3 feet for the +5 percent winds and 1.5- to 2.5-foot decrease for the -5 percent winds). For the south grid, the maximum increase along the barrier islands was approximately 2 feet due to the +5 percent winds and the maximum decrease along the barrier islands was approximately 2 feet for the -5 percent winds. Along the Mississippi River levees, waves increased approximately 0.5 foot for the +5 percent winds and the decrease was 0.5 to 1 foot for the -5 percent winds. In the wetland areas behind the barrier islands, there was a decrease in wave height of 0.5 to 1 foot for both the plus and -5 percent winds, most likely because winds were blowing offshore locally (reducing surge for the +5 percent winds). At the grid boundary, the wave heights increased 1.5 to 3.5 feet for the +5 percent winds and decreased 1.5 to 3 feet for the -5 percent winds. For the Mississippi-Alabama grid, the maximum increase

in wave height due to the +5 percent winds is 1 to 2 feet at the barrier islands (locally up to 2.6 feet offshore of Horn Island) and 0 to 1 foot at the interior shorelines (average of approximately 0.5 foot). The maximum decrease in wave height due to the -5 percent winds is 1 to 2 feet at the barrier islands and 0 to 1 foot at the shoreline. The difference in peak wave period over all grids was generally 1 second or less (increase in peak period for the +5 percent winds and decrease in peak period for -5 percent winds).

Although wind is the critical parameter for predicting waves and surge, the 5 percent increase and decrease in winds for the coupled simulations generally produced nearshore waves at the shoreline of ± 1 foot (or less) of the base simulations. The differences were larger, ± 1 to 3 feet, offshore of the barrier islands.

3.2.4.11 Bathymetry Sensitivity

Southern Louisiana is geomorphically active (wetland and barrier island loss, subsidence, and development). For the base case, an effort was made to use the most up-to-date and accurate bathymetry information to construct the STWAVE grids. These grids were derived from the ADCIRC bathymetry grids. Bathymetry interacts with wave processes through shoaling (which generally increases waves in shallower depths), refraction (which turns waves more shore normal in shallower depths), and depth-limited breaking (which reduces wave height when the breaking threshold is reached). In general, small errors in water depth result in small errors in wave parameters (shoaling is a function of depth to exponent 1/4 and breaking is approximately linear with depth) and the impact is typically local. A possible exception to this is wave attenuation across the barrier islands, which protect the areas in their shadow. The Chandeleur Islands experienced significant erosion during Katrina. To investigate the impact of that erosion on the nearshore waves and surge, STWAVE was run with the Chandeleur Islands in an eroded state. Bathymetry has not been measured since Katrina, but estimates of the new island configuration were taken from aerial photographs. Areas that changed from emergent to submerged were estimated to have a 3.3-foot (1-meter) water depth. Figure 108 shows the depth changes (positive change indicates deeper depths post-Katrina). The maximum depth changes were 7.4 feet. The Chandeleur Islands are on the Southeast STWAVE grid, so only that grid was run. Surge values from ADCIRC with the degraded Chandeleur Islands were used as input together with offshore waves and winds from the base runs. Figure 109 shows the differences in maximum significant wave height for the degraded Chandeleur Islands run minus the base run. The maximum increase in wave height is approximately 6 feet directly in the lee of the island. Close to the shoreline, the differences are reduced to near zero. There are (very) small differences in other parts of the grid resulting from small differences in the surge. The barrier islands do significantly reduce the wave height in the nearshore area, even in a degraded state. The degraded islands allow more wave energy to pass over them and propagate into the sound. For the Chandeleur Islands, the impact on the shoreline of the degraded islands was relatively small (because the wave height is

depth limited in the shallow wetland areas between Chandeleur Sound and Lake Borgne), but increased wave energy in Chandeleur Sound would likely cause further degradation of these wetlands. The protection afforded by barrier islands for the shoreline is dependent on the elevation of the islands, submergence of the islands during the storm, distance from the shore, and characteristics of the storm.

3.2.4.12 *Time Dependent Simulations*

STWAVE is a steady-state wave model, which means that the waves reach equilibrium with the local forcing conditions (wind, surge, and boundary waves). Thus, the STWAVE modeling assumes that the winds and surge vary slowly enough for the waves to reach quasi steady state. For Hurricane Katrina, the winds are time varying and the grid domains are relatively large; therefore, the time-dependent SWAN model (Booij et al., 1999; Booij et al., 2004) was used to evaluate the importance of time variation. Lake Pontchartrain was chosen for this test because the waves are all locally generated and time dependence is expected to have the greatest impact there. To test the time dependence, SWAN was run in time-dependent and steady-state mode for 29 August 2005 from 0000 UTC to 30 August 2005 0000 UTC. The simulation was made using 1-minute time steps for the time-dependent run and forcing the steady-state run to an accuracy of 99 percent with a maximum of 15 iterations (this is more stringent than the default). All other SWAN model defaults were used. SWAN was run with the same spatially varying surge and wind as STWAVE.

Figures 110 and 111 show the SWAN and STWAVE results with the data measured in Lake Pontchartrain. The time-dependent and steady-state SWAN gives essentially the same results through the peak of the storm, after a 3-hour model spinup. Thus, the steady-state solution is adequate for the simulations. STWAVE wave heights are 4 percent higher than SWAN at the peak of the storm and lower height on the building (11 percent) and waning (24 percent) legs of the storm. SWAN results are closer to the measurements on the building portion of the storm and STWAVE results are closer on the waning portion of the storm. The measurements are not reliable at the peak of the storm, when the wave heights are most critical. STWAVE peak periods are 8 percent longer than the SWAN peak periods through the peak of the storm and 23 percent shorter than SWAN periods after the storm peak. STWAVE shows better agreement with the wave period measurements through the storm peak, but both models are generally within 1 second of each other.

3.2.4.13 *Summary*

The nearshore wave generation and transformation model STWAVE was used to simulate waves for modeling the hurricane climatology. STWAVE provides wave parameters for the calculation wave run-up and overtopping on structures and passes radiation stresses to

the circulation model to calculate wave setup. This document provides a summary of the model, modeling methodology, limited validation from Hurricane Katrina, and sensitivity analyses. STWAVE was run with a 200-meter resolution over four nearshore grids. The outer grids obtained spectral boundary conditions from the large-scale WAM simulations. Surge and wind field input were interpolated from the circulation model ADCIRC. Radiation stress fields were fed back to ADCIRC. The sensitivity of model results to ± 5 percent changes in the wind field for an extreme event (Katrina) showed difference in wave height of 1 foot or less near the shore. Bathymetry sensitivity was evaluated by comparing model runs using pre-Katrina conditions and a post-Katrina eroded barrier island. Wave heights were higher by 5 feet in the lee of the islands, but differences were minimal along the shoreline. STWAVE is a steady-state model. The importance of time dependence in the solution was investigated on the Pontchartrain grid by comparing results from the SWAN model run in stationary and non-stationary mode. These results were essentially identical, indicating that a stationary solution is sufficient. STWAVE shows reasonable agreement with the limited measurements in Lake Pontchartrain for Hurricane Katrina.

3.2.5 Circulation Model

3.2.5.1 *ADCIRC Overview*

ADCIRC was selected as the basis for the surge modeling effort. This model has been and continues to be the standard coastal model utilized by the USACE. The domain and geometric/topographic description and resulting computational grid developed for the JCS effort was designated as the SL15 Grid. This provides for a common domain and grid from the Sabine River to Mobile Bay which extends inland across the floodplains of Southern Louisiana and Mississippi (to the 30- to 75-foot contour NAVD88 [2004.65]) and extends over the entire Gulf of Mexico to the deep Atlantic Ocean, as shown on Figure 112. The SL15 domain boundaries were selected to ensure the correct development, propagation, and attenuation of storm surge without necessitating nesting solutions or specifying ad hoc boundary conditions for tides or storm surge. The grid will be used for all coastal analysis for Louisiana and Mississippi to ensure consistency and matching solutions at state line/region boundaries.

3.2.5.2 *ADCIRC Model Description*

ADCIRC-2DDI, the two-dimensional, depth-integrated implementation of the ADCIRC coastal ocean model, was used to perform the hydrodynamic computations in this study (Luettich et al., 1992; Westerink et al., 1992; Westerink, 1993; Luettich and Westerink, 2004). The model uses the depth-integrated barotropic equations of mass and momentum conservation subject to the incompressibility, Boussinesq, and hydrostatic pressure approximations. The primitive, non-conservative continuity and momentum equations are

given below in a spherical coordinate system (Kolar et al., 1994; Luettich and Westerink, 1995).

$$\frac{\partial \zeta}{\partial t} + \frac{1}{R \cos \phi} \left(\frac{\partial UH}{\partial \lambda} + \frac{\partial (VH \cos \phi)}{\partial \phi} \right) = 0 \quad (8)$$

$$\begin{aligned} & \frac{\partial U}{\partial t} + \frac{1}{R \cos \phi} U \frac{\partial U}{\partial \lambda} + \frac{V}{R} \frac{\partial U}{\partial \phi} - \left(\frac{\tan \phi}{R} U + f \right) V \\ & = - \frac{1}{R \cos \phi} \frac{\partial}{\partial \lambda} \left[\frac{p_s}{\rho_0} + g(\zeta - \alpha \eta) \right] + \frac{v_T}{H} \frac{\partial}{\partial \lambda} \left[\frac{\partial UH}{\partial \lambda} + \frac{\partial UH}{\partial \phi} \right] + \frac{\tau_{s\lambda}}{\rho_0 H} - \tau \cdot U \end{aligned} \quad (9)$$

$$\begin{aligned} & \frac{\partial V}{\partial t} + \frac{1}{R \cos \phi} U \frac{\partial V}{\partial \lambda} + \frac{V}{R} \frac{\partial V}{\partial \phi} + \left(\frac{\tan \phi}{R} U + f \right) U \\ & = - \frac{1}{R} \frac{\partial}{\partial \phi} \left[\frac{p_s}{\rho_0} + g(\zeta - \alpha \eta) \right] + \frac{v_T}{H} \frac{\partial}{\partial \phi} \left[\frac{\partial VH}{\partial \lambda} + \frac{\partial VH}{\partial \phi} \right] + \frac{\tau_{s\phi}}{\rho_0 H} - \tau \cdot V \end{aligned} \quad (10)$$

where:

t = time;

λ, ϕ = degrees longitude and latitude;

ζ = free surface elevation relative to the geoid;

U, V = depth-averaged horizontal velocities;

H = $\zeta + h$ = total water column;

h = bathymetric depth relative to the geoid;

f = $2\Omega \sin \phi$ = Coriolis parameter;

Ω = angular speed of the Earth;

p_s = atmospheric pressure at the free surface;

g = acceleration due to gravity;

η = Newtonian equilibrium tide potential;

α = effective Earth elasticity factor;

ρ_0 = reference density of water;

$\tau_{s\lambda}, \tau_{s\phi}$ = applied free surface stress;

$$\tau_* = C_f \frac{(U^2 + V^2)^{1/2}}{H} = \text{bottom friction term};$$

C_f = nonlinear bottom friction coefficient; and

\bullet_T = depth averaged horizontal eddy viscosity coefficient.

A practical expression for the Newtonian equilibrium tidal potential, η , is given by Reid (1990).

Numerical solutions to the shallow water equations on unstructured grids using finite element methods have been under development for the past 20 years (Westerink and Gray, 1991; Kolar and Westerink, 2000). Unstructured finite element-based methods permit shallow water equation solutions that can localize resolution leading to globally and locally more accurate solutions within the realm of feasible computational expense. A significant problem for unstructured shallow water equation solutions has been avoiding non-physical spurious modes with wavelengths nearly twice the grid size without requiring adding artificial damping. The artificial spurious modes are related to a numerical dispersion curve which leads to dual wave numbers for one frequency in the forcing spectrum. The analytical dispersion curve for the shallow water equation is monotonic. Four finite element-based unstructured shallow water equation algorithms have emerged which are at least second order accurate in space, have noise free solutions without requiring artificial damping, and are sufficiently robust to be applied to the wide range of scales of motion and wide range of hydrodynamic balances that exist when computing flows in the deep ocean to computing flows in inlets, floodplains, and rivers. These algorithms include the Generalized Wave Continuity Equation (GWCE) formulation (Lynch and Gray, 1979; Kinmark, 1986; Kolar and Westerink, 2000), the Quasi-Bubble (QB) formulation (Galland et al., 1991); Raviart-Thomas based solutions, and recently the Discontinuous Galerkin Method (Dawson et al., 2006; Kubatko et al., 2006a, b; Kubatko et al., 2007). The most mature of these algorithms are the GWCE and the QB formulations, which are, in fact, functionally almost identical despite entirely different approaches to deriving them (Atkinson et al., 2004). It is the GWCE solution that we have selected as our current base algorithm in our shallow water equations code, ADCIRC (Luettich et al., 1992; Westerink et al., 1992; Westerink, 1993; Luettich and Westerink, 2004).

The GWCE is generated by combining the spatially differentiated momentum equation in its conservative form with the temporally differentiated continuity equation and adding the

continuity equation multiplied by a numerical parameter τ_0 (Kinnmark, 1986; Kolar and Westerink, 2000). The τ_0 parameter in fact controls the dispersion properties of the solution and its optimal selection avoids a folded dispersion curve and optimizes phase propagation properties. Extensive numerical experimentation and comparisons to the functionally equivalent QB finite element (FE) solution provide guidance in the specification of the τ_0 parameter as (Kolar et al., 1994; Atkinson et al., 2004):

$$\tau_0 = \frac{i\omega + 4\tau_*}{3} \quad (11)$$

where ω equals the forcing frequency.

The friction term τ_* increases as depth decreases and a higher τ_0 is required in shallow, nearshore regions (generally less than 30 feet deep); a smaller value is more appropriate in deep basins. However, τ_* is also proportional to the flow velocity. Therefore, it is also important to apply larger τ_0 values in high-flow regions that can be deep, such as rivers and inlets. Operationally, we have implemented our GWCE solution to accommodate spatially variable τ_0 and set $\tau_0 = 0.005$ in quiescent waters deeper than 30 feet outside of Southern Louisiana and Mississippi, we set $\tau_0 = 0.02$ in waters shallower than 30 feet outside of Southern Louisiana and Mississippi, and we set $\tau_0 = 0.03$ in waters shallower than 30 feet and/or in rivers and inlets where higher velocities lead to higher frictional resistance within Southern Louisiana and Mississippi (Feyen et al., 2000). In addition, we increase τ_0 within Southern Louisiana and Mississippi based on the total water column height and local currents:

$$\tau_0 = 0.02 + \frac{4\tau_*}{3} \quad (12)$$

This automated current dependent value optimizes both accuracy and robustness, particularly for the very high current speeds encountered during hurricanes.

The GWCE and the momentum equations are solved sequentially. The FE solution is implemented using Lagrange linear finite elements in space and 3 and 2 level schemes in time for the GWCE and momentum equations respectively. Details of the discretization and solution techniques used in ADCIRC are given in Luettich et al., 1992; Westerink et al., 1992; Westerink, 1993; Luettich and Westerink, 2004. The present simulations were done using an implicit discretization for all linear and some nonlinear terms in the equations and an explicit discretization for most nonlinear terms. This effectively imposes a Courant restriction on the time stepping solution. However, because GWCE solutions

are always more accurate for a Courant number, $C = \frac{\sqrt{gh}\Delta t}{\Delta x}$, below unity and because our wetting/drying procedure is Courant limited as well, this condition is not restrictive.

Modeling storm surge inundation requires that the model accurately represent wetting and drying processes at the mesh scale. ADCIRC applies a wet/dry algorithm that is based on a combination of nodal and elemental criteria (Luettich and Westerink, 1999; Dietrich et al., 2005). The algorithm requires all nodes within an element to be wet in order for that element to be included in the hydrodynamic computations. Two parameters are used to define the wetting/drying criteria. First, H_0 defines the nominal water depth for a node to be considered wet. Second, a minimum velocity U_{min} is specified that must be exceeded for water to propagate from a wet node to a dry node. Nodes are defined as initially dry if they lie above the defined starting water level or if they are below the starting water level but are within pre-defined regions, such as ring levees (e.g., New Orleans).

The algorithm proceeds through the following steps to update the wet and dry elements for the next time level. Wetting is accomplished by examining each dry element with at least two wet nodes with depth greater than $1.2 H_0$ (ensuring sufficient water depth to sustain flow to the adjacent node). The velocity of the flow from the wet nodes toward the dry node along each element edge is computed based on a simple force balance between the free surface gradient and the bottom friction. If this velocity exceeds U_{min} , then the third node and the element are wetted. Finally, a check is made for elements that are surrounded by wet elements to ensure sufficient water column height (greater than $1.2 H_0$ at all flow originating nodes) to allow flow to occur through these elements. While a purely nodal wetting scheme will allow these elements to wet, the elemental check may prevent this from occurring. For hurricane storm surge inundation, wet/dry parameters that are relatively unrestrictive have been found to be most effective: $H_0 = 0.10$ m, and $U_{min} = 0.01$ m s⁻¹. It is critical that all wet/dry checks be done at a small enough time interval so that the wetting/drying algorithm is not Courant surpassing. This latter condition artificially retards the wetting front as the surge progresses inland and the surge height will excessively build up behind the wetting front. Practically, this implies performing wet/dry checks at each model time step.

The ADCIRC model has been implemented in order to ensure an efficient solution and large computational platforms have been utilized to solve these problems. First, the sparse matrix that results from the GWCE formulation is solved via an efficient conjugate gradient solver that enables the solution of problems with a large number of degrees of freedom with cost linearly related to the number of nodes. Second, parallel processing techniques are used to run the ADCIRC model on distributed memory processors. Domain decomposition is employed to divide the computational mesh into portions that can be solved on individual processors; information is passed between these subdomains using

the MPI protocol. A number of dedicated (up to three) output processors eliminate any slowdowns when writing the large files to disk. When a relatively low ratio of interface-to-interior nodes is maintained to minimize interprocessor communications, linear or even super-linear speedups are achieved due to the on-chip memory on RISC-based chips. Thus, wall clock times are reduced by a factor at least equal to the number of processors.

3.2.5.3 *SL15 Domain/Grid Definition*

The SL15 model is an evolution of the earlier *EC2001* U.S. East Coast and Gulf of Mexico tide model and the S08 and TF01x2 Southern Louisiana storm surge models (Mukai et al., 2002; Westerink et al., 2007; Ebersole et al., 2007). These models all incorporate the western North Atlantic Ocean, the Gulf of Mexico, and the Caribbean Sea to allow for full dynamic coupling between oceans, continental shelves, and the coastal floodplain without necessitating that these complicated couplings be defined in the boundary conditions. The SL15 model extends the coverage of these earlier models to geographically include all the floodplains of Southern Louisiana and Mississippi. In addition, improved feature definitions, surface roughness definition, wave radiation stress definition, and grid resolution were all incorporated into the SL15 model.

The development of an accurate unstructured grid storm surge model of Southern Louisiana and Mississippi requires appropriate selection of the model domain and optimal resolution of features controlling surge propagation. The SL15 model domain, shown on Figure 113, has an eastern open ocean boundary that lies along the 60 degree west meridian, extending south from the vicinity of Glace Bay in Nova Scotia, Canada, to the vicinity of Coracora Island in eastern Venezuela (Westerink et al., 1994; Blain et al., 1994; Mukai et al., 2002; Westerink et al., 2006; Ebersole et al., 2007). This domain has a superior open ocean boundary that is primarily located in the deep ocean and lies outside of any resonant basin. There is little geometric complexity along this boundary. Tidal response is dominated by the astronomical constituents, nonlinear energy is limited due to the depth, and the boundary is not located near tidal amphidromes. Hurricane storm surge response along this boundary is essentially an inverted barometric pressure effect directly correlated to the atmospheric pressure deficit in the meteorological forcing; it can therefore be easily specified. This boundary allows the model to accurately capture basin-to-basin and shelf-to-basin physics. Hurricane forerunner and Gulf of Mexico resonant modes can be generated as the hurricane moves from the Atlantic Ocean into the Gulf of Mexico.

Much of the domain is bordered by a land boundary made up of the eastern coastlines of North, Central, and South America. The highly detailed/resolved region extends to the west of Beaumont, Texas, and to the east of Mobile Bay. These areas in Texas and Alabama were included in order to allow storm surge that affects Louisiana and Mississippi to realistically attenuate and laterally spread into the adjacent states. In Southern Louisiana and Mississippi, the domain includes a large overland region that is at

risk for storm surge induced flooding. Details of the domain with bathymetry and topography as well as levees and raised roadways across Southern Louisiana can be seen on Figures 114 through 119. The northern land boundary extends inland and runs along high topography or major hydraulic controls. From Texas, the land boundary runs along the 30- to 75-foot land contour to Simmesport, Louisiana. The boundary was positioned such that lower lying valleys and the adjacent highlands were included. From the vicinity of Simmesport at the Old River flood control, the domain boundary is defined along the west bank Mississippi River levee up to Baton Rouge. At Baton Rouge, the domain boundary runs along Interstate 12 to east of Hammond, Louisiana. Then the boundary heads straight east through Covington, Louisiana, and Abita Springs, Louisiana, until State Highway 41 is reached which runs along the Pearl River Basin. From here, the northern boundary encompasses the 30- to 75-foot contours incorporating valleys that penetrate north all the way to the eastern highlands of Mobile Bay. It is critical that boundary location and boundary condition specification do not hinder physically realistic model response.

We have incorporated critical hydraulic features and controls that both enhance and attenuate storm surge. Rivers and channels can be conduits for storm surge propagation far inland. Topographical features such as levee systems stop flow and can focus storm surge energy into local areas, resulting in the amplification of storm surge. Floodplains and wetlands cause attenuation of flood wave propagation. In Louisiana, there are many interconnected features including deep naturally scoured channels, wetlands, and an extremely extensive and intricate system of river banks, levees, and raised roadways. We have incorporated the Mississippi and Atchafalaya rivers, numerous major dredged navigation canals including the Gulf Intracoastal Waterway (GIWW), the IHNC, the Mississippi River Gulf Outlet (MRGO), Chef Menteur Pass, the Rigolets, and lakes and bays including Lake Pontchartrain, Lake Maurepas, Lake Borgne, Barataria Bay, Timbalier Bay, Terrebonne Bay, Lake Salvador, Lac des Allemands, Atchafalaya Bay, Vermilion Bay, White Lake, Grand Lake, Calcasieu Lake, and Sabine Lake. In Mississippi, we have incorporated St. Louis Bay, Biloxi Bay, Pascagoula Bay, and Mobile Bay as well as the connected channels. All significant levee systems, elevated roads, and railways have been specifically incorporated into the domain as barrier boundaries. These raised features are represented either as internal barrier boundaries or as external barrier boundaries when they are at the edge of the domain and compute overtopping using weir formulae. The levee and raised topographic systems are very extensive in Southern Louisiana and surround many rivers, lakes, and cities including the Mississippi River, the western shore of Lake Pontchartrain, the city of New Orleans, and the channels that intersect it (the IHNC and MRGO), between Thibodaux and Larose, at Morgan City, and around the Atchafalaya flood basin. Thus, all the federal levee systems have been incorporated as well as numerous state, local, and private levee systems. There are numerous highways and state roads that are elevated and act as hydraulic controls: Interstates 12 and 10, US 61, US 90, and US 11 and many of the state routes. In

Mississippi, we have incorporated the CSX railroad as well as Interstate 10 and a limited number of north-south raised roads.

The computational grid, shown on Figures 112 and 120 through 125, has been constructed to provide sufficient resolution for the tidal, wind, atmospheric pressure, and riverine flow forcing functions from the ocean basins to the coastal floodplain. Efficient and effective resolution of tidal response within the basins and on the shelf is determined by tidal wavelength and topographic length scale criteria. Based on propagation of the predominant tidal wavelength for the M_2 tide, the wavelength criteria determines the ratio of wavelength (λ) to node spacing (Δx). A minimum wavelength-to-grid spacing ratio $\lambda/\Delta x$ of at least 50 is required, and more satisfactory is closer to 100 (Westerink et al., 1994; Luetich and Westerink, 1995). The grid also has increased resolution at the shelf break guided by a topographic length scale criteria in order to capture the higher localized wave number content (Hagen et al., 2000; Hagen et al., 2001).

Hurricane forcing and response are also examined to determine the level of resolution required in order to accurately model hurricane effects. In deep water, under-resolution of the inverted barometer forcing function results in under-prediction of the peak inverted barometer effect. This phenomenon, which involves smearing of the inverted barometric pressure effect, results from insufficient resolution for the interpolation of the input atmospheric pressure field onto the hydrodynamic mesh. Enhanced resolution in shelf waters adjacent to hurricane landfall locations is critical because under-resolution can lead to over-prediction of peak storm surge (Blain et al., 1998).

The grid design provides localized refinement of the coastal floodplains of Southern Louisiana and Mississippi and of the important hydraulic features. The level of detail in Southern Louisiana and Mississippi is unprecedented, with nodal spacing reaching as low as 100 feet in the most highly refined areas. Unstructured grids can resolve the critical features and the associated local flow processes with orders of magnitude of fewer computational nodes than a structured grid because the latter is limited in its ability to provide resolution on a localized basis and fine resolution generally extends far outside the necessary area. Figures 126 to 130 show the distribution of the element size (in feet) across the grid for different areas. The SL15 grid is refined locally to resolve features such as inlets, rivers, navigation channels, levee systems, and local topography/bathymetry. Grid-sensitivity studies in rivers and in the Lake Pontchartrain-Lake Borgne inlet system indicate that under-resolution severely dampens tidal and surge propagation into rivers and inlets. Regardless of channel dimensions, a small number of meshing stipulations were adhered to while mapping inland waterway bathymetry in the model. The most stringent constraint was to set a maximum resolution of 100 feet throughout the grid in order to control computational cost. A finer level of resolution creates additional nodes, elements, and thus calculations per time step. In addition, a smaller time step is needed within the ADCIRC model in order to accommodate for the high spatial resolution. A Courant,

IDS 2

Friedrichs, Levy parameter less than 0.5 is desired when running the ADCIRC model. A second important attribute of channel meshes is the placement of a minimum number of nodes across a channel. When possible, at least five nodes were placed across a channel for two reasons. First and foremost, channels require high resolution in order to adequately capture bathymetric characteristics. Second, multiple nodes are placed within the channel to prevent the ADCIRC wetting and drying algorithm from artificially reducing the conveyance of the channel. In spite of this, it should be noted that computational cost was deemed very important; thus, the 100-foot minimum discretization requirement was obeyed more stringently than the five-node requirement. Rivers that are less than 500 feet across, such as the Amite River and the Blind River, consist of less than five nodes traversing each cross section. The waterways and structures controlling surge propagation are highly resolved with 150- to 300-foot node spacing. In addition, significant detail was added in the area between Lake Borgne and Lake Pontchartrain (Figure 130) to more accurately represent the exchange of water between these shallow water bodies. This entailed adding a representation of the CSX railway and US 90 as well as the GIWW and other channels. Further improvements were made along the south shore of Lake Pontchartrain by including the details of the West End Lake Shore Park and its marina and the New Orleans Lakefront Airport (Figure 124).

In addition, wave breaking zones have been identified based on local bathymetric gradients, and a swath of 150- to 700-foot grid resolution has been placed along the coast, over barrier islands, and around Lake Pontchartrain to ensure that the grid scale of the flow model is consistent with that of the STWAVE model. We accommodated the STWAVE forcing function by adding a high level of resolution where there were significant gradients in the wave radiation stresses and forcing of surge through wave transformation and breaking are the largest. We accommodated the four STWAVE grids shown earlier in this report and added resolution in these transformation/breaking zones along the coast from west of Sabine Lake to Vermilion Bay, Atchafalaya Bay, Terrebonne Bay, Timbalier Bay, Barataria Bay, Breton Sound, Chandeleur Sound, Mississippi Sound, and along the shores of Lake Pontchartrain. These high-resolution zones allow for the strong wave radiation stress gradients to fully force the water body in these important regions and ensure that the resulting wave radiation stress induced setup is sufficiently accurate. Barrier islands were in particular very highly resolved to 150 to 250 feet due to the significant wave breaking and the resulting important wave radiation stresses as well as the very high currents that develop over the features.

The unstructured grid is easily identified by the variation from the large elements in deep water to the very highly refined area around Southern Louisiana and Mississippi (Figures 126 through 130). This wide range of element sizes demonstrates the significant advantages of unstructured numerical methodologies: application of resolution is governed by local geometric and local flow scales, and the cost of the computation is minimized while accuracy is maximized. Furthermore, even with the large, basin-scale domain it is

possible to apply very high resolution within coastal regions in order to provide appropriate scaling of features and flow in these areas. The SL15 computational grids contain more than 2,130,000 nodes and 4,180,000 elements. Grid resolution varies from approximately 12 to 15 miles in the deep Atlantic Ocean to about 100 feet in Louisiana and Mississippi. The high grid resolution required for the study region leads to a final grid with more than 90 percent of the computational nodes placed within or upon the shelf adjacent to Southern Louisiana and Mississippi, enabling sufficient resolution while minimizing the cost of including such an extensive domain. Therefore, use of a large-scale domain only adds 10 percent to the computational cost of the simulations. The result, however, is the application of highly accurate boundary conditions and full dynamic coupling between all scales from basins to inlets.

3.2.5.4 Bathymetric/Topographic Definition

Geometry, topography, and bathymetry in the SL15 model were all defined to replicate the prevailing conditions in August 2005 prior to Hurricane Katrina with the exception of some of the barrier islands and area between Lake Pontchartrain and Lake Borgne that were included as post-Katrina September 2005 configurations. The bathymetric and topographic data were interpolated to the SL15 computational mesh by moving progressively from the coarsest and deepest to finest and shallowest areas of the computational domain.

In order to simplify the specification of accurate tide and hurricane storm surge boundaries, the Gulf of Mexico and a portion of the Atlantic Ocean was included in the computational mesh. Open ocean bathymetric depths were first interpolated from a 5° x 5° regular grid based on the ETOPO5 values. The DNC bathymetric values were then applied over much of the Atlantic, Gulf of Mexico, and Caribbean. Subsequently, bathymetric values were applied using the NOAA depth-sounding database. Thus, bathymetric values were applied with a priority/availability system with preference being given to the NOAA sounding database, then the DNC database, and then the ETOPO5 database. This preference is related to the accuracy of each database (Mukai et al., 2002). Bathymetric values were evaluated at computational nodes using an element-based gathering/averaging procedure instead of a direct interpolation procedure. The gathering/averaging procedure searches for all available sounding/bathymetric survey values within the cluster of elements connected to one specific node. It then averages these values and assigns the average value as the depth/bathymetric elevation to that node. This gathering/averaging procedure essentially implements grid scale filtering to the bathymetric data and ensures that bathymetry is consistent with the scale of the grid. Bathymetry was locally checked with available NOAA navigational charts; in regions with missing or incorrect data, supplemental data from the USACE MVN, USGS, or NOS bathymetric charts were applied. Bathymetry was typically specified to tidal MLLW and then adjusted to NAVD88 (2004.65) by adding the difference between NAVD88

(2004.65) and MLLW at the nearest NOAA datum location (on average over the region adding 0.44 foot) so that the correct datum was defined.

Inland bathymetry for Southern Louisiana and Mississippi was taken primarily from regional bathymetric surveys from the USACE MVN and other sources. Inland lakes and other channels were defined using the extensive data sources outlined in Section 3.1.1.4. Particular care was taken to define bathymetry for the channels. Due to the scale, averaging methods were not appropriate and background base grids were prepared directly from the sounding tracks that were then used to interpolate channel values. Quality checks were also performed on the bathymetry prior to putting the model into production. First and foremost, the connectivity of the flow features was inspected. Transitions between features were smoothed so that flow was not cut off or re-routed in a physically inaccurate manner. Next, the channels were quality checked for smoothness. In sections of some channels, especially at channel intersections, survey data were not available or thorough enough to correctly capture the intersection bathymetry. The presence of steep, fluctuating gradients is not physically realistic. Thus, ridges artificially interpolated into the channels were removed in order to represent the channel conveyance in a manner more analogous with the channel's natural state. Finally, grid quality checks were done within the mesh module in order to ensure that the grid quality leads to accurate numerical performance.

Topography in both Louisiana and Mississippi was obtained predominantly using the Atlas lidar in Louisiana and the Mississippi Coastal Analysis Project lidar in Mississippi as specified in Section 3.1.1.3. USGS NED data were applied in the western edge of Louisiana and the portions of Texas and select other regions in the grid as well as described in Section 3.1.1.3. Where no data were available in the wetlands, the LA-GAP land cover data were applied with assumed topographic heights of 0.80 meter where there is marshland and 0.40 meter where there is water. Grid scale averaging details can be found in Section 3.1.1.3.

In addition, USGS post-Katrina lidar data were applied to the Chandeleur Islands. USACE post-Katrina lidar data were applied to the Mississippi Sound Islands with the exception of Half Moon Island, Deer Island, and Singing River Island where MARIS data were applied.

The topographic data were applied to the grid by searching for all lidar points within a rectangle defined by the average distance from the node for which we are assigning a topographic value to the connected nodes. This rectangular averaging paradigm was applied because the search algorithms to find all the topographic values work significantly faster than the unstructured grid element cluster gather/averaging schemes used for the bathymetric data. Given the number of on land nodes and the tremendous size of the lidar databases, speed is critical. Finally, we note that the rectangular averaging scheme also

effectively implements grid scale averaging to the topographic values assigned to the nodes in the grid.

3.2.5.5 Feature Definition

Levee and road systems that are barriers to flood propagation are features that generally fall below the defined grid scale and represent a non-hydrostatic flow scenario. It is most effective to treat these structures as sub-grid scale parameterized weirs within the domain. ADCIRC defines these as barrier boundaries by a pair of computational nodes with a specified crown height (Westerink et al., 2001). Once the water level reaches a height exceeding the crown height, the flow across the structure is computed according to basic weir formulae. This is accomplished by examining each node in the defined pair for their respective water surface heights and computing flow according to the difference in water elevation. The resulting flux is specified as a normal flow from the node with the higher water level to the node with the lower water level for each node pair. Weir boundary conditions also are implemented for external barrier boundaries, which permit surge that overtops levee structures at the edge of the domain to transmit flow out of the computational area.

Levee and road crown heights are important in that they stop or slow the flow of water and lead to localized storm surge buildup. Levees and roads are included in the model as sub-grid scale features and are handled as weirs that accommodate both super- and sub-critical overflows. All levee heights are defined using the most recent surveys available from the USACE MVN. Road and railroad crown heights in Louisiana were generally taken from the Atlas lidar surveys. Note that the CSX railway between the Rigolets and Chef Menteur Pass in particular was important to understand and represent correctly due to it being an important control in the flow of water between Lake Borgne and Lake Pontchartrain. According to the Atlas lidar surveys, the railway has a height of 11 to 12 feet NAVD88. However, CSX railway personnel involved in the reconstruction said that the gravel bed was entirely washed out during the storm and that the remaining compacted bed was at no more than 6 feet (obtained during Ebersole and Westerink 2006 site visit). It is believed that the bed will rapidly wash out under combined high water and wave action and is therefore included in the model at an approximate value of the harder core of the railroad (6 feet). In addition, US 90 sustained some damage and estimates of the lowered values were made. In general, road heights were applied relative to NAVD88 and levee heights were applied relative to NAVD88 (2004.65) from adjusted Atlas lidar, localized 1-foot by 1-foot lidar data, and pre- and post-storm surveys carried out by the USACE.

3.2.5.6 *Bottom and Lateral Friction Process*

Throughout most of the domain, the standard quadratic parameterization of bottom stress is applied. In order to model the spatially variable frictional losses, we apply a Manning n formulation in order to compute the bottom friction coefficient,

$$C_f = \left[\frac{g n^2}{H^{1/3}} \right] \quad (13)$$

Nodal Manning n coefficients are spatially assigned using the LA-GAP, MA-GAP, and NLCD land type definition and the associated Manning n value defined in Section 3.1.2. Figures 131 through 134 show the applied Manning n values in Southwestern and Southeastern Louisiana. For open ocean, large inland lakes, sheltered estuaries, inland lakes, deep straight inlet channels, deep meandering rivers, and shallow meandering channels, n is assigned to equal 0.02, 0.02, 0.025, 0.025, 0.02, 0.025, and 0.045, respectively. We apply a grid scale rectangle surrounding the node of interest and again select all GAP or NLCD based land use values and average their associated Manning n. Again, this effectively implements grid scale averaging for the Manning n selection process. When C_f values are computed for a specific node and water column height, a lower limit equal to 0.003 is set.

Momentum diffusion and dispersion due to unresolved lateral scales of motion as well as the effects of depth averaging are accounted for by an eddy viscosity type closure model. A simple version of the standard isotropic and homogeneous eddy viscosity model implemented by Kolar and Gray (1990) is used, where ν_T is the constant depth-averaged horizontal eddy viscosity coefficient. A horizontal eddy viscosity value equal to $5 \text{ m}^2 \text{ s}^{-1}$ was found to accurately model flow-stage relationships in the Mississippi and Atchafalaya rivers as well as correctly model the tidal exchange in the Lake Pontchartrain – Lake Borgne system through the Rigolets and Chef Menteur Pass. It is necessary to define slip conditions at the wet/dry element interfaces because lateral boundary layers cannot be resolved at the defined grid scales and no slip conditions unrealistically restricted flows with the defined grids and lateral eddy viscosity values (Feyen et al., 2000).

The Manning n values for the water regions were decided upon by consulting with texts and charts and experience with various modeling efforts. The values were chosen to reflect the degree of resistance for the various flow reaches. The Manning n values were based on "Open Channel Hydraulics" (Chow, 1959) and the "Guide for Selecting Manning's Roughness Coefficients for Natural Channels and Flood Plains" (Arcement and Schneider, 1989).

3.2.5.7 Tide and River Forcing Functions

Water level fluctuations in the ocean's surface due to low frequency phenomena are specified through several forcing functions. First, the open ocean boundary is forced with the K_1 , O_1 , M_2 , S_2 , and N_2 tidal constituents, interpolating tidal amplitude and phase from Le Provost's global tidal model based upon satellite altimetry (Le Provost et al., 1998) onto the open ocean boundary nodes. Second, tidal potential forcing that incorporates an appropriate effective earth elasticity factor for each constituent was applied on the interior of the domain for these same constituents (Westerink et al., 1994; Mukai et al., 2002). The nodal factor and equilibrium argument for boundary and interior domain forcing tidal constituents were determined based on the starting time of the simulation (Luettich and Westerink, 2004).

The resonant characteristics of the Gulf of Mexico require a period of model simulation in order for the start-up transients to physically dissipate and dynamically correct tidal response to be generated. The model is run with tidal forcing for a minimum of 18 days before hurricane forcing so that the tidal signal can become effectively established; this spin-up time was determined through testing of model sensitivity to the generation of resonant modes using separate single semi-diurnal and diurnal tidal constituents. A hyperbolic tangent ramp function is applied to the first 12 days of the tidal forcing to minimize the generation of start-up transients.

At land boundary nodes outside of Southern Louisiana and Mississippi, a no-normal flow condition is applied. At land boundaries in Southern Louisiana and Mississippi, no normal flow and external barrier boundaries are specified. At river boundaries, a simple elevation or flux boundary condition would reflect tides and surge waves that are propagating upriver back into the domain. In order to prevent this non-physical reflection from occurring, a wave radiation boundary condition was developed that specifies flux into the domain while allowing surface waves to propagate out (Luettich and Westerink, 2003). The radiation condition is based on the relationship between the normal flow and elevation at the boundary. Using the analytical relationship for the celerity of a linear surface gravity wave ($q_{wave} = c\zeta_{wave}$ where $c = \sqrt{gH}$), the normal boundary flux, q_N , is linearly separated into a river component and a wave/surge component:

$$q_N = -q_{river} + q_{wave} = -q_{river} + c(\zeta - \zeta_{river}) \quad (14)$$

The model uses preliminary river flow data to define ζ_{river} and computes the water column height including the surge, ζ . The computed normal flow q_N at the radiation boundary is then used in the model.

River inflow to the Mississippi River at Baton Rouge and to the Atchafalaya River at Simmesport is specified as a flux per unit width as defined by the wave radiation boundary

condition. Historical hindcasts are simulated with discharge values averaged over the time of the storm available from stream gauge data from the hurricane event. A 2-day spin-up period with a 0.5-day hyperbolic ramping function is applied to the river boundary forcing prior to any additional model forcing. This allows for a dynamic steady state in the rivers to be established prior to interaction with any other forcing terms to properly define pre-tide and pre-storm river stage on the boundaries, ζ_{river} .

3.2.5.8 LMSL and Steric Water Level Adjustments

The computations are referenced to NAVD88 (2004.65), which is a geodetic equipotential surface, and therefore provides a sound reference for our computations when adjusted for the offset to LMSL. The average offset between LMSL and NAVD88 (2004.65) at 11 of 12 reported stations examined by IPET within Southern Louisiana is 0.44 foot as was detailed in Section 3.1.1.1.

Annual sea surface variability in the Gulf of Mexico is significantly influenced by the thermal expansion of surface ocean waters and by other factors including coastal currents, riverine runoff, variability in salinity, seasonal prevailing winds, and atmospheric pressure. Long-term sea level variability has been quantified at various stations throughout the Gulf of Mexico by NOAA (NOAA, 2001; 2007). Figure 135 shows this long-term variability at stations along the Louisiana and Mississippi coasts at Dauphin Island, Alabama; Grand Isle, Louisiana; and Sabine Pass, Texas. The increase in surface elevations is bi-modal with a rise in water levels in spring, a mid-summer decrease, a rise in later summer and fall, and finally a decrease in late fall and winter. In the eastern Gulf of Mexico, this bi-modal trend is much less pronounced. The maximum mid-September water level increase above the annual average at the three stations equals 0.46 foot at Dauphin Island, 0.59 foot at Grand Isle, and 0.52 foot at Sabine Pass. This gives a regional average of 0.52-foot maximum sea level rise in mid-September above the annual average water level along the Mississippi and Louisiana coastlines. This expansion is approximately captured in harmonically decomposed tidal records by the long-term Sa and Ssa harmonic constituents. Examination of the harmonic constants computed by NOAA for tidal stations in the Gulf of Mexico, shown in Table 20, shows that the combined amplitude of the Sa and Ssa constituents is on average just over 0.49 foot with a standard deviation of 0.10 foot. These values are very similar to the maximum average summertime expansion estimated from NOAA's seasonal sea surface values in the region (0.52 foot).

In order to make the seasonal sea surface adjustment for hindcast storms, NOAA's long-term sea level station data at Dauphin Island, Alabama; Grand Isle, Louisiana; and Sabine Pass, Texas; are interpolated to the time of landfall of the storm. Thus for Katrina, which occurred in late August, sea surface level increase above the annual average is regionally estimated as 0.34 foot above LMSL while for Rita the estimated increase in sea

surface level was 0.49 foot. For the hypothetical storm sets, we assume maximum end of summer increase and include the 95 percent confidence limits leading to an increase of 0.66 foot.

Initial water levels in all regions are therefore raised at the start of the computation with the combined average regional difference between LMSL and NAVD88 (2004.65) in addition to the steric increase in water. For Katrina, this adjustment equals 0.44 foot + 0.34 foot = 0.78 foot. For Rita the adjustment equals 0.44 foot + 0.49 foot = 0.93 foot. For the hypothetical storm set, we apply 0.44 foot + 0.66 foot = 1.10 feet. These adjustments are specified in both the initial conditions as well as in surface elevation-specified boundary conditions. Thus, the initial water levels are raised by this amount in areas where this water surface is such that it lies above the defined bathymetry/topography by more than h_0 and where the computational points do not lie within a specially defined dry ring levee region. In addition, the defined offset is added to the boundary conditions, which are located in the deep Atlantic Ocean.

3.2.5.9 Atmospheric Forcing Functions

The wind surface stress is computed by a standard quadratic drag law:

$$\frac{\tau_{s\lambda}}{\rho_0} = C_d \frac{\rho_{air}}{\rho_0} |W_{10}| W_{10-\lambda} \quad (15)$$

$$\frac{\tau_{s\phi}}{\rho_0} = C_d \frac{\rho_{air}}{\rho_0} |W_{10}| W_{10-\phi} \quad (16)$$

W_{10} is wind speed sampled at a 10-meter height over a 10-minute time period (Hsu, 1988). The ratio of the density of air to that of water, ρ_{air}/ρ_0 , is 0.001293. The drag coefficient, C_d , is defined by Garratt's drag formula which defines the drag coefficient as a linear function of wind speed (Garratt, 1977).

$$C_d = (0.75 + 0.067W_{10}) \times 10^{-3} \quad (17)$$

C_d is limited to an upper limit of 0.0035 corresponding to the upper limit of Amorocho and DeVries (1980). With the quadratic wind stress relationship to wind speed and the linear variation of the drag coefficient with wind speed, the surface shear stress is actually related to wind speed in a highly nonlinear fashion. It is clear from the recent literature that there does appear to be an upper limit on the drag coefficient associated with processes such as sheeting. However, what is unclear is the relationship between the roughness that the wind boundary layer sees and the net momentum flux to the water column. It is noted that, from the perspective of the water column, our drag coefficient does include momentum transfer due to processes like wave white capping. This effort therefore did

place a cap on the model at 0.0035, which is somewhat higher than that suggested in the meteorological literature, but implicitly includes the white capping process. Furthermore, the 0.0035 cap is consistent with that used in the WAM.

In order for either wind model output to be utilized as forcing in the ADCIRC model, some adjustments are necessary. OWI's IOKA analyses result in 30-minute averaged winds and the PBL model also outputs 30-minute averaged winds. However, the surface drag law is predominantly based upon 10-minute averaged wind data. The model output winds are adjusted to 10-minute averages by noting that shorter sampling periods lead to higher averaged winds with the assumption of a Gaussian distribution of wind speeds (Powell et al., 1996). The OWI IOKA and PBL output wind speeds are raised by a factor of 1.09 to produce 10-minute winds. Note that to convert to 1-minute averaged or peak wind speed, the 30-minute wind speed must be multiplied by a factor of 1.24 (Cox, personal communication, 2006; Cardone, personal communication, 2006).

A directional land masking procedure has been implemented that alters the wind speeds produced by the hurricane wind-field models, which assume open ocean marine conditions, to account for the wind boundary layer re-adjustment due to the higher surface roughness that exists over land. The land use type in Southern Louisiana and Mississippi was determined by USGS NLCD supplemented by the cypress forest data in Louisiana as outlined in Section 3.1.1.6. The Land Cover Classification raster map information is combined with land roughness lengths $z_{0,land}$ defined by the FEMA HAZUS program as detailed in Section 3.1.1.6. Wind boundary layer re-adjustments depend upon roughness conditions upwind of the location because the wind boundary layer does not adjust to a new roughness instantaneously. Therefore, upwind wind reduction factors are computed for 12 directions about the compass by examining all roughness coefficients up to 6 miles away. Then, the directional roughness used at each computational point within the mesh is based upon the existing wind direction. This upwind effect is particularly important in the nearshore region where winds are traveling either off or onshore and transitioning to or from open marine conditions. The directional roughness/wind reduction factors were computed with a weighted average of the roughness lengths for all pixels upwind of the computational mesh node in the USGS land classification raster image. Twelve upwind directions are chosen (every 30 degrees about the compass) so that each computational node chooses the closest of the 12 directional roughness/reduction factor directions to the current wind direction. Our approach has been to compute an arithmetic average using enhanced NLCD points within a control volume around each ADCIRC node. That way, the roughness field is defined at the appropriate grid scale, i.e., a finer discretization produces a more detailed characterization of the roughness while a coarser discretization captures a larger-scale average. First, all land use classes are converted to a roughness value prior to averaging. ADCIRC nodes are not assigned a land use "class". The averaging is done using the roughness parameters directly.

The weighted pixel land roughness $z_{0_{land}}$ within 6 miles upwind of the computational node are added together to get the weighted upwind land roughness coefficient:

$$z_{0_{land-directional}} = \frac{\sum_{i=0}^n w(i) z_{0_{land}}(i)}{\sum_{i=0}^n w(i)} \quad (18)$$

where the normalization parameter is computed by an inverse-distance weighted average according to:

$$w(i) = \frac{1}{\sqrt{2\pi\sigma}} e^{\left(-\frac{d(i)^2}{2\sigma^2}\right)}. \quad (19)$$

The distance from the computational mesh node and the pixel $d(i)$ is limited to 6 miles in each of the 12 directions. The weighting parameter σ determines the importance of the closest pixels and is set to 4 miles.

Each of the 12 equal 30-degree slices are split into five linear rays, each ray starting at the coordinates of the node and extending radially 6 miles distant. We collect every enhanced NLCD pixel along the ray and use these values in the weighted averaging formula given. Finally, the five ray averages are averaged to get an average $\bar{z}_{0_{land-directional}}$ value for each 30-degree slice at each ADCIRC node. The resulting upwind effect is particularly important in the nearshore region and results in reduced winds offshore when winds come from land and results in sustained marine winds overland when winds come off the water. Standard non-directional land masking procedures would incorrectly produce full marine winds in the near-offshore zone when winds come from land and result in reduced marine winds in the near-overland zone when winds come off the water. It is in these nearshore and low-lying overland regions experiencing either drawdown or flooding that accurate winds are critical because the wind stress term in the shallow water equations is inversely proportional to total water column height and thus the sensitivity to these winds is the greatest. Figures 136 through 151 show sample directional roughness coefficients for steady uniform northerly, southerly, westerly, and easterly winds. These figures clearly illustrate the wind boundary layer lag for winds coming off and onto land in nearshore regions.

The directional changes in surface roughness from open marine conditions do not fully characterize the changes in surface stress on the water column during storm surge inundation. As inundation takes place, the land roughness elements (e.g., marsh grass, crops, bushes) are slowly submerged and the drag is reduced. Therefore, the overland roughness length is reduced in the model depending upon the local water column height and assuming that the physical roughness height is $30z_{0_{land}}$ (Simiu and Scanlan, 1986).

The reduced roughness length $z'_{0_{land-directional-k}}$ is limited to the marine roughness value, which is reached as the water depth H increases:

$$z'_{0_{land-directional-k}} = z_{0_{land-directional-k}} - \frac{H}{30} \quad \text{for } z'_{0_{land-directional-k}} \geq z_{0_{marine}} \quad (20)$$

where the open marine roughness, $z_{0_{marine}}$, can be computed based on the Charnock relationship (Charnock, 1955) and the relationship between the friction velocity and the applied drag law (Hsu, 1988):

$$z_{0_{marine}} = \frac{0.018 C_d W_{10-marine}^2}{g} \quad (21)$$

The wind reduction factor, $f_{r-directional-k}$, is now calculated for each of the 12 directions as a ratio between the surface roughness for open marine conditions $z_{0_{marine}}$ and the weighted upwind land roughness adjusted for local inundation. The approximation of the wind speed reduction is based on applying a power law approximation to logarithmic boundary layer theory (Powell et al., 1996; Simiu and Scanlan, 1986):

$$f_{r-directional-k} = \left(\frac{z_{0_{marine}}}{z'_{0_{land-directional-k}}} \right)^{0.0706} \quad (22)$$

Actual wind reduction factors used at each node during the simulation are determined from the pre-computed directional roughness values closest to the wind direction at that time and place. The adjusted wind speeds used in the wind stress formulae are then computed from the H*WIND and PBL marine wind speeds as:

$$W_{10} = f_{r-directional-k} W_{10_{marine}} \quad (23)$$

Finally, the application of the directional wind boundary layer adjustments and inundation account for how the wind boundary layer is affected but do not characterize how the wind penetrates the physical roughness elements. There are large-scale features that shelter the water surface from the wind stress. These areas describe conditions such as heavily forested canopies, and they are in effect two-layered systems. Because these large roughness elements are exposed to the hurricane winds, shear stress at the water column surface is much smaller. It can be demonstrated that very little momentum transfer occurs from the wind field to the water column in heavily canopied areas (Reid and Whitaker, 1976). Finally, canopied areas can be identified with regions where the modified NLCD

defines Deciduous Forest, Evergreen Forest, Mixed Forest, Woody Wetland, or Cypress Forest. In canopied areas, no wind stress is applied to model the limited impact wind shear stress has on the water column in these areas. The resulting canopied areas in Southwestern and Southeastern Louisiana are shown on Figures 152 and 153.

3.2.5.10 *Wave Radiation Stress Forcing*

In our modeling system, we consider the interaction between the wind waves and the surge by applying wave radiation stress forcing. We do not include the effect on bottom friction or the influence of waves on surface roughness as they affect air-sea interaction. We force the ADCIRC computations with wave radiation stresses from the four to five localized STWAVE computations from western Louisiana, west of the Mississippi River, east of the Mississippi River, south of the Mississippi-Alabama coasts, and within Lake Pontchartrain. The level of resolution in the STWAVE forcing models is 600 feet and is consistent with the level of resolution that we have incorporated into the ADCIRC grid. Although the WAM is used to force the open water STWAVE computations, no forcing information is directly applied from these models to the ADCIRC circulation computation. We note that a preliminary ADCIRC simulation on SL15 is performed without wave radiation stress forcing and that this provides preliminary water level and current information for the STWAVE computations. Thus, the water levels provided to STWAVE do not include the effect of wave setup. This establishes a good level of two-way coupling between the two models. Studies by Slinn (personal communication, 2007) have shown that either further iterations or a finer in time coupling do not significantly affect the resulting surge elevation. The resulting STWAVE radiation stress gradients computed every half-hour were then interpolated to the unstructured ADCIRC grid using bi-quadratic interpolation within the structured wave grid. Because the four to five STWAVE grids overlap, a hierarchy was defined in order to define ADCIRC nodal wave radiation stress gradient values. The Lake Pontchartrain STWAVE was given the lowest priority in overlapping regions, followed by the Mississippi-Alabama grid, then the east of the Mississippi River grid, the west of the Mississippi River grid, and finally the western south Louisiana grid has the highest priority.

3.2.5.11 *Model Operational Parameter Definitions*

For hurricane storm surge inundation, wet/dry parameters that are relatively unrestrictive have been found to be most effective: $H_0 = 0.10$ m, and $U_{min} = 0.01$ m s⁻¹.

The applied computational time step in the simulations is 1.0 second.

Areas with a bathymetric level beneath the sea level, but which are protected by levees and are therefore not under water, can be categorized to be dry by an initially wet/dry parameter. If this parameter is set to 1 for a particularly node, this node is categorized as

dry at the cold start of the simulation. The areas which are initially categorized as dry are shown on Figure 154.

3.2.5.12 ADCIRC and STWAVE Model Performance

The SL15 grid, using 2,137,978 nodes, 4,184,778 elements, and a 1-second time step, had a run time of 1.08 wall-clock hours per day of simulation time when run on Sapphire, a CRAY XT3 with 2.6 GHz Opteron processors (ERDC; www.erd.c.hpc.mil). The grid also had a run-time speed of 1.08 wall-clock hours per day of simulation time on 256 cores on LoneStar, a Poweredge 1955 Xeon 5100 Series, 2.66 GHz dual-core based machine utilizing a high-speed Infiniband switch (University of Texas; www.tacc.utexas.edu). In order to handle the very large output files required for model coupling and analysis, three of the 256 cores are dedicated to writing the output files. A linear speedup curve is maintained up to at least 256 processors.

3.3 Hydrodynamic Modeling System Validation

3.3.1 Overview

In order to validate the modeling system, a tidal simulation and hindcasts of three hurricanes were performed. The tidal signals are low-energy processes that were independently validated using NOAA Tidal Harmonic Constituent Stations (Figure 155), while the hindcasts of Hurricanes Katrina and Rita were used to validate the JCS modeling system as a whole.

Hurricanes Katrina and Rita reached landfall in 2005. Rita and Katrina made landfall in the western and eastern portions of Louisiana, respectively, thus exercising various geographic locations within the modeling system. These hurricanes were very large and extremely powerful storms that caused extensive inland flooding in the central Gulf Coast. Both storms are well documented, and due to the fact Hurricanes Katrina and Rita occurred very recently, they have the most thorough documentation of wind, wave, and surge data for any large storms to date. In addition, the physical system is better defined for these two storms with better topographic and land use data than for any other storms.

In our validation simulations, the kinematic wind models, the wave models, and the surge model were validated separately and independently. Model “tuning” in terms of adjusting model parameters was not performed, but selective grid refinement and the improvement of the definition of raised features and channels in order to improve the quality of the simulations was performed. While geographic and grid refinement improve the quality of the solution, they do not constitute model tuning because this refinement process more accurately defines the existing physical system and is an ordered converging process. An assessment was made of the model’s skill by comparing measured and computed HWMs and hydrographs.

It can happen that adjusting a parameter such as Manning n compensates for other modeling deficiencies. Such a tuned model may better match the data for a specific storm, but for the wrong reason. The model may then not work well for other storms or certainly when the modeled storm transcends the data set. Typically, in regions where model results do not match the data, there are geometric details that have been neglected. We want to avoid ad hoc tuning of parameters and, instead, add grid resolution to capture the missing geometric details. Using grid resolution to improve the model is a more robust method of making corrections. Applying a well-defined physical system as well as friction parameters that are tied to a specific roughness type, instead of adjusting these to fit the measurements, is a much more robust and universal way of achieving excellent model performance. Note that the friction parameters are defined in the same way throughout Texas, Louisiana, and Mississippi. In addition, examining the performance of tides, HWM, and recession curves, separately, gives a much higher level of confidence that the model is in fact correctly simulating the physics.

3.3.2 Tidal Validation

As part of the model validation, tides were simulated using ADCIRC with the SL15-2005 model and were compared to available data at NOAA Tidal Harmonic Constituent Stations in the Gulf of Mexico. The SL15 model was forced using the seven dominant astronomical tidal constituents on the Atlantic open ocean boundary as well as the corresponding interior tidal potential forcing functions. The forced tides include the diurnal O_1 , K_1 , and Q_1 constituents and the semi-diurnal M_2 , N_2 , S_2 , and K_2 constituents. A total of 40 NOAA tidal stations were selected to quantify the model to measurement error for the dominant seven astronomical tides (Figure 155). The selected stations are listed in Table 21 and span from the Florida Keys in the east to Port Isabel, Texas, in the west. In Florida and Texas, where the SL15 domain does not include inland waters, only open water coastal tide gauges were selected. In Alabama, Mississippi, and Louisiana, where the SL15 model does resolve inland water bodies, both open water coastal as well as inland tidal stations were included in the analysis. The NOAA measured tidal data are based on a harmonic analysis of long-term recorded water level time histories (<http://tidesandcurrents.noaa.gov>). The most recent (as of March 2007) NOAA measured/analyzed harmonic constituent data for the seven astronomical tidal constituents are listed in Table 22. A comparison was made at all 40 of the selected NOAA stations between the amplitudes and phases of the NOAA measured/analyzed tidal constituents data with the corresponding amplitudes and phases predicted by the ADCIRC SL15 model for the seven selected constituents.

The SL15 model was forced on the 60 degrees West meridian open boundary with O_1 , K_1 , Q_1 , M_2 , N_2 , S_2 , and K_2 astronomical tidal amplitudes and phases interpolated onto the open ocean boundary nodes using data from Le Provost's FES95.2 global model (Le Provost et al., 1998). Le Provost created a worldwide ocean tidal database from a finite element hydrodynamic model in 1994, designated FES94.1 (Le Provost et al., 1995). In 1995, Le Provost revised and improved FES94.1 by assimilating a satellite altimeter-derived data set, thus creating FES95.2. FES95.2 has better accuracy than FES94.1 because of corrections to major constituents by

TOPEX/POSEIDON mission data assimilation and because of the increase in the number of constituents in the model. FES95.2 was used to force the open ocean boundary as it was in the ADCIRC *Eastcoast 2001* model (Mukai et al., 2002). The Mississippi and Atchafalaya rivers were forced with flow and radiation boundary conditions. Tidal potential amplitudes and the associated effective Earth elasticity factors for the seven forcing constituents are listed in Table 23 (Mukai et al., 2002). Earth elasticity factors, which reduce the magnitude of the tidal potential forcing due to Earth tides, are listed in Table 23 and range between 0.693 to 0.736 (Hendershott, 1981; Mukai et al., 2002).

The ADCIRC SL15 tide simulation was run in three parts from a cold start. First, a 2-day river spin-up with river flow forcing only is run to allow the rivers to reach a dynamic equilibrium. The river ramp time was specified equal to 0.5 day. After the 2-day spin-up, the radiation boundary conditions are applied, maintaining the flow down the rivers but allowing tides and surges to keep propagating out of the domain at the river boundaries. Flows down the Mississippi and Atchafalaya rivers were specified as 195,000 and 58,400 cubic feet per second (cfs), respectively. Second, a 43-day spin-up segment for tides was run, allowing the model tides to reach a dynamic equilibrium. The tide ramp was specified as 20 days. The relatively long 43-day duration of this spin-up was necessary in order to entirely eliminate start-up transients that tend to manifest themselves in the resonant Gulf of Mexico and Caribbean Sea basins. Third, a 60-day run was performed, during which time histories at the selected comparison stations were harmonically analyzed using a total of 23 harmonics as defined in Table 24. The tides are generally weak in the Gulf of Mexico with mixed semi-diurnal and diurnal tides on the Florida shelf up to Turkey Point, Florida, with the dominant M_2 constituent amplitude less than 1 foot; diurnally dominated tides between Panama City Beach, Florida, and Port Fourchon, Louisiana, with the dominant O_1 and K_1 constituents amplitudes up to 0.6 foot; and mixed tides again being prevalent between Eugene Island, Louisiana, and Port Isabel, Texas, with the largest diurnal constituents still less than 0.6 foot. Other astronomical constituents as well as nonlinear overtides and compound tides are very small in terms of affecting water surface elevations or currents. In addition, low frequency components that appear significant in NOAA's tidal analyses are in fact related to non-tidal driven meteorological effects. These were therefore not considered in the tidal analyses. Nonlinear overtides and compound tides were included in the SL15 harmonic decomposition in order to ensure accuracy in the resulting astronomical constituents using the relatively short 60-day analysis.

Figures 156 through 163 present measured versus computed amplitudes and phases for the seven astronomical constituents for Florida, Mississippi-Alabama, Louisiana, and Texas. Perfectly modeled tides would generate a one-to-one relationship on these figures, which is shown as a solid gray line. Error bands at 0.05 and 0.10 foot are defined for the amplitude plots and 10 and 20 degrees for the phases. For the ten stations in Florida, the match is very good, with all of the constituents at all of the stations falling very near or inside the error bands. For the 11 stations in Mississippi and Alabama, the constituents group together and only the phases of the K_2 constituent show significant errors. For the 15 stations in Louisiana, the K_2 constituent

continues to show significant phase errors, but the rest of the constituents provide a good match. This behavior continues for the stations in Texas, where only a K_2 constituent phase at one station shows significant error.

A quantitative assessment of the ADCIRC SL15 model's ability to simulate the tides is presented in Tables 25, 26, and 27. Table 25 lists the correlation coefficients, R^2 , for each of the four groups of NOAA stations in Florida, Mississippi-Alabama, Louisiana, and Texas. The R^2 values are consistently greater than 0.9, indicating an excellent match between the measured and computed amplitudes and phases, with the exception of the phases for Mississippi-Alabama, Louisiana, and Texas which range from 0.768 to 0.896. However, when the K_2 constituent is removed from the analysis, all of these values increase to greater than 0.937. By this standard, the SL15 model does well in simulating all of the non- K_2 harmonic constituents. We note that the amplitude of the K_2 constituent is very small, generally ranging from 0.01 to 0.04 foot. Furthermore, this constituent is difficult to separate from the larger S_2 constituent in a harmonic analysis as short as 60 days.

Table 26 shows the error statistics for the four groups of NOAA stations. Average error, average absolute error, and the standard deviation of the errors are shown for the amplitudes and phases. The amplitude errors have units of feet, and phase errors have units of degrees. In addition, the normalized root mean square error is computed for the amplitudes and is defined as:

$$E_{j-amp}^{c-m} = \left\{ \frac{\sum_{l=1}^L [\hat{\eta}_j^{computed}(x_l, y_l) - \hat{\eta}_j^{meas}(x_l, y_l)]^2}{\sum_{l=1}^L [\hat{\eta}_j^{meas}(x_l, y_l)]^2} \right\}^{1/2} \quad (24)$$

where L is the total number of elevation stations within a given region, (x_l, y_l) is the location of an elevation station, $\hat{\eta}_j^{computed}(x_l, y_l)$ is the computed model elevation amplitude for constituent j at station coordinates (x_l, y_l) , and $\hat{\eta}_j^{meas}(x_l, y_l)$ is the NOAA measured elevation amplitude for constituent j at station coordinates (x_l, y_l) . The normalized root mean square error is dimensionless.

We note that all of these error measures reflect the differences between the NOAA measured/analyzed and the SL15 model harmonic constituents. As such, these error measures also include the errors in the NOAA data. Nonetheless, most of these errors are low. The average amplitude error is always less than 0.015 foot, and the average absolute amplitude error is less than 0.035 foot. The normalized root mean square amplitude errors range from 0.075 to 0.188 foot. The average phase error range from 0 to 20 degrees, and the average absolute phase error range

IDS 2

from 9 to 26 degrees. Note that the phase behavior improves when the K_2 constituent is excluded from the analysis. Both amplitude and phase error ranges compare to the results of the *Eastcoast* 2001 tidal model of Mukai et al. (2002).

In order to evaluate how much of the model to measurement errors can be attributed to the SL15 model as opposed to errors in the NOAA measured/analyzed data, we compute and compare to estimated measurement errors. We compare the current (as of March 2007) NOAA published harmonic data, listed in Table 22, to previously measured, analyzed and published NOAA harmonic constituent data presented in Table 28. The NOAA measured/analyzed data normalized root mean square amplitude and absolute average phase errors values for the seven astronomical constituent at stations with multiple measured values are listed in Table 27. Overall, the normalized root mean square amplitude errors range between 0.041 and 0.134 foot, the average phase differences range between 5.8 and 18.4 degrees. Differences in values of tidal data between the two NOAA measurements/analyses can be explained by the shifting geometry/bathymetry of coastal regions as well as by the occurrences of non-tidal events. Non-tidal events include wind-driven events, such as hurricanes and tropical storms, radiational heating cycles of the surface waters, and riverine discharges. These factors can perturb observed tidal constituent values from analysis to analysis. This simple inter-comparison of the constituent data is only an estimate of the long-term reliability of this data. However, these estimates of the NOAA measurement/analysis error for each constituent should be taken into consideration when comparing modeled results to the available measured data since this variability is included in the model to measurement errors.

We compare the NOAA measurement/analysis data errors to our SL15 model to measurement normalized root mean square errors for amplitudes and average absolute phase errors for the same seven constituents in Table 27. For the amplitude errors, the measurement error typically represents 40 to 50 percent of the model to measurement error for the majority of the constituents. For the phase error, the percentage of error due to measurement is typically between 50 and 80 percent while for the K_2 constituents it is only 18 percent. Again, we note the relatively poor behavior of the K_2 constituent. Overall, however, the results in Table 27 indicate that a significant portion of the error between the model and the measurement data can be attributed to error in the measurements themselves.

The ADCIRC SL15 model simulates the tides in the Gulf of Mexico well, especially the dominant constituents. The K_2 constituent is not captured nearly as well although this constituent is very small and due to its proximity to the larger S_2 constituent may be difficult to harmonically extract given the length of record used in the model runs.

3.3.3 Katrina Hindcast/Validation

3.3.3.1 *Overview*

Hurricane Katrina was a relatively fast moving storm characterized by its low pressure, its intensity, and especially its large size. Hurricane Katrina approached the Mississippi shelf as a Category 5 storm and made landfall as a strong Category 3 storm on August 29, 2005, at 11:10 UTC along the southern reach of the Mississippi River in Plaquemines Parish just south of Buras, Louisiana (Knabb et al., 2005). The storm then tracked north through the town of Empire, passing over Lake Borgne and making a second Gulf of Mexico landfall as a Category 3 hurricane on August 29, 2005, at 14:45 UTC near Little Lake just west of the Louisiana-Mississippi state line and approximately 1.5 miles east of the Lake Borgne entrance to the Rigolets Strait.

It is noted that the center of the storm tracked largely east of the city of New Orleans (about 28 miles due east at its closest point). However, the storm was in the vicinity of critical features of the HPS, the center track being as close as 10 miles due east of the St. Bernard Parish/Chalmette protection levee that runs along the MRGO and as close as 20 miles due east of the confluence of the GIWW and the MRGO. This confluence is a critical feature because it has adjacent protection levees that form a funnel shape, which can focus and amplify storm surge from the east.

3.3.3.2 *Katrina WAM Computations/Validation*

See Section 3.2.3.2 for detailed information on the WAM model validation as well as details specific to the WAM model application for the Hurricane Katrina JPM validation.

3.3.3.3 *ADCIRC Parameter Definitions*

The Mississippi and Atchafalaya rivers were forced with steady flows of 167,000 cfs and 70,000 cfs, respectively. Actual flow rates in the Mississippi River ranged from 167,000 cfs to 172,000 cfs between August 27 and August 31, 2005. Actual flow rates in the Atchafalaya River ranged from 70,000 cfs to 75,000 cfs between August 27 and August 31, 2005. Steady flows were applied to work with the river radiation boundary conditions used in these rivers.

In this Katrina hindcast simulation, the model read in wind speeds and atmospheric pressure fields provided by OWI for the period of 8/25/2005 00:00 UTC through 8/31/2005 00:00 UTC every 15 minutes. The wind and pressure fields were then computed by a linear interpolation in time.

The model read in wave radiation stress fields generated by the STWAVE model for the period of 8/28/2005 00:30 UTC through 8/30/2005 00:00 UTC every 30 minutes. The wave radiation stress field was then computed by a linear interpolation in time.

Unless noted otherwise, the parameters for the hurricane runs were the same as for the tides run described in Section 3.3.2.

3.3.3.4 ADCIRC Water Level and Current Computations

The progression and physics of Hurricane Katrina in Southeastern Louisiana and southwestern Mississippi is shown on a sequence of contour maps in a time period between August 29 at 7:00 UTC and August 29 at 23:00 UTC. To provide insight into the evolution of the storm, the winds, the surge levels, and the water currents during the Katrina event are shown in a sequence of plots at various times and scales of detail. In total, three different areas of detail are shown: Southeastern Louisiana and southwestern Mississippi, Lake Pontchartrain and metropolitan New Orleans, and the region between Lake Pontchartrain and Lake Borgne.

For the area of Southeastern Louisiana and southwestern Mississippi, Figures 164 through 174 show the contour maps of the wind speeds with superimposed wind vectors. Figures 175 through 185 show the surface water elevation contour maps with superimposed wind vectors. Figures 186 through 196 show the currents with superimposed current vectors. Figures 197 through 199 show the maximum wind speeds, maximum surface water elevation, and maximum currents reached during the Hurricane Katrina event. The figures show water elevations in feet, water currents in feet/second, and wind speeds in knots.

The next sequence of figures (Figures 200 through 232) shows the same information as Figures 164 through 196, but these figures give a more detailed view of Lake Pontchartrain and metropolitan New Orleans. Figures 233 through 235 show the maximum wind speed, maximum surface water elevation, and maximum currents reached during the Katrina event for this region.

The last sequence of figures of Katrina shows in great detail the area between Lake Pontchartrain and Lake Borgne. Figures 236 through 246 show the surface water elevation with superimposed wind vectors in knots. Figures 247 through 257 show the currents in feet/second with superimposed current vectors in feet/second. Figures 258 through 260 show the maximum wind speed, maximum surface water elevation, and maximum currents reached during the Katrina event for this region.

In general, the figures clearly show that storm response over Southern Louisiana was highly localized and varied rapidly over even a few miles. Surge heights are controlled

in part by physical features such as the protruding delta, the shelf, barrier islands, levees, river berms, raised roads (as well as by breaks in these features), inlets, channels, and rivers. Furthermore, the shallower the water, the more effective a given wind stress is at increasing surface water gradients and in piling up water against obstructions. The large size of Katrina for its duration, combined with the extreme waves generated during its most intense phase, enabled this storm to produce very large storm surges.

On August 29 at 7:00 UTC (shown on Figures 164, 175, 186, 200, 211, 222, 236, and 247), Hurricane Katrina had just been downgraded to a Category 4 storm, with the eye approximately 80 miles south of the initial landfall location. The predominantly easterly wind was blowing water into Breton and Chandeleur sounds as well as into Lake Borgne. In particular, water was being stopped by the Mississippi River levees and by the St. Bernard/Chalmette protection levee where surge was building up to 10 feet. The water level was also raised on the southwest end of Lake Pontchartrain where the railroad berm holds the water while water levels were suppressed in eastern Lake Pontchartrain. The combined water level rise in Lake Borgne and the drawdown of water in eastern Lake Pontchartrain caused a strong surface water gradient across the inlets that connect these two water bodies, Chef Menteur Pass and the Rigolets Strait. This gradient moved a current that drove water into Lake Pontchartrain, which was further reinforced by the easterly winds. The velocities in the Rigolets and Chef Menteur channels between those two water bodies were already 4 to 7 feet/second. This process initiated the critical rise of the mean water level within Lake Pontchartrain. Finally, note that the predominantly easterly and northerly winds to the west of the Mississippi River forced a drawdown of water away from the west-facing levees in these regions.

On 29 August at 10:00 UTC (shown on Figures 165, 176, 187, 201, 212, 223, 237, and 248), Hurricane Katrina was located 30 miles south of its initial landfall location and the winds over the critical regions were still predominantly from the east. Figure 165 shows very clearly the position of the eye and the highest wind velocities in the right front quarter of the storm. The wind speeds over the region mostly exceeded 64 knots, which means the winds were mostly at hurricane strength. The highest wind speeds, up to 90-95 knots, were located south of the Mississippi delta and had a southeasterly to easterly direction. Winds in Lake Borgne, which was due north of the storm center and directly in its path, were east-northeasterly at speeds of 55 to 65 knots. Lake Pontchartrain was in the left-front quadrant of the storm, a little more distant from the eye of the storm, and winds there were from the north-northeast at 40 to 55 knots.

Surge was building up to about 18 feet along the Mississippi levees between Buras and Pointe A La Hache. The easterly wind direction over Breton Sound pushed the water in against the levees in this region. The water level in the IHNC was already 11 feet. The difference in water level between Lake Borgne and the eastern part of

Lake Pontchartrain was already about 6 feet and the currents in Chef Menteur Pass and the Rigolets Strait were increasing to 5 to 8 feet/second. We also note the high velocities (up to 9 feet/second) over the Chandeleur Islands and around the Mississippi River delta.

On 29 August at 11:00 UTC (shown on Figures 166, 177, 188, 202, 213, 224, 238, and 249), Hurricane Katrina was nearing landfall. The eye was located westward from the southern Plaquemines Parish levees, and the highest wind velocities were located just eastward from the delta. The surge continued to build up against the levees of lower Plaquemines Parish reaching elevations up to 19 feet. The surge in this region had started to propagate up the Mississippi River and also extended broadly into Breton Sound. Farther north, surge continued to build up against the St. Bernard/Chalmette protection levee due to the northeasterly winds, up to 13 feet. The difference in water level between Lake Pontchartrain and Lake Borgne continued to increase up to 7-8 feet.

On 29 August at 12:00 UTC (shown on Figures 167, 178, 189, 203, 214, 225, 239, and 250), the eye location had caused a significant shift in wind patterns. The storm had just made landfall and most of the waters surrounding Southeastern Louisiana were exposed to wind speeds greater than 80 knots. Because the center of the storm was very close at this time, the different water bodies in the area were being exposed to different and rapidly changing wind conditions. Winds in Breton Sound continued to blow from the south and southeast at speeds between 80 and 100 knots. Winds over Lake Borgne were blowing from the northeast at speeds of approximately 90 knots. In Lake Pontchartrain, winds were shifting rapidly and were from the north-northeast at speeds ranging from 55 to 80 knots depending on location within the lake (higher wind speeds on the east side of the lake).

Surge had started to be blown off the southernmost east-facing levees of Plaquemines Parish, although surge continued to build up farther north along the river levees. Surge had reached 16 feet along the St. Bernard/Chalmette protection levee and was being driven through the GIWW into the IHNC and Lake Pontchartrain. In addition, the northeasterly winds over Lake Pontchartrain were building up surge against the lake levees of Jefferson Parish and Orleans Parish. In addition, the strong surface water gradient aided by the winds between Lake Borgne and Lake Pontchartrain continued to drive water from Lake Borgne into Lake Pontchartrain. This process was enhanced by the drawdown in the northeast corner of Lake Pontchartrain. The currents in Chef Menteur Pass and the Rigolets Strait were increasing to 7 to 10 feet/second. Note the higher velocities in Lake Pontchartrain around eastern New Orleans. The current vectors on Figures 189 and 225 show that large amounts of water were pushed inside Breton Sound, Chandeleur Sound, and the Mississippi Sound.

On 29 August at 13:00 UTC (shown on Figures 168, 179, 190, 204, 215, 226, 240, and 251), the storm continued to move in a northern direction over Lake Borgne. The wind patterns over the area were quickly changing. The wind directions in Lake Pontchartrain were starting to move from northeast to north-northwest. The surge that built up against the lower Mississippi River levees was propagating rapidly in a northeasterly direction toward Chandeleur Sound. The component of the surge propagating up the Mississippi River reached 16 feet. Surge was also being driven from the west in southern Plaquemines Parish near the city of Venice. Surge was peaking along the St. Bernard Parish/Chalmette protection levee and in the funnel defined by levees along the GIWW and the MRGO. Within Lake Pontchartrain, surge was strongly focused on the south side of the lake and a well-defined drawdown existed along the north shore. It is noted that surge had not built up along the concavity in the Mississippi River along English Turn, due to the change in the direction of the winds.

On 29 August at 14:00 UTC (shown on Figures 169, 180, 191, 205, 216, 227, 241, and 252), Hurricane Katrina was located over Lake Borgne. Compared to a few hours before, the wind-field pattern had completely changed. In Lake Pontchartrain, the wind blew from a north-northwestern direction. Due to the western wind direction, the water was pushed away from the lower Plaquemines Parish and Mississippi River delta levees. The surge originating along these levees continued to propagate across Chandeleur Sound toward the Mississippi Sound in a northeasterly direction. Surge was attenuating along lower Plaquemines on the east side of the river, as was the surge that was propagating up the Mississippi River itself, due to winds from the west and north. Water continued to pile up from the west along the levees near Venice. Surge along the St. Bernard/Chalmette protection levee and in the GIWW/MRGO funnel were attenuating. Water was being blown from the north of Lake Pontchartrain and continued to build up along the southern shores of Lake Pontchartrain to around 9 feet. Water was accumulating from the east and overtopping the CSX railroad between Lake Borgne and Lake Pontchartrain. The gradient in water level between the northern and southern sides of Lake Pontchartrain increased to about 7 feet. Nevertheless, the difference in water level in Lake Borgne and Lake Pontchartrain was also still increasing and still causing high volumes of water to flow into Lake Pontchartrain.

On 29 August at 15:00 UTC (shown on Figures 170, 181, 192, 206, 217, 228, 242, and 253), Hurricane Katrina was near its second landfall at the Louisiana-Mississippi border. The surge that propagated from southern Plaquemines Parish had combined with the local surge being generated by the strong southerly winds and was dramatically increasing water levels between Bay St. Louis and Biloxi with peaks reaching 24 feet. Water was blown from west to east in Lake Pontchartrain. In addition, water was overtopping the CSX railroad west of Lake Borgne and the Mississippi Sound. Water was also driven in a westerly direction across Mobile Bay.

IDS 2

On 29 August at 16:00 UTC (shown on Figures 171, 182, 193, 207, 218, 229, 243, and 254), Hurricane Katrina continued to move north. Surge along the state of Mississippi shoreline was spreading inland and continued to build up driven by the winds from the south to levels reaching 29 feet. Water was being blown from west to east across Lake Pontchartrain and water continued to move from Lake Borgne into Lake Pontchartrain from the east, overtopping the CSX railroad and US 90. Note the sustained difference between the surge level in Lake Borgne (up to 18-20 feet) and Lake Pontchartrain (12 feet). The currents in the Rigolets Strait were still up to 6 to 9 feet/second. The hurricane had made landfall for the second time, and water had started flowing back from Chandeleur Sound into the Gulf of Mexico. Note the increase in velocity at the Chandeleur Islands.

On 29 August at 17:00 UTC (shown on Figures 172, 183, 194, 208, 219, 230, 244, and 255), surge continued to propagate inland along the state of Mississippi shore. Winds were still blowing from the west across Lake Pontchartrain causing a drawdown in the west and a surge in the east while water very forcefully penetrated from Lake Borgne due to the water level differentials. The wind velocities were decreasing. The current vectors in Chandeleur Sound and the Mississippi Sound had started to turn toward the Gulf of Mexico, causing high velocities over the Chandeleur Islands and the Mississippi Sound Islands. Note the difference between the surge level at the gulf-side of the Chandeleur Islands and the sound-side. These islands acted like a barrier, resisting the high sound waters flowing back to the open Gulf of Mexico.

On 29 August at 20:00 UTC (shown on Figures 173, 184, 195, 209, 220, 231, 245, and 256), Hurricane Katrina had moved well inland. Surge along the state of Mississippi coast was subsiding. However, high water remained in Lake Pontchartrain as well as Lake Maurepas. The gradient in water levels between the western and eastern sides of Lake Pontchartrain was reducing. In addition, water was withdrawing from Lake Borgne. Note that water was still flowing into Lake Pontchartrain. The water level in the Gulf was back to its normal level. The barrier islands still captured the surge within Breton Sound, Chandeleur Sound, and the Mississippi Sound. Most of the water got out through the area between the Chandeleur Islands and the Ship Islands.

On 29 August at 23:00 UTC (shown on Figures 174, 185, 196, 210, 221, 232, 246, and 257), these processes continued. Note that water in Lake Pontchartrain was at 7 feet and was only slowly leveling due to the lack of strong water surface elevation gradients. Water continued to flow from Lake Borgne into Lake Pontchartrain at a slow rate due to the decreasing surface water gradients between these lakes. The outflow of surge was heavily resisted by the barrier islands, which caused the surge levels in the Mississippi Sound to be about 8 feet.

Figures 197 through 199, 233 through 235, and 258 through 260 show the maximum wind velocities, surge levels and currents speeds occurring during Hurricane Katrina for the three different scales of interest. The maximum wind velocities occurred along the storm track to the south and east of the Mississippi delta. In Lake Pontchartrain, the maximum wind velocities varied between 60 knots in the northwestern part to 75 knots in the southeastern part. The figures show the reduction in wind speed coming off of land as well as over the marshes south and west from the Mississippi.

The maximum surge level occurring during Hurricane Katrina was about 30 feet along the Mississippi shoreline. Peak water levels in Southeastern Louisiana were computed to be about 18 to 19 feet along the east-facing Mississippi River and back levees that protect communities along the river in south Plaquemines Parish. The maximum water level occurred midway along the levee system and decreased to the north to a minimum peak value of less than 14 feet near English Turn. Adjacent to the levees along the MRGO, maximum computed water levels were 16 to 17 feet. The model predicted a low gradient in water level within the GIWW/MRGO, decreasing water levels from east to west, with a peak water level of about 14 feet at the confluence of the GIWW/MRGO and the IHNC. From this point south to the IHNC Lock, water levels were fairly constant, approximately 14 feet. From the confluence to the northern extent of the IHNC, a high water level gradient was computed, decreasing from a value of 14 feet at the confluence to approximately 9 feet in Lake Pontchartrain at the Lakefront Airport. In Lake Pontchartrain, the maximum surge level was about 8 to 9 feet along the entire southern and eastern shorelines. Note that these computed peak water levels do not include the effects of wave setup or run-up right at the levee systems. This maximum level occurred between 14:00 to 17:00 UTC, shifting from the southern shoreline to the eastern shoreline. At 23:00 UTC, the water level in the lake was still about 7 feet, which indicates that water once captured inside the lake cannot move out again because the surge levels in Lake Borgne are not reduced.

The maximum velocities occurred across the barrier islands, the Mississippi delta, along the inlets of Mobile Bay and St. Louis Bay, and in the channels separating Lake Borgne and Lake Pontchartrain. The maximum velocities at the barrier islands and the Mississippi delta occurred during the first stage of the hurricane.

3.3.3.5 System Validation Using HWMs and Hydrographs

The ADCIRC Hurricane Katrina hindcast was validated by comparing computed water elevations to available excellent and good HWMs in Louisiana and Mississippi as well as to hydrographs in Louisiana. All water level values were computed with respect to NAVD88 (2004.65) and were compared to observed water levels and HWMs relative to the same datum as described in the IPET Report (USACE, 2007).

Essentially, the IPET Report states that all reconstructed hydrographs were based on elevations referenced in NAVD88 2004.56. "Time-tagged digital images from the Lake Pontchartrain – New Orleans lakefront were taken by several individuals who were in buildings or vessels during Katrina's passage. Using these images (which contained physically identifiable reference marks), logs of observations, and nearby HWMs, hydrographs were constructed for the 17th Street Canal entrance, the New Orleans Lakefront Airport, and the IHNC Lock. ... Recorded and constructed hydrographs are presented in the following sections. Note that all elevations are presented in the time-dependent vertical datum NAVD88 (2004.65)" (USACE, 2007).

Reference levels for Hurricane Rita HWM data were NAVD88-2004.65. The hydrograph reference level for Rita from USGS was NAVD88-2004.65. All reference levels for HWM for Hurricane Katrina were NAVD88 2004.65 (USACE, 2007). If unknown reference level, no adjustments were made and the raw data were used as is. This is apparent in some of the comparisons for hydrographs in Hurricane Katrina.

Plots of modeled versus recorded peak storm surge values at all Hurricane Katrina HWM locations identified as either excellent or good are presented on Figures 261 and 262. These measured HWMs were obtained from two sources. The USACE provided 206 marks shown on Figures 263 and 264, which were used to plot Figure 261 (USACE, 2007). URS certified and provided 193 marks shown on Figures 265 and 266, which were used to plot Figure 262 (URS, 2006d; URS, 2006e). The HWMs were collected at the locations shown on Figure 263. We note that no adjustments were made in either the observed HWMs or the ADCIRC computed water levels. Plotting observed HWMs against ADCIRC HWMs; it is expected that the data points lie along a 1:1 line. If a data point is above this line, then this indicates over-prediction in storm surge by the model, and a point under the line indicates under-prediction. Linear regression analysis of the data was used to generate a best-fit line through the data and the origin. The results of this analysis were used to compare the slope of the best-fit line to the expected 1:1 line. This best-fit line was generated in a least squares manner, and the overall quality of fit was given by the correlation coefficient R^2 . For USACE marks, comparisons were made to 206 HWMs and are shown on Figure 261. The slope of the line through all data points is 1.0007, indicating that the model is on average over-predicting surge by only 0.07 percent. The average error is -0.14 foot while the average absolute error is 1.31 feet. The correlation coefficient (R^2) is 0.9317, demonstrating that the modeled peak surge is closely related to the recorded peak surge and the results are clustered about the 1:1 line. For URS marks, comparisons were made to 193 HWMs and are shown on Figure 262. The slope of the line through all data points is 1.0315, indicating that the model is on average over-predicting surge by 3.15 percent. The average error is 0.45 foot while the average absolute error is 1.24 feet. The correlation coefficient (R^2) is 0.9460. The URS marks show more over-prediction, but give a better

correlation. From both sets of HWMs, it is clear that the model captures physical processes in Hurricane Katrina storm surges very well.

The marks along the south shore of Lake Pontchartrain depicted by red circles on Figures 264 and 266 are shown as red triangles on Figures 261 and 262, while the other marks are shown as blue rectangles. The fact that the model under-predicts at these points along the south shore of Lake Pontchartrain indicates the necessity of local Boussinesq models to capture local wave setups against lake shore structures. For the USACE marks, the model predicted the maximum water levels within ± 1.5 feet at 63 percent of the 206 locations and within ± 3.0 feet at 96 percent of the 206 locations. For the URS marks, the model predicted the maximum water levels within ± 1.5 feet at 75 percent of the 193 locations and within ± 3.0 feet at 98 percent of the 193 locations. The URS marks give better statistical figures because the USACE marks include more locations along the south shore of Lake Pontchartrain where the model solution needs to be improved using Boussinesq models. Overall, the statistical numbers presented clearly support the validity of the model.

Figures 267 through 276 show colored circles at the USACE excellent and good HWMs. The colors of the circles were determined based on the levels of errors between the measured HWMs and ADCIRC solutions. Red, orange, and light green circles indicate over-predictions by the model. Red circles indicate errors greater than 3 feet, orange circles indicate errors greater than 1.5 feet and less than 3 feet, and light green circles indicate errors greater than 0 foot and less than 1.5 feet. Green, blue, and dark blue circles indicate under-predictions by the model. Green circles indicate errors less than 0 foot and greater than -1.5 feet, blue circles indicate errors less than -1.5 feet and greater than -3.0 feet, and dark blue circles indicate errors less than -3.0. Hence, the circles in green or light green indicate the HWMs predicted within ± 1.5 -foot error range. These plots allow identification of the level of error associated with each HWM. In general, note that typically missing features, processes, and/or poor grid resolution are associated with the larger errors. Inadequate resolution in the circulation and wave models leads to the under-prediction of wave-induced setup on the south shore of Lake Pontchartrain. Farther inland, the model generally tends to over-predict surge unless the area is connected to well defined and resolved inland waterways. This over-prediction is likely related to inadequate resolution farther upstream of the HWM locations not adequately allowing flow through to locations farther upstream.

Time series of model response during Hurricane Katrina are compared to water level data at tidal and river gauges. Hydrographs at eight stations shown on Figure 277 are plotted with the data records and model output on Figure 278. The model shows a very good match to both the tidal signal and the storm surge. Furthermore, the datum levels appear to be well matched. The comparison at the mouth of the Mississippi River at Southwest Pass indicates that the modeled tides are well represented in the region. The

peak storm surge is over-predicted by about 1.3 feet. However, nearby HWMs indicate that the observed peak value may somewhat under-represent the surge in the region. Specifically, there are three nearby HWMs that indicate peak still water levels of 8.9, 8.6, and 8.5 feet. These three values more closely match the ADCIRC predicted value. The pre/post-storm mean water levels and tidal amplitudes also agree well, which indicates that the model is well capable of capturing tidal signals and post storm draw down. The comparison at Grand Isle similarly shows good agreement. The gauge at Carrollton in the Mississippi River adjacent to New Orleans indicates that the model correctly captures the propagation of tides and surge up the Mississippi River. The tides are slightly over-damped; the computed peak water level is approximately 2.5 feet less than the measured value. It is noted that the recording station failed after the peak surge passed New Orleans. The model results at Little Irish Bayou on the Lake Pontchartrain side of Chef Menteur Pass shows rising water levels matching recorded levels. This gauge failed well before high water levels were reached. Model results at the location of the gauge in Lake Pontchartrain, Midlake, appear to match with the portion of the record that is available. The gauge failed in the middle of the storm and recorded water levels intermittently. It is noted that the ADCIRC model shows two peaks occurring in the lake. The first corresponds to high water being driven by winds from the north and northeast piling water against the south shore of the lake. The second and slightly larger and broader peak corresponds to the massive intrusion of water coming in from Lake Borgne and driven by high waters associated with the second landfall of the storm on the Louisiana-Mississippi coast. It is noted that the drainage rate at Midlake is slightly slower in the model than the measured rate. The comparison at the 17th Street Canal indicates that the model is under-predicting peak surge by about 2 feet. More detailed local Boussinesq models have indicated that there is more wave setup than computed with this regional model (as much as 1.5-2 feet). Note that simulating wave setup properly would require grid resolution on the order of 5 to 15 feet in order to capture the interaction of the breaking waves with the local roads (e.g., Lakeshore Drive), topography, and the levee structures themselves. For this study, that interaction was considered in the high-resolution hydrodynamics component of the project. When compared to the ADCIRC hydrograph, the measured hydrograph does show a good correspondence between the timing of the two peaks. The first is again associated with the wind-driven peak from the westerly and northerly winds while the second is associated with the intrusion of high water from Lake Borgne. Again, modeled drainage rates are slightly lower than measured. The comparison at Bayou LaBranche shows good agreement in terms of the timing of peaks and rising and drainage rates. The discrepancy, which is consistent in time, is attributed to a discrepancy in datum levels as the measured pre-storm water level is lower by about 1 foot than the other stations in Lake Pontchartrain. Finally, water levels at Pass Manchac on the west side of the lake compare to within 1.2 feet of the measured values, showing excellent agreement in terms of timing and reproduction of all hydrograph features.

3.3.4 Rita Hindcast/Validation

3.3.4.1 Overview

Hurricane Rita was one of three major hurricanes in the Gulf of Mexico during the 2005 season. Hurricane Rita developed in the Gulf of Mexico in late September 2005, tracked across the Gulf from the southeast to the northwest, and made landfall near Sabine Pass and the border between Louisiana and Texas shortly before 08:00 UTC on September 24, 2005 (Knabb et al., 2006). Like Hurricane Katrina (2005), Rita was a Category 5 hurricane while over the central Gulf of Mexico that weakened to a Category 3 hurricane prior to making landfall. With regard to several measures, Rita was even more powerful than Hurricane Katrina (with a lower central pressure of 895 mb and higher 155-knot maximum winds), although it did not cause the same level of damage because it lost more strength as it made landfall, it produced less surge due to its landfall location, and it made landfall in a less populated region. Rita's maximum surge occurred to the east of the landfall location, along the coastline to the south of Calcasieu Lake with high water approximately 15 feet above NAVD88 (2004.65). The overland flooding in Southwestern Louisiana was extensive.

Rita's southeast to northwest track and its large size produced easterly winds blowing across the entire state in the early stages of the storm. These easterly winds pushed water onto westward facing shores including those of Breton Sound, Lake Borgne, Lake Pontchartrain, Calcasieu Lake, and many other water bodies in Southwestern Louisiana. There was up to 7 to 9 feet of surge on the east bank of New Orleans and Lake Pontchartrain despite the fact that Rita made landfall more than 250 miles away. When the storm made landfall, much of the region had already been inundated by these inland and estuarine waters. The storm surge from the sea was able to more readily propagate northward over land that was already flooded.

In this section, the development and propagation of Hurricane Rita's surge is examined in detail. First, a progression through the storm is presented. Information for wind velocity, water elevation, and water velocity is presented and discussed for two regions (Southwestern and Southeastern Louisiana) at 14 time snaps during the storm. These progressions show that the overland flooding in Southwestern Louisiana was extensive, that the hurricane winds created significant water velocities in the Gulf of Mexico before the hurricane made landfall, and that a significant amount of surge was created near New Orleans, far from where Hurricane Rita made landfall.

Second, the maximum ADCIRC elevations and velocities are presented for both Southwestern and Southeastern Louisiana. These figures show that the maximum surge elevation was about 15 feet at the coastline south of Calcasieu Lake. However, significant storm flood elevations occur in other parts of the domain, including the

Lake Charles area north of Calcasieu Lake, the north edge of Vermilion Bay, and even along the highway levees to the southeast of New Orleans. In contrast, the maximum velocities occurred in localized regions within defined channels, such as Sabine Pass, the Calcasieu Shipping Channel, and even the exchanges between Lake Pontchartrain and Lake Borgne.

Third, a detailed error analysis is presented. Two sources of measured data were used: one was a set of HWMs obtained from FEMA collected by URS, and one was a set of hydrographs published by the USGS (McGee et al., 2006). The ADCIRC SL15 model does a good job of matching the HWMs, with the exception of the marks near Vermilion Bay, for reasons discussed later. The ADCIRC SL15 model does an excellent job of matching the hydrographs, with the exception of regions where the model does not contain a sufficient level of geographic and grid resolution. Both analyses suggest that even a higher level of resolution is needed in various regions to better define flooding conduits and the associated topographic and raised features.

3.3.4.2 Rita WAM Computations/Validation

See Section 3.2.3.2 for detailed information on the WAM model validation as well as details specific to the WAM model application for the Hurricane Rita JPM validation.

3.3.4.3 Rita STWAVE Computations and Wave Radiation Stress

Nearshore waves simulated by STWAVE for the Hurricane Rita validation indicate reasonable wave and radiation stress gradient fields for the forcing applied. Section 3.2.4 provides additional details of the STWAVE methodology applied for the Hurricane Rita JPM validation including STWAVE grid locations. The STWAVE simulations accounted for the effect of bottom friction through a dissipation term that applied Manning n coefficients. An interpolation procedure mapped the Manning n from the ADCIRC mesh onto each STWAVE grid. The USGS GAP data (USGS, 2000) provided the Manning n land roughness values applied in the ADCIRC model. At this time, very limited field data exist for the effects of coastal marsh vegetation on wave propagation during storm events with significant inundation. Verification of the bottom friction coefficients applied in STWAVE requires additional field data; programs are underway to collect data during future storm events in coastal Louisiana.

Figures 279 and 280 present the maximum significant wave height and mean wave period in each STWAVE grid cell for the West grid during the Hurricane Rita validation. The mean wave period represents the wave period associated with the maximum significant wave height for each cell. Maximum wave heights exceed 36 feet (11 meters) along the offshore boundary. Near the coastline, depth limited breaking occurs and wave heights reduce rapidly. The inundated land areas show wave heights

from approximately 0 to 6 feet (0 to 2 meters). Figure 280 shows mean wave periods near 14 seconds at the offshore boundary. For the inundated land areas, short-period wind-generated waves dominate with average values near 5 seconds.

Very limited wave data exist for nearshore and marsh areas during Hurricane Rita. During Hurricane Rita, the LSU WAVCIS program had two gages deployed near the Acadiana Bays region of coastal Louisiana. The wave record for Station CSI-3 (offshore of Marsh Island) stopped before maximum conditions during the storm's passage. Station CSI-14, located in West Cote Blanche Bay (91.56 West, 29.52 North), recorded a complete wave height record during Hurricane Rita's passage. Maximum wave conditions reached 6 feet (1.8 meters) at Station CSI-14. Figure 281 presents the maximum significant wave height for the West grid during the Hurricane Rita validation with a scale that resolves the nearshore waves. The plot contains a box that comprises the area near Station CSI-14. Figure 281 indicates maximum wave heights near 6.6 feet (2 meters) in the area near Station CSI-14 for the STWAVE Hurricane Rita validation. The STWAVE simulation provides a reasonable estimate of the wave height at this one location. Notably, the STWAVE model incorporates bottom friction, but does not incorporate dissipation because of viscous interactions between the waves and the muddy bottom known to occur in the Acadiana Bays.

Figures 282 and 283 present the maximum significant wave height and mean wave period in each STWAVE grid cell for the South grid during the Hurricane Rita validation. No field data exist to verify the STWAVE model results in the South grid. The plots show extremely large waves (swell conditions) with maximum wave heights over 35 feet (11 meters) near the offshore boundary and mean periods of approximately 14 seconds. The plots show the sheltering effects of the coastal marshes with depth-limited breaking seaward of the shoreline. In the interior coastal marshes, wave periods diminish and wind-generated seas become more prominent (lowering of mean period).

Figure 284 presents the magnitude of the maximum radiation stress gradients for the offshore area during the Hurricane Rita validation. Figure 285 presents the magnitude of the maximum radiation stress gradients for the western Louisiana area during the Hurricane Rita validation. The radiation stress gradients provide the forcing required by ADCIRC to generate wave-induced water level changes and currents. No field data exist to verify the STWAVE model results shown in the plots; however, the spatial location of the gradients and their magnitudes seem reasonable given the storm forcing during Hurricane Rita. Figure 284 shows the largest radiation stress gradients near the Mississippi River delta where extremely large waves break on the relatively steep slopes (relative to the surrounding coastal marshes) of the delta. Other areas of significant radiation stress gradients include the shoreline along western Louisiana, the Chandeleur Islands, and the barrier islands offshore of Mississippi. Some small circles of high radiation stress gradients do occur near the STWAVE West grid offshore boundary.

These areas of high radiation stress gradients occur near the WAM output points that provide the wave spectra for STWAVE. These small areas of radiation stress gradients should not cause any significant change to the water level because of the large water depth at the offshore boundary. Figure 285 shows the largest wave radiation stress gradients occur near the shoreline for the western Louisiana area. The magnitudes of these gradients are less than half of those observed on the Mississippi River delta in Figure 284.

3.3.4.4 *ADCIRC Parameter Definitions*

The Mississippi and Atchafalaya rivers are forced with steady flows of 181,000 cfs and 79,000 cfs, respectively. Actual flow rates in the Mississippi River ranged from 187,000 cfs to 190,000 cfs between September 19 and September 22, 2005. Actual flow rates in the Atchafalaya River ranged from 82,000 cfs to 86,000 cfs between September 19 and September 22, 2005. Steady flows are applied to work with the river radiation boundary conditions used in these rivers.

In this Rita hindcast simulation, the model reads in wind speeds and atmospheric pressure fields provided by OWI for the period of 9/18/2005 00:00 UTC through 9/26/2005 00:00 UTC every 15 minutes. The wind and pressure fields at a fractional time are then computed by a linear interpolation in time.

The model reads in wave radiation stress fields generated by STWAVE model for the period of 9/23/2005 00:30 UTC through 9/26/2005 00:00 UTC every 30 minutes. The wave radiation stress field at a fractional time is then computed by a linear interpolation in time.

Unless noted otherwise, the parameters for the hurricane runs were the same as for the tides run described in Section 3.3.2.

3.3.4.5 *ADCIRC Surge and Current Computations - Rita*

To illustrate the progression of the storm surge throughout Southern Louisiana, the ADCIRC elevation contours and wind vectors will be presented for the same 14 time snaps. Hurricane Rita made landfall shortly before 08:00 UTC on September 24, 2005, and these 14 time snaps are centered on that time. They show the storm surge building in the Gulf of Mexico, reaching a maximum of about 15 feet along the coastline to the south of Calcasieu Lake, and then propagating overland through the lakes and marshes of Southwestern Louisiana. They also show the storm surge building up on the Mississippi-Alabama shelf, against the levees in Plaquemines Parish, propagating north into English Turn, and steadily filling Lakes Pontchartrain and Maurepas.

The wind contours and vectors are shown on Figures 286 through 313. Data-assimilated IOKA winds for Hurricane Rita were obtained from OWI. They provide coverage for the entire Gulf of Mexico and all of Southern Louisiana for the 6 days from September 18 through 24, 2005. In this section, 14 time snaps have been selected centering around the hurricane's landfall. For each time snap, the wind speed contours and vectors in both Southwestern Louisiana, where the hurricane made landfall, and Southeastern Louisiana, where the hurricane created significant storm surge in the vicinity of the New Orleans metropolitan region, will be presented.

Figures 286 and 287 show the system at 12:00 UTC on September 23, 2005, or about 20 hours before Hurricane Rita made landfall. The eye of the storm was about 160 miles south of Atchafalaya Bay or about halfway along the Louisiana coastline. As shown on Figure 286, the effects of the hurricane were becoming evident in Southwestern Louisiana. Coastal winds were predominantly easterly and northeasterly up to about 55 knots in the areas nearest to the eye of the storm, which forced water out of many of the coastal water bodies, including Sabine Lake, Calcasieu Lake, and Vermilion Bay. As shown on Figure 287, the winds were easterly in Southeastern Louisiana. The winds were already strong in this region, with wide coverage 40-knot winds pushing water against the levees in Plaquemines Parish. We note the pronounced directional land masking that occurred as a result of the directional surface roughness and associated wind boundary layer adjustments included in the model.

Figures 288 and 289 show the system at 18:00 UTC on September 23, 2005, or about 14 hours before landfall. As shown on Figure 288, the eye of the hurricane is almost visible and was positioned about 115 miles from shore to the west of Vermilion Bay. The wind speeds had increased significantly. In Sabine Lake and Calcasieu Lake, the wind was blowing in a southwestern direction, which was pushing water away from the north and east sides of these lakes. In Vermilion Bay, the wind was blowing in a western direction, which was pushing water out of the bay and over the land to the west. As shown on Figure 289, the winds continued to blow toward the west in Southeastern Louisiana. The land roughness coverage in Plaquemines Parish and in the region around Terrebonne Bay acted to decrease the magnitude of the wind, but the land still saw wind speeds of up to 40 knots.

Figures 290 and 291 show the system at 24:00 UTC on September 23, 2005, or less than 8 hours before landfall. The eye of Hurricane Rita is visible, as shown on Figure 290, and was located 75 miles from shore halfway between Grand Lake and Calcasieu Lake. Note that the maximum winds occurred in the region to the northwest of the eye; this region corresponds to the region with the maximum ADCIRC velocities in a later section. Also note the effect of the wind reduction factors on the wind magnitudes on land. The wind speed had reached 50 knots or more in the bodies of water along the coastline, such as Calcasieu Lake and Vermilion Bay. However, the wind reduction

factors cut down the wind speed on land, to where it was 40 knots or less. As shown on Figure 291, the winds had shifted to the northwest. As will be discussed in the section on the ADCIRC water elevations for Hurricane Rita, these northwestward winds took the storm surge that had built along the levees in Plaquemines Parish and pushed it to the northwest, where it built against the highway levees near New Orleans.

Figures 292 and 293 show the system at 03:00 UTC on September 24, 2005. These snapshots are about 5 hours before landfall of Hurricane Rita. The eye was located 50 miles south of Vermilion Bay. On Figure 292, note the behavior of the storm itself. The winds rotated around the eye itself, which contained winds with little or no speed. However, the maximum wind speeds occurred to the northwest of the eye, and they had magnitudes of about 85 knots. Meanwhile, the velocities over the coastal and inland water bodies of water were about 55 knots or higher. Also note that, except for the region to the west of Sabine Lake, the hurricane winds did not blow away from the coastline. Instead, the winds were blowing westward or even northwestward, and they were already blowing surge into Louisiana. As shown on Figure 293, in Southeastern Louisiana the winds continued to blow to the northwest, pushing surge along the Mississippi River levees and toward New Orleans.

Figures 294 and 295 show the system at 06:00 UTC on September 24, 2005, or less than 2 hours before landfall. The center of the storm was located 20 miles from shore halfway between Sabine Lake and Calcasieu Lake. On Figure 294, note that the region of maximum winds was positioned just south of Calcasieu Lake; the maximum wind speed was about 85 knots. As is discussed in a later section, this region corresponds to the regions with the maximum ADCIRC velocities and the maximum storm surge. As shown on Figure 295, the winds continued in a northwesterly direction. In bodies of water, such as Terrebonne Bay, Barataria Bay, and Lake Pontchartrain, the wind speeds were about 40 knots. Over land, the wind speeds were reduced to about 25 or 30 knots.

Figures 296 and 297 show the system at 07:00 UTC on September 24, 2005, which was less than 1 hour before landfall of Hurricane Rita. As shown on Figure 296, the eye had not yet made landfall, but the maximum winds had. The wind speed at the coastline south of Calcasieu Lake was about 80 knots, and the wind speed over Calcasieu Lake was about 75 knots. In Sabine Lake to the west and Grand Lake to the east, the wind speeds were about 65 knots. The full effect of Hurricane Rita was being felt throughout Southwestern Louisiana. As shown on Figure 297, in Southeastern Louisiana the winds continued to blow to the northwest. At this stage of the hurricane, about 9 feet of storm surge had built up along the highway levees to the southeast of New Orleans, and the hurricane winds continued to hold it there.

Figures 298 and 299 show the system at 08:00 UTC on September 24, 2005, or 20 minutes after Hurricane Rita made landfall. On Figure 298, it can be seen that the

eye had made landfall near Sabine Pass. Note that the winds had already begun to die down. The maximum wind speed was about 75 knots, and it occurred to the southwest of Calcasieu Lake. The wind speeds to the east, such as the region north of Vermilion Bay, were about 35 knots. However, note how strong the winds remained in the region around Calcasieu Lake. The maximum storm surge occurred at the coastline to the south of Calcasieu Lake, and these winds continued to blow that surge inland. As shown on Figure 299, Southeastern Louisiana continued to be battered by northwestward winds. The wind speeds varied from 45 knots to about 35 knots across the region.

Figures 300 and 301 show the system at 09:00 UTC on September 24, 2005, or about 1 hour after landfall. As shown on Figure 300, the eye was still visible over Sabine Lake, but the storm shows signs of deterioration. However, because of the counter-clockwise rotation of the hurricane, strong winds continued to blow northward along the coastline south of Calcasieu Lake. As will be shown later, the continued strength of these winds pushed the water northward, through Calcasieu Lake, and into the Lake Charles region. On Figure 301, note that there was no deterioration in the winds in Southeastern Louisiana. They continued to blow to the northwest, and their magnitudes continued to be 45 knots in the Gulf and 25 to 30 knots over land.

Figures 302 and 303 show the system at 10:00 UTC on September 24, 2005, or more than 2 hours after landfall. On Figure 302, note that the eye is no longer visible in the ADCIRC model. However, the counter-clockwise rotation of the storm continued to blow northward over Calcasieu Lake, where the maximum wind speeds were about 65 knots. As shown on Figure 303, the winds in Southwestern Louisiana were beginning to die down. The contour of 30 knots had shifted farther west, so that a larger region of the Gulf at the right edge of the figure had wind speeds less than 30 knots. A similar decrease in wind speeds was happening throughout the region.

Figures 304 and 305 show the system at 11:00 UTC on September 24, 2005, or about 3 hours after landfall of Hurricane Rita. Figure 304 shows that the winds were finally dying down over Calcasieu Lake itself, where the maximum wind speed was about 58 knots. However, a large region of the system continued to experience winds of 50 knots or greater, and thus the storm surge continued to be pushed against the coastline south of Calcasieu Lake. As shown on Figure 305, the winds continued to decrease in Southeastern Louisiana. As shown in the section about the ADCIRC water elevations for Hurricane Rita, the decrease in the wind speeds in this region allows the storm surge to decrease as well.

Figures 306 and 307 show the system at 12:00 UTC on September 24, 2005, or about 4 hours after landfall. On Figure 306, note that the size of the region where the winds were 50 knots or greater decreased. The wind speeds over Sabine Lake and

IDS 2

Calcasieu Lake were about 52 knots. On Figure 307, which shows Southeastern Louisiana, the wind speeds continued to decrease. Most of the open water in the right half of the figure had wind speeds less than 30 knots, and the wind speeds on land were in the range of 20 to 25 knots. The decrease in intensity of Hurricane Rita was occurring throughout the entire region.

Figures 308 and 309 show the system at 15:00 UTC on September 24, 2005, or more than 7 hours after landfall. On Figure 308, note that the wind speeds had noticeably decreased. Sabine Lake continued to feel winds of 50 knots or greater, but the winds over parts of Calcasieu Lake were less than 50 knots in magnitude. They continued to blow north and northeast, pushing the surge northward through the lake and toward the Lake Charles region. As shown on Figure 309, the wind speeds decreased to 30 knots or less for most of Southeastern Louisiana. These magnitudes were not enough to continue piling up surge against the highway levees to the southeast of New Orleans; therefore, the storm surge was receding.

Figures 310 and 311 show the system at 18:00 UTC on September 24, 2005, or about 10 hours after Hurricane Rita made landfall. On Figure 310, note that the wind speeds decreased significantly, so that the maximum wind speed was about 40 knots over Sabine Lake. The magnitude was even less throughout most of the rest of Southwestern Louisiana. On Figure 311, for Southeastern Louisiana, a similar decrease in wind speeds was observed. In addition, the winds shifted to the north throughout most of the region.

Figures 312 and 313 show the system at 21:00 UTC on September 24, 2005, or about 13 hours after landfall. On Figure 312, note that the maximum wind speeds occurred over the two lakes near where Hurricane Rita made landfall. The wind speed was about 34 knots over Sabine Lake and 33 knots over Calcasieu Lake. As shown on Figure 313, the wind speeds decreased significantly in Southeastern Louisiana. In open water, the wind speed was 25 knots or less throughout most of the region, and, on land, the wind speed was 20 knots or less.

Hurricane Rita, like many Gulf hurricanes, traveled at an angle from the southeast toward the northwest. In much of western Louisiana, the early storm winds blew southward and southwestward, which caused water to be blown away from the shore. As the hurricane approached the shore, the winds shifted to blow westward, causing water to be blown along the coastline. These westward winds blew water from the existing bodies of water, such as Calcasieu Lake and Vermilion Bay, into the surrounding marshland. Finally, when the hurricane made landfall, the winds shifted to blow northwestward or purely northward, causing the maximum storm surge to be blown from the Gulf and into Southwestern Louisiana. In eastern Louisiana, the winds tended to be sustained from the east and southeast during the entire event. This led to

water piling up against the levees of Plaquemines Parish, the Mississippi River levees at English Turn, the funnel at the confluence of the MRGO and GIWW, and into Lakes Borgne and Pontchartrain.

Figures 314 and 315 show the system at 12:00 UTC on September 23, 2005, or about 20 hours before landfall. Figure 314 shows the ADCIRC surface water elevation contours and wind vectors for Southwestern Louisiana. Sabine Lake is shown in the west, Calcasieu Lake is shown farther east, Grand Lake is to the east, and Vermilion Bay is shown on the eastern edge. This region includes the cities of Port Arthur, which is located to the west of Sabine Lake, Lake Charles, which is located to the north of Calcasieu Lake and connected to it via a shipping channel, Lake Arthur, which is located to the north of Grand Lake, and Abbeville, which is located to the northeast of Vermilion Bay. This figure shows the hydraulic connectivity that exists in the region and the beginnings of the effect of the hurricane storm surge.

The three lakes and Vermilion Bay are connected to the Gulf of Mexico through a combination of natural waterways and shipping channels. Calcasieu Lake is connected via a relatively short shipping channel directly south of the lake; the position of this channel is shown on Figure 314 where State Highway 82 (represented as a weir in the ADCIRC SL15 model) bends and runs north-south before continuing along the south side of the lake. This shipping channel passes the city of Cameron, Louisiana. Sabine Lake is connected to the Gulf of Mexico via Sabine Pass, which acts as the division between the states of Louisiana and Texas. Grand Lake is connected to the Gulf via Upper and Lower Mud Lakes, which extend to the south and west of the lake. These lakes are difficult to see on Figure 314 because this region contains some low-lying marsh that begins wet in the model, and Vermilion Bay has connectivity to the Gulf of Mexico on either side of Marsh Island.

In addition to the hydraulic connectivity between these lakes and the Gulf of Mexico, there is also connectivity between the lakes themselves. Some of this additional connectivity is due to the low-lying, marshy texture of the surrounding land, which allows the storm surge to propagate inland. This behavior is evident at the stage of the hurricane depicted on Figure 314; the area in the center of the figure, between State Highway 82 and the coast, was inundated already in these early stages of the hurricane. The remainder of the additional connectivity is due to man-made shipping channels, most notably the GIWW, which is depicted on Figure 314 as a thin blue line that runs along the north sides of these three lakes and Vermilion Bay. The majority of the storm surge due to Hurricane Rita did not propagate through the GIWW, but this channel did carry some surge, and several of the HWMs and elevation stations to which we will be comparing our results were placed along the GIWW; therefore, its location is significant.

Figure 315 shows the ADCIRC elevation contours and wind vectors for Southeastern Louisiana. Note how much build-up was occurring in this region, which is more than 250 miles away from the eye of the storm at any given time as it traveled through the Gulf of Mexico. The winds blew westward and pushed water against the west edge of Lake Pontchartrain, against the east side of New Orleans, and against the levees along the lower Mississippi River. The surge already reached 7 feet in parts of Plaquemines Parish.

Figures 316 and 317 show the system at 18:00 UTC on September 23, 2005. The landfall of Hurricane Rita did not occur until about 14 hours later, but the effects of the hurricane were already pronounced. As shown on Figure 316, the counter-clockwise rotation of the hurricane caused the winds in this region to blow northeasterly at this stage, and thus the wind pushed the water in these water bodies to the southwest. The dark blue contour is about 1 foot below sea level, and the green contour in the Gulf of Mexico and in the southwest corners of the lakes is about 3 feet above sea level. Thus, there was a gradient of 3 feet in these lakes. In Sabine Lake, water was pushed from the entrance of the GIWW in the northeast down to the Sabine Pass in the south. In Calcasieu Lake, water was pushed from the system of lakes and channels near Lake Charles in the north to the southwest corner of the lake. In fact, flooding occurred in the region between Calcasieu Lake and the coast; thus, some of flooding was due to water from the lake and not from the Gulf. In the area to the west of Grand Lake, extensive inundation occurred as water was pushed from Grand Lake and other bodies of water to the east, and Vermilion Bay was draining as water was pushed westward toward State Highway 82.

On Figure 317, the westward winds in Southeastern Louisiana continued to create storm surge near New Orleans. The railroad embankment between Lake Pontchartrain and Lake Borgne stopped surge and funneled it toward the confluence of the GIWW and MRGO toward the IHNC. Storm surge built up against the river levees in Plaquemines Parish, where the maximum surge was almost 8 feet above NAVD88 (2004.65).

Figures 318 and 319 show the system at 00:00 UTC on September 24, 2005. As shown on Figure 318, the drawdown prior to landfall intensified. The gradient in Sabine Lake intensified, from a minimum of more than 4 feet below sea level in the northeast to a maximum of almost 3 feet above sea level in the southwest. A similar gradient existed in Calcasieu Lake; the drawdown was not as significant in the northeast, but the overland flooding in the southwest reached 5 feet above sea level. In the area surrounding Grand Lake, extensive flooding occurred. State Highway 27, which runs north-south between Calcasieu Lake and Grand Lake, acted as a levee to prevent the flood from propagating farther west; instead, the water built up against it. It was difficult to make out the natural shore of Vermilion Bay because the flooding to its west was so widespread.

Also, note the widespread drawdown that occurred in the Gulf of Mexico itself. There is a small region to the southwest of Calcasieu Lake where the elevation was more than 1 foot below sea level, and there was a larger region to the southwest of Sabine Lake where the elevation was similar. To the west of Sabine Lake, the hurricane winds blew to the south, almost directly offshore, and pushed water from the coast.

As shown on Figure 319, the hurricane winds shifted to blow slightly northwestward. The storm surge built to 5 feet throughout most of Lake Pontchartrain, Lake Borgne, and the Mississippi Sound. State Highway 39 began to bear the brunt of the storm surge to the southeast of New Orleans, where the maximum water elevation reached 9 feet. The storm surge pushed against State Highway 39 remained in this region for several hours, as the hurricane winds continued to push northwestward.

Figures 320 and 321 show the system at 03:00 UTC on September 24, 2005. As shown on Figure 320, the landfall of Hurricane Rita was only 5 hours away, and the winds intensified and shifted to blow westward over Grand Lake. The elevation gradients everywhere also intensified. In Sabine Lake, the elevation ranged from 7 feet below sea level at the entrance to the GIWW to 3 feet above sea level in the southwest. In Calcasieu Lake, the range was from 3 feet below to 3 feet above sea level, and extensive flooding occurred to the west of the lake. In Grand Lake, the gradient ran purely east-west.

It is interesting to note how much flooding had already occurred. The water from the lakes and marshes in this region endured the full brunt of hurricane winds, which caused it to spread outside the lakes and into the surrounding, low-lying topography. For example, the region around Grand Lake was completely flooded because water flowed out of Grand Lake and the other bodies of water farther east. Most of this water was held back by State Highway 27, but some of it pushed through the GIWW to the region immediately east of Calcasieu Lake. The water that began in Calcasieu Lake was pushed to the south and west, and it was building up against the north side of State Highway 82. The water from Sabine Lake was pushed to the south and to the Gulf of Mexico. Large portions of Southwestern Louisiana were already inundated.

As shown on Figure 321, Southeastern Louisiana continued to be battered by hurricane winds blowing toward the northwest. For the first time, contours of 6 feet above NAVD88 are visible at the west edge of Lake Pontchartrain and the east edge of the confluence of the GIWW/MRGO. Nine feet of storm surge continued to be trapped against State Highway 39 to the southeast of New Orleans.

As shown on Figure 322, time is advanced forward by 3 hours to 06:00 UTC on September 24, 2005. Hurricane Rita made landfall about 2 hours later. At this point in the hurricane, the winds were shifting to the northwest, and thus they pushed the storm

surge onto the coast. The surge reached 9 feet on the south side of Calcasieu Lake, and it was flowing over State Highway 82 and up Calcasieu Pass. In Calcasieu Lake itself, a gradient of almost 8 feet existed from east to west. Water that had been pushed from Grand Lake in the east made its way past State Highway 27, through the GIWW and other connectivity due to marshland, and was flowing into the east side of Calcasieu Lake. Some of the water from Calcasieu Lake had been pushed west, along the north side of State Highway 82, and was flowing into the south end of Sabine Lake. Water from the Gulf was also flowing up Sabine Pass and into the south end of Sabine Lake. The eastern half of Grand Lake was 2 feet or more below NAVD88 (2004.65). Meanwhile, the storm surge in the Gulf of Mexico reached 9 feet and was being forced toward the coast at Calcasieu Pass.

Contrast the amount of flooding shown on Figure 322, which represents the surge at 2 hours before landfall, with the amount of flooding shown on Figure 314, which represents the surge at 20 hours before landfall. There was some overland flooding along the coastline shown on Figure 314 but the regions between the three lakes were dry. As shown on Figure 322, however, these regions were mostly flooded, with anywhere from 1 to 4 feet of water. The hurricane had not yet made landfall, and most of Southwestern Louisiana south of the GIWW was inundated.

Figure 323 shows Southeastern Louisiana at the same time, about 2 hours before landfall. The 9-foot contour is clearly visible in the surge southeast of New Orleans; the hurricane winds continued to blow northwestward and push the storm surge against the highway levees. In addition, 6 feet of storm surge was building against the levees near Houma, Louisiana. Large portions of Southern Louisiana were inundated by about 5 feet of storm surge.

As shown on Figures 324 and 325, time is advanced forward to 07:00 UTC on September 24, 2005. Hurricane Rita made landfall within the hour. As shown on Figure 324, the surge had built to 13 feet along the coastline south of Calcasieu Lake, and it was flowing over State Highway 82 and up Calcasieu Pass. In the region along the coastline to the east of the main surge, the water was building up against State Highway 82 or barely overtopping it. In the region along the coastline to the west of the main surge, the water was propagating overland toward the highway and was flowing into Sabine Pass. As shown on Figure 325, not much had changed in Southeastern Louisiana. The winds continued to blow to the northwest, and their magnitudes and directions did not change significantly over the next few hours. About 9 feet of surge existed southeast of New Orleans and about 6 feet of surge was building southeast of Houma.

Figures 326 and 327 show the system at 08:00 UTC on September 24, 2005. Figure 326 shows the ADCIRC elevation contours and wind vectors for Southwestern Louisiana.

Hurricane Rita had made landfall, and the counterclockwise hurricane winds were blowing over the Gulf of Mexico and pushing the surge toward Calcasieu Lake. The maximum surge built to 13 feet above NAVD88 and spread along the coast from State Highway 27 in the east to halfway to Sabine Lake in the west.

Note the sharp gradients just south of Calcasieu Lake, between the southern edge of the lake and State Highway 82. At the coast, the surge had built to 13 feet on the Gulf-side of the highway, and was forced northward by the hurricane winds. However, in the lake itself, the elevations were still below sea level. In fact, there is a small patch of ADCIRC elements along the southeast shoreline of Calcasieu Lake that had dried because the water in the lake had been forced elsewhere during the earlier parts of the storm. Thus, there was a sharp gradient between the surge at the coastline and the partially emptied lake. ADCIRC did an excellent job of capturing this gradient; notice how the contour lines are bunched together in the region south of the lake.

As shown on Figures 328 and 329, time is advanced forward to 09:00 UTC on September 24, 2005. These figures represent the system about 1 hour after landfall of Hurricane Rita. Figure 328 shows the ADCIRC elevation contours and wind vectors in Southwestern Louisiana. The worst of the storm surge still existed at the coastline, where the water elevation was 13 feet, but it was not as intense or widespread. Instead, surge was propagating into Calcasieu Lake and over the swamps and marshland around it. ADCIRC captured the flood wave as it inundated; for example, note the gradients to the southwest of Calcasieu Lake, where the water elevation decreased from 11 feet to 4 feet at the front of the wave. A similar gradient was visible along the coast as the surge moved inland. The gradient was well-defined as shown on Figure 329, but it was only because of the resolution in ADCIRC that this gradient was possible.

As shown on Figures 330 and 331, time is advanced forward to 10:00 UTC on September 24, 2005. Figure 330 shows the ADCIRC elevation contours and wind vectors for Southwestern Louisiana. Note the extent of the storm surge in Vermilion Bay, which is well to the east of where Hurricane Rita made landfall. The water elevation was 8 feet or higher in most of Vermilion Bay and the region to its northwest. This surge was heading toward Abbeville, but it was dampened by the marshes and farmland between Vermilion Bay and Abbeville. Figure 331 shows the ADCIRC elevation contours and wind vectors for Southeastern Louisiana. In this region, the winds continued to blow to the northwest, and the magnitudes and locations of the storm surge had not changed significantly. About 9 feet of surge built against the highway levees to the southeast of New Orleans, and about 6 feet of surge built against the levees to the southeast of Houma, Louisiana.

As shown on Figures 332 and 333, time is advanced forward to 11:00 UTC on September 24, 2005. These figures represent the system about 3 hours after landfall.

On Figure 332, note the extent of the flooding. Calcasieu Lake had been filled in with surge to the point where its natural shoreline is not immediately distinguishable in the image from its inundated surroundings. Sabine Lake was slowly filling via surge moving from the Gulf of Mexico through Sabine Pass, but overland surge from the east was also flowing into the lake. A black line of extreme gradient is visible on the south side of Grand Lake, where 4 feet of surge was flowing into a lake with a level currently 2 feet below sea level.

It is important to note the surge that propagated up the Calcasieu Shipping Channel to the north of Calcasieu Lake. The overland surge had not reached this far north, but surge moved up this system of interconnected channels and lakes. This system was added specifically to model the region around the cities of Sulphur and Lake Charles, Louisiana. This hydraulic connectivity allowed the surge to propagate well north of Calcasieu Lake and toward Lake Charles; without this additional resolution, this component of the storm surge would not be modeled correctly.

Figures 334 and 335 represent the system at 12:00 UTC on September 24, 2005, or about 4 hours after Hurricane Rita made landfall. Figure 335 shows the ADCIRC elevation contours and wind vectors for Southwestern Louisiana. At this point in the storm, the winds had shifted to the north over much of this region and to the northeast over Sabine Lake. These winds pushed surge up all four of the water bodies, but most notable Calcasieu Lake and Vermilion Bay, where the storm surge was 8 feet or more above NAVD88 (2004.65). Figure 335 shows the ADCIRC elevation contours and wind vectors for Southeastern Louisiana, where the storm surge was finally beginning to recede. The surge elevation had decreased to less than 9 feet in the region to the southeast of New Orleans. The surge was smaller throughout the region, including in the open Gulf of Mexico outside of the barrier islands, where the water elevations were less than 1 to 2 feet above NAVD88 (2004.65).

Figures 336 and 337 show the system at 15:00 UTC on September 24, 2005, or about 7 hours after landfall. On Figure 336, the surge had inundated the majority of Southwestern Louisiana. For Calcasieu Lake and its immediate surroundings, the water elevation was about 6 feet. It would be 6 feet in Grand Lake, too, except the surge was still filling the lake after it was partially emptied in the preliminary stages of the storm. Note that Sabine Lake was filling from the north side; more surge was flowing through the GIWW and over land than was entering from Sabine Pass in the south. The hurricane winds and the momentum of the surge allowed it to inundate a little more of the region, but the water began to drain within the next few hours. As shown on Figure 337, in Southeastern Louisiana the winds had shifted to the north, which was slowing down the recession of the storm surge. More than 4 feet of surge continued to inundate large portions of Southern Louisiana. More than 8 feet of surge continued to

be held against the levees to the southeast of New Orleans. However, the overall flooding was not as severe as it was in earlier stages of the storm.

Figures 338 and 339 show the system at 18:00 UTC on September 24, 2005, or about 10 hours after Hurricane Rita made landfall. Figure 338 shows Southwestern Louisiana, where significant overland flooding continued even though the water elevations in the Gulf of Mexico had returned to their normal levels. The hurricane winds had shifted to the northeast, and they continued to push the maximum surge through Calcasieu Lake and into the regions to its north. The northern parts of Calcasieu Lake had 7 feet of surge, and overland surge of 9 feet or more was inundating the surrounding region. In Sabine Lake, the northeast winds maintained a gradient from southwest to northeast because the winds were balanced by a surface gradient that would otherwise drive water to the southeast and through Sabine Pass. Figure 339 shows Southeastern Louisiana, where the same behavior was observed; the surge was slowly receding into the Gulf, which had already normalized. A storm surge of 7 feet continued to be blown against the highway levees near New Orleans. However, the wind speeds decreased enough to allow surge to begin receding into the Gulf of Mexico.

Figures 340 and 341 show the system at 21:00 UTC on September 24, 2005, or about 13 hours after landfall. The system continued to normalize. On Figure 340, the northeast winds tried to push surge up the Calcasieu Shipping Channel toward Lake Charles, Louisiana, but the water elevations continued to decrease as water receded back through Calcasieu Lake and into the Gulf of Mexico. On Figure 341, the observation is similar in Southeastern Louisiana; a significant amount of flooding existed, but it was noticeably less severe than in earlier stages of the storm. The floodwaters were receding.

Thus, the progression of Hurricane Rita as represented by the ADCIRC water elevations reveals interesting behavior in Southern Louisiana. In the southwest, where the hurricane made landfall, drawdown was not observed in the Gulf of Mexico in the hours preceding the storm. Instead, the westward winds forced water out of the lakes and bays in that region and into the marshes and bayou in the surrounding area. Then, when Hurricane Rita made landfall, a 15-foot surge of water hit the coastline south of Calcasieu Lake. This storm surge drove water up the lake and through the Calcasieu Shipping Channel to the Lake Charles area. In Sabine Lake, water was pushed out Sabine Pass before the storm, and then the northeast winds after the storm prevented water from rushing back into Sabine Lake. In the southeast, the west and northwest winds pushed water against the Mississippi River levees in Plaquemines Parish and then up to the highway levees southeast of New Orleans, where 9 feet of surge remained pressed against those levees for several hours during the storm. In addition, a significant amount of water was driven into Lake Pontchartrain. Not only

did Hurricane Rita inundate Southwestern Louisiana where it made landfall, but it also flooded significant parts of Southeastern Louisiana near New Orleans.

The third progression of time snaps is for ADCIRC velocity contours and vectors. Information will be presented from the same 14 time snaps as in the previous sections, and for the same two regions that cover Southwestern and Southeastern Louisiana. This progression through Hurricane Rita will show that the maximum water velocities were confined to natural and manmade channels, where large flows moved at large velocities. Large velocities were also associated with the overtopping of the low-lying Chandeleur Islands. However, significant velocities also occurred over regions within the Gulf itself, corresponding well with the regions of maximum wind velocities. Wind-driven currents tend to be more significant when the wind direction is not directed onshore. Finally, currents flowing down unconstrained surface water elevation gradients tend to occur, especially at the time of peak surge at the shore.

Figures 342 and 343 show the system at 12:00 UTC on September 23, 2005, or about 20 hours before landfall of Hurricane Rita. Figure 342 shows Southwestern Louisiana, where the hurricane had not yet had an impact on the water velocities. The eye is not shown on the figure; it is farther south. As shown in the lower right portion of the figure, its impact was beginning to be felt, with the velocities already above 3 feet/second. However, the velocities were less than 3 feet/second throughout the rest of that region. The story is different on Figure 343, which shows Southeastern Louisiana. In addition to the larger velocities near Terrebonne Bay shown in the lower left of this figure, the larger velocities also occurred in Southwest Pass, in the Gulf of Mexico as water bends around the delta, over the Chandeleur Islands, and in the Rigolets as water was driven into Lake Pontchartrain. It was in these exchanges where the maximum velocities occurred, as storm surge was pushed through conduits that are accustomed to handling large flows.

Figures 344 and 345 show the system at 18:00 UTC on September 23, 2005, or about 14 hours before landfall. Figure 344 shows Southwestern Louisiana, where the large velocities associated with the hurricane were apparent. The green contoured areas had velocities of about 5 feet/second that were being pushed northwest toward the coast. Figure 345 shows Southeastern Louisiana, where the regions discussed above continued to handle flow with large velocities. The velocities were greater than 3 feet/second in Southwest Pass and over the Chandeleur Islands, and the velocities were even greater in the Gulf of Mexico around the Mississippi River delta and in the exchange between the two lakes.

Figures 346 and 347 show the system at 00:00 UTC on September 24, 2005, or less than 8 hours before landfall. A significant region in the Gulf of Mexico contained water velocities with magnitudes of 7 feet/second or greater. Note that this region corresponds

to the region where the maximum winds occurred, northeast of the eye itself. These large winds were pushing the water around in the Gulf of Mexico. Note that these winds were not directed toward the shore and therefore were effective in moving the water along with the wind. The behavior was different in Southeastern Louisiana, as shown on Figure 347. Note that the maximum surge in this region occurred along the levees in Plaquemines Parish and the highways southeast of New Orleans. However, the velocities along those levees were relatively small. Because the levees stop the flow, the currents were modest and the surge built up. The maximum velocities occurred in other parts of the region, as discussed above.

Figures 348 and 349 show the system at 03:00 UTC on September 24, 2005, or about 5 hours before landfall of Hurricane Rita. In Southwestern Louisiana, as shown on Figure 348, the surge continued to move toward the shore. The maximum velocities were about 7 feet/second as the water moved over the shelf; they increased when the surge approached the coastline. Note the large velocities in Vermilion Bay caused by water being pushed into regions that had been drained partially by the hurricane winds earlier in the storm. However, because currents were becoming more energetic in western Louisiana as the hurricane approached landfall, they became less energetic in eastern Louisiana as is shown on Figures 348 and 349, respectively. The maximum velocities were already beginning to die down in this region. Southwest Pass velocities decreased to less than 3 feet/second. In other places, such as the Chandeleur Islands and the Gulf around the delta, the velocities were still greater than 3 feet/second, but decreasing in time.

Figures 350 and 351 show the system at 06:00 UTC on September 24, 2005, or less than 2 hours before Hurricane Rita made landfall. Note the velocity magnitudes in Southwestern Louisiana, as shown on Figure 350. As the surge approached the coastline, the maximum velocities increased to 8 feet/second or greater. Again, note that the region of maximum velocities corresponds well with the region of maximum winds; the water was still being pushed around. As shown on Figure 351, not much had changed in Southeastern Louisiana. As shown in the progression of water elevations, once the surge built up against the levees in Southeastern Louisiana, it remained there throughout much of the storm. Thus, a plot of ADCIRC water velocities shows that most of the velocities were relatively small and on the order of 1 to 2 feet/second.

Figures 352 and 353 show the system at 07:00 UTC on September 24, 2005, or less than 1 hour before landfall. As shown on Figure 352, the velocities in the Gulf of Mexico had already begun to diminish; the maximum velocity in the Gulf of Mexico was 8 feet/second or less. Conversely, the velocity magnitudes increased in Calcasieu Pass and in the southern part of Calcasieu Lake as the storm surge began to pour over and through State Highway 82 and into the lake. Also note that the velocities in the exchange between the Gulf of Mexico and Vermilion Bay increased as surge flowed

around Marsh Island and into the bay. As shown on Figure 353, the only significant velocities occurred in the exchange between Lake Pontchartrain and Lake Borgne and in the Gulf of Mexico as the flow curved around the Mississippi River delta.

Figures 354 and 355 show the system at 08:00 UTC on September 24, 2005, or just after landfall. As shown on Figure 354, the velocities had already decreased significantly. The velocities in the Gulf of Mexico were about 6 feet/second or less, and the region of noticeable velocities had decreased in size. The winds in the most intense part of the storm were blowing directly toward the shore where the flow was slowed by the roads, topography, and surface roughness. Therefore, maximum currents were no longer associated with a direct pushing process by the maximum winds. Instead, the highest currents were to the west down the surface water elevation gradient that occurred to the west. Larger velocities are also visible as a yellow line in the southern part of Calcasieu Lake. The storm surge was making its way over and through the thin strip of land between Calcasieu Lake and the Gulf of Mexico. The larger velocities occurred at the south edge of the lake. As shown on Figure 355, only a few regions exhibited velocities with magnitudes greater than 3 feet/second, as discussed above.

Figures 356 and 357 show the system at 09:00 UTC on September 24, 2005, or more than 1 hour after the hurricane made landfall. Figure 356 shows Southwestern Louisiana. The larger velocities in Calcasieu Lake persisted as storm surge continued to pour into the southern part of the lake, down a strong surface gradient, and in addition pushed by southerly winds. Also note the large velocities in Sabine Pass, where the winds shifted to allow surge to penetrate into Sabine Lake. Significant velocities also occurred southeast of White Lake and in Vermilion Bay and Cote Blanche Bay. In all three cases, water flowed into existing bodies of water; for White Lake, it flowed over State Highway 82, whereas for the bays it flowed from the Gulf of Mexico. This behavior created water velocities of 5 feet/second or greater in these regions. Figure 357 shows Southeastern Louisiana, where the only points of interest remain the exchange between Lake Pontchartrain and Lake Borgne and the Mississippi River delta. The maximum surge in this region was being pushed against the highway levees to the southeast of New Orleans, but it was not flowing with a large velocity.

Figures 358 and 359 show the system at 10:00 UTC on September 24, 2005, or about 2 hours after landfall. As shown on Figure 358, the velocities in Calcasieu Lake had decreased, but the water continued to flow at velocities of 5 feet/second or greater throughout much of the lake. Note the behavior in Sabine Lake, where surge flowed through Sabine Pass at large velocities and then pushed north through the lake. The velocities in Sabine Pass reached about 9 feet/second. As shown on Figure 359, only a few regions exhibit velocities with magnitudes greater than 3 feet/second, as discussed above.

IDS 2

Figures 360 and 361 show the system at 11:00 UTC on September 24, 2005, or about 3 hours after Hurricane Rita made landfall. Figure 360 shows Southwestern Louisiana, where the velocities began to die down. Large velocities persisted in Sabine Pass, but the line of large velocities along the south edge of Calcasieu Lake disappeared. Instead, water moved upward through Sabine Lake and Calcasieu Lake at 5 feet/second or less. Surge continued to pour into the south side of White Lake. However, the behavior in and around Vermilion Bay had been diminished, so that the velocities were on the order of 1-2 feet/second. As shown on Figure 361, the larger velocities persisted in the exchange between Lake Pontchartrain and Lake Borgne and around the Mississippi River delta.

Figures 362 and 363 show the system at 12:00 UTC on September 24, 2005, or more than 4 hours after landfall of Hurricane Rita. In Southwestern Louisiana, as shown on Figure 362, the velocities had decreased significantly. Only in Sabine Pass were the velocities greater than 7 feet/second, and only in Sabine Lake were the velocities greater than 4 feet/second. Throughout the rest of the domain, including Calcasieu Lake, the velocities decreased as the inundation ended and the surge began to recede.

Figures 364 and 365 show the system at 15:00 UTC on September 24, 2005, or about 7 hours after landfall. Figure 364 shows Southwestern Louisiana, where the velocity magnitudes decreased further. Only the Calcasieu Shipping Channel in the center of Calcasieu Lake had velocities greater than 3 feet/second; the rest of the lake had velocities that are smaller. Even Sabine Lake only had velocities greater than 3 feet/second in the southwest portion of the lake. The maximum velocities were occurring outside Sabine Pass, in the Gulf of Mexico, as the water in the Gulf moved across the deeper shipping channel. Figure 365 shows Southeastern Louisiana. Note that the velocities decreased in the exchange between Lake Pontchartrain and Lake Borgne, so that the exchange is not immediately distinguishable on the figure from the surrounding topography. Velocities greater than 3 feet/second did exist in this region, most notable near the Mississippi River delta and north of the Chandeleur Islands.

Figures 366 and 367 show the system at 18:00 UTC on September 24, 2005, or about 10 hours after landfall, and Figures 368 and 391 show the system at 21:00 UTC on September 24, 2005, or about 13 hours after landfall. The behavior in these two time snaps was similar. In Southwestern Louisiana, the only significant velocities occurred within known channels, such as Sabine Pass, the Calcasieu Shipping Channel, and the exchange between Vermilion Bay and the Gulf of Mexico. The storm surge was receding, and thus flowing through these channels to the Gulf of Mexico. In Southeastern Louisiana, the only significant velocities occurred as the flow was moving around land structures, such as the Mississippi River delta or the Chandeleur Islands.

Thus, the maximum ADCIRC velocities occurred in channels in Southwestern Louisiana. Sabine Pass, the Calcasieu Shipping Channel, and other conduits carried the most flow at the highest velocities. In addition, large water velocities were observed as surge flowed off of shallow land, down steep surface water elevation gradients, and into existing bodies of water. This behavior was most significant at the south shore of Calcasieu Lake, where the surge flowed into the lake after inundating State Highway 82 and the thin strip of land between the lake and the Gulf of Mexico. It was also significant near other lakes, including White Lake, where storm surge re-entered a natural body of water after flowing overland.

However, large velocities were also observed in the Gulf of Mexico itself. The strong winds on the northeast side of Hurricane Rita blew water around a circular trajectory in the Gulf of Mexico. When these winds were directed onshore, as they were when Rita made landfall and as they were in the eastern part of the state, water piled up and developed a significant mound of water. Finally, water also ran down steep surface water elevation gradients once water had piled up against the coast, both to the west along the shore and to the north inland.

Figures 370 and 371 show the maximum elevation contours for Southwestern and Southeastern Louisiana, respectively. On Figure 370, note that the maximum elevation was about 15 feet above NAVD88 (2004.65), and it occurred along the coastline to the south of Calcasieu Lake. For the most part, elevations decreased with increased distance from where the hurricane made landfall. However, there were some local maximums that are worth discussing. First, note the elevations on the north side of Calcasieu Lake and in the Lake Charles area. Water that was pushed by the hurricane winds through Calcasieu Lake was able to make its way up the Calcasieu Shipping Channel and over the surrounding land. Then it built up against the natural topography or the highways in this region. Second, note the elevations on the north side of Vermillion Bay. In this region, the maximum elevations were about 9 feet above NAVD88 (2004.65) or slightly greater, but they decrease significantly over land. As noted below, the HWMs in this region indicate that the storm surge reached 12 feet above NAVD88.

On Figure 371, note that the maximum elevation is about 10 feet, and it occurred against the highway levees to the southeast of New Orleans. As discussed above, the hurricane winds pushed surge onto the Mississippi-Alabama shelf where it was held by the Mississippi River levees, the levees of metropolitan New Orleans, and the topography of the region. The surge levels remained fairly steady throughout much of the storm. In addition, significant amounts of water were pushed into English Turn and the funnel that is defined by the confluence of the MRGO and GIWW and the adjacent levees. Furthermore the regional surface water elevation gradients and regional winds between Lake Borgne and Lake Pontchartrain as well as between Lake Pontchartrain and

Lake Maurepas drove a substantial volume of water into Lake Pontchartrain and Lake Maurepas (water levels increased to 6 feet NAVD88 (2004.65)). However, there were some local maximums in other regions, and much of the domain was inundated by 4 feet or more of surge. Hurricane Rita made landfall in Southwestern Louisiana, but its effects were also significant in the southeastern part of the state.

Figures 372 and 373 show the maximum ADCIRC velocity contours for Southwestern and Southeastern Louisiana, respectively. Note that the contours in these figures are not smooth because these maximum velocities were sampled at every hour during the storm, instead of every time step as for the maximum elevations. Nonetheless, they give an adequate representation of the velocity behavior during Hurricane Rita. On Figure 372, note that the velocities were greater than 7 feet/second in large portions of the Gulf of Mexico as the hurricane approached the coastline. As was discussed above, the hurricane winds pushed the water along with the winds, and the largest velocities correspond well with the largest winds. However, the maximum velocities occurred in channels along the coastline, including Sabine Pass and the Calcasieu Shipping Channel, where the velocity reached 9 feet/second.

On Figure 373, note that the region of maximum elevations does not correspond with the region of maximum velocities. The velocities along the highway/river levees to the south of New Orleans were small, on the order of 1 to 2 feet/second. Instead, the maximum velocities occurred where flow was bending around or flowing over complicated bathymetry, such as the Mississippi River and the Chandeleur Islands. The velocities in these regions reached 4 feet/second. Maximum velocities also occurred in the exchange between Lake Pontchartrain and Lake Borgne, as large flows were pushed into and then out of Lake Pontchartrain. High current speeds lined up with the winds did not develop in large regions because the water was very effectively stopped by the levees of Southeastern Louisiana, leading to the development of the substantial surge in the region.

3.3.4.6 System Validation using HWMs and Hydrographs

In the sections that follow, an error analysis will be performed on the Hurricane Rita hindcast simulation. Because Hurricane Rita happened recently, there is a wealth of information about the behavior and impact of the storm. This analysis will focus on two sets of data: a set of 62 HWMs distributed throughout Southern Louisiana, and a set of 23 hydrographs in Southwestern Louisiana.

The HWMs were obtained from FEMA/URS and cover all of Southern Louisiana, from Sabine Lake in the west to Lake Pontchartrain in the east. With one significant exception, the ADCIRC SL15 model produces maximum water elevations that match well with the HWMs. In the region around Calcasieu Lake, where the hurricane made

IDS 2

landfall, the match is excellent. The exception is around Vermilion Bay, where the measured peak values from the HWMs are significantly higher than the predicted peak values from ADCIRC. As will be discussed below, this behavior may be due to Vermilion Bay's highly viscous gelatinous-like waters.

The hydrographs were obtained from USGS and cover Southwestern Louisiana around Calcasieu Lake. Again, with rare exceptions, the ADCIRC SL15 model produces time histories of water elevations that match well with the hydrograph data. In the region around Calcasieu Lake itself, the matches are excellent. The exceptions are far to the north of Grand Lake, where the resolution in the ADCIRC SL15 model is not good enough to capture the connectivity that allows the surge to propagate so far inland. Improvements in resolution in this area would lead to improvements in the match to the USGS hydrographs.

The information for a total of 84 HWMs was obtained from FEMA/URS. These HWMs were deemed to be of good quality. Some of these marks fell outside the ADCIRC SL15 model or within elements that were not wetted during the Rita hindcast simulation. Thus, the analysis herein will focus on the 62 HWMs that were within the defined domain and wetted.

The errors at these 62 HWMs are shown on Figures 374 and 375. Southwestern Louisiana is shown on Figure 374, where Hurricane Rita made landfall along the coastline south of Calcasieu Lake. The errors at the HWMs around Calcasieu Lake are shown as green, indicating that the predicted peak values are within 1.5 feet of the measured peak values. Similar behavior is observed farther west, near Sabine Lake, where only two HWMs show errors of greater than 1.5 feet. Note that the worst behavior is in and around Vermilion Bay, where the ADCIRC SL15 model is under-predicting. This problem will be discussed below. Figure 375 shows the errors at the HWMs in Southeastern Louisiana. Note that all of the errors on the north side of Lake Pontchartrain are within the 1.5-foot error tolerance. There are only four points in the lower left of the figure, near Terrebonne Bay, that are slightly outside of this tolerance.

A scatter plot of the HWMs is shown on Figure 376. The measured HWM is plotted along the horizontal axis, and the predicted HWM from the ADCIRC SL15 model is plotted along the vertical axis. Thus, HWMs that fall below the one-to-one line are under-predicted by the ADCIRC SL15 model. If ADCIRC modeled perfectly every HWM, then all of the scatter points on Figure 376 would fall on the one-to-one line.

Overall, the slope of the best-fit line through all of the scatter points is 0.976, and the correlation is 0.74. These results are acceptable. Many of the worst HWMs are concentrated around Vermilion Bay; these marks are shown in red on Figure 376. Note

that all of these marks are being under-predicted, sometimes by as much as 3 feet. Not enough surge is reaching the north edge of Vermilion Bay in the ADCIRC SL15 model.

The problem may be that too much water is being allowed to flow out of Vermilion Bay in the early stages of the storm. As shown in the progression of ADCIRC water elevations above, the hurricane winds first blow southwestward, then westward, and finally northwestward over Vermilion Bay as Hurricane Rita makes landfall, and these winds push water out of the bay toward the Gulf and then into the marshes and land to the west and north. When the storm makes landfall, water has to flow back into the bay from the Gulf across a bay that has been partially dried before making its way north to where the HWMs are located. If the existing water in Vermilion Bay had remained there during the early stages of the hurricane, then the bay would have seen higher elevations. In fact, it may be realistic to assume that more water would remain in Vermilion Bay than is being modeled; the bay is filled with highly viscous muddy water which behaves like gelatin, and thus its contents will be less susceptible to being blown by hurricane winds (Sheremet et al., 2005; Stone et al., 2003). The under-prediction in Vermilion Bay is likely related to the very muddy waters in the bay due to the shallow waters combined with the high viscosity of the clay materials that comprise the floor of the bay and mix into the water column, creating a more dense liquid. Because of the shallow water column, high viscosity, and high frictional coefficients, the water in the bay may not be as easily blown about as a typical water column. Then, when the winds turn, the refilling and surge development process would be slower.

Thus, a best-fit line for all of the non-Vermilion Bay scatter points is also presented. The slope of its best-fit line is 1.05, and the correlation is 0.86. These results are acceptable, and they indicate that the ADCIRC SL15 model is modeling correctly Hurricane Rita in the rest of the domain. Note how all of the blue scatter points fall near or within the 1.5-foot error band.

Figure 377 shows the errors between the measured and predicted peak value, arranged in increments of 1.5 feet. Note that 33 of the 62 HWMs are modeled within 1.5 feet of their measured peak values. The HWMs that have errors greater than 1.5 feet are mainly under-predicted; they correspond to the locations near Vermilion Bay. Note that the average error is 1.02 feet of under-prediction.

To validate the ability of ADCIRC to simulate inundation and recession due to hurricane storm surge, ADCIRC model results were compared with hydrograph data published by the USGS for Hurricane Rita. The USGS placed a total of 23 water-level sensors along the Louisiana and Texas coastlines (McGee et al., 2006). A summary of the locations of these sensors is given in Table 29. The locations of these sensors are shown on Figure 378. In this section, the performance of ADCIRC in reproducing the hydrographs at these stations will be presented. The order in which the stations will be

IDS 2

presented will match the order in which the stations are listed in Table 29. Hydrographs for the 23 USGS stations are shown on Figures 379 and 380.

The first station is B15b, which is located along State Highway 82 on the north end of Sabine Pass. The Texas portion of this highway is not represented in the ADCIRC SL15 grid, and thus the station is placed in the middle of the simulated Sabine Pass, which is significantly wider in the model than in real life. This discrepancy between real and modeled phenomena explains part of the difference between the water levels produced by ADCIRC and the observed water levels. However, it should be noted that the water levels in the USGS hydrograph data are significantly higher than the HWMs in this region. As discussed above, the three HWMs in Sabine Pass and Sabine Lake range from 3.9 to 5.6 feet, and ADCIRC does a good job of reproducing the water levels at those locations. However, the maximum water level in the USGS hydrograph for Station B15b is 9.35 feet above NAVD88. ADCIRC shows the tides being affected by the surge and shows a small peak of 3.82 feet for the hurricane itself.

The next two stations did not wet in the ADCIRC SL15 model. The second station is LA2, which is located along State Highway 90 near Mermentau, Louisiana. This station is located along a tributary to the north of Lake Arthur. The storm surge must have worked its way up this tributary and gradually raised the water level. However, this behavior did not occur in ADCIRC, where the surge moved into Lake Arthur and beyond, but not to the extent that it reaches this station. The third station is LA3, which is located along State Highway 90 near Welsh, Louisiana. This station is similar to Station LA2 in that they both are located along tributaries north of Grand Lake. Station LA3 is located along a small tributary that eventually deposits into Mud Lake and then Grand Lake. Storm water slowly propagated up this tributary in the observations. However, this behavior also did not occur in ADCIRC. More resolution is needed along these tributaries in order to correctly model the storm surge from Hurricane Rita along the narrow channels along which these stations were placed.

The next two stations wetted, but in a different manner than what was observed. The fourth station is LA7, which is located along State Highway 14 at the northeast end of Lake Arthur. This station is much closer to the Gulf, and the hindcast does simulate storm surge reaching it. However, the peak surge reaches this station about 2 days earlier in ADCIRC than in the USGS hydrographs, and it causes a larger maximum elevation than was observed. As the storm recedes in the ADCIRC model, the elevation begins to match the recession portion of the USGS hydrograph, specifically at the beginning of September 27. The fifth station is LA8, which is located along State Highway 14 along a tributary north of Mud Lake and southeast of Hayes, Louisiana. This station is similar to LA7 in that it experiences a much earlier and stronger surge in the hindcast than was observed. The common thread is that both

stations lie on tributaries to the north of Grand Lake. More resolution is needed in these areas.

Beginning with the sixth station, the hydrographs match very well. The sixth station is LA9, which is located along State Highway 82 on a canal that connects While Lake and Vermilion Bay. The ADCIRC SL15 model resolves the canal and the highway and the model results match extremely well with the observed hydrograph data. The peak height is within a tenth of a foot, and the qualitative behavior of the inundation and recession is correct. There is a slight phase difference, in that the ADCIRC peak happens a few hours earlier than the USGS peak.

The seventh station is LA9b, which is located along State Highway 333 and the GIWW northwest of Vermilion Bay. This station is also represented well in ADCIRC, but only after it was moved southward so that it lies within the GIWW; this representation allows ADCIRC to accurately capture the timing of the inundation, peak, and recession. However, the peak in the ADCIRC model is more than 2 feet lower than the peak in the USGS hydrograph. This discrepancy may be due to the problems in Vermilion Bay related to HWMs, as discussed at the beginning of this section. The station is located to the northwest of Vermilion Bay, where more surge is needed in order to match the HWMs.

The eighth station is LA10, which is located along State Highway 82 to the southwest of Vermilion Bay. The ADCIRC results match the timing of the peak almost exactly; however, the ADCIRC peak is about 1.5 feet higher than the USGS peak. The overall match in other parts of the hydrograph, including both the inundation and recession periods, is excellent.

The ninth station is LA11, which is located along State Highway 82 on the north end of Lower Mud Lake. The highway and the tributary connecting Lower and Upper Mud Lakes are both resolved well in the ADCIRC SL15 model. The station was moved in ADCIRC so that it did not fall inside a levee and did fall inside the tributary. The ADCIRC model does a good job of matching the peak, the timing of the peak, and the recession.

The tenth station is LA12, which is located along State Highway 82 to the southeast of Calcasieu Lake. The ADCIRC SL15 model includes the highways in this region, but it does not include the small canal in which the station is located. The peak in the ADCIRC model is timed correctly, and the maximum water level from ADCIRC is only low by about 0.5 foot.

The 11th station is LC2a, which is located along US 210 in the city of Lake Charles, Louisiana, to the north of Calcasieu Lake. ADCIRC does an excellent job of simulating

IDS 2

the storm surge at this location; the timing and magnitude of the peak match well with the data from the USGS hydrographs. Too much drawdown occurs in the model, but the model does not damp the peak surge.

The 12th station is LC2b, which is located along State Highway 71 to the north of the city of Lake Charles, Louisiana. This station is located along a tributary that runs south into Calcasieu Lake, and its location was changed in the ADCIRC model to better represent this real-life connectivity. The modeled hydrograph matches well with the data from the USGS hydrograph. The timing and magnitude of the peak are excellent.

The 13th station is LC5, which is located along State Highway 384 and a tributary/channel to the east of Calcasieu Lake. ADCIRC matches the qualitative behavior at this station, including the hitch in the water levels during the inundation phase. The ADCIRC peak is about 1.5 feet higher than the USGS peak.

The 14th station is LC6a, which is located along State Highway 27 on the west side of Calcasieu Lake. This station was moved in the ADCIRC model so that it did not lie within a levee; it now lies on the eastern side of the levee, nearer to Calcasieu Lake. The timing of the peak is correct in ADCIRC, but the magnitude of the peak is high by more than 2 feet. This discrepancy may be due to a bridge to the west of the station that is not represented in ADCIRC. The water from the lake would propagate through this bridge, instead of building up against the levee, and thus the height of the peak would be lower. We need to resolve this opening in the ADCIRC model.

The 15th station is LC7, which is also located along State Highway 27 on the west side of Calcasieu Lake. ADCIRC does a reasonable job of matching the observed hydrograph data. The southwest corner of Calcasieu Lake is located to the south of this station; therefore, the storm surge propagates across the lake and toward this station without any problems.

The 16th station is LC8a, which is located along State Highway 82 on the south side of Calcasieu Lake in Cameron, Louisiana. ADCIRC matches the timing of the peak extremely well, and the peak is only low by about 0.3 foot.

The 17th station is LC8b, which is located along State Highway 27 to the east of Calcasieu Lake in what looks like a marsh. This station was moved in the ADCIRC model so that, instead of lying inside the levee, it is now represented as lying on the west side of the levee. This move made a significant change in the hydrograph. We now have excellent matches of both the timing and magnitude of the peak.

The 18th station is LC9, which is located along State Highway 27 to the southwest of Calcasieu Lake. This station was moved in the ADCIRC model so that it would be

IDS 2

represented to the southeast of the neighboring levee. The ADCIRC peak is 1 foot lower than the peak from the USGS hydrograph. However, there is a body of water to the southeast of this station that is not represented in the ADCIRC SL15 model. Placing a water body in that location would speed the propagation of the surge and cause the maximum surge elevation to happen earlier and with a greater magnitude, which would match the observed data.

The 19th station is LC11, which is located along State Highway 82 to the southwest of Calcasieu Lake and very near the Gulf of Mexico. This station was moved in the ADCIRC model so that it would be represented to the south of the neighboring levee. This move allowed ADCIRC to represent well the behavior at this station; the timing of the peak is excellent, and the magnitude of the ADCIRC peak is within 1 foot of the USGS peak.

The next two stations are located along Bayou Road to the southeast of Sabine Lake. The 20th station is LC12, which is located along Bayou Road to the southeast of Sabine Lake. The 21st station is LC13, which is located at the intersection of Bayou Road and State Highway 82 to the southeast of Sabine Lake. Station LC13 was moved in the ADCIRC model so that it would be represented to the south of the nearby levee. At both stations, the ADCIRC results are within 1 foot of the peak from the USGS hydrograph, and the timing is excellent.

The 22nd station is LF3, which is located near State Highway 167 in Abbeville, Louisiana. This station is far to the north of Vermilion, and thus surge does not reach this location in the ADCIRC model. It does not even wet in ADCIRC. To improve the behavior at this station, the drawdown problem in Vermilion Bay needs to be solved, and the stream that cuts through Abbeville and on which this station is located needs to be added.

The 23rd and final station is LF5, which is located along the same stream as LF3 but farther south and closer to Vermilion Bay. ADCIRC is within about 2 feet of the peak from the USGS hydrograph, but that makes a big difference in the recession stage. The behavior could be worse, because this station is north of Vermilion Bay and thus its surge is limited by the drawdown problems there.

The ADCIRC SL15 model does an excellent job of reproducing the behavior of Hurricane Rita, as measured by the set of 23 USGS hydrographs. ADCIRC models correctly the qualitative behavior at 18 stations, and its maximum water level is within 1.5 feet of the USGS maximum water level at 15 stations. At the handful of stations where ADCIRC does not model correctly the behavior, the problem is a lack of resolution. An improvement in resolution in a few key areas, including Sabine Pass and

the region to the north of Grand Lake, would correct the behavior at the first five stations. However, the overall behavior of the ADCIRC SL15 model is excellent.

3.4 Wind Forcing Model Sensitivities

3.4.1 Overview

The SL15 ADCIRC circulation model was validated by hindcasting Hurricanes Katrina and Rita using H*WIND/IOKA data-assimilated “best winds” generated by NOAA’s HRD and OWI’s kinematic wind models (Powell et al., 1998; <http://www.oceanweather.com>). Conversely, wind fields generated for the 152 synthetic storms for analysis of the surge level statistical surfaces were produced using OWI’s seven-layer PBL dynamic wind model. Winds are the dominant factor in the development and propagation of hurricane storm surge; thus, accurate wind fields for replication of historical events and simulation of potential future events are essential to the hydrodynamic modeling process.

In addition to the H*WIND/IOKA “best winds” based simulations, Hurricanes Katrina and Rita were also hindcast using the seven-layer PBL model. The PBL hindcast winds were generated in the same way as the 152 synthetic storms with the exception that historical track, pressure, and radius to maximum wind data were used as input. Comparisons of the resulting storm surge from the two sets of wind fields for both Katrina and Rita demonstrate that the use of the PBL-generated winds renders satisfactory results, although in general not as accurate as the H*WIND/IOKA simulations. A complete description of the “best winds” hindcasts for Hurricanes Katrina and Rita using H*WIND/IOKA winds can be found in Sections 3.3.3 and 3.3.4, respectively.

3.4.2 Hurricane Katrina

Results from the validation simulation of Hurricane Katrina using H*WIND/IOKA assimilated winds compare well to the results of a Hurricane Katrina simulation using the seven-layer PBL model. The simulations differ only in the specified wind fields, allowing the quantification of storm surge sensitivity caused by wind field variability. Figures 381 and 382 show the differences in maximum wind speed during the Katrina event. H*WIND/IOKA winds are as much as 16 knots faster to the east of the storm track, which passes over the Mississippi River delta, Lake Borgne, and the Pearl River Basin. PBL winds are higher nearly everywhere else as the storm approaches and makes landfall. PBL winds are as much as 17 knots higher in the vicinity of the eye of the storm and 25 knots higher on the west side of Lake Pontchartrain, although in general only 4 to 8 knots higher elsewhere.

Differences in maximum event surge levels can be seen on Figures 383 and 384. The maximum surge level for the H*WIND/IOKA simulation reached 27.5 feet, while the PBL simulation reached as high as 30.4 feet, both in Southwest Mississippi. The differences between the

computed maximum event surge levels are less than 2.5 feet throughout most of the domain and less than 1 foot over large portions of the domain. One exception is the Bonne Carré Spillway, where the PBL model exhibits surges of up to 4 feet higher, which are caused by higher northerly winds on the west side of Lake Pontchartrain. H*WIND/IOKA maximum surge values are more than 1.5 feet higher east of the eye of the storm as can be expected given the stronger H*WIND/IOKA winds in this region. There are also discrete areas in northern reaches of Lake Borgne, the Pearl River Basin, Barataria Bay, and west Lake Pontchartrain that display higher surges in the H*WIND/IOKA simulation although the maximum winds are less in those areas than the PBL simulation. These higher surges are due to differences in wind direction and duration of high winds that the maximum wind speed plots do not illustrate as well as the fact that localized response in a geometrically complex region is driven by regional scale winds. A comparison of the storm surge results for the two wind fields to each other shows that approximately 64 percent of the more than 2 million ADCIRC nodes in the production grid are within 0.5 foot and nearly 82 percent of the nodes are within 1 foot. A histogram showing the frequency in which surge level differences occurred can be seen on Figure 385.

Observed HWMs have also been compared to the solutions for both the H*WIND/IOKA and PBL simulations. Both solutions are compared to two sets of what were independently defined as reliable HWMs of excellent or good quality. One set of HWMs was compiled by the USACE (USACE, 2007) and the second was assembled by URS (URS, 2006d; URS, 2006e). The results can be seen on Figures 386 through 389, which plot modeled versus observed HWMs for the two wind fields and two different data sets. Points falling on the one-to-one line define a perfect match between the modeled and observed HWMs. Error statistics for the comparisons are summarized in Table 30.

Figure 386 shows the ADCIRC simulation forced by H*WIND/IOKA winds compared to the observed USACE HWMs. The overall agreement between the modeled and observed values is very good, with an R^2 value of 0.93, an average difference equal to 0.08 foot, and a standard deviation of 1.53 feet. A model standard deviation which accounts for the estimated error in the observations themselves equals 1.41 feet. A comparison of USACE HWMs to the solution with the PBL wind field solution is shown on Figure 387. The statistics of this comparison indicate that the PBL-driven high water levels have slightly larger error levels than the H*WIND/IOKA best winds with an R^2 value of 0.87, an average difference equal to 0.75 foot, and a standard deviation of 1.82 feet. The model standard deviation, which accounts for the estimated error in the observations themselves, now equals 1.72 feet. H*WIND/IOKA and PBL results compared to URS HWMs are presented on Figures 388 and 389, respectively. The agreement for both simulations is also very good although the best winds are slightly better than the PBL winds ($R^2=0.95$ and $R^2=0.93$, average errors of 0.61 foot and 1.16 feet, model to observed standard deviations of 1.42 feet and 1.75 feet, and model standard deviations equal to 1.34 feet and 1.67 feet, respectively). Although the PBL forced surge levels were not as accurate as the H*WIND/IOKA forced surge levels when compared to observed HWMs, in general the results were satisfactory for Hurricane Katrina.

3.4.3 Hurricane Rita

In this section, the storm surge resulting from H*WIND/IOKA assimilated winds and the seven-layer PBL model are analyzed for Hurricane Rita. Again, wind fields were the only difference in system forcing for the two scenarios; hence, the difference in wind field results in the difference in surge values. Figures 390 and 391 show the differences in maximum event wind speeds. PBL winds are up to 12 knots higher in the vicinity of the track, whereas the H*WIND/IOKA winds are higher in nearly all other locations. H*WIND/IOKA winds are as much as 10 knots faster in discrete locations, though generally only 2 to 6 knots faster.

Figures 392 and 393 present the differences in maximum event surge levels in Southwestern and Southeastern Louisiana, respectively. The maximum surge level for the best-estimate wind simulation reached 15.9 feet, while the PBL simulation reached as high as 17.4 feet, both southwest of Lake Calcasieu. PBL results generally displayed higher surges of 1.5 feet or less in the region in the vicinity of the storm landfall location. The H*WIND/IOKA winds produce higher surges elsewhere; however, including being higher by up to 1 foot in southern Lake Pontchartrain, 2.5 feet in the northeastern reaches of Plaquemines Parish in the vicinity of English Turn, and 1 foot in the Houma region. A small area southwest of Houma exhibits H*WIND/IOKA generated surges up to 3.5 feet higher than those of the PBL winds. This disparity is due to small differences in surge levels that caused considerably different overtopping rates over a raised feature; thus, there were large surge level differences on the protected side of the feature. A comparison of the storm surge results for the two wind fields to each other shows that approximately 70 percent of the more than 2 million ADCIRC nodes in the production grid are within 0.5 foot and nearly 87 percent of the nodes are within 1 foot. A histogram showing the frequency in which surge level differences occurred can be seen on Figure 394.

Comparisons of the observed FEMA HWMs to the solutions for both H*WIND/IOKA and PBL wind fields are shown on Figures 395 and 396 for Hurricane Rita. Both figures show results for two sets of HWMs. The first set of HWMs includes the available FEMA observations, while the second set of HWMs consists of only the FEMA-assessed locations outside of Vermilion Bay. In general, Vermilion Bay shows results that are worse than in other locations, likely due to the clay soils that result in gelatin-like suspension in the water in this bay (Huh et al., 1991).

On Figure 395, the ADCIRC validation solution, forced by H*WIND/IOKA winds, is compared to the observed HWMs. Statistical information for both the H*WIND/IOKA and PBL simulations can be found in Table 31. The overall agreement between the modeled and observed values is very good when excluding Vermilion Bay data, with an R^2 value of 0.87, an average difference equal to 0.04 foot, and a standard deviation of 1.11 feet. A model standard deviation, which accounts for the estimated error in the observations themselves, equals 0.91 foot. Overall agreement for all HWMs, including those located in Vermilion Bay, is also satisfactory, with an R^2 value of 0.76, an average error of -0.44 foot, and standard deviation of 1.33 feet. A model

IDS 2

standard deviation, which accounts for the estimated error in the observations themselves, equals 1.19 feet.

Figure 396 displays the solution forced by the PBL wind fields. The agreement is also very good ($R^2=0.79$) for HWMs outside of Vermilion Bay, and degrades when including Vermilion Bay in the HWMs ($R^2=0.60$). Average errors of -0.11 foot and -0.95 foot, standard deviations of 1.59 feet and 1.91 feet, and model standard deviations of 1.46 feet and 1.81 feet were determined for all the HWMs outside of Vermilion Bay and all HWMs, respectively. Although the PBL-forced surge levels were not as accurate as the H*WIND/IOKA forced surge levels, in general the results at HWMs were satisfactory for Hurricane Rita. This is especially the case when only HWMs outside of Vermilion Bay were considered.

3.5 Quality Assurance/Quality Control Procedures

3.5.1 Overview

This section discusses the post-processing procedures for the combined JCS FEMA/LACPR hurricane storm surge modeling of Southeastern Louisiana, including the QA/QC protocol used to check the results of the nearshore wave model, STWAVE, and the hydrodynamic storm surge model, ADCIRC. For each model, a limited review was performed on 100 percent of the production runs and a detailed review on more than 25 percent of the production runs. Storms for the detailed review were chosen prior to commencing production runs for the entire suite. A fixed number of both large and small storms were designated for the detailed review set, which were otherwise selected randomly. If the limited review indicated that there were problems with the solution, the detailed review procedures were implemented for these simulations as well in order to help identify the problem and to further check the simulation once the problem was fixed.

3.5.2 Nearshore Wave Model, STWAVE

3.5.2.1 *Post-processing*

For each hurricane scenario, STWAVE generates files for maximum predicted wave heights and mean wave periods over the course of the simulation, from which contour plots of the fields were produced. These fields were generated for each of the four STWAVE grids for Southeastern Louisiana described in Section 3.2.4, covering regions south of New Orleans, southeast of New Orleans, Lake Pontchartrain, and eastern Mississippi and Alabama and abbreviated S, SE, Pont, and MS-AL herein. The plotting software Generic Mapping Tool (GMT) was chosen to produce these static plots because it is platform independent, open source, and can be run in batch mode, which facilitates producing a large number of graphs associated with the probabilistic modeling of hurricane inundation. GMT provides its output in postscript format, which

was then converted to other output formats as necessary. For this work, .tiff was chosen initially, but due to the large file sizes, .png format was added later in the process.

A MATLAB routine was developed that converts the STWAVE grid into a format that was then used by GMT's plotting routines. Grid, storm, and variable identification information, as well as maximum wave height for each particular STWAVE grid over the course of the storm, was included. To the extent possible, all file manipulation and invoking of GMT software was done with Unix shell scripts written to minimize human error. Example maximum wave height and mean wave period plots can be found in Figures 397 and 398, respectively.

3.5.2.2 *Limited Review*

Once GMT graphs were generated, each plot was reviewed to ensure that the results were consistent with expected behavior. If anomalous behavior was found, the plots were regenerated to make sure that the problem was not a plotting or file specification error. If irregularities persisted in the second set of graphs, then the simulation was rerun in order to eliminate the possibility of run-time and file errors. In the case that the errors still persisted, the results were further scrutinized in order to debug the source of error, be it in the Fortran codes, the grid used, or the forcings applied to the system.

The STWAVE review process revealed two types of results that initiated more detailed review: 1) input file or model code errors and 2) local wave height features near the offshore model boundary. Errors relating to the application of incorrect input files such as an incorrect interpolation file or incorrect synchronization information led to maximum wave height and period plots with errors over the entire grid. Comparison of model results to storms with similar characteristics provided evidence of incorrect model execution. Figure 399, which shows an error in the wave field due to a grid interpolation problem, is an example of this. After correcting the problem, the wave field looked like that shown in Figure 397.

In addition, at the start of the production simulations, STWAVE QA/QC reviews discovered an error in the full-plane model code that caused incorrect model results in the Lake Pontchartrain grid, indicated by distinct banding in the wave height time series and maximum wave height plots. The STWAVE technical team corrected the error, which was related to the referencing of the bottom friction coefficient, and the model production team reran all affected storms with the corrected code.

The STWAVE QA/QC review process also documented instances of wave height anomalies near the offshore grid boundaries in the S, SE, and MS-AL grids. The wave height anomalies featured small local wave height variations near the boundary and only occurred for certain storm paths and intensities. Investigation by the STWAVE

technical team revealed that the wave height anomalies were related to either the boundary interpolation procedure or the wave growth algorithm within STWAVE. The nested wave modeling procedure required mapping of the offshore wave model (WAM) results onto the nearshore wave model (STWAVE) boundaries. The WAM results were interpolated to the STWAVE model at discrete points along the offshore boundary of the STWAVE grids. Technical review of the STWAVE model revealed proper implementation of the interpolation procedure within the limits of the model. Thus, the team searched earlier stages of the process to find that wave height anomalies occurred due to a non-constant WAM generated wave field along the STWAVE boundary. Nesting the regularly spaced WAM grid with STWAVE grids of varying orientations created a fluctuating offshore boundary condition in the STWAVE model. This was especially true when a large range of wave heights and high winds are present in the system. After further investigation by the STWAVE technical team, it was noted that the effects on the wave height were limited to the offshore region near the boundary and did not propagate into inland areas of the STWAVE model. Because of this, the team did not make any changes to the STWAVE model or the interpolation method between the offshore and nearshore grids.

The STWAVE QA/QC reviews also noticed distinct bands (presented as lines of discontinuity in the wave height contours) in the wave field near the offshore boundary for only certain storms. The wave height discontinuity was evident in the maximum wave height plots of the limited reviews and the animations created in the detailed review. STWAVE, a spectral wave model, requires frequency and direction bins to define the wave spectrum. Investigation of the wave discontinuity revealed it occurs at the point where the peak wave period increased by one period band (i.e., 13.5 to 14.9 seconds) in a region of strong winds. Ideally, period bands would have negligible ranges, such as 13.5 to 13.6. However, computational cost limitations inhibited the period band sizes for this suite of simulations. Thus, when a wave period increases by a large band value, such as 13.5 to 14.9, the discrete location within the STWAVE model sees a corresponding increase in energy. Within the STWAVE model, the wave period limits the amount of energy the spectrum can hold. Therefore, a change in the wind conditions can allow the peak period to increase by a discrete band and this gives the wave height an extra boost (due to a change in the energy limitation). Technical review of the STWAVE model indicated proper implementation of the energy transfer algorithm within the limits of the model. The effects on the wave height were limited to the offshore region and did not propagate into inland areas. Based on the review of STWAVE model execution within the production system, the STWAVE model code was not changed to address the local wave height anomalies observed in certain storms. The localized wave height differences did not propagate to inland areas and should not affect the wave-induced water level changes in nearshore areas.

3.5.2.2.1 Detailed Review

Following the limited review QA/QC procedures, a detailed review was performed for 25 percent of the storms, which were selected prior to model production. In addition, the QA/QC team conducted more extensive reviews for storms that had errors detected by the limited review process. For these reviews, the time evolution of wave height and period were plotted using the SMS (Surface Modeling System) software package. Production runs were set up to output results every 30 minutes over the course of approximately the last 2 days of simulation, resulting in movies consisting of 93 frames. Again, results were critically evaluated in order to ensure that the evolving fields were physically realistic. If anomalous behavior was suspected, the same error diagnostic procedure described above was followed: first checking for plotting errors, second looking for production run errors, third inspecting the codes, forcings, and grids in detail for errors. The detailed reviews allowed further examination of behaviors noticed in the limited reviews, such as the distinct banding and WAM boundary condition interpolation. In addition, the detailed reviews discovered other errors such as phasing issues between STWAVE and ADCIRC input, as well as coding errors for incorrect indexing of frictional coefficients. Figure 400 presents a snapshot of the SMS time evolution results showing wave heights in the SE STWAVE grid for storm 056.

3.5.3 Hydrodynamic Storm Surge Model, ADCIRC

3.5.3.1 *Post-processing*

As with STWAVE, plots of the maximum surge elevations were post-processed for each simulation. Since the large SL15 basin scale domain was designed in order to capture the development and propagation of storm surge onto the continental shelf and adjacent floodplain, results were examined over a range of scales. Results plotted at the basin scale lack detail in Southern Louisiana. Consequently, the global output files for the entire computational domain were parsed into a number of pre-defined zoom windows, which was done within the GMT software. Three views for each simulation of storms making landfall in Southeastern Louisiana were chosen, shown as “BE” box limits in Figure 401. The BW views are for Western Louisiana, which will be the subject of a future FEMA report utilizing the same modeling procedures. Latitudes and longitudes at the borders of these views are shown beneath the figure in Table 32. For both the east and west scenarios, the same extended view was utilized, as it captures a wide view of the results for all of Louisiana, Mississippi, Alabama, and part of Texas.

3.5.3.2 *Levee Treatment Validations under High Flow Conditions*

Prior to preparing the final plots, ADCIRC output was carefully checked for possible outliers in the reported maximum surge values. It became apparent during some early scenarios that when sub-grid scale raised features such as levees are massively overtopped (i.e., when the water column above the crest of a raised feature is significantly greater than the height of the feature itself), the weir algorithm in ADCIRC may result in localized perturbations in the elevation field. For these drowned features, the simplified momentum balance that forms the basis for the weir overflow equation is not sufficient for capturing the now two-dimensional flow field. Furthermore, the boundary flux forcing algorithm itself is locally only first order accurate, which can render systemic errors that become locally significant when the overtopping water column and associated flux rates are large. The systemic error manifests itself in an artificial wedge of water that builds up on both the front and back of the raised feature that is being massively overtopped. The effect is very local, no more than two elements away from the levee. In short, these unphysical results in the elevation field occur when weir formulations are applied to non-weir conditions. The best way to solve this problem is to apply the full equations of motion with the drowned features treated as a bathymetric “hump” in the domain. However, the current configuration of ADCIRC precludes a dynamic gridding algorithm that would allow such switching between pairs of levee nodes and a continuous mesh over the raised features during run time. Note that a future version of ADCIRC will have the option for a Discontinuous Galerkin solution of the shallow water equations, which is amenable for dynamic adaptation.

To minimize the local perturbations so that they do not artificially increase high water statistics, two options are available with the current version of ADCIRC. First, the local perturbations could be damped by increasing the lateral eddy viscosity and/or bottom friction to artificially high values, but this has the detrimental effect of over-damping the physical components of the solution away from the levee. Second, the solution could be selectively filtered. Selective filtering was the option that was chosen. Consequently, a post processing code was written which examined water surface elevations near all sub-grid scale raised features including levees roads and railroads, and filtered perturbations using a small bandwidth filter. Thus, the unphysical wedges of water near raised features were adjusted to reflect the physically accurate surge levels two element layers away from the features.

As a final step in the process before plotting, a code sorted the filtered maximum elevation field into bins and produced a histogram of maximum elevation values. This was analyzed for any remaining outliers, defined to be maximum elevation bins that contain fewer than 15 nodes and are more than 0.1 meter higher than the next nearest bin. If such nodes were found, then the maximum elevation field was inspected manually within the SMS software. If the node(s) are part of a smooth field, then

IDS 2

nothing was changed in the elevation field; if the node(s) was isolated and appeared to be a perturbation near a wetting front or a massively overtopped raised sub-grid scale feature, then the high value was smoothed using nearest neighbor averaging. About 10 percent of the scenarios needed this additional hand filtering of approximately one to ten nodes for each scenario.

To validate the filtering process, a second production grid was prepared that is identical to the original grid, except that the low-lying CSX railroad that runs from New Orleans, Louisiana, to Waveland, Mississippi, which was treated as an internal weir boundary in the original grid, was removed in the section between Lake Pontchartrain and Lake Borgne and through the Pearl River basin, and meshed over so that the full dynamic equations could be used to compute elevations and currents over the bathymetric rise associated with the railroad bed. The crown of this railroad lies approximately 4 feet above the surrounding topography and can be overtopped by as much as 30 feet of surge for large storms. Differences in the maximum water surface elevation between two sample simulations are shown in Figures 402 and 403. As can be seen, the results are nearly identical away from the railroad, differing at most by 0.3 foot for the high intensity storm (Figure 402). For the low intensity storm (Figure 403), there is no discernable difference away from the railroad. For the high intensity storm of Figure 402, the maximum differences are near the railroad itself, and even these, at about 1.0 foot maximum, are within acceptable tolerances. For the low intensity storm (Figure 403), the maximum difference near the railroad is on the order of 0.2 foot. These results indicate that the stated treatment of surge elevation perturbations near raised features that are massively overtopped is an accurate and reasonable means of approximating a physically accurate surge field.

3.5.3.3 *Limited Review*

Once results have been filtered for physically-unrealistic elevations, GMT plots were made for the maximum elevation field for the three zooms noted above; each was analyzed to make sure the resulting field was physically realistic. Note that GMT can produce maximum fields for radiation stresses, flow speed, etc., but these were not scrutinized on a regular basis unless the elevation field indicated some problems. If needed, time series of water levels at various stations were generated, although it was found early in the process that the maximum water surface maps served as good diagnostic tools. When anomalous behavior was detected, the same three step error diagnostic process that is described in the STWAVE section above was followed: first checks for plotting errors were made; second checks were made to ensure that the production runs followed the proper protocol; and third, if the errors still persisted, checks were made for runtime, forcing function and grid errors.

Four classes of problems were identified during the limited review process: runtime problems, incorrect file linkages, incorrect input data, and problems with the finite element grid design. The first type of problem typically occurred due to computer disk write failures or due to broken MPI communication between processors. This type of failure was catastrophic in that all or part of the output was missing. The solution was to re-run the sequence of simulations. The second class of problems was associated with either incorrectly placed grids or forcing function files. These failures would either be catastrophic or very obvious because forcing functions would typically have been incorrectly mapped, resulting in clearly incorrect solutions. The third class of problems was associated with incorrect input data or forcing function data. The main problem was river switching where the grid generation software switched the order of the Mississippi and Atchafalaya rivers, but it was not switched in the parameter file with the river flow data in it. Another problem encountered was that either levees or natural berms were not correctly defined. Figure 404 shows the artificial flooding of low lying areas due to poor resolution of the natural levees along the canals and waterways. After correcting the topography of the area, the water stays within the banks of the canal (until a hurricane storm surge arrives), as shown in Figure 405. Another issue encountered for a few slow moving storms was the synchronization of the winds and waves. This issue was apparent because the model ran into an end of an input file. All runs were then carefully checked for correct synchronization. Finally, the fourth class of problems was associated with local problems in the finite element mesh. This was related to elements that were simply too small to run with a one second time step and resulted in CFL (Courant-Friedrichs-Levy) related instabilities. These poorly formed elements were either very thin sliver elements with one side closer than 1 foot, or were simply small equilateral elements with sides less than 90 feet. The instabilities, of course, only occurred when these small elements were wetted. The elements were corrected and the production grid was updated with corrected elements. We note that for this type of error, all previous runs in the process were not affected since the corrected elements were never wetted in the previous simulations.

3.5.3.4 Detailed Review

As with the STWAVE process, a detailed review was performed for 25 percent of the storms in each storm set (the same scenarios for both STWAVE and ADCIRC received detailed reviews). In addition, the QA/QC team conducted more extensive reviews for storms that had errors detected by the limited review process. Again, the detailed review consisted of making a movie with the SMS software package of the time-dependent elevation and wind fields, which were then checked. Computed elevations at all nodes were used to plot the contour fields, but the wind field was sampled on a 30- by 30-kilometer grid so that the vector plots are discernible at this scale. A sample snapshot taken from the movie for storm 087 of the Southeast Louisiana 2007 scenario is shown in Figure 406. Note that SMS allows the user to zoom into any

area for closer inspection. It is noted that problems were always detected in the limited review stage and that no additional problems were detected in the detailed review stage. However, the detailed review did help identify the source of the problem in cases for which the limited review indicated a problem.

3.5.3.5 *Mass Balance*

Continuous Galerkin finite element models, a class in which the current production version of the ADCIRC hydrodynamic model falls, are globally mass conservative to machine precision. However, mass conservation on any given element is not exact and can experience a very small amount of mass loss/gain usually on an alternating "checkerboard" pattern. Consequently, if one inspects mass balance for a patch of elements, say those clustered around a node that forms the support for the associated finite element basis function, then local mass conservation errors are negligible.

The question of elemental conservation is somewhat clouded because there is not agreement in the literature as to the best way to check local mass conservation. With regard to finite element models, two competing criteria have emerged: one that advocates computing boundary fluxes with a method consistent with the weak weighted residual form of the governing equations, and a much more rigorous one that directly integrates the continuity equation over a control volume that coincides with a finite element or an entire cluster of finite elements. The advantage of the former is that it defines some sort of element edge based flux that ensures perfect mass conservation at the element level, although it is uncertain what the accuracy and consistency of this flux might be, and the value of this flux at nodal points is non-unique. The advantage of the latter is that it has been shown to be a good surrogate variable for discretization error and, as such, it can be used as an indicator for areas in need of grid refinement. The ADCIRC community has adopted the latter approach for computing mass balance errors because of the superior diagnostics it provides and due to its ability to determine if transport computations driven with these flows will result in localized mass losses/gains that result in artificial oscillations. With this tool, local mass balance errors have been effectively minimized and hence local truncation errors. We note that the optimal selection of τ_0 lowers local truncation errors and ensures optimal amplitude and phase accuracy.

Local mass conservation was checked at the element level for the operational grid to ensure that mass was correctly conserved at this level. Figure 407 provides a histogram of the errors for storm 002. The errors are expressed as a percent of the still water volume; they represent the average per time step error over the course of the simulation. As can be seen, over 93 percent of the domain has a relative error less than 0.01 percent in magnitude, and over 72 percent of the domain has a relative error less than

0.001 percent in magnitude. The highest errors that occur are near levees and near the wetting front (Figure 408), which is attributable to the use of simplified momentum balances in these regions (i.e., the weir discharge equation is used to compute fluxes passing over a levee in lieu of the full dynamic equations) or very thin layers of water that are prevalent as the wetting front propagates inland. The errors are within tolerances normally associated with modeling of such a complex dynamic system.

4.0 STORM CLIMATOLOGY AND STORM WIND-FIELD METHODOLOGY

4.1 Storm Climatology and Joint Probability Method Introduction

Over the last several months, a team of USACE, FEMA, NOAA, private sector, and academic researchers have been working toward the definition of a new system for estimating hurricane inundation probabilities.

4.1.1 The Joint Probability Method

The JPM was developed in the 1970s (Myers, 1975; Ho and Meyers, 1975) and subsequently extended by a number of investigators (Schwerdt et al., 1979; Ho et al., 1987) in an attempt to circumvent problems related to limited historical records. In this approach, information characterizing a small set of storm parameters was analyzed from a relatively broad geographic area. In applications of this method in the 1970s and 1980s, the JPM assumed that storm characteristics were constant along the entire section of coast from which the sample was drawn. Recent analyses suggest that this assumption is inconsistent with the actual distribution of hurricanes within the Gulf of Mexico.

The JPM used a set of parameters, including 1) central pressure; 2) radius of maximum wind speed; 3) storm forward speed; 4) storm landfall location; and 5) the angle of the storm track relative to the coast, to generate parametric wind fields. Furthermore, initial applications of the JPM assumed that the values of these five parameters varied only slowly in storms approaching the coast; therefore, the values of these parameters at landfall could be used to estimate the surge at the coast. Recent data show that this is not a good assumption (Figure 409). Kimball (2006) has shown that such decay is consistent with the intrusion of dry air into a hurricane during its approach to land. Other mechanisms for decay might include lack of energy production from parts of the hurricane already over land and increased drag in these areas. In any event, the evidence appears rather convincing that major hurricanes begin to decay before they make landfall, rather than only after landfall as previously assumed.

The conventional JPM used computer simulations of straight-line tracks with constant parametric wind fields to define the maximum surge value for selected combinations of the basic five storm parameters. Each of these maximum values was associated with a probability:

$$p(c_p, R_{\max}, v_f, \theta_l, x)$$

where

c_p is the central pressure,

R_{\max} is the radius of maximum wind speed

v_f is the forward velocity of the storm

θ_l is the angle of the track relative to the coast at landfall

x is the distance between the point of interest and the landfall location (25)

These probabilities were treated as discrete increments and the cumulative distribution function (CDF) was defined as:

$$F(x) = \sum p_{ijklm} \mid x_{ijklm} < x \quad (26)$$

where the subscripts denote the indices of the five parameters used to characterize the hurricanes.

Similar to the Empirical Simulation Technique (EST) (Borgman et al., 1992), this method is nonparametric; however, the conventional JPM included a range of parameter combinations that typically made extrapolation beyond the range of simulations unnecessary. This is an advantage over the conventional EST because it removes the need to assume a particular parametric form for the CDF in critical ranges of values.

Another potential advantage of the JPM over methods that depend heavily on historical storms was that the JPM considered storms that might happen, whereas the EST considered only storms that did happen. Assuming that, for the purpose of surge generation, storm characteristics can be represented adequately by the set of parameters used, it is possible to construct a Katrina-like storm (high intensity combined with large size) even if one has not happened previously. Likewise, it is possible to interpolate between re-curved storms such as Opal and Wilma to understand possible hurricane impacts in the Tampa area, even though neither of these storms produced significant surges in the Tampa area.

Perhaps the biggest controversy in JPM applications during the 1970s and 1980s centered on the definition of this five-dimension joint-probability function. The lack of data on historical storms prior to 1950 made it very difficult to derive representative distributions, even for extended sections of coast. For example, information on storm size (radius of maximum wind speed was lacking for most historical storms; consequently, a statistical estimate of r_{\max} (as a function of latitude and central pressure) was frequently substituted for actual values in the probability distribution. One wind field factor not considered in early JPM applications was the variable peakedness of hurricane wind fields. This term is represented in terms of the Holland B parameter in recent hurricane wind models and will be discussed in a subsequent section of this report.

One point of interest that should not be lost here is the importance of capturing the mean statistical behavior of any time-varying properties used in JPM applications. For example, surges derived from previous JPM applications, under the assumption of that storm characteristics near the coast were constant, may have been biased low because they were based on statistics at landfall. Because storms are consistently more intense off the coast (as shown on Figure 409), the modeled offshore storms are less intense than the actual offshore storms, under this assumption. Of course, some calibration was performed in these studies; therefore, this might have been somewhat accounted for via calibration procedures. Calibration tends to be somewhat storm specific; therefore, such calibration could still leave considerable residual bias in the final results.

4.1.2 JPM Measures of Variability in Expected Extremes

Most applications of the JPM only considered the definition of the mean CDF from the simulations, and little attention was paid to quantifying the dispersion (uncertainty) of what could happen within a particular time sample. This is potentially a major shortfall in the JPM as it was originally applied.

4.1.3 The Modified JPM (JPM-OS)

In this section, a method for estimating storm surges via a modified JPM will be developed, including estimation of some key climatological characteristics of hurricane tracks, intensities, and sizes. The term JPM-OS will be used here to denote this new methodology, because the underlying concept of this methodology is to provide a good estimate of the surges in as small a number of dimensions as possible, while retaining the effects of additional dimensions by including the ϵ term within the estimated CDF for surges. This approach will also attempt to minimize the number of runs required by improving methods used for interpolating between combinations of variables in different simulations.

4.1.3.1 Estimation of Spatially Varying Probabilities

In our new approach, the recommended treatment of geographic variation is to use the Chouinard et al. (1997) method for determining optimal spatial size for estimating hurricane statistics. In this method, the optimal size for spatial sampling is estimated in a manner that balances the opposing effects of spatial variability and uncertainties related to sample size. Although the final, definitive statistics are still being developed, a brief description of the method is included here, along with the preliminary results.

We begin by estimating the omni-directional statistical properties for storm frequency and intensity. Work performed by Gabriel Toro of Risk Engineering showed that the optimal spatial sample (kernel) size was in the range of 160 km for frequency analyses, but found that the optimal spatial size for intensities reached a plateau above about

200 km and did not drop off substantially at higher spatial kernel sizes. For purposes of this study, we took the basic data set of 22 hurricanes, which had central pressures less than 955 mb, shown on Figures 410 through 412, and defined their locations and intensities along the line shown on Figure 413. Although this line includes the west coast of the Florida peninsula for completeness within the analysis, results will only be presented for the section of coast west of this peninsula. This hurricane sample covers the interval 1941 through 2005. Section 4.4 provides a synopsis of some work supporting the selection of this period of record.

For our frequency analysis, we selected a “line-crossing” methodology, rather than an “area-crossing” (such as used in the Toro analysis presented on Figure 414) because the frequency of landfalling storms is inherently better posed in this context. The location of this line is shown on Figure 413 and distance in this system will be referenced in this report via an “increment number.” This “increment number” is based on integer values of the distance in degrees longitude at 29.5 degrees latitude, as explained in the caption on Figure 413.

After a number of sensitivity studies, we were able to show that the results for spatial samples for spatial kernels above 250 km or so did not vary markedly and settled on a sample size of ± 3 degrees (333 km) along this line. Results from this analysis are converted into an estimate of the frequency of hurricanes (which attain a minimum central pressure of 955 mb or less) making landfall within contiguous 1-degree increments along the reference line. Figure 415 gives the results of this analysis. As can be seen here, the “line-crossing” frequency estimate is consistent with the spatial-area frequency estimates obtained by Toro on Figure 414. It should be noted that the Toro analysis was based on 52 storms (all storms above Category 2 intensity within the Gulf of Mexico) rather than the 22-storm subset used here.

For each 1-degree increment along the coast, pressure differentials at the time of landfall for all storms making landfall within the ± 3 -degree distance along the reference line were used to define a best-fit (conditional) Gumbel distribution, i.e., the distribution of hurricane intensity given that a hurricane (with central pressure less than 955 mb) does occur. The Gumbel coefficients for the pressure differentials are shown on Figure 416. Combining the storm frequency estimates with these values, we can estimate the omnidirectional probability of intensity along the Gulf Coast at the time of landfall.

Figure 417 shows the (smoothed) distribution of the 50-year, 100-year, and 500-year central pressures based on the OWI information. Also shown on this figure are the estimates using the same derivation methodology, but based on the official NOAA values for landfalling central pressures. As can be seen here, the two methods yield very similar results, except for some divergence as the Louisiana-Texas border is approached. This curious aspect of the otherwise excellent agreement was found to be

related to a single spurious value in the OWI files for Hurricane Audrey. Once this was fixed, the region of good agreement extended across the entire region.

Interpretation of these values to “off-coast” values should refer to Figure 409, which suggests that the off-coast central pressures should be on the average around 10 to 15 mb lower than these values. For comparison, return periods based on independent analyses performed by David Levinson (National Climate Center) suggest that the 100-year central pressure offshore was in the range of 894 to 908 mb for a broad portion of the central Gulf of Mexico, which is reasonably in agreement with the values derived here, based on 1-degree increments of coast. However, in performing this comparison, it is essential to bear in mind that the estimates are appropriate for the recurrence within a 1-degree section of coastline. To compare the estimates on Figure 417 with values for the entire Gulf of Mexico, Peter Vickery performed an independent analysis of extremes based on 1) a statistical combination of all of the coastal segments and 2) an extremal analysis of NOAA’s landfalling pressures. As can be seen on Figure 418, the estimates of landfalling central pressures shown on Figure 417 can be used to provide a very consistent estimate for landfalling central pressures along the U.S. coast from Texas to the northwest Florida coast. And, as can be seen on Figure 419, a similar analysis for a single 1-degree increment shows, as expected, a little more randomness for this (smaller) set of points but a similar good general agreement in the tail of the distribution. Figure 420 shows a comparison of another independent check on the probability distribution based on a comparison to the results of Toro’s analysis performed for FEMA Region 4 along the Mississippi coast. These tests confirm the general estimation methodology used here is quite robust for hurricanes along the U.S. Gulf of Mexico coasts.

Several independent analyses over the last several months have shown that storm size is not independent of storm intensity; recently, Shen (2006) has shown that the potential intensity achievable by a hurricane is very sensitive to the size of a hurricane eye.

Figures 421 and 422 show the relationships between R_p and central pressure from OWI analyses of all storms exceeding Category 2 within the Gulf of Mexico at their time of maximum strength (52 storms – shown on Figure 421) and the 22-storm sample of landfalling storms (Figure 422). Equation 34 in Section 4.2 gives an estimate of the conditional probability of storm size as a function of central pressure. Figure 423 gives the mean angle of storm heading as a function of distance along the reference line shown on Figure 413, along with the standard deviation of the heading angles around this mean value. The direction convention used here is that a heading of due north represents an angle of zero degrees. Storms heading more westerly than due north will have positive angles, while storms heading more easterly will have negative angles. These estimates were derived by the same spatial averaging procedure used in deriving the central pressures and frequencies. A circular normal distribution is used here to

represent the storm heading probability distribution as a function of location along the reference line.

Figure 424 presents the estimated forward storm speed as a function of central pressure. This figure suggests that storm intensity and the forward speed of the storm are approximately independently distributed. However, if we plot forward storm speed as a function of storm heading at landfall for the 14-storm subset that intersect with the 29.5-degree latitude portion of the reference line on Figure 413 and for the entire 22-storm sample of landfalling storms (shown on Figures 425 and 426), we see that there is a tendency for higher forward speeds to be associated with lower storm heading angle (a correlation of 0.52 which is significant at the 0.05 level of significance with 21 degrees of freedom in a "Student's t" test). This is consistent with the expected behavior of re-curving storms that become swept up in stronger westerly circulations. The primary exception to the overall relationship is Hurricane Betsy, represented by the point in the upper right-hand corner of Figure 424. This storm moved very fast into the New Orleans area after crossing the lower portion of the Florida peninsula.

Putting all of the pieces of information together, for any point in our five-dimensional parameter space (retaining appropriate interrelationships among parameters), we see that the final estimates of joint probability densities can be written as:

$$p(c_p, R_p, v_f, \theta_l, x) = \Lambda_1 \cdot \Lambda_2 \cdot \Lambda_3 \cdot \Lambda_4 \cdot \Lambda_5$$

$$\Lambda_1 = p(c_p | x) = \frac{\partial F[a_0(x), a_1(x)]}{\partial c_p} = \frac{\partial}{\partial x} \left\{ \exp \left\{ -\exp \left[\frac{c_p - a_0(x)}{a_1(x)} \right] \right\} \right\} \text{ (Gumbel Distribution)}$$

$$\Lambda_2 = p(R_p | c_p) = \frac{1}{\sigma(\Delta P)\sqrt{2\pi}} e^{-\frac{(\bar{R}_p(\Delta P) - R_p)^2}{2\sigma^2(\Delta P)}}$$

$$\Lambda_3 = p(v_f | \theta_l) = \frac{1}{\sigma\sqrt{2\pi}} e^{-\frac{(\bar{v}_f(\theta_l) - v_f)^2}{2\sigma^2}}$$

$$\Lambda_4 = p(\theta_l | x) = \frac{1}{\sigma(x)\sqrt{2\pi}} e^{-\frac{(\bar{\theta}_l(x) - \theta_l)^2}{2\sigma^2(x)}}$$

$$\Lambda_5 = \Phi(x) \tag{27}$$

where the overbars denote average values of the dependent variable for a specified value of an independent variable in a regression equation, $a_0(x)$ and $a_1(x)$ are the Gumbel coefficients for the assumed Gumbel form of the central pressures, and $\Phi(x)$ is the

frequency of storms per year per specified distance along the coast (taken as 1 degree in examples presented here).

Figures 28, 427, and 428 show three sets of synthesized tracks that are being used in the ongoing New Orleans area study. These central tracks (Figure 28) essentially mimic the behavior of intense landfalling historical storms in the record, while preserving the geographic constraints related to land-sea boundaries. These storms preserve the historical pattern of the tracks better than simply shifting the same storm tracks east or west along the coast because they capture the observed variations in mean storm angles along the coast.

4.1.3.2 Estimation of the ϵ Term

Although there may be some degree of nonlinearity in the superposition of tides and storm surges, numerical experiments have shown that for the most part linear superposition provides a reasonable estimate of the (linearly) combined effects of tides and surges. Thus, the tidal component of the ϵ term, represents the percentage of time occupied by a given tidal stage and can be directly derived from available tidal information along the coast.

Careful analyses appropriate for formulating Holland B parameters for ocean response modeling have shown that this parameter falls primarily in the range of 1.1 to 1.6 offshore and 0.9 to 1.2 at the coast (Section 4.6). For Gulf of Mexico hurricanes, a mean value of 1.27 in offshore areas is assumed with a standard deviation of 0.15, while at the coast the corresponding mean and standard deviation is 1.0 and 0.10, respectively. Via numerical experiments, the maximum storm surge generated by a hurricane has been found to vary approximately linearly with variations in the Holland B parameter, at least for changes of the Holland B parameter in the range of 10 to 20 percent.

Off-coast track variations affect surges at the coast primarily through the effects of these track variations on wave fields, rather than by their effects on direct wind-driven surges. As noted previously, wave fields tend to integrate wind field inputs over 10s of hours; consequently, off-coast track variations tend to shift the wave fields somewhat while maintaining the general form and magnitude of the wave height contours. Near-coast radiation stresses are approximately proportional to gradients in wave energy fluxes, which, in turn, can be related to the square of the wave height gradient. In shallow water, where contributions of radiation stresses to surges are most important, wave heights tend to be depth limited. It is only in the incremental region, where larger waves make additional contributions due to increased energy losses offshore, that larger wave conditions affect the total wave setup at the coast. Numerical sensitivity studies suggest that once incident waves become much larger than about 10 meters, most of the additional energy loss is in depths that do not contribute very much to wave setup. For

this reason, plus the fact that in general the wave setup term tends to be only about 15 to 30 percent of the total surge, we expect the effect of storm track variations on wave setup at the coast to be fairly small (due to the fact that surge response is on a much faster scale than wave generation, where we noted that the “straight-track” approximation was not very good). We will assume that the deviations around the mean surge will be approximately Gaussian. A standard deviation of 20 percent of the calculated wave setup contributions to the total surge (determined by subtracting the direct wind-only surge from the total surge due to winds and waves combined) will be used within this distribution.

Model errors combined in calibration/verification runs of ADCIRC have shown that this combination of model and forcing in the Louisiana-Mississippi coastal area provides relatively unbiased results with a standard deviation in the range of 1.75 to 2.50 feet. Relative errors associated with the use of PBL winds increase the value of the standard deviation to 2.00 to 3.50 feet. This is not to surprising because the accuracy of HWMs (the primary measurements to which the model results are compare) are quite variable.

Combining all of these terms, under the assumption that they are each independently distributed, gives

$$p(\varepsilon) = \iiint \delta(\varepsilon_1 + \varepsilon_2 + \varepsilon_3 + \varepsilon_4 - \varepsilon) p(\varepsilon_1) p(\varepsilon_2) p(\varepsilon_3) p(\varepsilon_4) d\varepsilon_1 d\varepsilon_2 d\varepsilon_3 d\varepsilon_4 \quad (28)$$

Where:

- ε_1 is the deviation between a storm at a random tide phase and a zero tide level;
- ε_2 is the deviation created by variation of the Holland B parameter;
- ε_3 is the deviation created by variations in tracks approaching the coast; and
- ε_4 is the deviation created primarily by errors in models and grids.

Three of the terms, ε_1 , ε_3 and ε_4 , are treated here as though they are approximately independent of the magnitude of the surge, while the remaining term, ε_2 , has been found to depend essentially linearly with the magnitude of the surge. For a monochromatic tide, the tidal elevation distribution, ε_1 , is known to be bimodal distributed around its zero value; however, in nature, the effect of combining several tidal components with varying phases is to force the distribution toward a unimodal distribution. The probabilities of terms ε_3 and ε_4 are assumed to be normally distributed; thus, the probability distribution of the sum of these two terms will also be a normal distribution with the variance given by the sums of the individual variances of the two terms.

Figure 429 gives a numerical example of the combination of all four terms assuming a storm surge of 15 feet, as might be associated with a particular deterministic model execution based on a set of track and PBL parameters. As can be seen on this figure, the overall magnitude of these effects can add or subtract substantially to the total water depth. In this case, the distribution appears similar to a Gaussian distribution because it is dominated by the term with the largest variance (deviations due to the omission of the Holland B parameter); however, the other terms have been included within the integral for $p(\epsilon)$. Table 33 shows an example of the effect of adding this term on expected surge levels for selected return periods. In this example, a Poisson frequency of 1/16 was used in combination with a Gumbel distribution, with parameters $a_0 = 9.855$ and $a_1 = 3.63$. For this example, the effect of adding the ϵ term is less than 0.5 foot for return periods up to 175 years and only exceeds 1 foot at return periods greater than 400 years. However, for risk-based calculations, which often include very large return periods (1,000 to 10,000 years), this term can become as large as 2 to 3 feet, even for the case where the effects of all neglected factors are assumed to be distributed around a mean deviation of zero. The effect could of course be larger if the deviations were biased.

From Table 33 and the above discussion, we see that the effect of the ϵ term becomes much more pronounced at large return periods. Thus, older applications of the JPM that neglected this term were probably reasonably accurate at the 100-year return period, but were likely to have been progressively biased low at higher return periods. The important points to stress here are twofold. First, any neglect or suppression of natural variability in a procedure to estimate extremes will lead to some degree of underestimation of the estimated extremes, whether using a JPM or an EST approach; therefore, it is important to recognize and attempt to quantify all significant factors affecting surge heights at the coast. Second, to avoid making the number of dimensions in the JPM unmanageable, the estimated effects of the neglected factors contributing to extreme surges should be addressed statistically, such as we have done here via the addition of the ϵ term to the JPM integral.

4.1.3.3 Treatment of Subsidence and Sea Level Rise

Rather than treat subsidence and sea level rise within the ϵ term, it is simpler to include this in a separate analysis. For purposes of design, as a first approximation to the non-overtopping situations, estimates of subsidence and sea level rise can be added linearly to the expected surge levels. Thus (as a purely hypothetical scenario), if 2 feet of local subsidence is anticipated along with 1 foot of sea level rise over a design lifetime (say 100 years as an example), a levee design set for 20 feet would need to “evolve” to 23 feet in order to provide the same level of protection at the end of the design lifetime. Other options might be to overbuild the design at the outset to account for anticipated

subsidence and sea level rise. In either case, it will be critical to constantly monitor the changing water levels to ensure that the design level of protection is maintained.

4.1.3.4 *Sampling of Storm Parameters for the JPM-OS*

In the conventional JPM, each simulation was typically treated as representative of its entire discrete probability range (i.e., all of the probability for each multi-dimensional box centered on its mean position). In these applications, the computational burden was considerably less than what is considered appropriate for surge simulations today (see subsequent section on the computational effort recommended for today's applications). Even in the original JPM, however, a scaling relationship between the pressure differential of a storm and computed surge levels was used to reduce the number of computer runs. This relationship, based on theoretical considerations and confirmed numerically in several studies, shows that surges are linearly proportional to the pressure differential of a storm at all areas close to the area of maximum storm impact. This information can be used effectively to interpolate between two different numerical results within the JPM integral. Such an interpolation provides added resolution along the pressure differential axis in this integral, which is very important due to the highly nonlinear characteristics of the probability of pressure differentials $[P(\Delta P)]$.

In addition to the scaling relationship between surge levels and pressure differentials, the JPM-OS attempts to sample the parameter space in a fashion that can be used to estimate surges (develop the response surface) in an optimal manner. This method has been developed via hundreds of simulations on relatively straight coasts, as well as on coasts with other simple geometries, and is in the process of being extended to more complex coasts. It attempts to alleviate the need for very closely spaced parameter values in numerical simulations (essentially track spacing and number of storm sizes, forward speeds, and track angles considered), thereby potentially greatly reducing the total number of computer runs required for JPM execution. The initial set of runs for the New Orleans area consists of 152 hurricanes traveling along tracks shown on Figures 28, 427, and 428. To put this number of runs in perspective, because a major storm only affects each 1-degree section of coast once per 16 years and the section of coast being studied is only about 2.5 degrees, this number of hurricanes would only be expected in the simulated area every 853 years. Consequently, unless we have selected these storms in a very unrepresentative fashion, we expect this number of storms (combined with an accurate methodology for surge simulation) to provide a fairly accurate description of the general characteristics of hurricane surges at least up to the 500-year return period. A description of the parameters of these storms is given in Section 4.5, along with a discussion of some scaling relationships between storm parameters and surges that have been found in our numerical studies.

4.1.3.5 *Specification of Variations in Pre-landfalling Hurricanes*

Whereas the original JPM considered storm size, intensity, and wind field distribution to be constant in storms approaching the coast, the new JPM uses information from recent storms to estimate the rate of change of these parameters for pre-landfall conditions. In general, these trends show that storms tend to fill by about 10 to 15 mb (Figure 409), become slightly (15 to 30 percent) larger (Figure 430), and have less peaked wind speed distributions (Holland B parameter decreasing from about 1.27 to around 1.0) over the last 90 nautical miles of coastal water before landfall. Because all of our probabilities have been developed based on landfalling characteristics, the offshore characteristics must be estimated from a generalized transform:

$$p(\Delta P, R_p, v_f, \theta_l, x)_{\text{offshore}} = p(\Delta P, R_p, v_f, \theta_l, x)_{\text{landfall}} J^{-1} \quad (29)$$

where J is the Jacobian for the transform from nearshore to offshore conditions. However, because 1) storm heading during approach to the coast is relatively constant, 2) the forward speeds are assumed to be constant during approach to land, and 3) the points of intersection (x) are identical for each offshore and landfall case, the transform can be viewed in only two dimensions, ΔP and R_p . Details will be given in Section 4.5.

4.1.4 Summary

Some of the key issues addressed in this section, along with relevant conclusions, are as follows:

1. The JPM provides a sound method for estimating inundation probabilities. However, given the number of degrees of freedom in hurricane characteristics affecting coastal surges and the computational burdens associated with coastal surge simulations, it is critical to reduce the number of factors considered to a minimum, while maintaining sufficient detail to properly model hurricane wind fields for surge prediction.
2. After a discussion of various alternatives, it is recommended that the same five parameters used in older JPM studies (storm intensity, storm size, forward speed of the storm, angle of the storm track with the coast, and track location) be used to characterize storms for simulating coastal surges. With this number of dimensions within the JPM integral, it is essential to 1) allow these characteristics to exhibit observed variations during their approach to land, and 2) retain and quantify a statistical "error" term that adds the suppressed variability back into the estimated extremes. Previous applications of the JPM did not consider this term.

3. Similar to the EST, it is recommended that uncertainty in the stage-frequency relationships be estimated via re-sampling methods.
4. As will be discussed in Section 4.4 and as has been noted in many journal publications, it appears that a 40-year cycle is a dominant feature within the recent hurricane record. We have experienced one full “high-activity” portion of a cycle and about two-thirds of a second “high-activity” portion of a cycle. It is recommended that a comparable proportion of “low-activity” years be included within the record being used for estimating inundation probabilities. Following this logic, we will use the full “low-activity” interval (approximately 30 years) between the two recent “high-activity” intervals plus a period equivalent to two-thirds of the recent “low-activity” interval within our sample period. This yields 1941 through 2005 as our period of record for coastal inundation analyses.
5. The topic of future climatic variability has been dealt with in a recent manuscript by Resio and Orelup. In this manuscript, it is shown that the hurricane record within the Gulf of Mexico does not exhibit a strong secular trend, in contrast to the record in the Atlantic Basin. The Resio and Orelup manuscript showed that “high-activity” intervals dominated the extreme surge population for return periods greater than 50 years or so. As a sensitivity study, they investigated the consequences of a doubling of “high-activity” years, even though there is no evidence that such a doubling is imminent. Results of this study showed that such a climate scenario would produce about a 12 percent increase in surge levels at the 100-year level, with decreasing effects at longer return periods.
6. Historically, the storms that appear to have had the most impact on coastal areas within the Gulf of Mexico have all moved along the central paths shown on Figure 28. These storms include Rita, Ivan, Camille, and Katrina in the historical record from 1941 through 2005; thus, the set of tracks on this figure have been nicknamed the RICK-fan.
7. The JPM-OS represents an attempt to combine statistical information over an interval of the coastline in order to gain more confidence in information relevant to the definition of extreme surges at a point. This approach also allowed us to incorporate information on the general behavior of storms in coastal areas (such as storm decay and variations in storm size and the peakedness of the wind distribution along a transect) into our simulations of extreme events.

4.2 Expedient Estimation of Return Periods for Specific Historical Storms

On one hand, the most accurate characterization of the return period for a specific storm water level is to wait until the stage-frequency relationships have been developed and see where the water levels from that storm fall on this curve. Inspection of such an approach would show that water levels from a specific storm would fall at different return periods at different locations. A different albeit more approximate approach, which does not have to wait until the final results of simulations are complete, is

IDS 2

to treat the storm water level potential in terms of the primary parameters affecting peak surge levels, typically storm intensity, storm size, angle of approach to the coast, forward storm speed, the geometry of the coast, and the offshore bathymetric slope.

4.2.1 Application to Hurricane Katrina

Figure 431, taken from Irish et al. (submitted for journal publication), shows the dependence of peak surge on storm intensity (peripheral pressure minus central pressure) and size (scaling radius for the pressure field). These values were generated from ADCIRC simulations using the OWI PBL model for wind fields. In these runs, storms were held at constant intensity and size during the approach to the coast. This figure is appropriate for a very shallow offshore slope (1:10,000), found to be approximately representative of the continental shelf east of the Mississippi River in this area. Sensitivity studies of the effects of storm speed and storm approach angle showed that these factors were of secondary influence on surges at the coast, at least within the ranges of expected values for large, intense storms. Sensitivity studies also showed that although the coastal geometry in the New Orleans area (the presence of the Mississippi River delta and river levees) tends to modify local storm surge levels, this factor did not change the relative ranking of the different storms.

Assuming that we can neglect the secondary factors, then the relative ranking, and thus the return period for a specific event, can be deduced from a combination of Figure 431 and a specification of the joint probability structure of storm intensity and storm size. The estimation of the latter is a key part of the same methodology being used in the JPM-OS application in this area.

The frequency of storms along a coast has units of number of storms per year per length of coastline. For our application, we will assume that a storm within 0.5 degree longitude is the relevant parameter for our purpose here. This is equivalent to assuming that the surge within ± 0.5 degree remains sufficiently close to the peak value that can be considered approximately equal to the peak (within 10 percent). Although a continuous method can be used for this estimation method, the results were quite similar and the discretized method is easier to explain. Figure 413 shows a line along the Gulf of Mexico coastline that will be taken as the "sample line" for landfalling conditions in our analysis. A centered, running average of landfalling conditions over a distance of 6 degrees along this line was used to estimate the frequency of storms and to accumulate samples for extremal analysis within contiguous 1-degree (longitude; 29.5 degrees latitude) increments along the coast. The New Orleans area is located in Increment 7 along the coast in this scheme.

The storm sample used in this analysis is the 22-storm sample shown on Figures 410 through 412 (essentially all storms with central pressures less than 955 mb during their transit through the Gulf of Mexico since 1941). Eleven of these storms fell within ± 3 degrees of the center of the New Orleans section of coast. Because this is not a very large number, we restrict our analysis to

a two-parameter (Gumbel) distribution here. The conditional Gumbel distribution of hurricane pressure differential was found to be given by

$$F(\Delta p | hurricane) = e^{-e^{-z}} \quad (30)$$

Where F is the condition CDF (i.e., the expected CDF given a hurricane) and z are given by the best two-parameter fit:

$$z = \frac{\Delta p - a_0}{a_1} \quad (31)$$

Where a_0 and a_1 are the distribution parameters and Δp is the pressure differential. For Increment 7 along the coast, the value of a_0 and a_1 are 56.557 and 16.463, respectively. The frequency of occurrence of hurricanes for this coastal segment is 0.0486 per year per degree (or once per every 20.6 years or so). Because the contours on Figure 431 denote lines of equal surge, the probability of a storm capable of generating a storm surge equal to or greater than that produced by Hurricane Katrina can be estimated by the sum of the probabilities in regions A, B, and C, delineated by different R_p limits on Figure 432 or:

$$F(\eta) = \int A + \int B + \int C \quad (32)$$

It can be shown that all three of these integrals can be written in a common form:

$$\int (A, B, C) = \int_{R_1}^{R_2} \int_{\Delta p(R)}^{\infty} \frac{\partial F(\Delta p)}{\partial \Delta p} P(R_p | \Delta p) d\Delta p dR_p \quad (33)$$

where the limits of the first integral are made to match the region shown on Figure 432. The conditional probability for size is given by a Gaussian distribution of the form:

$$P(R_p | \Delta p) = \frac{1}{\sigma(\Delta p)\sqrt{2\pi}} e^{-\frac{x^2}{2}}$$

where

$$x = \left(\frac{R_p - \bar{R}_p(\Delta p)}{\sigma(\Delta p)} \right) \quad (34)$$

In this equation, a linear regression ($\bar{R}_p = 14. + 0.3 * (110. - \Delta p)$ with units for R_p and \bar{R}_p in nautical miles and units for Δp in mb implied) was used to represent the conditional mean for storm size and the standard deviation was taken as $\sigma(\Delta p) = 0.44 \bar{R}_p(\Delta p)$. The sum of all three integrals is 0.0518, which can be interpreted as slightly more than 1 hurricane in 20 can produce a surge of Katrina's level in the New Orleans area. When one is divided by the product of the two frequency parameters, it yields an estimate of 397.6 years for the return period of a storm capable of producing a surge of comparable magnitude to Katrina. For practical purposes, Katrina would seem to fall in the range of a 400-year storm, in terms of storm surge generation. It should be noted that the methodology described here pertains to the area of maximum surges within a storm; consequently, the surges at some distance from area of maximum surge will certainly not be 400-year surges for those points.

4.2.2 Application to Hurricane Rita

The same procedure outlined above, modified to consider the different offshore slope, was applied to Hurricane Rita, with a landfall in Increment 10 of our analysis. A slope of 1:1000, which is characteristic of the shelf region in the area west of the Mississippi River, was adopted in the idealized surge modeling referenced here. The return period for this storm from this analysis is 89.7 years. Again, for practical purposes, this can be taken to imply that Rita was somewhere in the neighborhood of a 90-year storm, in terms of storm surge.

4.3 Selection of Wind Model for Coastal Surge Estimation

Ocean response models for waves and surges require winds at a constant reference level with some suitable averaging interval (typically around 20 to 30 minutes) and a specified drag law to convert these winds into estimates of momentum fluxes from the atmosphere to the ocean. Two different models (Thompson and Cardone, 1996; Vickery et al., 2000) were investigated for application to coastal surge modeling as part of a general investigation of modeling for coastal inundation.

The dynamic (PBL) model of Thompson and Cardone (1996) has been selected for use in estimating hurricane wind fields. In older storms, the "best-estimate" wind fields will be virtually identical to the initial guess wind fields due to the lack of information available for assimilation into the PBL wind fields. Comparisons of OWI and Vickery PBL winds from Hurricane Katrina, along east-west and north-south transects through the center of the storm, to OWI's "best-estimate" winds are shown on Figures 433 and 434, respectively. Figure 435 shows a similar set of comparisons for both the east-west and north-south transects for Hurricane Betsy. As can be seen on these figures, OWI's PBL winds capture most of the broad-scale structure of the wind fields.

The Vickery PBL model does not perform as well as the OWI PBL model in comparisons with the OWI "best-estimate" winds. This is not too surprising, because the OWI "best-estimate" analysis is likely to have been considered in deriving the PBL parameters. The abrupt drop-off of wind speeds in the

Vickery wind is an artifact of the version of the Vickery code that was available for testing during the time of this comparison. This problem is being remedied and is not a property of the general solution capabilities inherent to the Vickery model.

Because the relaxation time for coastal surge is on the order of hours rather than 10s of hours, as for the generation of waves, offshore complexities of storm tracks tend to affect wave fields much more than they affect coastal surges. Because tracks of major storms tend to lack the complexity exhibited by minimal hurricanes and tropical storms and because wave generation tends to produce a wave field that represents the integrated effects of winds over many hours, the effect of track variation on wave fields should be rather minimal. It should also be recognized that PBL winds have long been shown to be capable of providing accurate wind field estimates for purposes of hindcasting waves in hurricanes (Cardone et al., 1976).

The use of PBL winds is also consistent with the approach of Vickery et al. (2000) or estimating wind hazards in U.S. coastal areas, which were found to provide very reasonable wind estimates when compared to both on-land and offshore wind observations. Given all of the problems associated with using historical wind fields with indefinite degrees of freedom in their formulation, it would seem that a very careful study of the differences between PBL-driven surges and "best-estimate"-driven surges should be undertaken for a small set of hurricanes before any clear advantage to using "best-estimate" wind fields for surge prediction can be claimed.

A very important improvement pertinent to PBL wind field estimation is the availability of carefully estimated size parameters for all historical storms (from OWI). These parameters were compiled specifically for driving ocean response models (e.g., wave and surge models) and allow improved estimation of the joint probability of intensity-size relationships in Gulf of Mexico hurricanes.

As a final element of this section, the Holland B parameter will be briefly described. This description is excerpted from the section on Meteorology in the Coastal Engineering Manual (Resio et al., 2002).

Myers (1954), Collins and Viehmann (1971), Schwerdt et al. (1979), and Holland (1980) all present descriptions and justifications of various parametric approaches to wind-field specification in tropical storms. Cardone et al. (1992) use a modified form of Chow's (1971) moving vortex model to specify winds with a gridded numerical model. However, because this numerical solution is driven only by a small set of parameters and assumes steady-state conditions, it produces results that are of similar form to those of parametric models. The Holland model differs from previous parametric models in that it contains a parameter (the Holland B parameter) which allowed the peakedness of winds in a hurricane to vary. This model will be described here to demonstrate the role of the Holland B parameter in this model.

IDS 2

In the Holland model, hurricane pressure profiles are normalized via the relationship:

$$\beta = \frac{P - P_c}{P_n - P_c} \quad (35)$$

where:

p is the surface pressure at an arbitrary radius (r);

p_c is the (surface) central pressure in the storm; and

p_n is the ambient surface pressure at the periphery of the storm.

Holland showed that the family of β -curves for a number of storms resembled a family of rectangular hyperbolas and could be represented as:

$$\begin{aligned} r_p^B \ln(\beta^{-1}) &= A \\ \text{or} \\ \beta^{-1} &= \exp\left(\frac{A}{r_p^B}\right) \\ \text{or} \\ \beta &= \exp\left(\frac{-A}{r_p^B}\right) \end{aligned} \quad (36)$$

where:

A is a scaling parameter with units of length; and

B is a dimensionless parameter which controls the peakedness of the wind speed distribution.

This leads to a representation for the pressure profile as

$$P = P_c + (P_n - P_c) \exp\left(\frac{-A}{r_p^B}\right) \quad (37)$$

IDS 2

Which then leads to a gradient wind approximation of the form:

$$U_{gr} = \left[\frac{AB(p_n - p_c) \exp\left(\frac{-A}{r_p^B}\right)}{\rho_a r^B} + \frac{r^2 f^2}{4} \right]^{1/2} - \frac{rf}{2} \quad (38)$$

where:

U_{gr} represents the gradient approximation to the wind speed.

In the intense portion of the storm, this equation reduces to a cyclostrophic approximation (a flow in which the pressure gradient force is balanced only by centrifugal acceleration) given by:

$$U_c = \left[\frac{AB(p_n - p_c) \exp\left(\frac{-A}{r_p^B}\right)}{\rho_a r^B} \right]^{1/2} \quad (39)$$

where:

U_c represents the cyclostrophic approximation to the wind speed; which yields explicit forms for the radius to maximum winds as:

$$R_{\max} = A^{\frac{1}{B}} \quad (40)$$

where:

R_{\max} is the distance from the center of the storm circulation to the location of maximum wind speed, compared to r_p which is the pressure-scaling radius;

The maximum wind speed can then be approximated as:

$$U_{\max} = \left(\frac{B}{\rho_a e} \right)^{1/2} (p_n - p_c)^{1/2} \quad (41)$$

where:

U_{\max} is the maximum velocity in the storm; and

e is the base of natural logarithms, 2.718.

If B is equal to 1 in this model, the pressure profile and wind characteristics become similar to results of Myers (1954), Collins and Viehmann (1971), Schwerdt et al. (1979), and Cardone et al. (1976). In the case of the Cardone et al. model this similarity would exist only for the case of a storm with no significant background pressure gradient. Although the Cardone et al. PBL model initially did not consider the effects of the Holland B parameter, it now does include this term in its formulation (Thompson and Cardone, 1996). The Vickery et al. (2000) model also includes the Holland B term in its formulation.

4.4 Selection of Period of Record for Surge Estimation and Consideration of the Effects of Climatic Variability on Surge Extremes

An analysis of climatic variability was undertaken by Resio and Orelup (now submitted for publication to *J. Climate*). The following discussion includes some of the findings relevant to the selection of the period of record and the estimated effects of climatic variability on expected surge extremes. Three fundamental data sets are used in this study: 1) sea level pressures (SLPs) from the NOATL-tropic data set (a sub-domain of the total NCEP SLP data set that covers from 0 degrees to 40 degrees North latitude and from 5 degrees to 110 degrees West longitude); 2) sea surface temperature (SST) data downloaded from Extended Reconstructed Sea Surface Temperature (ERSST); and 3) information on hurricane characteristics taken from OWI files, now available in the public domain. Details on these data sets are available on appropriate web sites.

Empirical Orthogonal Functions (EOFs) have long been recognized as a powerful tool for encapsulating natural patterns within the atmosphere. In this study we used data from the 1950-2005 period (56 years) and defined 5-day mean SLP fields on a 2.5-degree by 2.5-degree grid. This resulted in 73 five-day intervals for every year without a leap year. Leap year was handled by adding that day into the time interval starting on February 25, which created one element encompassing 6 days once in every 4 years. Given that we were not interested in the seasonality of hurricanes but rather in inter-annual and longer variability, we defined mean pressure fields for each 5-day interval throughout the year, with the average taken over the 56 years included in this analysis. Calculated mean pressure fields for each 5-day interval were subtracted from individual mean 5-day pressure fields to produce a set of 73 x 56 pressure fields that were input into an EOF analysis.

The SST data used here represent a subset of the total ERSST data set and cover from 18 degrees to 30 degrees North latitude and from 58 degrees to 98 degrees West longitude on a 2-degree by 2-degree grid, with a land mask that restricts the data to only water points. Although SST patterns within the Gulf

exhibit considerable spatial variability, it is not clear that the variations in the spatial characteristics of these patterns play a major role in the inter-annual variability of hurricane genesis and/or development. Consequently, such variations are not considered here. Instead, mean monthly data for the entire Gulf of Mexico region for July through October were averaged together to provide a single measure of SST for each hurricane season from 1950 through 2005.

The data set for hurricane characteristics includes estimates of six hourly storm positions, along with several parameters that relate to hurricane shape, size, and intensity. Unlike previous data sets which have focused on short-duration (typically 1-minute maximum) wind speeds from flight level, this new data set also contains estimates of the highest sustained (30-minute average) surface-level (10-meter) wind speeds along the path of the storms. Because these are the appropriate winds for driving ocean response models, they provide a much more direct measure of hurricane surge and wave production. In the earlier storms in this data set (prior to 1990), these wind estimates were derived primarily from simulated wind fields based on a “slab model” of the lowest region of the atmosphere combined with a planetary boundary layer model (Thompson and Cardone, 1996). For most of the later storms, these wind fields have been extensively reworked by analysts to assimilate available measurements.

Most past studies of climatic variability have used storm frequency (sometimes stratified by Saffir-Simpson scale) to categorize storm activity in each year. However, for our purposes, we will define a single parameter that incorporates both intensity and frequency into one measure of hurricane activity. This measure of annual hurricane activity is obtained by calculating the estimated kinetic energy for each storm passing through the Gulf of Mexico at the time of its maximum intensity and then adding all maxima within a given year. At a fixed time, the total kinetic energy in a hurricane can be related to storm size and storm intensity as:

$$E_k \sim \iint V^2(x, y) dx dy = \iint V^2(r, \theta) r d\theta dr$$

given that $V(r, \theta) = V_{\max} \phi_1\left(\frac{r}{R_{\max}}\right) \phi_2(\theta - \theta_0)$ then

$$E_k \sim V_{\max}^2 R_{\max}^2 \tag{42}$$

Where V_{\max} is the maximum (30-minute average, 10 m) wind speed within the storm and R_{\max} is the radius to maximum winds at the same time. The value of the parameter E_k at the time of maximum wind speed during a storm’s passage through the Gulf of Mexico provides a good integrated measure of the storm intensity and size at the time of the storm’s maximum intensity. Summing all values of E_k for a season yields a surrogate for combined number, size, and intensity of storms in a year.

Figure 436 shows the cumulative hurricane kinetic energy per season as defined previously in this paper, smoothed over a running 5-year period. Because we are trying to extend the data as long as possible, the

“smoothed” data at either end of this record are defined only in terms of the existing data within the 5-year window. For example, the 2005 data consider only data from 2003, 2004, and 2005 in their average. Thus, as the ends are approached, a slight bias is created in terms of the mean position of the years contributing to this mean, culminating in a 1-year displacement at the beginning and end of the analysis along with a reduced averaging window. This figure shows two very notable peaks, one that commenced in the late-1950s and persisted until about 1970 and a second that began around 2000 and has persisted through 2005, with a broad trough in Gulf of Mexico hurricane activity between these two peaks. There does not appear to be any strong secular signal within this record. The first of these periods coincides with the very active seasons that included Hurricanes Carla, Hilda, Betsy, Beulah, and Camille, which devastated much of the Gulf Coast during the 1960s; while the second contains the recent set of intense hurricanes, including Lili, Charley, Ivan, Dennis, Katrina, and Rita.

Figure 436 shows that there are two intervals of high hurricane activity separated by an interval of relatively low hurricane activity in the years from 1950 to 2005. If this cycle is real, it seems advisable to use a sampling scheme that preserves the expected long-term ratio of high-activity and low-activity years. Because we obviously want to retain both the early (1960-1970) interval of high activity and latest (partial) interval (2000-2005) of high activity in our sample, we should include about two-thirds of the 30-year low-activity interval preceding 1960 in order to achieve this balance. This suggests that including approximately 20 years of the 30-year low-activity interval (1941-1960) is appropriate. Thus, the total record sample length recommended for surge estimation in the Gulf of Mexico is 1941-2005.

Figure 437 shows estimated return periods for central pressures for the total sample within the Gulf of Mexico for different estimation methods. The estimation methods examined are 1) analysis of only quiescent years (Group 1); 2) analysis of only active years (Group 2); 3) analysis of both quiescent-year and active-year samples, treated as though they are drawn from separate populations (Equation 4 from the Resio and Orlup manuscript, reproduced below); and 4) analysis of both quiescent-year and active-year samples as though they are a single population.

Equation 4 from Resio and Orlup:

$$T(x) = \frac{1}{1 - \sum \lambda_n \beta_n F_n(x)}$$

where

- $T(x)$ is the return period for x ;
- λ_n is the frequency of storms in Group n ;
- $F_n(x)$ is the cumulative distribution function (CDF) for storms in Group n ; and
- β_n is the proportion of years in Group n .

(43)

These results, combined with integrations of the full probability integral for surges along a straight coast from the Irish et al. computer runs, yield the results shown in Table 34 for the expected variations in

wave and surge extremes within the Gulf of Mexico, given a doubling of the high-activity years (from 0.25 of the total time to 0.5 of the total time). There is nothing in the Gulf of Mexico record that suggests such a scenario is imminent; therefore, this prediction should probably be taken as an upper limit of what could happen rather than what will happen.

4.5 Selected Storm Sample for Simulations

In this section, the terms R_{max} (storm-size scaling radius) and C_p (central pressure) should be taken as equal to R_p and C_p , as defined elsewhere in this study. Tracks 1 through 5 are defined as shown on Figure 28. This set of tracks has been nicknamed the “RICK-fan” because it mimics the tracks of Rita, Ivan, Camille, and Katrina. Track 1 is the westernmost and Track 5 is the easternmost track in this set. Tracks 1b-4b fall midway between the five primary tracks. One primed Track 4' is located about 40 nautical miles north of the landfall point for Track 4 to allow for storms entering the north-south aligned portion of the coast in this area.

One of the issues affecting our storm selection is implicit in the spacing of the tracks shown on Figure 28. This spacing is approximately 0.6 degree longitude at a latitude of 29.5 degrees, equivalent to a distance of about 31 nautical miles in the along-coast direction. Studies of surge response on idealized, open coasts have shown the distribution of surges along the coast scale quite nicely with this parameter for a wide range of storm sizes and offshore slopes (Figures 438 through 440). Figure 441 provides a plot with all three of the storm sizes plotted together. A second factor that influences along-coast surge variations is the presence of large geometric features in the coastal configuration, such as the Mississippi River, its deltas, and the river levees south of New Orleans. Figure 442 shows a general setup for a numerical study to examine this effect. Figure 442 shows the distribution of surges along the coast. It is apparent in this figure that the effect of the land protrusion is to add a second scale to the along-coast surge distribution. In the New Orleans area, this scale is likely to be of more significance than the simple open coast scaling. In the New Orleans area, this effect will tend to dominate the second source of along coast variation for storm within about 30 nautical miles or so of the eastern edge of the land protrusion. In this context, the storm track spacing for the New Orleans area should be quite reasonable.

In the more general case of storms along a straight coast, any single storm will produce a patten with a shape similar to those shown on Figures 438 through 440. Figure 443 shows a plot of where surges from two storm tracks might fall if they were separated by 31 nautical miles on each of these figures. This represents the worst case in which neither of the simulated storms captures the peak condition that could be generated by these hurricanes. This case is the worst possible since it has the maximum distance from the peak on both sides. Since tracks are assumed to be distributed uniformly along the coast, the expected value would be the mean of all points between the two lines. The bias introduced into the estimated extreme from this set of tracks can be estimated as:

IDS 2

$$\frac{E(\eta_1 + \eta_2)}{E(\eta_{1-2})} = \frac{\frac{\eta_1 + \eta_2}{2}}{\frac{1}{(x_2 - x_1)} \int_{x_1}^{x_2} \eta(x) dx} \quad (44)$$

Which can be calculated numerically for each of the different radii to maximum winds considered. For the three cases shown, the calculated values are 0.794, 0.907, and 0.959 for the 10-, 20-, and 30-nautical mile cases, respectively, which translates into low biases of approximately 20 percent, 9 percent, and 4 percent in these “worst-case” situations. It should be noted that the sampling pattern itself should not introduce a bias in either direction (high or low); consequently, in other sections of the coast, where the exact peak is attained, the simulated value is actually higher than the denominator in this equation. Historically, this problem of low and high values along the coast has been addressed by some sort of

smoothing along the coast. The smoothing interval of approximately $\frac{R_{max}}{2}$ should work relatively well for this purpose.

Along each of the tracks modeled, the central pressure is allowed to vary during a simulated intensification interval until its intensity reaches a plateau. This plateau is maintained until the storm comes within 90 nautical miles of the coast; at that time, the pressures decay according to the (linear interpolation) relationship:

$$C_p(s) = \lambda_0 C_p(s_0) - (1 - \lambda_0) \Delta P_{decay}$$

where

C_p is the central pressure at s

s is the distance along the storm track, with s_0 located 90 nm from landfall

λ_0 is an interpolation multiplier (=1 at 90 nm from landfall and =0 at landfall)

ΔP_{decay} is the total change in central pressure over 90 nm approach to landfall

(45)

The pressure decay term is somewhat dependent on storm size; therefore, the following relationship was used to represent this term:

$$\Delta P'_{decay} = R_p - 6 \quad (\text{with } R_p \text{ given in nautical miles})$$

constrained by $\Delta P_{decay} = \text{Max}(\Delta P'_{decay}, 18); \text{Min}(\Delta P'_{decay}, 5)$

(46)

IDS 2

Once a storm is 1 hour past landfall, the pressure decay factor due to Vickery is applied:

$$C_p = P_\infty - \delta P$$

where

$$\delta P = \delta P_0 e^{-a\Delta t}$$

where

δP is the local pressure differential

δP_0 is the pressure differential one hour after landfall

a is an empirical constant

Δt is time after landfall minus 1 hour

(47)

As noted in this study, Rmax and the Holland B parameter are allowed to vary linearly over the same distance as Cp for all storms except the smallest storm class used in this application. For that class (Rmax = 6 nautical miles), the storm is assumed to retain its intensity, its size, and its Holland B parameter all the way to landfall. Figure 444 shows a typical variation of storm parameters for a storm in which the characteristics vary during their approach to the coast. This figure shows the characteristic “spin-up” time for the hurricane (based on historical times required to reach peak storm intensities) and the variations during its approach to the coast.

Four different Cp – Rp combinations are defined as:

A. 3 Cp and 3 Rmax Values

Cp=960 Rmax=(21.0, 35.6, 11.0)

Cp=930 Rmax=(17.7, 25.8, 8.0)

Cp=900 Rmax=(14.9, 21.8, 6.0)

The loop structure for JPM run sequencing is (from inner loop working outward):

- Rmax
- Cp
- Track

Flood Insurance Study: Southeastern Louisiana

IDS 2

Thus, the sequence of runs for any track using Combination A is:

	Cp	Rmax
1.	960	15.4
2.	960	21.0
3.	960	35.6
4.	930	11.7
5.	930	17.7
6.	930	25.8
7.	900	6.0
8.	900	14.9
9.	900	21.8

B. 2 Cp and 2 Rmax Values

Cp=960 Rmax=(18.2,24.4)

Cp=900 Rmax=(12.5,18.4)

The sequence of runs for any track using Combination B will be:

	Cp	Rmax
1.	960	18.2
2.	960	24.4
3.	900	12.5
4.	900	18.4

IDS 2

C. 2 Cp and 1 Rmax Values

Cp=960 Rmax=17.7

Cp=900 Rmax=17.7

The sequence of runs for any track using Combination C will be:

- | | Cp | Rmax |
|----|-----|------|
| 1. | 960 | 17.7 |
| 2. | 900 | 17.7 |

D. 1 Cp and 1 Rmax Value

Cp=930 Rmax=17.7

Defining three angles as the central angles in the RICK-fan \pm 45 degrees should cover most of the important range for estimating the response surface of the surges. With the secondary variables (tidal phases, Holland B variations, wind-field variations around the PBL central estimate, etc.) added to the integral, this should provide a very reasonable estimate of the surge CDF. Figures 427 and 428 provide the geographic information on these tracks. The tracks approaching the New Orleans area from the southeast are extremely similar to the tracks of the 1947 storm, Betsy, and Andrew in this area. During the 1941-2005 interval, no tracks approached New Orleans from the southwest; however, other storms such as the 1893 storm did approach New Orleans from this direction. In fact, the 1893 track is fairly similar to one of the hypothetical tracks out of the southwest. A track from this direction represents the fact that these storms have become caught up in the more westerly flow (winds blowing toward the east). For a storm to maintain its strength it cannot move too far west or too close to land; consequently, the track of a major storm is constrained somewhat to come from the region from which all the hypothetical (+45 degree) tracks emerge in order for these storms to strike the New Orleans area.

The effect of storm heading angle on surges at the coast appears to be twofold. First, the overall along-coast pattern is broadened; the storm moves along the coast at the same time that it moves toward landfall. Second, there is a relatively slow variation in the maximum surges produced by a storm as a function of the angle of the storm track with the coast; however, as shown on Figure 445, maximum surge is relatively weakly dependent on the angle of storm intersection with the coast. In general, the hurricane approaching slightly (15 to 30 degrees) from west of straight onto a straight east-west coast produces a somewhat higher surge (5 percent or so) than hurricanes moving perpendicularly to the coast. On the other hand, hurricanes approaching the straight east-west coast from a more easterly direction will tend to produce lower surges than produced by hurricanes moving perpendicular to such a coast. This appears to be a fairly broad pattern that can be represented via interpolation.

IDS 2

The effect of forward storm speed is addressed by considering three different forward velocities: Vf=(11,6,17) knots, where 11 is around the mean and the 6-knot and 17-knot speeds span almost the entire range of Vf values at landfall for storms with Cps less than 950. Note that a few of the track-angle combinations are dropped due to either their very oblique angle with respect to the shore or they were exiting storms from the New Orleans area moving toward the northeast. Increased forward storm speed contributes to higher wind speeds in the hurricane PBL model. Consequently, one effect of increasing forward storm velocity is to increase the surge at the coast by a factor which is similar to increasing the wind speeds within the hurricane, i.e.

$$\eta_1 = \eta_2 \left(\frac{v_{\max} + 0.5v_{f_1}}{v_{\max} + 0.5v_{f_2}} \right)^2$$

where

η_1 is the surge at the coast in storm 1, with forward speed = v_1

η_2 is the surge at the coast in storm 2, with forward speed = v_2

v_{\max} is the maximum wind speed of a stationary storm

v_{f_i} is the forward storm velocity of the i^{th} storm

(48)

A second effect of storm speed is to change the duration that a flood wave has to propagate inland. Thus, a slowly moving storm may produce more extensive inland flooding than a faster moving storm. By covering essentially the entire range of forward storm speeds observed in major storms within the Gulf of Mexico (Figures 425 and 426), we should be able to quantify the range of the effects of storm speed on surges in the New Orleans area.

The information below provides information on the variation parameter combinations used in the New Orleans 152-storm study:

4.5.1 Primary Tracks

Track	
<u>(Vf=11)</u>	<u>1 2 3 4 4' 5</u>
Mean angle	9 9 9 9 9 (use Cp-Rmax combination set A) – storms 1-45
-45	4 4 4 4 (use Cp-Rmax combination set B) – storms 46-61
+45	4 4 4 4 (use Cp-Rmax combination set B) – storms 66-81
TOTAL = WAS 81 – NOW 77	

Flood Insurance Study: Southeastern Louisiana

IDS 2

Track

<u>(Vf= 6)</u>	<u>1</u>	<u>2</u>	<u>3</u>	<u>4</u>	<u>4'</u>	<u>5</u>	
Mean angle	2	2	2	2	2		(use Cp-Rmax combination set C) – storms 82-91
-45	1	1	1	1			(use Cp-Rmax combination set D) – storms 92-95
+45	1	1	1	1			(use Cp-Rmax combination set D) – storms 97-100
TOTAL = 18							

Track

<u>(Vf=17)</u>	<u>1</u>	<u>2</u>	<u>3</u>	<u>4</u>	<u>4'</u>	<u>5</u>	
Mean angle	1	1	1	1	1		(use Cp-Rmax combination set D) – storms 101-105
-45	1	1	1	1			(use Cp-Rmax combination set D) – storms 106-109
+45	1	1	1	1			(use Cp-Rmax combination set D) – storms 111-114
TOTAL = WAS 14 – NOW 13							

4.5.2 Secondary Tracks

Track

<u>(Vf=11)</u>	<u>1b</u>	<u>2b</u>	<u>3b</u>	<u>4b</u>			
Mean angle	2	2	2	2			(use Cp-Rmax combination set C) – storms 115-122
-45	2	2	2				(use Cp-Rmax combination set C) – storms 123-128
+45	2	2	2				(use Cp-Rmax combination set C) – storms 131-136
TOTAL = 20							

IDS 2

Track

<u>(Vf= 6)</u>	<u>1b</u>	<u>2b</u>	<u>3b</u>	<u>4b</u>	
Mean angle	2	2	2	2	(use Cp-Rmax combination set C) – storms 137-144
-45	1	1	1		(use Cp-Rmax combination set D) – storms 145-147
+45	1	1	1		(use Cp-Rmax combination set D) – storms 149-151
TOTAL = 14					

Track

<u>(Vf=17)</u>	<u>1b</u>	<u>2b</u>	<u>3b</u>	<u>4b</u>	
Mean angle	1	1	1	1	(use Cp-Rmax combination set D) – storms 152-155
-45	1	1	1		(use Cp-Rmax combination set D) – storms 156-158
+45	1	1	1		(use Cp-Rmax combination set D) – storms 160-162
TOTAL = 10					

GRAND TOTAL = 152

Tables 11 and 12 present the parameters and tracks for the 152 storms used in this study.

4.6 Characteristics of Holland B Parameter and Rmax

4.6.1 Introduction

Using pressure data collection during hurricane reconnaissance flights, coupled with additional information derived from the Hurricane Research Division’s H*Wind snapshots of hurricane wind fields, an analysis of the radius to maximum winds and the Holland B parameter was performed. The reconnaissance data incorporate flights encompassing the time period 1977 through 2001, but the analysis was limited to include only those data collected at the 700-mb or higher level.

The Holland B parameter was found to be inversely correlated with both the size of a hurricane and the latitude of a hurricane. A weak positive correlation of B with central pressure deficit and sea surface temperature was also observed. A statistical relationship between the Holland B

parameter and a non-dimensional parameter incorporating central pressure, radius to maximum winds, sea surface temperature, and latitude was developed.

A qualitative examination of the variation of B, central pressure, and radius to maximum winds as a function of time suggests that along the Gulf of Mexico coastline (excluding southwest Florida), during the final 6 to 24 hours before landfall, the hurricanes weaken as characterized by both an increase in central pressure and the radius to maximum winds, and a decrease in the Holland B parameter. This weakening characteristic of landfalling storms was not as evident for hurricanes making landfall elsewhere along the U.S. coastline.

4.6.2 Flight Level Data Analysis Methodology

Upper level aircraft data available at NOAA site were used to estimate Holland's pressure profile parameter (B). The upper level aircraft data set used here contains 4,546 radial profiles from 62 Atlantic storms. For every storm, data have been organized based on the different flights that passed through the storm. For each flight, the airplane traversed through the hurricane a number of times in different directions. For every pass, the data were collected from the center of the storm to a certain radius (usually 150 km). Available data are then organized according to their radial distance from the center of the storm. For each bin (based on the radius from the center of the storm) flight level pressure, flight altitude, dew point temperature, wind speed, and air temperature are available. Each profile from every flight and every storm is treated as an independent observation. Holland (1980) describes the radial distribution of surface pressure in a hurricane in the form:

$$p(r) = p_0 + \Delta p \cdot \exp\left[-\frac{A}{r^B}\right] \quad (49)$$

where $p(r)$ is the surface pressure at a distance r from the storm center, P_0 is the central pressure, Δp is the central pressure difference, A is the location parameter, and B is the Holland's pressure profile parameter. Holland (1980) showed that $RMW = A^{\frac{1}{B}}$ where RMW is the radius to maximum winds, and thus Equation 49 can be expressed as:

$$p(r) = p_0 + \Delta p \cdot \exp\left[-\frac{RMW^B}{r}\right] \quad (50)$$

The surface pressure and radial distance are transformed to the form of Equation 50. The missing quantities in Equation 50 are RMW and B . The first estimate of RMW is made from the recorded wind speed profile, i.e., RMW is the radius to the measured maximum wind speed. From here on, the radius corresponding to the maximum wind speed in a profile is referred to as RMW . To

estimate the optimum values of B and RMW, RMW and B are varied over the range (0.5 RMW, 1.5 RMW) and (0.5, 2.5), respectively. The algorithm calculates an optimum B value by minimizing the mean of the square differences between the measured and the modeled surface pressure in a range of 0.5 RMW to 1.5 RMW for different B and RMW values. Mathematically, the mean square error between the measured and the modeled surface pressure can be written as:

$$\varepsilon^2 = \frac{\sum_{i=0.5RMW}^{1.5RMW} (P_{obs_i} - P_{theo_i})^2}{n} \quad (51)$$

Where P_{obs_i} is the measured pressure, P_{theo_i} is the theoretical pressure calculated using Equation 50, and n is the number of data points in the range [0.5 RMW, 1.5 RMW]. The values of B and RMW chosen correspond to those yielding the minimum mean square error, ε^2 . The corresponding r^2 value for the fit is given by:

$$r^2 = 1 - \frac{\varepsilon^2}{\sigma^2} \quad (52)$$

Where σ is the standard deviation of the measured pressure data in the range of [0.5 RMW, 1.5 RMW].

A QC criterion was used to filter out profiles. Each of the filtered profiles has at least one of the following characteristics associated with it: (a) Flight level pressure is less than 700 mb (i.e., height greater than 3,000 m); (b) Central pressure difference is less than 25 mb; (c) Radius to maximum winds is greater than two-thirds of the sampling domain; (d) the distance of aircraft's closest approach to the center is greater than half of the radius to maximum winds; (e) data are available for less than one-third of the sampling range (i.e., less than 50 km); and (f) visual inspection which involved eliminating profiles with a considerable amount of data missing in the range of interest (0.5 RMW, 1.5 RMW). The rationale for using criterion (a) is the higher the measurement height, the less representative measurements are of the surface observations. Criterion (b) results in the data associated with Category 1 or higher hurricanes only. The rationale for using criteria (c), (d), (e), and (f) is to ensure that there is a sufficient number of measurements on both sides of the radius to maximum winds to have a clear representation of the shape of the profile.

The use of the QC criteria eliminated 2,291 profiles from a set of 4,556 profiles. Table 35 presents the count of the eliminated pressure profiles based on the filtering criteria. It is clear that criteria (a) and (b) are the most common reasons for profile elimination. Storm-by-storm percentage of the retained profiles is given in Table 36. For some storms, no profiles were retained because all the profiles either had a central pressure difference of less than 25 mb (e.g., Chantal, 1995) or a flight level pressure of less than 700 mb (e.g., Hugo, 1989). Figure 446

IDS 2

presents a few examples of pressure profiles that were eliminated from the analysis. Both the measured pressure data and the corresponding fit to Holland's equation are shown. It is observed that each of the subplots on Figure 446 is compromised by at least one of the above mentioned QC criteria.

Figures 447 and 448 present examples of pressure profiles that were retained for analysis. Each row on Figures 447 and 448 corresponds to a complete airplane traverse in one direction. The shaded regions on Figures 447 and 448 represent the error minimizing range of 0.5 RMW to 1.5 RMW. The fit parameters (i.e., the B value), the central pressure difference, and the RMW are also provided in the title of every profile. For a given traverse through a hurricane, differences in the B values for two different profiles are due to the change in the radius to the maximum winds and the central pressure difference. The geographical distribution of the filtered profiles, based on the storm center, is shown on Figure 449. The filtered profiles have a wide geographical distribution and provide a wide domain of hurricane climatic characteristics. The filtered data set has an average RMW of 46 km (standard deviation of 22 km), an average central pressure difference of 51 mb (18 mb), and an average location of 25.84 degrees North (5.74 degrees North) and 74.78 degrees West (12.82 degrees West). Seventy-one percent of the fits yield r^2 values greater than 0.95 and 80 percent of the fits have a mean square error less than 2.5 mb. The maximum mean square error was 24.6 mb, which occurred for one of Hurricane Opal's profiles where Holland's equation overestimated the pressures at all points.

4.6.3 Supplemental H*WIND Data

The flight level data encompass storms through to 2001, and thus to supplement the data set with more recent storms, some additional storms analyzed using the H*Wind methodology were added. The only storms added were the intense storms from the 2004 and 2005 seasons that had been re-analyzed using the most recent Stepped Frequency Microwave Radiometer calibrations. The intense storms that have been re-analyzed include Hurricanes Katrina (2005) and Hurricane Ivan (2004). Hurricane Rita was added to the data set even though it had not been re-analyzed because at its most intense, the storm had a minimum central pressure of less than 900 mb. Using the wind-field model described in Vickery (2005), and the values of central pressure, RMW, storm translation speed, and the maximum sustained wind speed, a B value chosen so that the maximum surface level wind speed (1-minute sustained value) obtained from the model match the H*Wind estimate of the maximum wind speed. Thus, the estimated B values are obtained through an indirect measure, matching the maximum wind speed rather than the shape of the entire wind field.

Figures 450 through 455 present plots of RMW, maximum 1-minute surface level wind speed, the derived B parameter, and central pressure as a function of time for the three aforementioned hurricanes, in addition to the data derived for Hurricanes Dennis (2005), Bret (1999), and Lili (1999). These three additional storms are given to examine the change in the characteristics of

IDS 2

the storms as they approach land. Each plot also presents the central pressure(s) at landfall as given in the National Hurricane Center hurricane reports.

These six hurricanes represent all the Gulf of Mexico landfalling hurricanes in the H*Wind database that include information on both wind speeds and central pressure in each of the H*Wind snapshots. Additional storms are given in the H*Wind database that do not have central pressures provided on the H*Wind snapshots. All of the six hurricanes show an increase in central pressure and a decrease in the magnitude of the Holland B parameter as they approach the Gulf Coast. An increase in the radius to maximum winds as the hurricanes approach landfall is also evident in five of the six cases examined.

A similar analysis of hurricane characteristics for hurricanes making landfall in regions other than along the Gulf of Mexico coast did not indicate that there is a strong tendency for the storms to weaken and enlarge before landfall. Tendencies of the Holland B parameter for landfalling storms can be seen in Table 37.

4.6.4 Statistical Model for Rmax

4.6.4.1 All Hurricanes

The RMW for all points (flight level data plus H*Wind data) in the data set having a central pressure of less than 980 mb was modeled as a function of central pressure difference and latitude in the form:

$$\ln(RMW) = 3.559 - 7.229 \times 10^{-5} \Delta p^2 + 5.296 \times 10^{-4} \Psi^2;$$

$$r^2 = 0.266, \bullet_{\ln RMW} = 0.449 \tag{53}$$

An analysis of the errors (difference between the regression model estimates and the data) indicates that the model error reduced with increasing $\bullet p$, as indicated on Figure 456.

The error, $\bullet_{\ln RMW}$, is modeled in the form:

$$\bullet_{\ln RMW} = 0.460 \qquad \bullet p \bullet 87 \text{ mb} \tag{54a}$$

$$\bullet_{\ln RMW} = 1.1703 - 0.00817 \bullet p \qquad 87 \text{ mb} \bullet \bullet p \bullet 120 \text{ mb} \tag{54b}$$

$$\bullet_{\ln RMW} = 0.190 \qquad \bullet p > 120 \text{ mb} \tag{54c}$$

Figure 457 presents the modeled and observed values of RMW plotted vs. $\bullet p$. The modeled data are given as the median estimates and the range defined by $\pm 2 \bullet_{\ln RMW}$. The modeled range reflects the reduction in $\bullet_{\ln RMW}$ as a function of $\bullet p$.

4.6.4.2 *Gulf of Mexico Hurricanes*

In order to determine if the characteristics of the RMW associated with the Gulf of Mexico storms differed from that obtained using the all storm data, the RMW – $\bullet p$ and RMW- \bullet relationships were re-examined. For this analysis, the Gulf of Mexico storms included all hurricanes west of 81 degrees West and north of 18 degrees North. The RMW for all storms (flight level data plus H*Wind data) in the Gulf of Mexico data set with central pressures less than 980 mb was modeled as a function of central pressure difference in the form:

$$\ln(RMW) = 3.859 - 7.700 \times 10^{-5} \Delta p^2 \quad r^2=0.290, \bullet_{\ln RMW} = 0.390 \quad (55)$$

The RMW was found to be independent of latitude. As in the all storm case, the model error reduces with increasing $\bullet p$, as indicated on Figure 458.

The error, $\bullet_{\ln RMW}$, for Gulf of Mexico hurricanes is modeled in the form:

$$\bullet_{\ln RMW} = 0.396 \quad \bullet p \bullet 100 \text{ mb} \quad (56a)$$

$$\bullet_{\ln RMW} = 1.424 - 0.01029 \bullet p \quad 100 \text{ mb} \bullet \bullet p \bullet 120 \text{ mb} \quad (56b)$$

$$\bullet_{\ln RMW} = 0.19 \quad \bullet p > 120 \text{ mb} \quad (56c)$$

Figure 459 presents the modeled and observed values of RMW plotted vs. $\bullet p$ for the Gulf of Mexico hurricanes. The modeled data are given as the median estimates and the range defined by $\pm 2 \bullet_{\ln RMW}$. The modeled range reflects the reduction in $\bullet_{\ln RMW}$ as a function of $\bullet p$.

Figure 460 presents the median values of the RMW computed using Equation 53 (all hurricane RMW model) computed for latitudes of 25 degrees North (Southern Gulf of Mexico) and 30 degrees North (Northern Gulf of Mexico), where it is seen that, for the Northern Gulf of Mexico storms, the all hurricanes RMW model overestimates the size of the Gulf of Mexico hurricanes, indicating that Gulf of Mexico hurricanes are smaller than Atlantic hurricanes.

4.6.5 RMW (Rmax) for Landfalling Storms

Figure 461 presents the values of the RMW for storms making landfall along the Gulf and Atlantic coasts of the United States. In the case of Gulf Coast storms, no statistically significant correlation exists between the RMW and either latitude or Δp . In the case of hurricanes making landfall along the Atlantic coast, the RMW is positively correlated with latitude and negatively correlated with the Δp^2 . As a group (i.e., both Atlantic and Gulf coast landfalling hurricanes), the RMW is also positively correlated with latitude, and negatively correlated with the Δp^2 . Using only landfall values of RMW, the following statistical models best define the relationship between RMW, Δp , and latitude.

Gulf of Mexico coast landfalling hurricanes:

$$\ln(RMW) = 3.558 \quad \bullet_{\ln RMW} = 0.457 \quad (57a)$$

Atlantic coast landfalling hurricanes:

$$\ln(RMW) = 2.556 - 5.963 \times 10^{-5} \Delta p^2 + 0.0458 \psi ; \quad r^2 = 0.336, \bullet_{\ln RMW} = 0.456 \quad (57b)$$

Gulf and Atlantic coast landfalling hurricanes:

$$\ln(RMW) = 2.377 - 4.825 \times 10^{-5} \Delta p^2 + 0.0483 \psi ; \quad r^2 = 0.203, \bullet_{\ln RMW} = 0.457 \quad (57c)$$

The ability of the RMW models developed using the flight level and H*Wind data (primarily open ocean data) to model the landfalling hurricane RMW was tested by computing the mean errors (in log space) and the resulting standard deviations and r^2 values using the landfall RMW data and the flight level/H*Wind derived RMW models. The error, $\mu_{\ln RMW}$, is defined as model RMW minus observed RMW, thus a mean positive error indicates the model overestimates the size of the landfalling hurricanes. The comparisons yield the following findings:

Gulf of Mexico landfalling hurricanes with Gulf of Mexico RMW model:

$$\mu_{\ln RMW} = 0.032 ; \quad r^2 = -0.008 \quad \bullet_{\ln RMW} = 0.459$$

Atlantic coast landfalling hurricanes with the all hurricane RMW model:

$$\mu_{\ln RMW} = 0.058 ; \quad r^2 = 0.356 \quad \bullet_{\ln RMW} = 0.450$$

Gulf and Atlantic coast landfalling hurricanes with the all hurricane RMW model for the Atlantic coast and Gulf of Mexico RMW model for the Gulf Coast:

$$\mu_{\ln RMW} = 0.043; \quad r^2=0.219 \quad \sigma_{\ln RMW} = 0.453$$

A comparison of the model errors noted above to those resulting from the statistical analyses of the landfalling storms alone indicates that the models derived from the flight level and H*Wind data can be used to define the characteristics of landfalling hurricanes. In the case of landfalling Gulf of Mexico hurricanes, the use of the Gulf of Mexico RMW model, which contains the negative correlation between RMW and ϕ^2 , is not statistically significantly different from the uncorrelated RMW- ϕ relationship derived from the landfalling hurricanes alone. This observation suggests that there are an insufficient number of landfalling intense storms in the historical data to discern such a relationship.

4.6.6 Statistical Model for Holland's B Parameter

The B values computed as discussed above were found to be correlated to the radius to maximum winds, central pressure difference, latitude, and sea surface temperature. Only points associated with central pressures of less than 980 mb are included in the analysis. Figure 462 presents the variation of B as separate linear functions of the RMW, Δp , latitude (ϕ), and the mean SST T_s . It is clear from the data presented on Figure 462 that B decreases with increasing RMW and increasing latitude. A weak positive correlation of B with Δp is seen as is a weak positive correlation with sea surface temperature.

In order to incorporate the effects of RMW, Δp , latitude (ϕ), and T_s into a single model, a new non-dimensional variable, A, was developed as:

$$A = \frac{RMW \cdot f_c}{\sqrt{2R_d T_s \cdot \ln \left(1 + \frac{\Delta p}{P_c \cdot e} \right)}} \quad (58)$$

The numerator of A is the product of the RMW (in meters) and the Coriolis force, defined as $2\phi \sin \phi$, represents the contribution to angular velocity associated with the Coriolis force. The denominator of A is an estimate of the maximum potential intensity of a hurricane. From Emanuel (1988), the maximum wind speed in a tropical cyclone is:

$$V_{\max} = \sqrt{2R_d T_s \ln \left[\frac{p_{\max}}{P_c} \right]} \quad (59)$$

where V_{\max} is the maximum wind speed, R_d is the gas constant for dry air, p_{\max} is the pressure at $r=RMW$, T_s is the SST in degrees Kelvin (K), and p_c is the pressure at the storm center.

Using Holland's Equation it can be shown that:

$$\frac{p_{\max}}{p_c} = 1 + \frac{\Delta p}{p_c e} \quad (60)$$

Hence, both the numerator and denominator of A have the units of velocity, and A is non-dimensional. Modeling B as a function of the square root of A yields a linear model (Figure 463) with B negatively correlated with \sqrt{A} and has an r^2 of 0.34, with a standard deviation of the error equal to 0.225. The relationship between B and \sqrt{A} is expressed as:

$$B = 1.732 - 2.237\sqrt{A} ; \quad r^2=0.336, \bullet_B = 0.225 \quad (61)$$

In order to determine if the relationship between B and A is valid for intense storms, the point values of B and the model values of B were plotted as a function of RMW for strong hurricanes (i.e., storms with a central pressure of < 930 mb) as shown on Figure 464. The data presented on Figure 464 indicate that in the case of strong storms with large RMW (RMW > 40 km) the relationship between B and A described earlier breaks down, with the true values of B being less than those predicted by the model. Although only two storms with large RMW and low central pressures exist in the data analyzed (Hurricane Katrina in the Gulf of Mexico and Hurricane Floyd in the Atlantic), the data indicate that the likelihood of a storm with a central pressure less than 930 mb and an RMW greater than 40 km, combined with a B value greater than about 1.1, is remote. The mean value of B for these large, strong hurricanes is 1.01, and the estimated standard deviation is 0.082. In cases where these strong storms are simulated, B should be constrained to lie within the range of 0.85 to 1.18 (i.e., mean $\pm 2\bullet$).

As in the case of the analysis of Gulf of Mexico hurricanes with respect to the behavior of RMW with Δp and latitude, B values for all hurricanes within the Gulf of Mexico were extracted and analyzed alone. Unlike the results seen for the RMW where the Gulf of Mexico hurricanes were found to be smaller than the other hurricanes, the variation of B with A for the Gulf of Mexico hurricanes is essentially identical to that seen in the all hurricane case. Figure 465 presents the individual B values for the Gulf of Mexico and Atlantic hurricanes along with the model predicted mean values of B where it is clearly evident that there is, for practical purposes, no difference in the variation of B with A between the two regions.

Note that two simpler, but less elegant, models relating B with RMW and latitude were examined modeling B as a function of $f_c RMW$ and B as a function of \sqrt{C} , where C is defined as:

$$C = \frac{RMW \cdot \sin \psi}{\sqrt{T_s \cdot \ln \left(1 + \frac{\Delta p}{P_c \cdot e} \right)}} \quad (62)$$

Where in Equation 62, T_s is expressed in degrees Celsius (C) rather than degrees K.

The regression model relating B to \sqrt{C} is given in the form:

$$B = 1.756 - 0.194\sqrt{C} ; \quad r^2=0.368, \bullet_B = 0.220 \quad (63)$$

The regression model relating B to $f_c RMW$ is given in the form:

$$B = 1.793 - 0.326\sqrt{f_c RMW} ; \quad r^2=0.357, \bullet_B = 0.221 \quad (64)$$

Both of these models yield marginally improved r^2 values than does the model relating B to the non-dimensional relative intensity parameter, but have the small disadvantage in that the independent variable is not non-dimensional. The limitations of these models when applied to large intense storms are the same as those evident in the case of the non-dimensional model. The reduction to the r^2 value when changing the independent variable in the non-dimensional parameter given in Equation 58 to the dimensional parameter given in Equation 62 is due solely to the conversion of the SST from degrees C (Equation 62) to degrees K (Equation 58). For practical purpose, any of the three linear regression models given in Equations 61, 63, or 64 can be used to model the Holland B parameter, with Equation 64 requiring the least computational effort.

4.6.7 Comparisons of Flight Level vs. Landfall Analysis B Values

Figure 466 presents a comparison of the Holland B parameters derived from the flight level data to those used in the wind-field model described in Vickery (2005) for estimating the wind speeds associated with landfalling storms. Overall, the comparisons indicate that the two values of B are similar, with the B values used within the wind-field model in post storm analyses being slightly lower than those derived from the flight level data. The largest difference between the two estimates of the Holland B parameter occurs in the case of Hurricane Erin for the landfall along the Florida Panhandle.

Figure 467 presents the same information as Figure 466, but is limited to hurricanes with central pressures of 964 mb or less. The comparisons indicate that the B values used within the hurricane wind-field model to match the surface observations of wind speeds and pressures is about 7 percent less than those derived from the flight level data. This difference could be due to either

changes in the characteristics of the pressure field between the 700 mb level and the surface, or biases in the wind-field model. Note that a 7 percent reduction in B corresponds to approximately a 3.5 percent reduction in the maximum modeled wind speed. However, comparisons of modeled and observed peak gust wind speeds and time series of the surface level pressures suggest that there is no such bias in the wind model.

4.6.8 Summary

The Holland pressure profile parameter, B, was found to decrease with increasing latitude and increase with decreasing RMW. A weak positive correlation between B and both Δp and SST was also observed. The effect of all four of these parameters was accounted for by defining a new non-dimensional parameter, A, defined by Equation 61, however; a two-parameter model (with dimensions) relating B to the RMW and the Coriolis parameter is an equally good predictor of B.

The limited data for large (as defined by RMW) hurricanes, having low central pressures, ($p_c < 930$ mb) indicates that B has an upper limit of ~ 1.2 . The relationship between B and A was found to be the same in the Atlantic Basin and in the Gulf of Mexico.

A qualitative examination of the characteristics of intense hurricanes making landfall along the Gulf of Mexico coast (excluding southwest Florida) suggests that these hurricanes weaken in the last 6 to 24 hours, with this weakening characterized by an increase in the central pressure, and increase in the radius to maximum winds and a decrease in the Holland B parameter. The reason for this weakening is beyond the scope of this investigation.

The few cases where flight level data were available up to the time a hurricane makes landfall indicates that, in most cases, B tends to decrease as the hurricane approaches land. Recognizing that the data set is limited, this observation suggests that using the statistical model for B derived using open ocean (or open Gulf) data may result in an overestimate of B for landfalling storms. This potential overestimate of the magnitude of the Holland B parameter along the Gulf Coast associated with the use of a statistical model developed using open water hurricane data may be further exaggerated because of the decrease in the Holland B parameter just before landfall observed in the limited number of landfalling cases examined.

4.7 Integration Method

There are several ways that one could approach the integration of the storm probabilities within the JPM. Each of these can be justified under a particular set of assumptions. Three of these will be discussed here. Before we proceed to examine these, a brief overview of the integration procedure is in order.

The integration is performed by summing discretized probabilities to approximate Equation 55 in the main text of this study (with \mathcal{E} now included within the same probability function as the other five parameters), i.e.,

$$F(\eta) = \sum \sum \dots \sum p(c_p, R_{\max}, v_f, \theta_l, x, \varepsilon) H[\Psi(c_p, R_{\max}, v_f, \theta_l, x) - \eta + \varepsilon] \Delta(c_p, R_{\max}, v_f, \theta_l, x, \varepsilon)$$

where

$F(\eta)$ is the CDF for surge levels (η)

$p(c_p, R_{\max}, v_f, \theta_l, x, \varepsilon)$ is the probability density function for the multivariate set of parameters;

$H[z]$ is the Heaviside function (=1 if $z \geq 0$, = 0, otherwise);

$\Psi(c_p, R_{\max}, v_f, \theta_l, x)$ is the result of the numerical simulation for a particular parameter combination;

$\Delta(c_p, R_{\max}, v_f, \theta_l, x, \varepsilon)$ is the increment of parameter space encapsulated within a discretization.

(65)

There are three primary aspects of this equation that contribute to the accuracy of approximations to $F(\eta)$:

1. the accuracy in the specification of $p(c_p, R_{\max}, v_f, \theta_l, x, \varepsilon)$;
2. the accuracy in the numerical simulations $\Psi(c_p, R_{\max}, v_f, \theta_l, x)$; and
3. the influence of the discretization size on the approximation.

The first two of these are fairly intuitive, but the third is often more difficult to explain and quantify because the size of the discrete increments required for a given accuracy is dependent on the behavior of the probability function itself. We shall now proceed to examine three approaches to the integration.

4.7.1 The Case of Simple Models Combined with Many Simulations

One approach to estimating coastal hazards would be to utilize simple models with many simulations. In this context, one could discretize each parameter in the hurricane parameterization considered here $(c_p, R_{\max}, v_f, \theta_l, x)$ and even add some additional probabilistic attributes to the storms (for example: variations in the Holland B parameter, variable storm decay during approach to the coast, suite of variations in offshore storm tracks associated with each landfalling storm). Given n parameters with m categories used to represent each parameter, n^m simulations would be required in this approach. For example, for the five-dimensional representation, with five categories in each parameter, 3,125 simulations would be required to populate the JPM integral.

This approach would produce a very accurate discretization of the probability function; however, inaccuracies in the simulations do not vanish by simply increasing the number of simulations. For example, if simplified models predict values that are 30 percent too high or too low at a given point along the coast for the portion of the parameter space that contains the primary contribution to surges at the $1 - F(\eta) = 0.01$ level (the range of the nominal “100-year” surge event), no

increase in the number of simulations will converge to the correct answer for this range, nor will the addition of uncertainty make the error vanish.

For the case of wind fields, Powell et al. (2003) have shown that a parametric wind-field approach, which includes physical effects captured within an accurate planetary boundary layer model, can provide reasonable representations of wind speeds in coastal areas. This method also allows many simulations to be run and, therefore, represents a good application of this type of approach. Coastal surge generation requires that wave fields, direct wind-driven surges, and the interaction between these two driving mechanisms be modeled correctly. Parametric wave models for hurricanes have been known to be quite inaccurate for a number of years and are not used by any major wave modeling group in the world today, even in offshore areas. In nearshore areas, refraction, wave breaking, sheltering, and other physical mechanisms cannot be captured by parametric models. Also, surge models such as ADCIRC include much improved capabilities for depicting critical shallow-water physics and for representing small-scale coastal features. Because of this, the methodology described in the main text, which relies on state-of-the-art models to ensure unbiased estimates of coastal surges, is recommended; however, practical limitations related to computer run time (even on the largest supercomputers available today) presently preclude the execution of multiple thousands of runs using this complete prediction system.

4.7.2 The Case of Optimized Category Definition

Given that a priori information is available for the variation and co-variation of the variables used in the probability function, as well as for the sensitivity of coastal surges to variations in each of the variables, it is possible to construct an optimized set of discrete samples to simulate surges from the overall multivariate distribution. This approach is presently under development by Toro for applications within FEMA Region 4. As shown on Figure 420, Toro's independent check on the pressure distribution used here showed very good agreement. Similarly, preliminary comparisons between the two statistical methods appear to show good agreement for JPM applications.

4.7.3 The Case of Structured Interpolation on a Response Surface

Numerical studies using ADCIRC have shown that coastal surge response is very dependent on pressure differential (peripheral pressure minus central pressure), storm size (R_{\max}), and storm location relative to a site, as discussed in Section 4.5. Storm surge is less sensitive to forward storm speed and angle of the storm relative to the coast. Figure 468 shows the characteristic variation of surge elevations at coastal stations as a function of variations in pressure differential ($p_0 - c_p$), based on SLOSH tests along the coast of Mississippi. As noted in Section 4.3, the maximum wind speed in a slowly varying, stationary hurricane can be approximated as:

$$U_{\max} = \left(\frac{B}{\rho_a e} \right)^{1/2} (\Delta P)^{1/2}$$

where

B is the Holland B parameter;

ρ_a is the density of air;

e is natural logarithm base (= 2.718...); and

ΔP is the pressure differential between the storm periphery and its center. (66)

Because surges tend to be proportional to the wind stress, which for a capped coefficient of drag is proportional to the wind speed squared, it follows that the linear relationship between ΔP and surge is consistent with our theoretical expectation for this relationship.

Because a major portion of the surge response to hurricanes is captured by the variation of ΔP and R_p , the integration method selected for application here is based on the estimation of $\Delta P - R_p$ planes within the five-dimensional parameter space used in the JPM. Thus, for a fixed value of storm landfall location (x), storm track angle relative to the coast (θ_l), and storm speed (v_f), we can define a response function,

$$\eta_{\max}(x, y) = \phi_{kmn}(\Delta P, R_p, x, y) \quad (67)$$

where ϕ_{kmn} is the surge response function and the subscripts “k, m, and n” denote a specific track angle, storm speed, and landfall location, respectively. This notation reflects the fact that this response function must be defined for each spatial (x, y) point in the computations. Figure 469 shows an example of such a response function. As expected, the surge values increase essentially linearly with increasing pressure differential and also increase with increasing values of R_p .

Figures 470 and 471 show the characteristic variations of coastal surges as a function of storm angle relative to the coast (θ_l) and forward storm speed (v_f), respectively. As can be seen here, the variations tend to be quite smooth with either linear or slightly curved slopes in these figures. The JPM integration method employed here makes use of the “smoothness” of these functions to interpolate between discretized storm parameters.

An advantage of the approach used here is that the surge response is characterized with some level of detail in the important $\Delta P - R_p$ plane. To drive the relevance of this point home, let us examine the effects of discretization on a probability integral along the “pressure-differential”

axis. Given the linear variation of surge elevation with pressure differential, surge elevation can be written as

$$\eta = \lambda \Delta p \quad (68)$$

Where λ is a site-specific constant, and hence

$$F(\eta) = F(\lambda \Delta p) \quad (69)$$

If we assume that the pressure differential probability follows a Gumbel distribution, we can calculate this probability directly. Figure 472 shows a comparison of the CDFs for three different approximations to the return period as a function of surge level, given the value of $\alpha = 0.2$ in Equation 69 (just for an example here). As can be seen in this figure, for a fixed return period, deviations between the three-category approximation (categories with a width of 30 mb) and the continuous function can be as large as ± 3.0 feet. For the 3-mb categories, the deviations are, as expected, only about ± 0.3 foot. Although this pattern will be smoothed and obscured by the addition of many categories of storms, it is clear that the smaller categories provide an improved representation for the probabilities. Also, due to the physical basis for the pressure differential scaling used here, we can extrapolate to larger storms than those actually utilized in the storms. This will provide a somewhat conservative estimate if there is substantial levee overtopping; because the level of extrapolation used here is only about 18 percent ($\Delta P = 113$ mb to $\Delta P = 133$ mb), this should not present a serious problem.

In this approach, we do not treat the set of nine storms simulated for a given track, forward storm speed, and track angle as a discrete set of storms each with its own associated probability increment because this would give only a relatively crude representation of the actual probability structure. Instead, we interpolate between simulated values and extrapolate over relatively short distances in Δp and (R_{\max}) . For the integration used in the New Orleans area, the three Δp and three R_{\max} values were interpolated to increments of 1 mile in R_{\max} and 3 mb in Δp , over the range of 960 mb to 882 mb for offshore pressures (i.e., before they begin to decay) and 5 nautical miles to 40 nautical miles for R_{\max} values. This provides a very smooth response surface for the primary storm tracks in this area (the so-called RICK-fan tracks). For the ± 45 -degree tracks, the two values of Δp and R_{\max} are likewise used to develop a finely discretized (1 nautical mile by 3 mb) set of values over the Δp - R_{\max} plane. At this point, we have finely discretized categorizations within the Δp - R_{\max} plane for the five primary (RICK-fan) tracks and the eight additional ± 45 -degree tracks. Thus, we have a set of response functions $[\phi_{kmn}(\Delta P, R_p, x, y)]$ that are quite well defined for the central storm speed (11 knots) for these tracks.

Because the effect of variations in storm speed is fairly small and tends to have fairly linear slopes that are roughly independent of (R_{\max}) and $\bullet p$, only a small number of storms can be used to modify the functional form of $[\phi_{kmn}(\Delta P, R_p, x, y)]$ as a function of forward storm speed. This retains the overall structure of the response function for the alternative speeds, rather than assigning only a single surge value to all the responses for that storm speed. For the New Orleans area, two storms (with different combinations of $\bullet p$ and R_{\max}) were used to estimate the impact of a slower storm speed on the surge response function $[\phi_{kmn}(\Delta P, R_p, x, y)]$ compared to the primary (central) speed category (11 knots) for the RICK-fan set of tracks. Single storms were also used to estimate the impact of varying the forward speed from 11 knots to 6 knots, along the ± 45 -degree tracks and to estimate the effects of varying the forward speed from 11 knots to 17 knots for all storms. In the approach used here, the value of $[\phi_{kmn}(\Delta P, R_p, x, y)]$ for different speeds is obtained from the relationship:

$$\phi_{kmn}(\Delta P, R_p, x, y) = \phi_{k_0 p_0}(\Delta P, R_p, x, y) \Psi_{kmn}(\Delta P, R_p, x, y)$$

where

The subscript "0" refers to the central speed and angle categories for a specific landfall location; and

$$\Psi_{kmn}(\Delta P, R_p, x, y) = \frac{\partial \phi_{kmn}(\Delta P, R_p, x, y)}{\partial v_f} \delta v_f \quad (70)$$

For the cases in which a single storm is used to infer the variation with forward speed $\Psi_{kmn}(\Delta P, R_p, x, y)$ reduces to a constant.

This now provides a suitable set of interpolated, finely discretized values of surge heights as a function of \bullet p and R_{\max} for all forward storm speeds, storm angles, and storm tracks and the summation in Equation 65 can be rewritten as:

$$F(\eta) = \sum \sum \dots \sum P(\Delta p_i, R_{\max_j}, v_{f_k}, \theta_l, x_m, \epsilon_n) H[\Lambda(\Delta p_i, R_{\max_j}, v_{f_k}, \theta_l, x_m) - \eta + \epsilon] \Delta(\Delta p_i, R_{\max_j}, v_{f_k}, \theta_l, x_m, \epsilon_n)$$

where

$F(\eta)$ is the CDF for surge levels (η)

$p(\Delta p_i, R_{\max_j}, v_{f_k}, \theta_l, x_m, \epsilon_n)$ is the probability density function for the multivariate set of parameters;

$H[z]$ is the Heaviside function ($=1$ if $z \geq 0$, $=0$, otherwise);

$\Lambda(\Delta p_i, R_{\max_j}, v_{f_k}, \theta_l, x_m)$ is the interpolated value between simulations with a particular parameter combination;

$\Delta(\Delta p_i, R_{\max_j}, v_{f_k}, \theta_l, x_m, \epsilon_n)$ is the increment of parameter space encapsulated within a discretized category.

(71)

One concern addressed briefly in Section 4.5 is the sensitivity of the probability estimates to track spacing. The sufficiency of the spacing used here can be investigated by comparing results from the runs on the set of tracks that fell between the five major RICK-fan tracks to results of interpolations based on only the five initial tracks. Figures 473 through 476 show the results of these comparisons. In general, little or no bias is introduced into the probability integration, even if only the information from the primary tracks is used. Only at Track 4a, where the sites are switching from the “right-hand” (onshore winds) side of the storm to the “left-hand” (offshore winds) side of the storm in the area east of the Mississippi River does the variability exceed 10 percent of the surge values for surges greater than 10 feet.

4.8 Estimation of Confidence Bands for Surge Estimates

Three main types of uncertainty with respect to the estimation of extremes are relevant to understanding hurricane hazards along coasts. First, there is uncertainty that the actual sample of storms is representative of the “true” climatology today. Second, there is uncertainty in the events within future intervals of time, even if the “true” climatology is known exactly. And, third, there is uncertainty that some non-stationary process (sea level rise, subsidence, climate change, new development patterns, man-made alterations to the coasts, marsh degradation, etc.) will affect future hazards. The first of these has traditionally been addressed via sampling theory. The second can be addressed via re-sampling or “bootstrap” methods. The third must be estimated from ancillary information, often not contained within the initial hazard estimates themselves.

The first type of uncertainty listed above pertains to what used to be termed confidence bands (or control curves) for estimates of extremes. It cannot be estimated using re-sampling techniques because these techniques use the initial sample as the basis for their re-sampling and implicitly assume that the initial

sample represents the actual population characteristics. Thus, some parametric method must be used to obtain this information. There are many classes of distributions that can be used to fit the data. Because we are only using the parametric fits to estimate uncertainty and not to replace the non-parametric estimates obtained from the JPM, we are somewhat free to use any distribution for which the sampling uncertainty is known. Gringorten (1962, 1963) has shown that the expected RMS error of an estimated return period in a two-parameter Fisher-Tippett Type I (Gumbel, 1959) distribution is given by:

$$\sigma_T = \sigma \sqrt{\frac{1.1000y^2 + 1.1396y + 1}{N}}$$

where

σ is the distribution standard deviation;

σ_T is the rms error at return period, T;

N is the number of samples used to estimate the distribution parameters; and

y is the reduced Gumbel variate given by

$$y = (\eta - a_0) / a_1;$$

η is the variate of interest (surge level in this case); and

a_0 and a_1 are the parameters of the Gumbel distribution.

(72)

The reduced variate and return period are related by:

$$y = -\ln \left[\ln \left(\frac{T}{T-1} \right) \right]$$

(73)

Which for $T > 7$ approaches an exponential form given by:

$$\left(T - \frac{1}{2} \right) \rightarrow e^y$$

(74)

Equation 72 shows that the RMS error at a fixed return period is related to the distribution standard deviation and the square root of a nondimensional factor involving the ratio of different powers of y (y^2 , y^1 , and y^0) to the number of samples used to define the parameters. By the method of moments, the Gumbel parameters can be shown to be given by:

IDS 2

$$a_0 = \gamma a_1 - \mu \quad a_1 = \frac{\sqrt{6}}{\pi} \sigma$$

where γ is Euler's constant (= 0.57721...) and μ is the distribution mean. (75)

Thus, the distribution standard deviation is related to the slope of the line represented by Equation 74.

Although Equation 72 was initially derived for applications to annual maxima, it can be adapted to any time interval for data sampling in a straightforward manner. For the case of hurricanes, the average interval between storms (the inverse of the Poisson frequency used in the compound Gumbel-Poisson distribution) can be used to transform Equation 72 into the form

$$\sigma'_r = \sigma \sqrt{\frac{1.1000y'^2 + 1.1396y' + 1}{N'}}$$

where

σ is the distribution standard deviation;

σ'_r is the rms error at return period, T' (T/\hat{T} , where \hat{T} is the average years between hurricanes); and

N' is the number of samples used to estimate the distribution parameters (N/\hat{T}).

(76)

Because the form of Equation 74 is logarithmic, the slope is not affected by a multiplicative factor and, thus, the distribution standard deviation remains the same. N' in Equation 76 can be estimated from the equivalent total number of years in the sample divided by \hat{T} . The total number of years for this case is 65 (1941-2005, inclusive) times a factor, Z , which relates the spatial area covered by the sample used to the spatial extent of a hurricane surge. For relatively intense storms capable of producing surges that are exceeded only every 100 years or more, the along-coast extent of very high surges (at least 60 percent of the peak value) is about 60 nautical miles for a storm with a 20-nautical mile radius to maximum winds (see Figure 441). The parameter estimation used to derive the values shown on Figure 416 covered ± 3.5 degrees longitude along 29.5 degrees North latitude. The value of Z is given by

$$Z = \frac{\text{Distance along coast}}{\text{Width of a single sample}} \quad (77)$$

which, in this case, is 365.5 nautical miles divided by 60 nautical miles, or approximately 6.1. Thus, the effective number of years is 396.

4.9 JPM-OS Implementation Methodology

4.9.1 Overview

The JPM-OS software computes frequency of occurrence surges at specific geographic points or stations. For each of these points a surge response (value) for all storms (in this case 152 storms) is required. This response value is the maximum or peak value of the surge recorded for the entire simulation. The JPM-OS code produces a stage vs. frequency of occurrence table for all points in the input file. There are requirements and preparation steps which must be performed to create the required input file and are described as follows.

4.9.2 JPM-OS Software Input Requirements

It is mandatory that all storm simulations are completed and, for each of these simulations, a file is created that contains the peak surge value obtained for the entire simulation for all nodes in the ADCIRC grid or grids. Thus, for 152 storms, 152 peak files must be created. Note that proper setup and compilation of the ADCIRC software will create these peak surge values for all nodes at the time step of model execution. If not created specifically during ADCIRC execution, the peak surge values are obtained from the time history of the surge values, set up at 0.5-hour time step for these simulations. In this case, the peak surge files were created during model execution for all 152 storms, thus increasing the accuracy of the results.

4.9.3 Methodology Steps

The primary steps in the workflow are as follows:

- a. Complete all ADCIRC/STWAVE storm simulations;
- b. Create surge peak files for each storm for all grid(s) nodes;
- c. Map all peak surge nodes to common grid (this step is only required if more than one grid was used in the simulations suite);
- d. Filter nodes for which no surge response was recorded for a specific storm; and
- e. Compute surge vs. frequency of occurrence using the JPM-OS software.

The first two steps have been discussed above. Step “c” is only required if multiple grids were used in the suite of simulations. If so, the grid nodes must be mapped to one common grid, using a nearest node approach, to record all peak surges at one grid node location. A nearest node approach is used rather than straight interpolation for two reasons. The first reason is that any grid changes that occurred during production were minimal, thus only a few nodes vary in

location between differing grid versions. Second, stage elevations have only slight gradients; thus, the difference in results between a nearest neighbor method and interpolation method were assumed inconsequential.

Step “d” is the filtering of nodes for which no surge response was produced by certain storm(s). This could be due to a number of reasons including, but not limited to, distance from the storm and/or high topographic elevation of the station. These points are tagged with a -99999 or “no-data” flag in the max peak files. For each of these points, the no-data flag is replaced with an elevation of 0.5 foot below the topographic elevation of the base grid at that point. It should be noted that any stage elevation below the nodal stage elevation is not considered during the JPM-OS analysis. However, a stage value of 0.5 foot below the topographic elevation will create smaller probabilistic gradients in the response surface and is thus used instead of -99999.

4.9.4 JPM-OS Computation

Once Steps “a” through “d” above are completed, an input file is created (probsf.inp) which contains a station ID, x and y coordinates of the station (latitude and longitude), station topographic elevation, and the values of surges for all storms in the suite. There is a header record, which must identify the appropriate storm number for each surge value.

4.9.5 JPM-OS Results

The software produces several output files, containing the 50-, 100-, and 500-year return period surge values for each point. Additional files are created for ease of import into a GIS. Graphics for each point are also produced which display the actual surge vs. frequency of occurrence curves.

4.9.6 Methodology Used for Adding 10-Year Storm Information to the JPM-OS Estimates for Low-Intensity Storms

A set of low-intensity storms was hindcast, covering all storm tracks, storm forward speeds (6, 11, and 17 knots), storm angles (central heading for each track ± 45 degrees), and storm sizes that had been used in the initial set of high-intensity storm hindcasts. We shall refer to the first set (the initial high-intensity set of model runs) as Set A and to the second set (the low-intensity storms) as Set B. The lowest pressure considered in Set A was 960 mb off the coast; whereas the pressures for the storms that were simulated in Set B were set to 975 mb off the coast. The primary matrices in the JPM-OS integral were modified to include an interpolation from an intensity equivalent to 960 mb off the coast to conditions equivalent to 975 mb off the coast (using 3-mb increments) and were then linearly extrapolated to 990 mb off the coast (still using 3-mb increments) to ensure that a sufficient range of conditions was included to capture the 10-year surge levels produced by tropical systems. This produced matrices that covered the same range of storm sizes, forward storm speeds, storm angles, and storm tracks considered within

Set A, extending estimates of surge response for storms with central pressures of 990 mb off the coast. The same near-coast filling rates and variations in size and Holland B parameters were used in Set B as were used in Set A.

Next, the probabilities for each small increment in our 5-dimensional space (storm track, storm intensity, storm size, storm forward speed, and storm angle) were estimated. For Set A the probabilities were estimated via the discretized estimate of the 5-dimensional joint probability density function shown below

$$\begin{aligned}
 p(c_p, R_p, v_f, \theta_l, x) &= \Lambda_1 \cdot \Lambda_2 \cdot \Lambda_3 \cdot \Lambda_4 \cdot \Lambda_5 \\
 \Lambda_1 &= p(c_p | x) = \frac{\partial F[a_0(x), a_1(x)]}{\partial c_p} = \frac{\partial}{\partial x} \left\{ \exp \left\{ -\exp \left[\frac{c_p - a_0(x)}{a_1(x)} \right] \right\} \right\} \quad (\text{Gumbel Distribution}) \\
 \Lambda_2 &= p(R_p | c_p) = \frac{1}{\sigma(\Delta P)\sqrt{2\pi}} e^{-\frac{(\bar{R}_p(\Delta P) - R_p)^2}{2\sigma^2(\Delta P)}} \\
 \Lambda_3 &= p(v_f | \theta_l) = \frac{1}{\sigma\sqrt{2\pi}} e^{-\frac{(\bar{v}_f(\theta_l) - v_f)^2}{2\sigma^2}} \\
 \Lambda_4 &= p(\theta_l | x) = \frac{1}{\sigma(x)\sqrt{2\pi}} e^{-\frac{(\bar{\theta}_l(x) - \theta_l)^2}{2\sigma^2(x)}} \\
 \Lambda_5 &= \Phi(x)
 \end{aligned} \tag{78}$$

where the overbars denote average values of the dependent variable for a specified value of an independent variable in a regression equation, $a_0(x)$ and $a_1(x)$ are the Gumbel coefficients for the assumed Gumbel form of the central pressures, and $\Phi(x)$ is the frequency of storms per year per specified distance along the coast (taken as one degree in examples presented here).

To represent the probabilities due to the storms in Set B, the same probabilities of the different speed classes and storm angles were used as were used in Set A; however, the storm frequency was adjusted to represent the occurrence rate for the low-intensity storms contained in Set B. For Set A, data from OWI had been found to suffice to estimate the probability density function; however, for Set B we had to rely on the more complete set of data contained online in NOAA's HURDAT file. In the area covered by the track region contained in the JPM integral, there were 5.4 small storms for every track during the last 58 years (1940-2007). Over this relatively small range of pressures this was converted to a constant rate of 0.09 storm per year per track (for all combinations of sizes, forward speeds, and angles) for the six pressure increment categories used in the JPM integral contribution by the small storms.

The storm size probabilities were generated using the same conditional distribution used in Set A, but because this distribution depends on storm size, this produced a shift of the overall probability distribution toward higher values in Set B. The probability of storm intensity for the region from 960 mb to 990 mb could not be estimated from the OWI data set used in the formulation of the Set A probabilities because it only contained storms that were Saffir Simpson Category 2 and larger, which roughly equates to a 970-mb storm. To investigate these small storms, the HURDAT data set from NOAA was used. Analyses showed very little trend in the storm probabilities; thus, the probability density function for these low-intensity storms was assumed to be constant over the range from 960 mb to 990 mb.

Storm Set B, the low-intensity storms, were created as stated above, by using a minimum pressure of 975 mb off the coast. All other storm parameters were kept as defined in Storm Set A. Storms in Set A, high-intensity storms, were grouped into four $C_p - R_p$ (Central pressure – scaling Radius) combinations along primary and secondary tracks (see Section 4.5.) Creation of Storm Set B followed this combination and storms were created for all tracks, and the 975 mb off the coast C_p was combined with each R_p , V_f , H_b , and mean angle parameters. This combination produced a total of 71 storms for both eastern and western Louisiana. Tables 38 through 40 identify both the low- and high-intensity storm parameter combinations and the east and west storm numbers.

4.9.7 Blending Across Louisiana-Mississippi Border

The blending region was initiated along a line with a southern point at latitude 30.1582609854 degrees North and longitude 89.6080251925 degrees West and a northern point at latitude 30.3948431074 degrees North and longitude 89.6803389732 degrees West. Blending started at the southern tip of this line and ran to the northern tip of this line, with a linear interpolation over the region from 30 degrees North to the southern tip of the line to smooth the transition into this blended area. The blending algorithm was a simple linear (orthogonal) distance interpolation extending over a distance of 0.0494461 degree (latitude) from the line noted above. On the western side of this blending region, the weighting was 1.0 on the FEMA Region 6 values. On the eastern side of this blending region, the weighting was 1.0 on the FEMA Region 4 values. Inside this blending region, the blended value was given by

IDS 2

$$\text{Value}_{\text{blended}} = w_1 \text{Value}_{\text{Region 4}} + w_2 \text{Value}_{\text{Region 6}}$$

where

$$w_1 = \frac{(\text{distance from eastern boundary of blending region})}{0.0494461}$$

and

$$w_2 = 1.0 - w_1 \tag{79}$$

5.0 REFERENCES

- Amorocho, J., and J.J. DeVries. 1980. "A new evaluation of the wind stress coefficient over water surfaces." *J. Geophys. Res.*, 85(C1), 433-442.
- Arcement, G.J., and V.R. Schneider. 1989. "Guide for Selecting Manning's Roughness Coefficients for Natural Channels and Flood Plains", *U.S. Geological Survey Water-Supply Paper 2339*, U.S. Geological Survey, Denver, Colorado.
- ASCE. 1990. "Minimum design loads for buildings and other structures", *ASCE 7-88*, New York.
- ASCE. 1996. "Minimum design loads for buildings and other structures", *ASCE 7-95*, New York.
- Atkinson, J.H., J.J. Westerink, and J.M. Hervouet. 2004. "Similarities between the Quasi-Bubble and the Generalized Wave Continuity Equation Solutions to the Shallow Water Equations," *International Journal for Numerical Methods in Fluids*, 45, 689-714.
- Barnes, H.H. 1967. "Roughness Characteristics of Natural Channels," *U.S. Geological Survey Water-Supply Paper 1849*, U.S. Geological Survey, Washington D.C.
- Berger, R.C., and S.E. Howington. 2002. "Discrete Fluxes and Mass Balance in Finite Elements," *ASCE J. Hydraulic Engineering*, 128(1), 87-92.
- Blain, C.A., J.J. Westerink, and R.A. Luetlich. 1994. "The influence of domain size on the response characteristics of a hurricane storm surge model." *J. Geophys. Res., [Oceans]*, 99 (C9), 18467-18479.
- Blain, C.A., J.J. Westerink, and R.A. Luetlich. 1998. "Grid convergence studies for the prediction of hurricane storm surge." *Int. J. Num. Meth. Fluids*, 26, 369-401.

Flood Insurance Study: Southeastern Louisiana

IDS 2

Booij, N., J. G. Haagsma, I. L.H. Holthuijsen, A.T.M.M. Kieftenburg, R.C. Ris, A.J. van der Westhuysen, and M. Zijlema. 2004. *SWAN Cycle III Version 40.41 Users Manual*, Delft University of Technology, Delft, The Netherlands, 118 p, <http://fluidmechanics.tudelft.nl/swan/index.htm>.

Booij, N., R.C. Ris, and L.H. Holthuijsen. 1999. "A Third-Generation Wave Model for Coastal Regions, Part I: Model Description and Validation," *J. Geophys. Res.*, 104(C4), 7649-7666.

Borgman, L.E, M. Miller, L. Butler, and R. Reinhard. 1992. "Empirical simulation of future hurricane storm histories as a tool in engineering and economic analysis", *Proc. Fifth Intn'l, Conf. on Civil Engr. In the Ocean*, ASCE, November, College Station, Texas.

Cardone, V. 2006. Oceanweather, Inc. Personal communication.

Cardone, V.J., A.T. Cox, J.A. Greenwood, and E.F. Thompson. 1994. "Upgrade of the tropical cyclone surface wind field model." *Miscellaneous Paper CERC-94-14*, U.S. Army Corps of Engineers. Available at: ERDC Vicksburg (WES), U.S. Army Engineer Waterways Experiment Station (WES), ATTN: ERDC-ITL-K, 3909 Halls Ferry Road, Vicksburg, Mississippi, 39180-6199.

Cardone, V.J., and A.T. Cox. 1992. "Hindcast Study of Hurricane Andrew, Offshore Gulf of Mexico." *Rep. Joint Industry Project*. Oceanweather, Inc., Cos Cob, Connecticut.

Cardone, V.J., C.V. Greenwood, and J.A. Greenwood. 1992. "Unified program for the specification of hurricane boundary layer winds over surfaces of specified roughness." *Contract Report CERC-92-1*, U.S. Army Corps of Engineers. Available at: ERDC Vicksburg (WES), U.S. Army Engineer Waterways Experiment Station (WES), ATTN: ERDC-ITL-K, 3909 Halls Ferry Road, Vicksburg, Mississippi, 39180-6199.

Cardone, V.J., W.J. Pierson, and E.G. Ward. 1976. "Hindcasting the directional spectra of hurricane generated waves". *J. PetroleumTechnologies*, 28, 385-394.

Charnock, H. 1955. "Wind stress on a water surface." *Quart. J. Royal Met. Society*, 81: 639-640.

Chouinard, L.E., C. Liu, and C.K. Cooper. 1997. "A model for the severity of hurricanes in the Gulf of Mexico". *J. Waterways, Harbor and Coastal Engineering.*, ASCE, 123, 113-119.

Chow, S. 1971. "A study of the wind field in the planetary boundary layer of a moving tropical cyclone". M.S. Thesis, New York University.

Chow, V.T. 1959. "Open Channel Hydraulics," McGraw-Hill Book Company, New York.

Collins, J.I., and M.J. Viehmann. 1971. "A simplified model for hurricane wind fields", *Paper 1346, Offshore Technology Conference*, Houston, Texas.

Flood Insurance Study: Southeastern Louisiana

IDS 2

Cox, A. 2006. Oceanweather, Inc. Personal communication.

Cox, A.T., and V.J. Cardone. 2000. "Operational system for the prediction of tropical cyclone generated winds and waves." *6th International Workshop on Wave Hindcasting and Forecasting*, November 6-10, 2000, Monterey, California.

Cox, A.T., J.A. Greenwood, V.J. Cardone, and V.R. Swail. 1995. "An interactive objective kinematic analysis system." *Fourth International Workshop on Wave Hindcasting and Forecasting*, Banff, Alberta, Canada, Atmospheric Environment Service, 109-118.

Dawson, C., J.J. Westerink, J.C. Feyen, and D. Pothina. 2006. "Continuous, Discontinuous and Coupled Discontinuous-Continuous Galerkin Finite Element Methods for the Shallow Water Equations," *Int. J. for Num. Meth. Fluids*, 52, 63-88.

Dietrich, J.C., R.L. Kolar, and K.M. Dresback. (in press). "Mass Residuals as a Criterion for Mesh Refinement in Continuous Galerkin Shallow Water Models", *ASCE J. Hydraulic Engineering*.

Dietrich, J.C., R.L. Kolar, and R.A. Luetlich. 2005. "Assessment of ADCIRC's Wetting and Drying Algorithm." School of Civil Engineering and Environmental Science, University of Oklahoma, Norman, Oklahoma, 73019. cdietrich@ou.edu.

Dokka, R.K. 2006a. Professor, Louisiana State University College of Civil and Environmental Engineering, Geodesy, Geoinformatics and Surveying Group. Unpublished data.

Dokka, R.K. 2006b. "Modern-day tectonic subsidence in coastal Louisiana," *Geology*. April.

Dokka, R.K., G.F. Sella, and T.H. Dixon. 2006. "Tectonic control of subsidence and southward displacement of southeast Louisiana with respect to stable North America", *Geophysical Research Letters*. December.

Ebersole, B.A., and J.J. Westerink. 2006. On-site visit. March.

Ebersole, B.A., J.J. Westerink, D.T. Resio, and R.G. Dean. 2007. "Performance Evaluation of the New Orleans and Southeast Louisiana Hurricane Protection System, Final Report of the Interagency Performance Evaluation Task Force", *Volume IV – The Storm*, U.S. Army Corps of Engineers, Washington, D.C. March 26.

Emanuel, K.A. 1988. "The maximum intensity of hurricanes." *J. Atmos. Sci.*, 45, 1143-1155.

ERDC. "Opteron processors." <http://www.erdc.hpc.mil/>.

Federal Emergency Management Agency. 1992. "Converting the National Flood Insurance Program to the North American Vertical Datum of 1988."

Flood Insurance Study: Southeastern Louisiana

IDS 2

Federal Emergency Management Agency. 2005. "HAZUS: Hazard loss estimation methodology." <http://www.fema.gov/hazus/index.shtm>.

Feyen, J.C., J.H. Atkinson, and J.J. Westerink. 2000. "Issues in hurricane surge computations using a GWCE-based finite element model." *Proc., XIII Conf. on Computational Methods in Water Resources*, Vol. II, L. Bentley, J. Sykes, C. Brebbia, W. Gray, and G. Pinder, Eds., 865-872.

Galland, J., N. Goutal, and J. Hervouet. 1991. "A new numerical model for solving the shallow water equations." *Adv. Water Res.*, 14: 138-148.

Garratt, J.R. 1977. "Review of drag coefficients over oceans and continents." *Mon. Wea. Rev.*, 105, 915-929.

Garster, J., B. Bergen, and D. Zilkoski. 2007. "Performance Evaluation of the New Orleans and Southeast Louisiana Hurricane Protection System, Final Report of the Interagency Performance Evaluation Task Force, Volume II – Geodetic Vertical and Water Level Datums", U.S. Army Corps of Engineers, Washington, D.C. March 26.

General Bathymetric Chart of the Oceans, *British Oceanographic Data Centre Centenary Edition-2003*, <http://www.bodc.ac.uk>.

GMT: The Generic Mapping Tools, <http://gmt.soest.hawaii.edu/>.

Google. 2007. Google Earth. <http://earth.google.com/>.

Gringorten, I.I. 1962. "A simplified method of estimating extreme values from data samples," *J. Appl. Meteorol.*, vol. 2,82-89.

Gringorten, I.I. 1963. "A Plotting Rule for Extreme Probability Paper," *J. Geophys. Res.*, Vol. 68, No. 3, pp. 813-814.

Gumbel, E.J. 1959. "Multivariate distributions with given margins." *Revista da faculdade de Ciencias. Serie A* 2(2):178–218

Gunther, H. 2005. *WAM Cycle 4.5 Version 2.0*, Institute for Coastal Research, GKSS Research Centre Geesthacht, 38pp.

Hagen, S.C., J.J. Westerink, and R.L. Kolar. 2000. "Finite element grids based on a localized truncation error analysis." *Int. J. Num. Meth. Fluids*, 32, 241-261.

Hagen, S.C., J.J. Westerink, R.L. Kolar, and O. Horstmann. 2001. "Two dimensional unstructured mesh generation for tidal models." *Int. J. Num. Meth. Fluids*, 35, 669-686.

Hartley, S., R. Pace, III, J.B. Johnston, M. Swann, C. O'Neil, L. Handley, and L. Smith. 2000. *A GAP analysis of Louisiana: Final report and data: Lafayette, Louisiana, U.S. Department of the Interior, U.S. Geological Survey.*

Flood Insurance Study: Southeastern Louisiana

IDS 2

Hendershott, M.C. 1981. "Long waves and ocean tides," *Evolution of Physical Oceanography*. B.A. Warren and C. Wunsch, ed., MIT Press, Cambridge, MA, 292-341

Henderson, F.M. 1966. "Open Channel Flow," Macmillan Publishing Company, New York.

Ho, F.P., and V.A. Myers. 1975. "Joint Probability Method of Tide Frequency Analysis applied to Apalachicola Bay and St. George Sound, Florida," *NOAA Technical Report NWS 18*, 43p.

Ho, F.P., J.C. Su, K.L. Hanevich, R.J. Smith, and F.P. Richards. 1987. "Hurricane Climatology for the Atlantic and Gulf Coasts of the United States," *NOAA Technical Report NWS 38*, completed under agreement EMW-84-E-1589 for FEMA, 194 p.

Holland, G. 1980. "An analytical model of the wind and pressure profiles in hurricanes." *Monthly Weather Review*, 108, 1212-1218.

Holthuijsen, L.H., N. Booij, and R.C. Ris. 1993. "A spectral wave model for the coastal zone," *Proc. of 2nd Int. Symposium on Ocean Wave Measurement and Analysis*, New Orleans, USA, 630-641.

Hsu, S. 1988. *Coastal Meteorology*. Academic Press, 260 pp.

Hubertz, J.A. 1992. "User's guide to the Wave Information Studies (WIS) wave model, version 2.0." *WIS Report 27*, U.S. Army Engineer Waterways Experiment Station, Vicksburg, MS.

Hughes, T.J.R., G. Engel, L. Mazzei, and M.G. Larson. 2000. "The Continuous Galerkin Method is Locally Conservative," *J. Computational Physics*, 163(2), 467-488.

Huh, O.K.; H.H. Roberts, L.J. Rouse, and D.A. Rickman. 1991. "Fine grain sediment transport and deposition in the Atchafalaya and Chenier Plain sedimentary system." In: *Proceedings Coastal Sediments '91*. Seattle, Washington, pp. 817-830.

Irish, Resio, & Ratcliff. 2006. "The influence of hurricane size on coastal storm surges", submitted to *J. Phys. Oceanog.*

Jensen, R.E., V.J. Cardone, and A.T. Cox. 2006. "Performance of third generation wave models in extreme hurricanes", *Ninth International Workshop on Wave Hindcasting and Forecasting*, Banff, Alberta, Canada, Atmospheric Environment Service.

Kalnay, E., M. Kanamitsu, R. Kistler, W. Collins, D. Deaven, L. Gandin, M. Iredell, S. Saha, G. White, J. Woollen, Y. Zhu, M. Chelliah, W. Ebisuzaki, W. Higgins, J. Janowiak, K.C. Mo, C. Ropelewski, J. Wang, A. Leetmaa, R. Reynolds, R. Jenne, and D. Joseph. 1996. "The NCEP/NCAR 40-year reanalysis project." *Bulletin of the American Meteorological Society*. American Meteorological Society, Boston, Massachusetts. Vol. 77, no. 3, pp. 437-471 (1 p.3/4).

IDS 2

Kimball, S.K. 2006. "A modeling study of hurricane landfalls in a dry environment," *Mon. Wea. Rev.*, 134, 1901-1918.

Kinnmark, I. 1986. "The Shallow Water Wave Equations: Formulation, Analysis, and Application," *Lecture Notes in Engineering*, 15, Springer-Verlag, Berlin, 187 pp.

Knabb, R.D., J.R. Rhome, and D.P. Brown. 2005. "Tropical Cyclone Report, Hurricane Katrina, 23-30 August 2005," National Hurricane Center, NOAA, 20 December, http://www.nhc.noaa.gov/pdf/TCR-AL122005_Katrina.pdf

Knabb, R.D., J.R. Rhome, and D.P. Brown. 2006. "Tropical Cyclone Report, Hurricane Rita, 18-26 September 2005," National Hurricane Center, NOAA, 17 March, http://www.nhc.noaa.gov/pdf/TCR-AL182005_Rita.pdf

Kolar, R.L., and J.J. Westerink. 2000. "A Look Back at 20 Years of GWC-Based Shallow Water Models," *Computational Methods in Water Resources XIII, Vol. 2*, Bentley et al., eds. 899-906, Balkema.

Kolar, R.L., and W.G. Gray. 1990. "Shallow Water Modeling in Small Water Bodies," *Computational Methods in Surface Hydrology, Gambolati et al.*, eds., Computational Mechanics Publications/Springer-Verlag, Southampton/Berlin, 149-155.

Kolar, R.L., J.J. Westerink, M.E. Cantekin, and C.A. Blain. 1994. "Aspects of nonlinear simulations using shallow water models based on the wave continuity equation." *Comput. Fluids*, 23, 523-538.

Komen, G., L. Cavaleri, M. Donelan, K. Hasselmann, S. Hasselmann, and P.A.E.M. Janssen. 1994. *Dynamics and Modelling of Ocean Waves*. Cambridge University Press, Cambridge, UK, 560 pages.

Kubatko, E.J., J.J. Westerink, and C. Dawson. 2006a. "An Unstructured Grid Morphodynamic Model with a Discontinuous Galerkin Method for Bed Evolution," *Ocean Modeling*, 15, 71-89.

Kubatko, E.J., J.J. Westerink, and C. Dawson. 2006b. "Discontinuous Galerkin Methods for Advection Dominated Problems in Shallow Water Flow," *Computer Methods in Applied Mechanics and Engineering*, 196, 437-451.

Kubatko, E.J., J.J. Westerink, and C. Dawson. 2007. "Semi-discrete Discontinuous Galerkin Methods and Stage Exceeding Order Strong Stability Preserving Runge-Kutta Time Discretizations," *Journal of Computational Physics*, 222, 832-848.

Le Provost, C., A.F. Bennett, and D.E. Cartwright. 1995. "Ocean tides for and from TOPEX/POSEIDEN," *Science* 267, 639-642.

Le Provost, C., F. Lyard, J. Molines, M. Genco, and F. Rabilloud. 1998. "A hydrodynamic ocean tide model improved by assimilating a satellite altimeter-derived data set." *J. Geophys. Res. [Oceans]*, 103, 5513-5529.

Flood Insurance Study: Southeastern Louisiana

IDS 2

Lillicrop, J. 2006. Coastal Engineering Research Center, U.S. Army Corps of Engineers, USACE Waterways Experiment Station, Vicksburg, Mississippi. Personal communication.

Link, L.E., J.J. Jaeger, J. Stevenson, W. Stroupe, R.L. Mosher, D. Martin, J.K. Garster, D.B. Zilkoski, B.A. Ebersole, J.J. Westerink, D.T. Resio, R.G. Dean, M.K. Sharp, R.S. Steedman, J.M. Duncan, B.L. Moentenich, B. Howard, J. Harris, S. Fitzgerald, D. Moser, P. Canning, J. Foster, and B. Muller. 2006. "Performance Evaluation of the New Orleans and Southeast Louisiana Hurricane Protection System," *Volume I – Executive Summary and Overview, Draft Final Report of the Interagency Performance Evaluation Task Force*, U.S. Army Corps of Engineers, Washington, D.C. June.

Louisiana State University. 2004. Louisiana Lidar. <http://atlas.lsu.edu/lidar/>.

Luettich, R.A., and J.J. Westerink. 1995. "Continental shelf scale convergence studies with a barotropic model." *Quantitative Skill Assessment for Coastal Ocean Models, Coastal and Estuarine Studies Series No. 47*, D.R. Lynch and A.M. Davies, Eds., Amer. Geophys. Union, 349-371.

Luettich, R.A., and J.J. Westerink. 1999. "Elemental wetting and drying in the ADCIRC hydrodynamic model: upgrades and documentation for ADCIRC version 34.XX." *Contractors Report*, U.S. Army Corps of Engineers. Available at: ERDC Vicksburg (WES), U.S. Army Engineer Waterways Experiment Station (WES), ATTN: ERDC-ITL-K, 3909 Halls Ferry Road, Vicksburg, Mississippi, 39180-6199.

Luettich, R.A., and J.J. Westerink. 2003. "Combined discharge and radiation boundary condition in the ADCIRC hydrodynamic model: theory and documentation." *Contractors' Report*, U.S. Army Corps of Engineers New Orleans District. Available at: U.S. Army Engineer Corps of Engineers, New Orleans, ATTN: CEMVN-IM-SM Library, P.O. Box 60267, New Orleans, Louisiana, 70160-0267.

Luettich, R.A., and J.J. Westerink. 2004. "Formulation and Numerical Implementation of the 2D/3D ADCIRC Finite Element Model Version 44.XX". Available at: http://adcirc.org/adcirc_theory_2004_12_08.pdf.

Luettich, R.A., J.J. Westerink, and N.W. Scheffner. 1992. "ADCIRC: an advanced three-dimensional circulation model for shelves, coasts and estuaries, report 1: theory and methodology of ADCIRC-2DDI and ADCIRC-3DL." *Tech. Rep. DRP-92-6*, U.S. Army Corps of Engineers. Available at: ERDC Vicksburg (WES), U.S. Army Engineer Waterways Experiment Station (WES), ATTN: ERDC-ITL-K, 3909 Halls Ferry Road, Vicksburg, Mississippi, 39180-6199.

Lynch, D.R., and W.G. Gray. 1979. "A wave equation model for finite element tidal computations." *Comput. Fluids*, 7, 207-228.

McGee, B.D., B.B. Goree, R.W. Tollett, B.K. Woodward, and W.H. Kress. 2005. "Hurricane Rita Surge Data, Southwestern Louisiana and Southeastern Texas, September to November 2005," *U.S. Geological Survey Data Series 220*.

Flood Insurance Study: Southeastern Louisiana

IDS 2

McGee, B.D., B.B. Goree, R.W. Tollett, B.K. Woodward, and W.H. Kress. 2006. "Hurricane Rita Surge Data, Southwestern Louisiana and Southeastern Texas, September to November 2005." *U.S. Geological Survey*, <http://pubs.water.usgs.gov/ds220>.

Mississippi Automated Resource Information System. 2006. Mississippi island 10 meter by 10 meter DEM. <http://www.maris.state.ms.us/HTM/DownloadData/DEM.html>.

Mukai, A., J.J. Westerink, and R.A. Luetlich. 2001a. "Guidelines for Using the Eastcoast 2001 Database of Tidal Constituents within the Western North Atlantic Ocean, Gulf of Mexico and Caribbean Sea," *Coastal and Hydraulic Engineering Technical Note*, U.S. Army Engineer Research and Development Center.

Mukai, A., J.J. Westerink, R.A. Luetlich, and D. Mark. 2001b. "A Tidal Constituent Database for the Western North Atlantic Ocean, Gulf of Mexico and Caribbean Sea," *Technical Report*, U.S. Army Engineer Research and Development Center.

Mukai, A., J.J. Westerink, R.A. Luetlich, and D. Mark. 2002. "Eastcoast 2001: a tidal constituent database for the Western North Atlantic, Gulf of Mexico and Caribbean Sea," U.S. Army Corps of Engineers Research and Development Center, Coastal and Hydraulics Laboratory, *Technical Report, ERDC/CHL TR-02-24*. 201p. September.

Myers, V.A. 1954. "Characteristics of United States hurricanes pertinent to levee design for Lake Okeechobee, Florida," *Hydromet. Rep. No. 32*, U.S. Weather Bureau, Washington, D.C.

Myers, V.A. 1975. "Storm Tide Frequencies on the South Carolina Coast," *NOAA Tech. Rep. NWS-16*, 79 p.

Myers, V.A., and E.S. Jordan. 1956. "Winds and pressures over the sea in the hurricane of September 1938." *Monthly Weather Review*, 84 (7) 261-270 July 1956.

National Geodetic Survey: Vertical datums. <http://www.ngs.noaa.gov/>.

Niedoroda, A. 2007. URS Corporation, Tallahassee, Florida. Personal communication.

NOAA. 2001. "Sea Level Variations of the United States 1854-1999." *Technical Report NOS CO-OPS 36*, Silver Spring, Maryland. July.

NOAA. 2006. "Tides and currents." http://www.tidesandcurrents.noaa.gov/station_retrieve.shtml?type=Harmonic+Constituents.

NOAA. 2007. "Sea level stations." <http://www.tidesandcurrents.noaa.gov/sltrends/sltrends.html>.

Oceanweather, Inc. "Kinematic wind model data assimilation." <http://www.oceanweather.com/>.

Pourtaheri, Hasan. 2001. Personal communication.

Flood Insurance Study: Southeastern Louisiana

IDS 2

Powell, M., and S. Houston. 1996. "Hurricane Andrew's landfall in South Florida. Part II: Surface wind fields and potential real-time applications." *Wea. Forecasting*, 11, 329-349.

Powell, M., S. Houston, and T. Reinhold. 1996. "Hurricane Andrew's landfall in South Florida. Part I: Standardizing measurements for documentation of surface windfields." *Wea. Forecasting*, 11, 304-328.

Powell, M., S. Houston, L. Amat, and N. Morrisseau-Leroy. 1998. "The HRD real-time hurricane wind analysis system." *J. Wind Engr. Indust. Aero.*, 77-78: 53-64.

Powell, M.D., P.J. Vickery, and T.A. Reinhold. 2003. "Reduced drag coefficient for high wind speeds in tropical cyclones." *Nature*, 422 (6929): 279-283 March 20, 2003.

Reid, R.O. 1990. "Water Level Changes - Tides and Storm Surges, Handbook of Coastal and Ocean Engineering," Gulf Publishing Co.

Reid, R.O., and R. Whitaker. 1976. "Wind-driven flow of water influenced by a canopy." *J. Waterw., Harbors, Coastal Engr. Div.- Am. Soc. Civ. Eng.*, 102, WW1, 61-77.

Resio, D.T., and E.A. Orelup. 2006. "Potential effects of climatic variability in hurricane characteristics on extreme waves and surges in the Gulf of Mexico," submitted to *J. Climate*.

Resio, D., S. Bratos, and E. Thompson. 2002. "Meteorology and Wave Climate." In: Vincent, L., and Demirbilek, Z. (editors), *Coastal Engineering Manual, Part II, Hydrodynamics, Chapter II-2, Engineer Manual 1110-2-1100*, U.S. Army Corps of Engineers, Washington, DC.

Ris, R., L. Holthuijsen, J.M. Smith, N. Booij, and A. van Dongeren. 2002. "The ONR Test Bed for Coastal and Oceanic Wave Models", *Proceedings, ICCE 2002, World Scientific*, 380-391.

Ris, R.C. 1997. "Spectral modeling of wind waves in coastal areas," (Ph.D. Dissertation Delft University of Technology, Department of Civil Engineering), *Communications on Hydraulic and Geotechnical Engineering, Report No. 97-4*, Delft, The Netherlands.

Salinger, A. 2006. Personal communication.

Schwerdt, R.W., Ho, F.P., and R.R. Watkins. 1979. "Meteorological criteria for Standard Project Hurricane and Probable Maximum Hurricane Windfields, Gulf and East Coasts of the United States," *Tech. Rep. NOAA-TR-NWS-23*, National Oceanic and Atmospheric Administration.

Shen, W. 2006. "Does the size of hurricane eye matter with its intensity?" *Geophys. Res.Let.*, 33, L18813.

Sheremet, A., A.J. Mehta, B. Liu, and G.W. Stone. 2005. "Wave-sediment interaction on a muddy inner shelf during Hurricane Claudette." *Estuarine, Coastal and Shelf Science*, 63, 225-233.

Flood Insurance Study: Southeastern Louisiana

IDS 2

Simiu, E., and R. Scanlan. 1986. "Wind Effects on Structures." *Wiley Interscience*, 604 pp.

Slinn, D. 2007. Department of Civil and Coastal Engineering, University of Florida, Gainesville, Florida, 32611-6590. Personal communication.

Smith, J.M. 2000. "Benchmark Tests of STWAVE," *Proceedings, 6th International Workshop on Wave Hindcasting and Forecasting*, Environment Canada, 369-379.

Smith, J.M. 2001. "Modeling Nearshore Wave Transformation with STWAVE," *ERDC/CHL CHETN I-64*. U.S. Army Engineer Research and Development Center, Vicksburg, MS. <http://chl.wes.army.mil/library/publications/chetn/>

Smith, J.M. 2002. "Grid Nesting with STWAVE", *U.S. Army Engineer Corp Report*. <http://chl.erd.usace.army.mil/library/publications/chetn/pdf/chetn-i-66.pdf>.

Smith, J.M., and A.K. Zundel. 2006. "Full-Plane STWAVE: I. SMS Graphical Interface," *ERDC/CHL CHETN I-71*. U.S. Army Engineer Research and Development Center, Vicksburg, MS. <http://chl.wes.army.mil/library/publications/chetn/>.

Smith, J.M., and A.R. Sherlock. (in publication). "Full-Plane STWAVE: II. Model Overview," *Coastal and Hydraulics Engineering Technical Note CHETN I-73*, U.S. Army Engineer Research and Development Center, Vicksburg, MS.

Smith, J.M., H.E. Bermudez, and B.A. Ebersole. 2000. "Modeling Waves at Willapa Bay, Washington," *Proceedings, 27th International Conference on Coastal Engineering, ASCE*, 826-839.

Smith, J.M., A.R. Sherlock, and D.T. Resio. 2001. "STWAVE: Steady-State Spectral Wave Model User's Manual for STWAVE, Version 3.0." USACE, Engineer Research and Development Center, *Technical Report ERDC/CHL SR-01-1*, Vicksburg, MS 80 pp. <http://chl.erd.usace.army.mil/Media/2/4/4/erdch-sr-01-11.pdf>.

Smith, J.M., A. Militello, and S.J. Smith. 1998. "Modeling Waves at Ponce de Leon Inlet, Florida," *Proceedings, 5th International Workshop on Wave Hindcasting and Forecasting, Environment Canada*, pp. 201-214.

Smith, S.J., and J.M. Smith. 2001. "Numerical Modeling of Waves at Ponce de Leon Inlet, Florida." *J. Waterway, Port, Coastal and Ocean Engineering*, 127(3), 176-184.

Smith, J.M., and C.L. Vincent. 2002. "Application of Spectral Equilibrium Ranges in the Surf Zone." *28th International Conference on Coastal Engineering, July 2002, Cardiff, Wales*.

SMS: The Surface Water Modeling System, http://www.ems-i.com/SMS/SMS_Overview/sms_overview.html.

Flood Insurance Study: Southeastern Louisiana

IDS 2

Spargo, E., K. Hess, E. Myers, Z. Yang, and A. Wong. 2005. "Tidal Datum Modeling in Support of NOAA's Vertical Datum Transformation Tool." 9th International Conference on Estuarine and Coastal Modeling, October 31-November 2, 2005, Charleston, South Carolina.

Stone, G.W., A. Sheremet, X. Zhang, Q. He, B. Liu, and B. Strong. 2003. "Landfall of two tropical systems seven days apart along southcentral Louisiana, USA." *Proceedings of Coastal Sediments '03*, Clearwater Beach, Florida, USA, 333-334.

Suhayda, J. 2007. Taylor Engineering, Baton Rouge, Louisiana. Personal communication.

SWAMP Group. 1985. *Ocean Wave Modeling*, Plenum, New York, 256p.

Teng, C.C., and R.H. Bouchard. 2005. "Directional wave data measured from data buoys using angular rate sensors and magnetometers," *Ocean Wave Measurements and Analysis, Barcelona Spain, ASCE*

Thompson, E.F., and V.J. Cardone. 1996. "Practical Modeling of Hurricane Surface Windfields". *Journal of Waterway, Port, Coastal and Ocean Engineering* Vol 122, No. 4. July/August.

Thompson, E.F., J.M. Smith, and H.C. Miller. 2004. "Wave Transformation Modeling at Cape Fear River Entrance, North Carolina." *J. Coastal Research*, 20 (4), 1135-1154.

Tolman, H.L. 1997. "User Manual and System Documentation of WAVEWATCH-III version 1.15." *Technical Note*, 97 pp.

Tolman, H.L. 1999. "User Manual and System Documentation of WAVEWATCH-III version 1.18." *Technical Note*, 110pp.

University of Texas. "Infiniband switch Lonestar." <http://www.tacc.utexas.edu/>.

URS. 2006a. "Final coastal and riverine high-water marks collection for Hurricane Rita in Texas," Final Report for the Federal Emergency Management Agency.

URS. 2006b. "Final coastal and riverine high-water marks collection for Hurricane Rita in Louisiana," Final Report for the Federal Emergency Management Agency.

URS. 2006c. HMTAP Task Order 18, Mississippi Coastal Analysis Project, *Geospatial Technology Task Report* (Task 3).

URS. 2006d. "Final coastal and riverine high-water marks collection for Hurricane Katrina in Louisiana," Final Report for the Federal Emergency Management Agency.

Flood Insurance Study: Southeastern Louisiana

IDS 2

- URS. 2006e. "Final coastal and riverine high-water marks collection for Hurricane Katrina in Mississippi," Final Report for the Federal Emergency Management Agency.
- U.S. Army Corps of Engineers, New Orleans District. 2000. *Aerial Survey of Lake Pontchartrain Vicinity and Chalmette Loop Levee Systems*. May.
- U.S. Army Corps of Engineers, Mobile District. 2005. "Lidar Report Mississippi and Alabama Coastal Mapping".
- U.S. Army Corps of Engineers. 2006. "Model User's manual for STWAVE, Version 3.0," *ERDC/CHL SR-01-1*, Engineer Research and Development Center, Vicksburg, Mississippi.
- U.S. Army Corps of Engineers. 2007. "Performance Evaluation of the New Orleans and Southeast Louisiana Hurricane Protection System. Final Report of the Interagency Performance Evaluation Task Force; Volume IV – The Storm." 26 March.
- USGS. 2000. "A GAP Analysis of Louisiana," Final Report. June.
- USGS. 2004. National Elevation Dataset. <http://gisdata.usgs.net/ned/>.
- USGS. 2007. National Elevation Dataset accuracy. <http://ned.usgs.gov/Ned/accuracy.asp>.
- Vickery, P.J. 2005. "Simple empirical models for estimating the increase in the central pressure of tropical cyclones after landfall along the coastline of the United States." *Journal of Applied Meteorology*, 44 (12): 1807-1826 Dec 2005.
- Vickery, P. 2006. Principal Engineer, Applied Research Associates, Inc. Personal communication.
- Vickery, P.J., P.F. Skerjil, and L.A. Twisdale. 2000. "Simulation of hurricane risk in the U.S. using empirical track model," *J. Struct. Engr.*, 1222-1237.
- Vogelmann, J.E., S.M. Howard, L. Yang, C.R. Larson, B.K. Wylie, and N. Van Driel. 2001. "Completion of the 1990s National Land Cover Data Set for the Conterminous United States from Landsat Thematic Mapper Data and Ancillary Data Sources", *Photogrammetric Engineering and Remote Sensing*, 67:650-652.
- Weaver, R.J., and D.N. Slinn. 2005. "Effects of Wave Forces on Storm Surge," Submitted to *Coastal Engineering*.
- Wessel, P., and W.H.F. Smith. 1996. "A Global Self-consistent, Hierarchical, High-resolution Shoreline Database," *J. Geophys. Res.*, 101, #B4, pp. 8741-8743.
- Westerink, J.J. 1993. "Tidal prediction in the Gulf of Mexico/Galveston Bay using model ADCIRC-2DDI," Contractors Report to the U.S. Army Engineer Waterways Experiment Station, Vicksburg, Mississippi. January.

Flood Insurance Study: Southeastern Louisiana

IDS 2

Westerink, J.J., and W.G. Gray. 1991. "Progress in Surface Water Modeling," *Reviews of Geophysics, Supplement*, 29, 210-217.

Westerink, J.J., J.C. Feyen, J.H. Atkinson, R.A. Luettich, C. Dawson, H.J. Roberts, M.D. Powell, J.P. Dunion, E. J. Kubatko, and H. Pourtaheri. 2007. "A Basin to Channel Scale Unstructured Grid Hurricane Storm Surge Model Applied to Southern Louisiana," *Monthly Weather Review*, In Press.

Westerink, J.J., R.A. Luettich, A.M. Baptista, N.W. Scheffner, and P. Farrar. 1992. "Tide and storm surge predictions using a finite element model," *J. Hydraul. Eng.*, 118, 1373-1390.

Westerink, J.J., R.A. Luettich, and A. Militello. 2001. "Leaky Internal-Barrier Normal-Flow Boundaries in the ADCIRC Coastal Hydrodynamics Code." *Coastal and Hydraulic Engineering Technical Note IV-XX*, U.S. Army Corps of Engineers. Available at: ERDC Vicksburg (WES), U.S. Army Engineer Waterways Experiment Station (WES), ATTN: ERDC-ITL-K, 3909 Halls Ferry Road, Vicksburg, Mississippi, 39180-6199.

Westerink, J.J., R.A. Luettich, and J.C. Muccino. 1994. "Modeling Tides in the Western North Atlantic Using Unstructured Graded Grids," *Tellus*, 46A, 178-199.

Westerink, Joannes, B. Ebersole, and H. Winer. 2006. "Note on the Influence of the Mississippi River Gulf Outlet on Hurricane Induced Storm Surge in New Orleans and Vicinity." U.S. Army Corps of Engineers, Louisiana.

FIGURES

TABLES

APPENDIX A

OWI Storm Data

APPENDIX B

**OWI Model Sample Files –
Storm Track**

APPENDIX C

**OWI Model Sample Files –
TROP Format**

APPENDIX D

**OWI Model Sample Files –
PRE/WIN Format**